SCALABLE CONTROL OF ISLANDED MICROGRIDS

Matricola: 432907

Dipartimento di Ingegneria Industriale e dell'Informazione
Identification and Control of Dynamic Systems Laboratory

Università degli Studi di Pavia

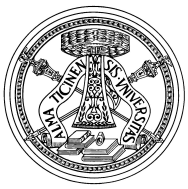

A Ph.D. dissertation by

Michele Tucci

Prof. Giancarlo Ferrari Trecate, advisor
Prof. Giuseppe De Nicolao, tutor

Pavia, 2014-2017

To my family

È una somma di piccole cose...
— Niccolò Fabi

Acknowledgements

This thesis would have never been possible without the support of many incredible people.

First of all, I must express my deepest gratitude to Professor Giancarlo Ferrari Trecate for his patience, expertise and motivation. He has really been my guide during these years, not only regarding academic matters. He is an amazing person and I will be always in debt for his great, incredible support.

I also wish to thank Professor Giuseppe De Nicolao for giving me the possibility to continue my PhD at the University of Pavia.

I would like to thank Professor Josep M. Guerrero and Professor Juan Carlos Vasquez; they gave me the opportunity to visit the Microgrid Research Laboratory at Aalborg University and to validate my theoretical results through experimental tests. A special thank goes also to Dr. Lexuan Meng and to Renke Han for their friendly cooperation.

Another big thanks goes to Dr. Stefano Riverso, Dr. Kostas Kouramas and Dr. Marcin Cychowski. They gave me the opportunity to join the Control & Decision Support group at the United Technologies Research Center-Ireland (UTRC-I) for five months and to improve my technical skills. In particular, I wish to express my sincere gratitude to Stefano; his friendship, insightful comments, discussions and suggestions have been crucial not only to my work in UTRC-I, but also to this thesis. He is one of the wiser person I ever met, and he will always be my reference as a Scientist.

Also, I would like to thank all people of the ICDS Lab and all the master students I had the possibility to work with. In particular, a big thanks goes to Alessandro, Giuseppe and Davide.

I wish to express my sincere gratitude to all people of the Automatic Control Laboratory at EPFL, from the secretaries to the research staff, post-docs, technical research assistants, professors, masters and PhD students. Thank you all for letting me be part of your incredible family during the last year and a half of my PhD journey. In particular, I wish to thank my *El Clásico* mates: Luca, Tomasz, Diogo and Tafarel. Moreover, I owe my gratitude to *My Bombers*: Mustafa and Pulkit. I will always be grateful to them for their friendship and for the positive attitude they have brought in the office. I really wish them all the best.

I am truly indebted to Marcello (Cellone) and Giorgio (Giorgione). I feel very lucky and glad to have met them; their sincere friendship and

unconditional support have been crucial to this work.

Likewise, I would thank my old friends Dappo, Gianni, Gioia, Meg and *My Girls* Eleonora and Federica for being always there and sharing many funny moments with me. Moreover, a huge thanks goes to Fra and Ste, my closest friends. This thesis would have never been possible without them.

Thanks Santa for having constantly tested my threshold of psychophysical tolerance throughout these years.

Last but not least, I thank Mamma, Papà, Guido and Federica, my family, from the deepest of my heart. Without their endless love, understanding and continuous encouragement I would not be here today. This work is dedicated to them.

Pavia, 15 January 2018

Michele

Abstract

In the recent years, the increasing penetration of renewable energy sources has motivated a growing interest for microgrids, energy networks composed of interconnected Distributed Generation Units (DGUs) and loads. Microgrids are self-sustained electric systems that can operate either connected to the main grid or detached from it. In this thesis, we focus on the latter case, thus dealing with the so-called Islanded microGrids (ImGs). We propose scalable control design methodologies for both AC and DC ImGs, allowing DGUs and loads to be connected in general topologies and enter/leave the network over time. In order to ensure safe and reliable operations, we mirror the flexibility of ImGs structures in their primary and secondary control layers. Notably, off-line control design hinges on Plug-and-Play (PnP) synthesis, meaning that the computation of individual regulators is complemented by local optimization-based tests for denying dangerous plug-in/out requests. The solutions presented in this work aim to address some of the key challenges arising in control of AC and DC ImGs, while overcoming the limitations of the existing approaches. More precisely, this thesis comprises the following main contributions: *(i)* the development of decentralized primary control schemes for load-connected networks (i.e. where local loads appear only at the output terminals of each DGU) ensuring voltage stability in DC ImGs, and voltage and frequency stability in AC ImGs. In contrast with the most commonly used control strategies available in the literature, our regulators guarantee offset-free tracking of reference signals. Moreover, the proposed primary local controllers can be designed or updated on-the-fly when DGUs are plugged in/out, and the closed-loop stability of the ImG is always preserved. *(ii)* Novel approximate network reduction methods for handling totally general interconnections of DGUs and loads in AC ImGs. We study and exploit Kron reduction in order to derive an equivalent load-connected model of the original ImG, and designing stabilizing voltage and frequency regulators, independently of the ImG topology. *(iii)* Distributed secondary control schemes, built on top of primary layers, for accurate reactive power sharing in AC ImGs, and current sharing and voltage balancing in DC ImGs. In the latter case, we prove that the desired coordinated behaviors are achieved in a stable fashion and we describe how to design secondary regulators in a PnP manner when DGUs are added/removed to/from the network. *(iv)* Theoretical results are validated through extensive simulations, and some of the proposed design algorithms have been successfully tested on real ImG platforms.

Acronyms

AC Alternating Current

aAC-KR approximate AC Kron Reduction

CPS Cyber-Physical System

DC Direct Current

DGU Distributed Generation Unit

EMS Energy Management System

GES Globally Exponentially Stable

GPS Global Positioning System

hKR hybrid Kron Reduction

ImG Islanded microGrid

KCL Kirchhoff's Current Law

KR Kron Reduction

KVL Kirchhoff's Voltage Law

LMI Linear Matrix Inequality

LQR Linear Quadratic Regulator

LV Low Voltage

mG microGrid

MV Medium Voltage

MPC Model Predictive Control

PCC Point of Common Coupling

PI Proportional Integral

PID Proportional Integral Derivative

PMS Power-Management System

PnP Plug-and-Play

PoL Point of Load

PSSS Periodic Sinusoidal Steady State

QSL Quasi-Stationary Line

RES Renewable Energy Source

RHP Right-Half-Plane

RMS Root Mean Square

THD Total Harmonic Distortion

VSC Voltage Source Converter

List of Figures

1.1 Schematic representation of a microgrid. Square blocks represent DGUs and loads, while arrows connecting numbered nodes are power lines. 3
1.2 Hierarchical control architecture for AC microgrids: control layers and associated tasks. 7
1.3 Hierarchical control architecture for DC microgrids: control layers and associated tasks. 7
1.4 Scalable control design methods. In the CPS in Figure 1.4a, the synthesis of local controller $\mathcal{C}_{[3]}$ requires information from subsystem 3 only (decentralized design). In the example in Figure 1.4b, the design of $\mathcal{C}_{[3]}$ exploits also information from the parents of unit 3, i.e. subsystems 2 and 4 (parent-based design). 11
1.5 Plug-and-play synthesis: automatic check of plug-in request in a CPS. When subsystem 5 is added to the network, the existence of a local controller $\mathcal{C}_{[5]}$ guaranteeing global properties is checked using information about subsystem 5 only (decentralized test in Figure 1.5a), or exploiting also information about its parent, i.e. subsystem 1 (parent-based test in Figure 1.5b). Notice that, in the latter case, also the children of subsystem 5 (subsystems 1 and 4) must perform the feasibility check. 13

2.1 Electrical scheme of a DC mG composed of two radially connected DGUs with unmodeled loads. 22
2.2 Single phase equivalent electrical scheme of an AC ImG composed of two radially connected DGUs with unmodeled loads. 24

3.1 Control scheme with integrators for the overall DC mG. . . 37
3.2 DC mG - Electrical scheme of DGU i, power line ij, and local PnP voltage controller. 39
3.3 Block diagram of closed-loop DGU i with pre-filter. 45
3.4 Overall DC mG control scheme with compensation of measurable disturbances $d_{[i]}(s)$. 48
3.5 Features of PnP controllers for Scenario 1 when the DGUs are not interconnected. 52

3.6 Scenario 1 - Voltage at PCC_1. 53
3.7 Scenario 1 - Voltage at PCC_2. 53
3.8 Features of PnP controllers for Scenario 1 when the DGUs are connected together. 54
3.9 Scenario 1 - Performance of PnP decentralized voltage control in presence of load switches at time $t = 3$ s. 55
3.10 Scenario 2 - Scheme of the mG composed of 5 DGUs until $t = 4$ s (in black) and of 6 DGUs after the plugging in of $\hat{\Sigma}^{DGU}_{[6]}$ (in green). Blue nodes represent DGUs modeled as in the dashed box in Figure 3.2, with a local load connected to each PCC. Black arrows identify RL power lines. 56
3.11 Features of PnP controllers for Scenario 2 with 5 interconnected DGUs. 57
3.12 Features of PnP controllers for Scenario 2 with 6 interconnected DGUs 58
3.13 Scenario 2 - Performance of PnP decentralized voltage controllers during the hot plug-in of DGU 6 at time $t = 4$ s. . . 59
3.14 Scenario 2 - Performance of PnP decentralized voltage controllers in terms of robustness to an abrupt change of load resistances at time $t = 8$ s. 60
3.15 Scenario 2 - Scheme of the mG composed of 5 DGUs after the unplugging of $\hat{\Sigma}^{DGU}_{[3]}$ at time $t = 12$ s. 61
3.16 Features of PnP controllers for Scenario 2 after the unplugging of DGU 3. 61
3.17 Scenario 2 - Performance of PnP decentralized voltage controllers during the hot-unplugging of DGU 3 at $t = 12$ s. . . 62
3.18 Bumpless control transfer scheme. The three switches close simultaneously at time $\bar{t}$. 68

4.1 Performance of PnP decentralized voltage controllers during the plug-in of DGU 6 at time $t = 4$ s. 83
4.2 Performance of PnP decentralized voltage controllers in terms of robustness to an abrupt change of load resistances at time $t = 8$ s. 84
4.3 Performance of PnP decentralized voltage controllers during the unplugging of DGU 3 at $t = 12$ s. 85
4.4 Visual comparison between the performance of the line-dependent and the line-independent approach when the plug-in of a DGU is performed. 86

4.5 Visual comparison between the performance of the line-dependent and the line-independent approach when the unplugging of a DGU is performed. 87
4.6 LMI results for combinations of R_t, L_t and C_t. Blue circles indicate feasible LMIs while red stars correspond to infeasible ones. The green box encloses typical DGU parameters for LV DC mGs. 97
4.7 Finding the maximum number of DGUs which can be connected to PCC_1 before obtaining a plug-in request failure. . 98

5.1 Graph representation of an mG. 106
5.2 Complete hierarchical control scheme of DGU i. 109
5.3 Hierarchical control scheme and Primary Loop (PL) approximations. 110
5.4 Simulation stages: numbered nodes represent DGUs, while black lines denote power lines. The secondary control layer is activated for the DGUs contained in the red area. Open switches in stages 1, 2, 3 and 6 denote disconnected DGUs. The arrow in stage 5 represents a step up in the load current of DGU 1. 123
5.5 Simulation results: evolution of measured output currents, output currents in p.u., voltages at PCCs and average PCCs voltage. Lines in the plots are associated with different DGUs and they are color-coded as in Figure 5.4. Simulation stages are those shown in Figure 5.4. 124
5.6 Experimental validation: mG setup (top-left), topologies of the electrical and communication graphs (bottom-left), and implemented control architecture (on the right). 126
5.7 Experimental results for the mG in Figure 5.6. In the time interval from 2.5 s to 15 s, DGUs are connected together and primary PnP voltage regulators are enabled. From time 15 s onwards, also the secondary control layer is active. At time 25 s, the local load of DGU 3 is halved. 126
5.8 Topology of $\mathcal{G}_1$. 132
5.9 Topology of $\mathcal{G}_2$. 133

6.1 Control scheme with integrators for the overall AC ImG. . . 147
6.2 AC ImG - Single-phase equivalent scheme of DGU i, power line ij, and local PnP voltage and frequency controller. . . 149

7.1 Example of network transformation. Red squares indicate DGUs with corresponding local loads I_{Li} (appearing, e.g., in Figure 6.2), while the blue circle in Figure 7.1a denotes the unique load at the common bus. Black arrows identify balanced power lines. 158

7.2 Electrical scheme of a bus-connected ImG composed of three DGUs and a common unmodeled load. 160

7.3 Bus-connected DGU equipped with local PnP regulator and virtual impedance loop. 161

7.4 Singular values for the closed-loop ImG with two DGUs. . . 163

7.5 Coordinated control layer: computation of correction terms ΔV_{PoL} and $\Delta\phi_{PoL}$. Parameters K_{PV} and $K_{P\phi}$ are the voltage and phase proportional coefficients, while T_{IV} and $T_{I\phi}$ are the voltage and phase integral time constants. 165

7.6 Scheme of the coordinated control. 166

7.7 Control scheme for the computation of ΔV_i^Q. Parameters K_{PQ} and T_{IQ} are the reactive power proportional term and the reactive power time constant, respectively. 168

7.8 Experimental validation: ImG setup and implemented control scheme. 169

7.9 Voltage regulation at the PCCs with resistive load (Section 7.5.2). Red, green and blue lines are, respectively, for VSCs 1, 2 and 3. Load change, plug-in and unplugging events are indicated with orange, magenta and black arrows, respectively. The plots in Figures 7.9a and 7.9b refer to the voltages of phase a of the three-phase converters composing the ImG (see the scheme in Figure 7.8b). 177

7.10 Voltage regulation at the PCCs with unbalanced load (Section 7.5.2). 178

7.11 Voltage regulation at the PCCs with nonlinear load (Section 7.5.2). Red, green and blue lines are, respectively, for VSC 1, 2 and 3. Load change, plug-in and unplugging events are indicated with orange, magenta and black arrows, respectively. The plots in Figures 7.11a and 7.11b refer to the voltages of phase a of the three-phase converters composing the microgrid (see the scheme in Figure 7.8b). 179

7.12 PnP regulators and coordinated controllers for voltage tracking at the PoL with nonlinear load. Red, green and blue lines are, respectively, for VSC 1, 2 and 3. Load change, plug-in and unplugging events are indicated with orange, magenta and black arrows, respectively. Moreover, the grey arrow denotes the activation of secondary controllers described in Section 7.4.1. The plots in Figures 7.12a and 7.12b refer to the voltages of phase a of the three-phase converters composing the microgrid (see the scheme in Figure 7.8b). 180

7.13 PnP regulators and coordinated controllers for voltage tracking at the PoL and reactive power sharing with nonlinear load. Red, green and blue lines are respectively for VSC 1, 2 and 3. Load change, plug-in and unplugging events are indicated with orange, magenta and black arrows, respectively. Moreover, the grey arrow denotes the simultaneous activation of secondary controllers described in Sections 7.4.1 and 7.4.2. 181

8.1 Graph representing an electrical network. 187

8.2 Example 8.1 - Original and reduced networks. Boundary and interior nodes are represented by red squares and blue circles, respectively. 190

8.3 Numerical examples: original and reduced networks. Red and blue boxes enclose boundary and interior nodes, respectively. 200

8.4 Example 8.3 - Evaluation of the output currents generated through aAC-KR and hKR, in presence of a linear load. . . 201

8.5 Example 8.4 - Evaluation of the features of aAC-KR and hKR in presence of a nonlinear load. 202

8.6 Example of a graph associated with an ImG. Red squares denote DGUs (i.e. boundary nodes), while blue circles represent loads (i.e. internal nodes). 204

8.7 21-bus network: red squares denote boundary nodes (i.e. DGUs), blue circles represent internal nodes (i.e. loads). . . 206

8.8 Simulation of a 21-bus ImG: Kron reduced networks. 208

8.9 Eigenvalues and singular values of the QSL ImG when all the switches are open, or only SW_1 is closed. 208

8.10 Eigenvalues and singular values with SW_1, SW_2 closed, and SW_3, SW_4 open. 209

8.11 Eigenvalues and singular values when SW_1, SW_2, SW_3 are closed, and SW_4 open. 209
8.12 Eigenvalues and singular values of the QSL ImG when all the switches are closed. 210
8.13 Performance of PnP control and approximate KR methods with a 21-bus network. Switches SW_1, SW_2, SW_3 and SW_4 are closed at times $t = 5$ s, $t = 6.5$ s, $t = 8$ s and $t = 9.5$ s, respectively. 211

9.1 Simulation of a 10-DGUs ImGs: considered network topologies. 227
9.2 Performance of PnP voltage and frequency control. Connection of DGU 10, load change at PCC 10, and disconnection of DGUs 3 and 7, are performed at times $t = 7.5$ s, $t = 10$ s and $t = 12$ s, respectively. 237
9.3 Results of subproblems SP1 and SP2 for different combinations of R_t, L_t and C_t. Blue circles indicate successfully passed tests while red stars correspond to failed ones. The green box encloses typical DGU parameters for LV and MV AC ImGs. 238

List of Tables

3.1 Electrical parameters of the mG with dynamics (3.48). . . . 67
3.2 Scenario 1 - Electrical setup of DGU $* \in \{1, 2\}$ and line parameters. . . . 70
3.3 Scenario 2 - Buck filter parameters for DGU $\hat{\Sigma}_{[i]}^{DGU}$, $i = \{1, \ldots, 6\}$. . . . 70
3.4 Scenario 2 - Power line parameters. . . . 71
3.5 Scenario 2 - Voltage references for DGUs $\hat{\Sigma}_{[i]}^{DGU}$, $i = \{1, \ldots, 6\}$. . . . 71
3.6 Scenario 2 - Common parameters of DGU $\hat{\Sigma}_{[i]}^{DGU}$, $i = \{1, \ldots, 6\}$. 71

4.1 Electrical and optimization parameters. . . . 99

5.1 Electrical parameters. . . . 136

7.1 Virtual impedance parameters. . . . 175
7.2 Voltage tracking at the PoL. . . . 176
7.3 Reactive power sharing. . . . 176
7.4 Electrical setup parameters. . . . 176

8.1 Example 8.1 - Line parameters of the original and reduced network. . . . 190
8.2 Parameters of the original networks. . . . 212
8.3 Parameters of the reduced networks. . . . 212
8.4 Parameters of the original 21-bus network. . . . 213
8.5 Linear loads parameters. . . . 214
8.6 Nonlinear loads connected to the buses. . . . 214
8.7 Equivalent parameters when SW_2, SW_3 and SW_4 are open. 214
8.8 Equivalent parameters when SW_1 SW_2 are closed, while SW_3 and SW_4 are open. . . . 215
8.9 Equivalent parameters when SW_1, SW_2 and SW_3 are closed, and SW_4 is open. . . . 215
8.10 Equivalent parameters when all the four switches are open. 215

Contents

1 Introduction **1**
- 1.1 Concept of microgrid . . . 1
- 1.2 Challenges in islanded microgrids . . . 4
- 1.3 Existing approaches to the control of islanded microgrids . . . 5
  - 1.3.1 Control of AC microgrids . . . 6
  - 1.3.2 Control of DC microgrids . . . 6
  - 1.3.3 Limitations of the existing control approaches . . . 8
- 1.4 Scalable control design . . . 9
  - 1.4.1 Scalable control design for cyber-physical systems . . . 9
  - 1.4.2 Plug-and-play design of local controllers . . . 10
  - 1.4.3 Scalable control design for microgrids . . . 12
- 1.5 Thesis contributions and overview . . . 14

2 Microgrid modeling **21**
- 2.1 Introduction . . . 21
- 2.2 Electrical model of DC DGUs and lines . . . 21
- 2.3 Electrical model of AC DGUs and lines . . . 23

I Scalable control of DC microgrids **27**

3 Line-dependent plug-and-play control of DC microgrids **29**
- 3.1 Introduction . . . 30
- 3.2 DC microgrid model . . . 31
  - 3.2.1 QSL model of a microgrid composed of 2 DGUs . . . 32
  - 3.2.2 QSL model of a microgrid composed of N DGUs . . . 35
- 3.3 Plug-and-play decentralized voltage control . . . 36
  - 3.3.1 Decentralized control scheme with integrators . . . 36
  - 3.3.2 Decentralized plug-and-play control . . . 38
  - 3.3.3 QSL approximations as singular perturbations . . . 44
  - 3.3.4 Enhancements of local controllers for improving performances . . . 45
  - 3.3.5 Algorithm for the design of local controllers . . . 48
  - 3.3.6 Plug-and-play operations . . . 49
  - 3.3.7 Hot plugging in/out operations . . . 50
- 3.4 Simulation results . . . 50

3.4.1 Scenario 1 . . . 50
3.4.2 Scenario 2 . . . 56
3.5 Final comments . . . 60
3.6 Appendix . . . 62
3.6.1 Proof of Theorem 3.1 . . . 62
3.6.2 How interactions among DGUs can destabilize a DC mG . . . 65
3.6.3 Bumpless control transfer . . . 67
3.6.4 Overall model of a microgrid composed of N DGUs 69
3.6.5 Electrical and simulation parameters of Scenario 1 and 2 . . . 70

4 Line-independent plug-and-play control of DC microgrids 73
4.1 Introduction . . . 73
4.2 DC microgrid model . . . 74
4.3 Design of stabilizing voltage controllers . . . 75
4.3.1 Structure of local controllers . . . 75
4.3.2 Conditions for stability of the closed-loop microgrid 76
4.3.3 Line-independent controller computation through LMIs 79
4.3.4 Plug-and-play operations . . . 81
4.4 Simulation results . . . 82
4.5 Final comments . . . 85
4.6 Appendix . . . 87
4.6.1 Proof of Proposition 4.2 . . . 87
4.6.2 Proof of Theorem 4.1 . . . 90
4.6.3 Feasibility of the LMI test (4.16) . . . 96

5 Consensus-based secondary control layer for stable current sharing and voltage balancing in DC microgrids 101
5.1 Introduction . . . 102
5.1.1 Microgrid modeling and primary control . . . 105
5.2 Secondary control based on consensus algorithms . . . 106
5.3 Modeling and analysis of the complete system . . . 108
5.3.1 Unit-gain approximation of primary control loops . . 108
5.3.2 First-order approximation of primary control loops . 115
5.3.3 Plug-and-play design of secondary control . . . 119
5.4 Validation of secondary controllers . . . 120
5.4.1 Simulation results . . . 120
5.4.2 Experimental results . . . 122
5.5 Final comments . . . 125

5.6 Appendix 127
5.6.1 Proof of Proposition 5.3 127
5.6.2 Proof of Theorem 5.1 128
5.6.3 Proof of Theorem 5.2 130
5.6.4 On the eigenvalues of $\mathbb{Q} = \mathbb{L}D\mathbb{M}$ 132
5.6.5 Electrical and simulation parameters 135

II Scalable control of AC islanded microgrids 137

6 Line-dependent plug-and-play control of AC islanded microgrids 139
6.1 Introduction 139
6.2 AC microgrid model 140
6.2.1 QSL model of a microgrid composed of 2 DGUs . . . 142
6.2.2 QSL model of a microgrid composed of N DGUs . . 145
6.3 Plug-and-play voltage and frequency control 146
6.3.1 Decentralized control scheme with integrators 146
6.3.2 Design of plug-and-play controllers 148
6.3.3 Plug-and-play operations 153

7 A hierarchical control architecture for bus-connected AC islanded microgrids 155
7.1 Introduction 156
7.2 Model of a bus-connected microgrid 157
7.3 Plug-and-play primary control layer 159
7.3.1 Control structure 159
7.3.2 Plug-and-play design of local controllers 161
7.3.3 Clock synchronization for primary control 162
7.3.4 Harmonic compensation by tuning the plug-and-play control bandwidth 162
7.4 Coordinated control 163
7.4.1 Voltage tracking at the PoL 164
7.4.2 Sharing of reactive power 167
7.5 Experimental results 167
7.5.1 Microgrid setup 167
7.5.2 Primary control layer validation 169
7.5.3 Primary and secondary layers validation 172
7.6 Final comments 172
7.7 Appendix 173

7.7.1 Proof of Lemma 7.1 . . . 173
7.7.2 Derivation of the approximate model (7.10) . . . 174
7.7.3 Electrical and control parameters of the experimental tests . . . 175

8 Plug-and-play control of AC islanded microgrids with general topologies 183
8.1 Introduction . . . 184
8.2 Kron reduction methods for electrical networks . . . 186
8.2.1 AC-KR . . . 187
8.2.2 Instantaneous KR . . . 191
8.3 Approximate KR methods . . . 192
8.3.1 Approximate AC-KR . . . 193
8.3.2 Hybrid KR . . . 194
8.3.3 Asymptotic equivalence between original and reduced network models . . . 196
8.3.4 Generalization to three-phase linear networks in dq coordinates . . . 198
8.4 Numerical examples . . . 199
8.5 Kron reduction of microgrids . . . 203
8.5.1 Islanded microgrid associated graph . . . 203
8.5.2 DGU and line electrical models . . . 203
8.5.3 Plug-and-play design for microgrids with general topologies . . . 204
8.6 Simulation of a 21-bus network . . . 205
8.6.1 Islanded microgrid topology . . . 206
8.6.2 Plug-and-play control design . . . 207
8.6.3 Simulation results . . . 209
8.7 Final comments . . . 211
8.8 Appendix . . . 212
8.8.1 Original and reduced parameters of Examples 8.3 and 8.4 . . . 212
8.8.2 Electrical parameters of the 21-bus network . . . 212

9 Line-independent plug-and-play control of AC islanded microgrids 217
9.1 Introduction . . . 217
9.2 AC microgrid model . . . 219
9.3 Design of plug-and-play stabilizing controllers . . . 220
9.3.1 Structure of local controllers . . . 220

9.3.2 Conditions for stability of the closed-loop microgrid 221
9.3.3 Computation of local controllers through numerical optimization . . . 224
9.3.4 Plug-and-play operations . . . 225
9.4 Simulation results . . . 226
9.5 Final comments . . . 228
9.6 Appendix . . . 229
9.6.1 Proof of Proposition 9.2 . . . 229
9.6.2 Proof of Theorem 9.1 . . . 231
9.6.3 Feasibility of the plug-in test (9.15) . . . 235

10 Conclusions and future research 239

III Appendices 243

A Mathematical notation and definitions 245
A.1 Basic notation . . . 245
A.2 Algebraic graph theory . . . 246
A.3 AC three-phase signals . . . 246
A.4 Signals representation . . . 246

Bibliography 266

Chapter 1

Introduction

Contents

1.1 Concept of microgrid 1
1.2 Challenges in islanded microgrids 4
1.3 Existing approaches to the control of islanded microgrids 5
1.3.1 Control of AC microgrids 6
1.3.2 Control of DC microgrids 6
1.3.3 Limitations of the existing control approaches . . 8
1.4 Scalable control design 9
1.4.1 Scalable control design for cyber-physical systems 9
1.4.2 Plug-and-play design of local controllers 10
1.4.3 Scalable control design for microgrids 12
1.5 Thesis contributions and overview 14

1.1 Concept of microgrid

Generation of electrical power is traditionally performed in a centralized fashion and the production of electric energy is mostly based on thermoelectric and nuclear plants, relatively small in number.

Over the past two decades, however, the scenario has started to change, moving towards local power generation using Renewable Energy Sources (RESs) like, e.g., solar cells, hydroelectric, natural gas, biomass, geothermal and wind power.

This paradigmatic shift in power system operation is motivated by different factors. At the top of the list, there is a surge of interest for discussions about environmental and health consequences of traditional electricity generation. Moreover, in the long term, a decrease in the use of nuclear plants is expected, due to their associated risks, especially after the events of Fukushima in March 2011. It is also a fact that fossil-fueled thermal power generation highly contributes to greenhouse gas emissions [VWB11]

which, in turn, have a remarkable impact on global warming and climate change [RMC+07]. These environmental and safety concerns have lead most of the developed countries to agree on international commitments for limiting global warming through progressive decarbonization (see, e.g., the Kyoto Protocol [Uni98] or the "Europe 2020" project [Eur98, dGC12]).

Another factor that is complicating the traditional generation structure is the increasing availability of RESs. Power generation based on RESs is referred to as distributed generation [AAS01], since the green power sources (termed Distributed Generation Units (DGUs)), are more numerous and more distributed along the grid than traditional generators. In this context, new control and operation strategies, allowing for more configurable and flexible transmission and distribution networks, are required in order to manage systems with a large number of RESs. This evolution of the traditional grid toward a new and more flexible *smart grid* is perceived as one of the major challenges in power distribution for the next years [Far10].

Microgrids are commonly recognized as one of the potential solution for facilitating the change in the traditional power systems operation. A microGrid (mG) is an autonomous electrical network composed of DGUs and loads, interconnected through power lines [Las02, LP04, GCLL13] (see Figure 1.1). Microgrids can operate either connected to the main grid or detached from it [GCLL13, FHE17, CDGH15, PMar]; in the latter case, these electrical networks are also referred to as Islanded microGrids (ImGs). There exist mGs in Alternating Current (AC), Direct Current (DC), as well as hybrid AC/DC mGs.

In AC mGs, RESs are interfaced to the network through power-electronic converters (notably, voltage-source inverters), and existing AC power system standards (such as frequency, voltage levels and principles of protection), are utilized for their operations [LM06].

Also DC mGs have started to gain interest in the recent years [DLVG16, EMM15], due to (i) the increasing number of DC loads (e.g. electronic appliances, LEDs and electric vehicles), (ii) the availability of efficient converters (Buck and Boost converters, employed in Low Voltage (LV) and Medium Voltage (MV) systems, respectively), and (iii) the need of interfacing DC energy sources (e.g. PV panels) and batteries with minimal power losses.

Overall, mGs find applications in rural areas, avionics, military bases, marine systems, hospitals and colleges [GCLL13, BWAT09], and have the following key features.

(i) They bring RESs close to the customers' loads, thus ensuring efficient

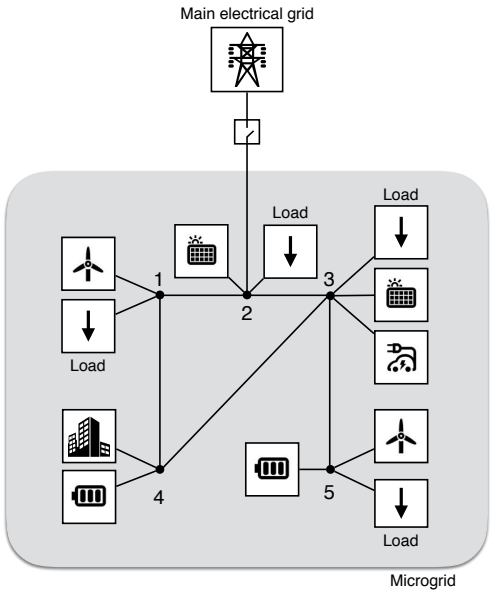

Figure 1.1: Schematic representation of a microgrid. Square blocks represent DGUs and loads, while arrows connecting numbered nodes are power lines.

power supply with reduced line losses.

(ii) Since mGs generate clean power, they reduce environmental pollution and global warming.

(iii) Microgrids can quickly switch to islanded operation mode in case of power grid failures, malfunctioning of electrical devices or lines tripping. This guarantees continuous power delivery to critical loads and helps system restoration.

(iv) Redundancy in generation units allows to increase the robustness of the electric system, enhancing, e.g., the mG resilience to faults. Moreover, defective or hacked components can be localized, isolated, fixed or replaced more easily.

(v) Microgrids can play a central role in the deregulation of the energy market by allowing the active participation of consumers and owners of small generation units [IA09].

In this thesis, we will focus on islanded AC and DC LV islanded microgrids. Moreover, we notice that, since DC mGs can be coupled to the

main grid through AC-DC converters only, they can be thought as always operating in islanded mode[1]. Hence, for the sake of simplicity, from now on we will omit the word "islanded" when referring to DC mGs detached from the main grid.

1.2 Challenges in islanded microgrids

In the following, we introduce the key challenges arising in ImGs and addressed in this thesis.

The first key objective is to ensure voltage and frequency stability (in the AC case), and voltage stability (in the DC case). Indeed, while in grid-connected AC mGs, collective voltage and frequency stability is guaranteed by the main grid, in islanded mode and in DC mGs, the control of the electrical quantities must be performed by DGUs. This represents a challenging task, especially if one allows for decentralized control schemes (in which each DGU is equipped with a local controller and different controllers do not communicate in real-time), and meshed network topologies (i.e. networks with loops in the electrical interconnection of DGUs).

Another important task considered in this thesis is accurate power sharing among DGUs. Power sharing is defined as the capability to achieve a desired steady-state distribution of the power outputs of all DGUs, while satisfying the load demand in the network [SSRS16]. In particular, in the present work, we address the problem of ensuring reactive power sharing in AC ImGs. This is an issue of practical interest in networks where generation sources and loads are in close proximity [SSRS16], as for mGs.

The last two problems studied in this thesis are current sharing and voltage balancing in DC mGs. Current sharing is understood as the ability of the DGUs to compensate constant load currents proportionally to given parameters (like, e.g., the converter ratings), independently of the mG topology and line impedances. This feature is crucial for preserving the safety of the system, as unregulated currents may overload generators and eventually lead to failures or system blackout [HHY$^+$16]. Voltage balancing, instead, refers to the goal of keeping the average output voltage of DGUs close to a prescribed level. Load devices are designed to be supplied by a nominal reference voltage: it is therefore important to ensure that the voltages at the load buses are spread around this value.

Besides the aforementioned challenges, several other important tasks

[1]This is due to the fact that converters have finite power rating, which can limit substantially the power transfer.

should be addressed in order to ensure reliable and secure operation of microgrids. Among these issues, we recall active power sharing and safe transition from grid-connected to islanded-operation mode (and vice-versa) in AC networks, as well as optimal power and energy management in both AC and DC microgrids. For these problems, which have not been studied in this thesis, we refer the reader to [GVM+11, JMLJ13, MSFT+17].

In the next section, we summarize some relevant approaches to the control of AC and DC islanded microgrids that have been proposed in the literature for addressing the challenges considered in the present work.

1.3 Existing approaches to the control of islanded microgrids

The most commonly used architecture for addressing the challenges discussed in Section 1.2 is hierarchical control [GVM+11]. Strongly inspired by the control concept proposed for conventional power systems [MBB97], hierarchical architectures allow to fulfill separate control tasks in different regulation layers.

At the primary level, DGUs are usually equipped with decentralized regulators for voltage and frequency regulation (in AC networks) and voltage control (in DC networks). On top of primary control schemes, secondary regulators are employed for ensuring more advanced behaviors, such as power sharing, current sharing and voltage balancing. These objectives are achieved by allowing local controllers to exchange information over a communication network.

In the light of the above considerations, mGs equipped with hierarchical control architectures represent a prominent example of Cyber-Physical Systems (CPSs). A CPS can be seen as a group of tightly coupled subsystems interacting with each other through physical or communication channels[2] [KM15, MS11]. In mGs, the physical layer is given by the electrical couplings among converters through power lines, while the cyber part is identified by the combination of (i) computational resources available at each DGU location and (ii) communication channels. The possibility to embed computational capabilities at the level of individual subsystems and to make subsystems exchange information through a network has started to receive attention in the recent years. It follows that the field of CPSs

[2]Other examples of CPSs can be seen in smart homes and buildings, alarm systems, data centers, robotics systems, autonomous vehicular systems and transportation [KM15].

is still an open research area. We refer the reader to, e.g., [KM15] for a review of recent advancements and open challenges regarding such complex systems.

In the following, we conduct a brief review of the existing approaches to control of mGs which are relevant for the scope of this thesis, differentiating between AC and DC systems.

1.3.1 Control of AC microgrids

The primary level of the hierarchical control architecture is usually decentralized and based on local inner voltage and current loops combined with decentralized droop controllers [GCLL13, CD96, KIL05, PL06, GMdV$^+$07]. Droop control makes each inverter of the ImG mimic the behavior of a synchronous generator of conventional power systems under the traditional primary control. Therefore, this control strategy consists in introducing artificial droops in inverters output frequencies and voltages, so as to obtain a sort of virtual inertia [VDH08]. Since droop control is decentralized, communication among DGUs is not required.

On top of primary controllers, a secondary control layer is often conceived to compensate frequency and voltage amplitude deviations introduced by droop regulators [CD96, KI06, IEE11], to compensate voltage unbalances [MZT$^+$16] or to ensure accurate power sharing [MASSG12, Lu13, SGV14]. The two latter objectives are typically addressed via distributed consensus algorithms relying on a communication network.

Finally, a tertiary control layer can be implemented for achieving additional advanced behaviors, which, however, are not considered in this work. Hence, we refer the reader to, e.g., [GVM$^+$11, VDBH$^+$05] for further details. Figure 1.2 shows a schematic representation of a hierarchical control architecture for AC microgrids.

1.3.2 Control of DC microgrids

At the primary layer, DGUs are typically equipped with decentralized regulators aiming to control local voltages and currents [DLVG16]. As for the AC case, the most popular solution for primary control is droop control [SDVG14b, ZD15, DLVG16], where local regulators are built on top inner voltage and current loops [GVM$^+$11]. The principle of conventional droop control applied to DC mGs is to linearly reduce the voltage reference for the voltage inner loop of each DGU by a quantity that is proportional to the corresponding output current [MSFT$^+$17, SDVG14b, SDVG14a].

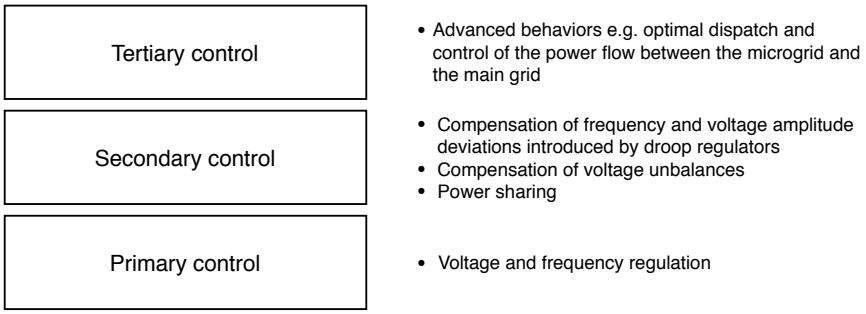

Figure 1.2: Hierarchical control architecture for AC microgrids: control layers and associated tasks.

An alternative approach to primary control of DC mGs has been presented in [ZD15]. In this paper, the authors propose a variant of the conventional primary droop regulators in which (i) inner current and voltage loops are not implemented, and (ii) the voltage reference to each generating unit is provided by Proportional Integral (PI) local regulators.

Secondary control is usually employed for compensating voltage deviations due to droop controllers or for achieving advanced behaviors, such as proportional current sharing among DGUs [MDRP$^+$16, ZD15, BDLG13, ADSJ14].

Similarly to the AC case, tertiary control layers are proposed in the literature for addressing other relevant challenges. However, since these issues are not considered in the present work, we refer the reader to [SDVG14b, GCLL13, ZD15] for additional information. In Figure 1.3, an example of a hierarchical control structure for DC microgrids is provided.

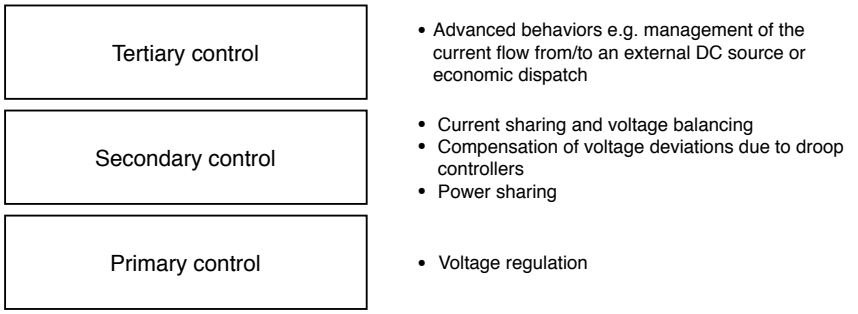

Figure 1.3: Hierarchical control architecture for DC microgrids: control layers and associated tasks.

1.3.3 Limitations of the existing control approaches

We start by discussing the main drawbacks of the control techniques for AC ImGs introduced in Section 1.3.1. First of all, we highlight that the conventional droop method was originally proposed for large power systems [ZW09], in which the output impedance of synchronous generators and the line impedances are mainly inductive. However, due to their short lengths, mGs lines can have non-negligible resistive parts [TJUM97]. Secondly, as mentioned in Section 1.3.1, primary droop regulators lead to deviations of steady-state frequency and voltage amplitude from their corresponding reference values. Furthermore, these deviations are highly affected by the load conditions.

Another fundamental issue of AC ImGs equipped with primary droop controllers is voltage and frequency stability [GCLL13]. Stabilizing each individual DGU, in fact, might be not enough, as the physical couplings through electric lines the can spoil overall stability. Stability proofs for droop-controlled AC ImGs have been proposed only recently [SPDB13, SOA$^+$14]. For other types of primary regulators, almost all studies focus on radial ImGs, and the case of meshed topologies has not been fully explored yet [GCLL13].

Next, we focus on the limitations of the control schemes for DC mGs discussed in Section 1.3.2. First, primary droop regulators do not ensure good voltage regulation, since they induce local voltage deviations [DLVG16]. Furthermore, voltage droop control itself cannot ensure accurate current sharing among the sources [MSFT$^+$17].

As for the AC case, a critical issue related to DC mGs equipped with decentralized droop controllers is voltage stability. To the best of our knowledge, a rigorous stability analysis has been performed only for specific mG topologies [SDVG14b, DLVG16]. The authors of [ZD15] provide a topology-independent stability analysis; however, it hinges on specific modeling and operational assumptions.

Overall, in absence of a reference topology for islanded mGs, an additional desired feature for the control architecture is *scalability* of the control design. This property, which is essential for developing modular control architectures that can be easily updated when the mG topology changes, is discussed in details in the next section.

1.4 Scalable control design

In Section 1.3, we have presented the most commonly used control architectures in the field of mGs for the online computation of the control actions. From the applicative point of view, it is also important to assess the complexity of the offline design of such controllers.

A desired feature for the offline control synthesis in complex CPSs (and, hence, also in mGs) is scalability, i.e. to guarantee that the complexity for designing local regulators is independent of the size of the overall system. Scalability is especially required when the number of subsystems changes over time, sensors and actuators are frequently replaced, or no global model of the plant is available.

In this section, we first focus on scalable control design in the field of CPSs. Then, we motivate the need for scalable synthesis procedures for mGs and review the existing control architectures in terms of offline design.

1.4.1 Scalable control design for cyber-physical systems

Control design methods for CPSs are called *scalable* if the computational cost for synthesizing a local controller capable to preserve collective network properties (e.g. stability or safety) is independent of the size of the overall system.

The first important point to highlight is that scalability of the control design does not necessarily follow from the implementation of decentralized architectures. Examples of design procedures for decentralized controllers which are not scalable can be found in [DC90] and [ZS10]; in these methods, the synthesis of local controllers guaranteeing collective stability for the whole system requires the knowledge of a certain number of closed-loop subsystems or the availability of the models of all subsystems. Therefore, the computational complexity of designing a single controller depends on the size the overall system.

Nonetheless, there exist several approaches to scalable design. A possibility is represented by *decentralized* design, where the computation of each local controller is performed using information from the corresponding subsystem only [BL88, Bai66, HST79] (see Figure 1.4a). Another possible approach is a bit more complex than the previous one, since it includes the additional constraint that the design of a local controller can use information at most from parents[3] of the corresponding subsystem (see Figure

[3]In a network of subsystems, the parent-child relationship is related to the coupling graph. For instance, in Figure 1.4, where couplings are given by the grey arrows, sub-

1.4b). For this reason, the latter method is referred to as *parent-based* design.

Both decentralized and parent-based design enjoy features which are important from the applicative point of view. These properties are collected in the following and denoted with "D" or "PB" if referred to decentralized or parent-based design, respectively.

(i) As already observed, both approaches are scalable. It means that the complexity of computing a local controller for each subsystem is independent of the total number of subsystems (D), or scales with the number of parents of the subsystem to control (PB).

(ii) No communication flow at the design stage is required (D), or it has the same topology of the coupling graph, which is usually sparse (PB).

(iii) If, at some point in time, a subsystem wants to join the existing network (thus performing a plug-in operation), no other subsystems (D), or at most subsystems that will have a new parent (PB), must retune their local controllers. All other controllers are not affected by the plug-in event. Similarly, if a subsystem leaves the network (thus performing an unplugging operation), no update of local controllers is needed (D), or, at most, only the children of the removed unit have to retune their regulators (PB).

Besides these key advantages, however, decentralized and parent-based design suffer from the following critical limitation. Since, at the design stage, the information flow for computing a single regulator is either absent or very limited, there is no guarantee that local control design will be always feasible irrespectively of the way subsystems are coupled with each other. This observation motivated the introduction of the control design methodology discussed next.

1.4.2 Plug-and-play design of local controllers

Plug-and-Play (PnP) design is a methodology that complements local control synthesis approaches described Section 1.4.1 with an automatic test for assessing the feasibility of the addition/removal of a subsystem to/from an existing network. In other words, whenever a plug-in/-out operation is required, the existence of local controllers preserving collective properties

systems 2 and 4 are parents of 3 because they influence its dynamics through physical couplings.

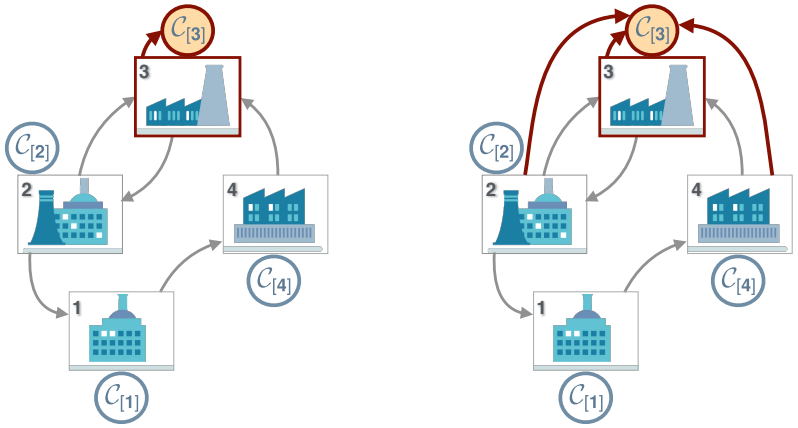

(a) Decentralized design.

(b) Parent-based design.

Figure 1.4: Scalable control design methods. In the CPS in Figure 1.4a, the synthesis of local controller $\mathcal{C}_{[3]}$ requires information from subsystem 3 only (decentralized design). In the example in Figure 1.4b, the design of $\mathcal{C}_{[3]}$ exploits also information from the parents of unit 3, i.e. subsystems 2 and 4 (parent-based design).

of the overall CPS (e.g. stability, safety and constraint satisfaction) is first verified. More in details, PnP design consists of the following steps.

1. Whenever a subsystem requests to join/leave the network, the existence of controllers capable to preserve global properties is checked in an automatic fashion. Similarly to the scalable design approaches described in the above section, this feasibility test can either exploit the model of the entering/leaving subsystem only (decentralized test), or require also information from parent subsystems (parent-based test). Notice that, in the latter case, also the children of the entering/leaving subsystem have to perform the automatic check. A graphical representation of this process is shown in Figure 1.5.
   If at least one of these tests fails, the plug-in/-out operation is denied, since it can be dangerous for the considered CPS.

2. If, on the other hand, the automatic checks succeed, then:

   - in case of a plug-in operation, one can proceed with local control design by employing one of the scalable approaches described in Section 1.4.1. In particular, only the regulator of the new

subsystem is computed (D), or, in addition, also local controllers of subsystems that will be children of the incoming unit must be retuned (PB).

- In case of an unplugging operation, no changes in the existing control scheme must be performed (D), or at most previous children of the leaving subsystem have to updated their local regulators (PB).

3. Finally, the plug-in/-out operation is performed online, with the guarantee that the desired collective properties of the considered CPS will be preserved.

PnP synthesis procedures are very attractive for CPSs with a number of subsystems which can vary over time. In particular, PnP design has interesting features from the modeling and the industrial point of view. At the modeling level, with PnP design there is no need to store a global model of whole system, which in some cases might not even exist. The computation of a local controller is based on the model of the corresponding subsystem only, and, at most, on the models of its parents. Moreover, the limited information flow at the design stage allows to cope with privacy requirements in multi-owner CPSs, where it might be undesirable for different players to disclose the complete model of the owned subsystem for allowing control design of another subsystem in the network.

PnP synthesis has also benefits at the industrial level, as it enables hardware replacement with minimal re-engineering effort. Indeed, the substitution of a faulty/old component with a fixed/new subsystem amounts to perform an unplugging operation followed by plug-in one; in this process, the feasibility of both operations is assessed automatically by the PnP design procedure.

In the recent years, PnP design has found application in the fields of control for constrained systems (where methods have been developed in the framework of decentralized [LKF15] and networked control structures [RFT15], and for Model Predictive Control (MPC) [RFFT13, RFFT15, ZPR$^+$13]), but also for distributed state estimation [RFSFT13, FC15] and fault detection [RBFTP16, BVL15, YJY16].

1.4.3 Scalable control design for microgrids

Microgrids are the key component of agile power systems that, according to [IA09], are one of the most promising emerging technologies.

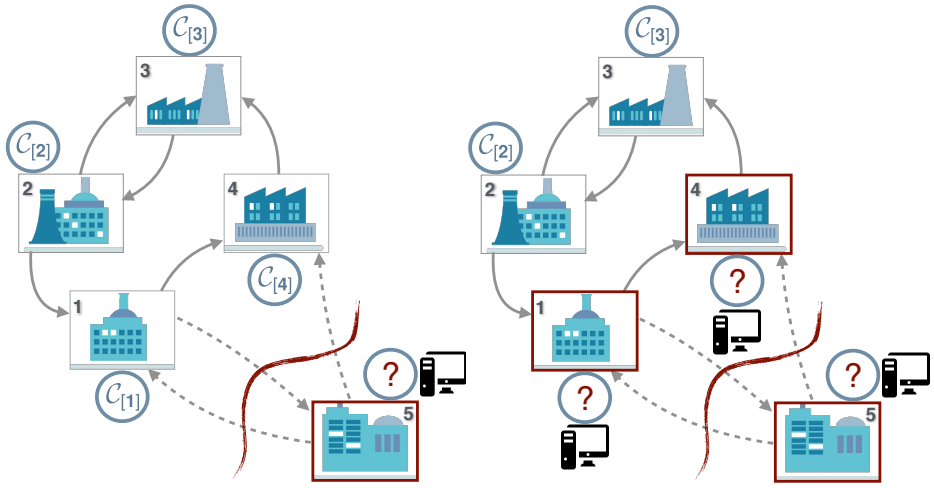

(a) Decentralized test. (b) Parent-based test.

Figure 1.5: Plug-and-play synthesis: automatic check of plug-in request in a CPS. When subsystem 5 is added to the network, the existence of a local controller $\mathcal{C}_{[5]}$ guaranteeing global properties is checked using information about subsystem 5 only (decentralized test in Figure 1.5a), or exploiting also information about its parent, i.e. subsystem 1 (parent-based test in Figure 1.5b). Notice that, in the latter case, also the children of subsystem 5 (subsystems 1 and 4) must perform the feasibility check.

In this vision, it is desirable to develop modular control architectures that can be easily updated when the mG topology changes, thus allowing DGUs and loads to enter/leave the network with minimal supervision efforts.

PnP design represents a very attractive methodology for guaranteeing a high level of flexibility in control of mGs. Notably, thanks to PnP design, DGUs owned by different players could enter/leave an existing mG in a seamless fashion, without requiring substantial intervention of a central authority. This is due to the fact that, as observed in Section 1.4.2, the design of each local regulator would require information about the corresponding DGU only, or, at most, about its neighboring subsystems.

In a broader perspective, since individual control tasks in mGs are separated into several hierarchical control levels (see Section 1.3), one can also think of developing PnP design methods embracing multiple control layers.

Some of the existing approaches to control of AC and DC ImGs do not allow to easily cope with flexibility and scalability. Besides droop con-

trol (which suffers from the limitations described in Section 1.3.3), almost all studies on AC ImGs equipped with other types of primary regulators focused on radial topologies only. Scalable design in the case of meshed topologies is still a largely unexplored problem [GCLL13].

As for the AC case, also most of the existing approaches to DC mGs control show limitations to scalability of the design. Indeed, voltage stability of the closed-loop mG has been studied only for specific topologies [DLVG16, SDVG14b, CRZ15], and the synthesis of local controller is often performed in a centralized fashion, i.e. exploiting information about all the DGUs and power lines in the network [MQLD14, MDRP$^+$16, HGK$^+$16].

1.5 Thesis contributions and overview

The aim of this thesis is to *develop scalable control design methodologies for both AC and DC ImGs, capable to guarantee safe and reliable PnP operations of DGUs and loads, in a topology-independent fashion.*

The presented contributions allow to address the challenges in ImGs detailed in Section 1.3, while overcoming the main limitations of the existing control approaches (see Section 1.3.3). More in details:

- we propose decentralized primary control schemes ensuring *offset-free* voltage (in DC mGs), and voltage and frequency (in AC ImGs) regulation. Moreover, assuming *load-connected* networks (i.e. where local loads appear only at the output terminals of each DGU), we show that our methods guarantee closed-loop stability (both in the AC and DC case), independently of the microgrid topology.

- For handling totally general interconnections of DGUs and loads in AC ImGs, we studied and exploited mathematical tools (such as Kron reduction [Kro39]) giving an equivalent load-connected model of the original network.

- We develop distributed secondary control schemes for accurate reactive power sharing in AC ImGs, and current sharing and voltage balancing in DC mGs. In the latter case, besides proving that the desired coordinated behaviors are achieved in a stable fashion, we describe how to design secondary regulators in a PnP manner when DGUs are added/removed to/from the network.

Theoretical results have been validated through simulations performed in PSCAD and PLECS, which are simulation environments for realistic electrical systems [Mul10, AH13]. Moreover, some of the developed design algorithms have been also tested on realistic mG platforms located at the Intelligent Microgrid Laboratory [Mic] (Aalborg University).

The thesis is divided in two main parts, describing the proposed control design methodologies for DC and AC islanded mGs, respectively.

Prior to Part I, in Chapter 2 we present the dynamic models of DC and AC mGs which have been considered in this work for mathematical analyses and control design purposes.

Chapter 3 In this chapter, we propose a new decentralized control design procedure for computing local voltage regulators in DC mGs with meshed topology. The offline control design is conducted in a PnP fashion, meaning that: (i) the possibility of adding/removing a DGU without spoiling the stability of the overall mG is checked through an optimization problem; (ii) when a DGU is plugged in or out, at most its neighboring DGUs have to update their controllers; and (iii) the synthesis of a local controller needs only information from the corresponding DGU and power lines connected to it. This ensures the scalability of control synthesis when the mG size changes over time. Moreover, voltage stability of the overall closed-loop mG is formally proved.
Chapter 3 is based on the following papers.

- [TRV+16] M. Tucci, S. Riverso, J. C. Vasquez, J. M. Guerrero, and G. Ferrari-Trecate, "A Decentralized Scalable Approach to Voltage Control of DC Islanded Microgrids," *IEEE Transactions on Control Systems Technology*, vol. 24, no. 6, pp. 1965-1979, 2016.

- [TRV+15b] M. Tucci, S. Riverso, J. C. Vasquez, J. M. Guerrero, and G. Ferrari-Trecate, "Voltage Control of DC Islanded Microgrids: a Decentralized Scalable Approach," in *Proceedings of the 54th IEEE Conference on Decision and Control*, 2015, pp. 3149-3154.

- [TRV+15a] M. Tucci, S. Riverso, J. C. Vasquez, J. M. Guerrero, and G. Ferrari-Trecate, "A Decentralized Scalable Approach to Voltage Control of DC Islanded Microgrids," Tech. Rep., 2015, [Online]. Available: `arXiv:1503.06292`.

Chapter 4 In this chapter, we propose an extension of the control design approach for voltage stabilization in DC mGs presented in Chapter 3. In particular, primary regulators are still designed in a PnP fashion; however, local control synthesis is now independent of the parameters of power lines. Since the proposed methodology is totally decentralized, the plug-in/-out operations of DGUs do not require anymore to update controllers of neighboring subsystems. In order to show the stability of the closed-loop mG, we exploit structured Lyapunov functions, the LaSalle invariance theorem and properties of graph Laplacians.
Chapter 4 is based on the following publications.

- [TRFTar] M. Tucci, S. Riverso, and G. Ferrari-Trecate, "Line-Independent Plug-and-Play Controllers for Voltage Stabilization in DC Microgrids," *IEEE Transactions on Control Systems Technology*, 2017. To appear.
- [TRFT16] M. Tucci, S. Riverso, and G. Ferrari-Trecate, "Voltage Stabilization in DC Microgrids through Coupling-Independent Plug-and-Play Controllers," in *Proceedings of the 55th IEEE Conference on Decision and Control*, 2016, pp. 4944-4949.
- [TRFT17] M. Tucci, S. Riverso, and G. Ferrari-Trecate, "Voltage Stabilization in DC Microgrids: an Approach based on Line-Independent Plug-and-Play Controllers," Tech. Rep., 2017, [Online]. Available: `arXiv:1609.02456`.

Chapter 5 In this chapter, we propose a secondary consensus-based control layer for current sharing and voltage balancing in DC mGs. The presented scheme is build on top of a primary layer capable to guarantee collective voltage stability. To this aim, one can employ, e.g., the decentralized regulators described in Chapters 3 and 4. Under reasonable approximations of primary control loops, we prove exponential stability of the mG equipped with the proposed hierarchical scheme, current sharing, and voltage balancing. In addition, we show how to design secondary controllers in a PnP fashion when DGUs are added/removed to/from an existing mG.
Chapter 5 is based on the following published and submitted papers.

- [TMGFTed] M. Tucci, L. Meng, J. M. Guerrero, and G. Ferrari-Trecate, "Stable Current Sharing and Voltage Balancing in DC Microgrids: a Consensus-Based Secondary Control Layer," *Automatica*, 2017. Submitted.

- [TMGFT17] M. Tucci, L. Meng, J. M. Guerrero, and G. Ferrari-Trecate, "Plug-and-Play Control and Consensus Algorithms for Current Sharing in DC Microgrids," in *Proceedings of the 20th IFAC World Congress*, 2017, pp. 12440-12445.

- [TMGFT16] M. Tucci, L. Meng, J. M. Guerrero, and G. Ferrari-Trecate, "A Consensus-Based Secondary Control Layer for Stable Current Sharing and Voltage Balancing in DC Microgrids," Tech. Rep., 2016, [Online]. Available: `arXiv:1603.03624`.

The second part of the thesis focuses on the proposed PnP synthesis procedures for scalable control of AC ImGs.

Chapter 6 In this chapter, we summarize the decentralized scheme for voltage and frequency control in AC ImGs proposed in [RSFT15]. According to this methodology, (i) the offline synthesis of local stabilizing controllers hinges on information about the corresponding DGU and lines connected to it, and (ii) PnP operations are enabled. Hence, when a DGU is plugged in or out, only subsystems physically connected to it must update their local controllers.
This review chapter will be instrumental in describing our extensions of the approach in [RSFT15] (see Chapters 7, 8 and 9).

Chapter 7 In this chapter, we present a distributed hierarchical control architecture for AC ImGs. At the primary level, DGUs are equipped with local regulators ensuring collective voltage and frequency stability. Similarly to the method described in [RSFT15], the design of primary regulators is performed in a decentralized fashion, thus enabling PnP operations of DGUs. Compared to the approach in [RSFT15], we extend the control synthesis procedure to ImGs with a different topology. Notably, while in [RSFT15] authors focused on *load-connected* ImGs only (i.e. where local loads appear at the output terminals of each DGU), in this chapter we consider *bus-connected* topologies (i.e. networks with a common load, supplied by all the DGUs).
At the secondary level, we propose a distributed scheme for accurate reactive power sharing.
Chapter 7 hinges on the following publications.

- [RTV$^+$ar] S. Riverso, M. Tucci, J. C. Vasquez, J. M. Guerrero, and G. Ferrari-Trecate, "Stabilizing Plug-and-Play Regulators and Secondary Coordinated Control for AC Islanded Microgrids with Bus-Connected Topology," *Applied Energy*, 2017. To appear.

- [RTV$^+$17] S. Riverso, M. Tucci, J. C. Vasquez, J. M. Guerrero, and G. Ferrari-Trecate, "Plug-and-Play and Coordinated Control for Bus-Connected AC Islanded Microgrids," Tech. Rep., 2017, [Online]. Available: `arXiv:1703.10222`.

Chapter 8 In this chapter, we propose two methods for simplifying AC electrical networks with general topologies. The developed procedures are based on Kron reduction, a standard tool in classic circuit theory for replacing an electrical network with a simpler one while preserving the behavior of electrical variables at target nodes.
Our approximate algorithms, which allow to overcome the main drawbacks of existing approaches to instantaneous Kron reduction, ensure the asymptotic equivalence between original and reduced models, even if the signals are unbalanced.
The proposed methods can be applied to any linear electrical network. In particular, we show that they represent a key tool for developing topology-independent control design algorithms for AC ImGs.
Chapter 8 is based on the following published and submitted papers.

- [FTRFTed] A. Floriduz, M. Tucci, S. Riverso, and G. Ferrari-Trecate, "Approximate Kron Reduction Methods for Electrical Networks with Applications to Plug-and-Play Control of AC Islanded Microgrids," *IEEE Transactions on Control Systems Technology*, 2017. Submitted.

- [TFRFT16] M. Tucci, A. Floriduz, S. Riverso, and G. Ferrari-Trecate, "Plug-and-Play Control of AC Islanded Microgrids with General Topology," in *Proceedings of the 15th European Control Conference*, 2016, pp. 1493-1500.

- [TFRFT15] M. Tucci, A. Floriduz, S. Riverso, and G. Ferrari-Trecate, "Kron Reduction Methods for Plug-and-Play Control of AC Islanded Microgrids with Arbitrary Topology," Tech. Rep., 2015, [Online]. Available: `arXiv:1510.07873`.

Chapter 9 In this chapter, we propose an extension of the PnP control scheme for voltage and frequency stabilization in AC ImGs described in

[RSFT15]. Differently from [RSFT15], the presented scalable design approach is line-independent. This implies that (i) the synthesis of each local controller requires only the parameters of the corresponding DGU (and not the model of power lines connecting neighboring DGUs), and (ii) whenever a new DGU is plugged in, subsystems physically coupled with it do not have to retune their regulators because of the new power line connected to them. Similarly to the line-independent algorithm for DC mGs discussed in Chapter 4, we rigorously analyze stability of the closed-loop AC ImGs. Notably, we first exploit the fact that DGU interactions can be represented by means of a graph Laplacian, and then resort to the LaSalle invariance principle.
Chapter 9 is based on the following published and submitted works.

- [TFTed] M. Tucci, and G. Ferrari-Trecate, "A Scalable, Line-Independent Control Design Algorithm for Voltage and Frequency Stabilization in AC Islanded Microgrids," *Automatica*, 2017. Submitted.
- [TFT17b] M. Tucci, and G. Ferrari-Trecate, "Voltage and Frequency Control in AC Islanded Microgrids: a Scalable, Line-Independent Design Algorithm," in *Proceedings of the 20th IFAC World Congress*, 2017, pp. 13922-13927.
- [TFT17a] M. Tucci, and G. Ferrari-Trecate, "A scalable Line-Independent Design Algorithm for Voltage and Frequency Control in AC Islanded Microgrids," Tech. Rep., 2017, [Online]. Available: `arXiv:1703.02336`.

Chapter 10 This chapter is devoted to conclusions and future research directions.

Appendix A In this appendix we provide basic definitions and notations used in this thesis.

Chapter 2

Microgrid modeling

Contents

2.1 Introduction 21
2.2 Electrical model of DC DGUs and lines 21
2.3 Electrical model of AC DGUs and lines 23

2.1 Introduction

We introduce the dynamical models of DGUs and lines underlying the mathematical analyses developed in the next chapters. Following the organization of the thesis, we start by presenting the considered dynamical models for DC mGs. Then, we focus on AC ImGs, which are slightly more complex than their DC counterparts as they require the introduction of additional concepts and notations. For the sake of simplicity, in both cases, the models derivation is performed considering a 2-DGUs network. The obtained results, however, can be straightforwardly generalized to mGs composed of an arbitrary number of DGUs. These models will be introduced in Chapters 3 and 6 of the thesis.

2.2 Electrical model of DC DGUs and lines

Let us consider the scheme in Figure 2.1, in which DGUs i and j are connected through an RL DC power line (with $R_{ij} > 0$ and $L_{ij} > 0$). In each DGU, the generic renewable resource is modeled with a DC voltage source; this approximation is justified by the observation that changes in the power supplied by renewables take place at a timescale which is slower than the one we are interested in for stability analysis. Moreover, renewables are usually equipped with storage units damping stochastic fluctuations. Each source is interfaced to a local DC load connected to the Point of Common Coupling (PCC) via a Buck converter with its corresponding series LC

filter. We also assume the aforementioned loads are unknown and act as current disturbances (I_L) [RSFT15, BK13].

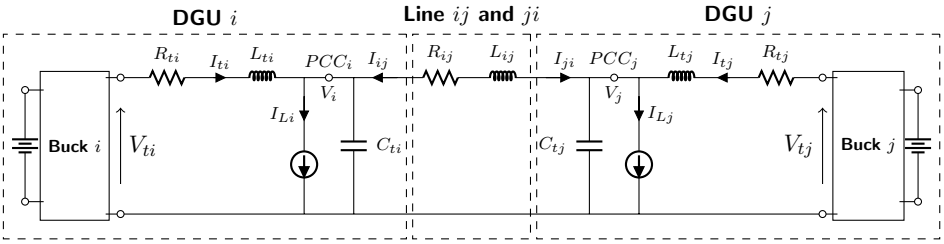

Figure 2.1: Electrical scheme of a DC mG composed of two radially connected DGUs with unmodeled loads.

By applying Kirchhoff's Voltage Law (KVL) and Kirchhoff's Current Law (KCL) to the electrical scheme of Figure 2.1, one obtains the following set of equations:

$$\text{DGU } i: \begin{cases} \dfrac{dV_i}{dt} = \dfrac{1}{C_{ti}} I_{ti} + \dfrac{1}{C_{ti}} I_{ij} - \dfrac{1}{C_{ti}} I_{Li} & \text{(2.1a)} \\ \dfrac{dI_{ti}}{dt} = -\dfrac{R_{ti}}{L_{ti}} I_{ti} - \dfrac{1}{L_{ti}} V_i + \dfrac{1}{L_{ti}} V_{ti} & \text{(2.1b)} \end{cases}$$

$$\text{Line } ij: \quad \left\{ L_{ij} \frac{dI_{ij}}{dt} = V_j - R_{ij} I_{ij} - V_i \right. \tag{2.1c}$$

$$\text{Line } ji: \quad \left\{ L_{ji} \frac{dI_{ji}}{dt} = V_i - R_{ji} I_{ji} - V_j \right. \tag{2.1d}$$

$$\text{DGU } j: \begin{cases} \dfrac{dV_j}{dt} = \dfrac{1}{C_{tj}} I_{tj} + \dfrac{1}{C_{tj}} I_{ji} - \dfrac{1}{C_{tj}} I_{Lj} & \text{(2.1e)} \\ \dfrac{dI_{tj}}{dt} = -\dfrac{R_{tj}}{L_{tj}} I_{tj} - \dfrac{1}{L_{tj}} V_j + \dfrac{1}{L_{tj}} V_{tj} & \text{(2.1f)} \end{cases}$$

As in [RSFT15], we notice that from (2.1c) and (2.1d) one gets two opposite line currents I_{ij} and I_{ji}. This is equivalent to have a reference current entering in each DGU. We exploit the following assumption to ensure that $I_{ij}(t) = -I_{ji}(t)$, $\forall t \geq 0$.

Assumption 2.1. *Initial states for the line currents fulfill* $I_{ij}(0) = -I_{ji}(0)$. *Furthermore, it holds* $L_{ij} = L_{ji}$ *and* $R_{ij} = R_{ji}$.

Remark 2.1. *Equations* (2.1c) *and* (2.1d) *represent an expansion of the line model obtained introducing only a single state variable*[1]*. System* (2.1) *can also be seen as a system of differential-algebraic equations, given by (2.1a)-(2.1c), (2.1e), (2.1f) and* $I_{ij}(t) = -I_{ji}(t)$.

2.3 Electrical model of AC DGUs and lines

The mathematical model of a DGU in an AC ImG can be derived by following a similar procedure to the DC case. However, since we are now dealing with three-phase electrical signals, (i) renewable sources will be interfaced to the network via alternating current converters, and (ii) a widely used reference frame transformation will be employed for mapping three-phase AC signals into constant ones, thus simplifying the control design and analysis.

In the sequel, we assume three-phase electrical signals without zero sequence components and balanced network parameters[2]. Moreover, note that we do not assume balanced signals; hence, the case of unbalanced load currents is included in this framework.

Following the approach in [RSFT15, BK13, EDI12, MKKG10], we consider an ImG composed of two parallel DGUs denoted with i and j, respectively. As shown in the equivalent single-phase electrical scheme in Figure 2.2, each DGU is composed of a DC voltage source for modeling a generic renewable resource (this approximation is justified by the same motivations of the DC case), a three-phase Voltage Source Converter (VSC), an LC three-phase filter and a step-up transformer ($\mathrm{Y}-\Delta$), which interfaces the DGU to the network at the corresponding PCC. The transformer parameters, except the transformation ratio k, are included in R_t and L_t. Each DGU provides real and reactive power to its corresponding local load connected to the PCC. As for the DC case, loads are assumed to be unknown and their effect on the network is accounted for by their absorbed currents (I_L), which in turn are seen as disturbances. DGUs are coupled with each other through three-phase RL power lines (with $R_{ij} > 0$ and $L_{ij} > 0$).

Remark 2.2. *We highlight that the use of single-phase equivalent networks, (as, for instance, in Figure 2.2), is allowed by the fact that inverter output filters, shunt capacitors, step-up transformers and three-phase lines between DGUs are balanced. On the other hand, we recall that, in the considered*

[1] For a definition of expansion of a system, we defer the reader to Section 3.4 in [Lun92].
[2] See, e.g., [AWA07] for basic definitions.

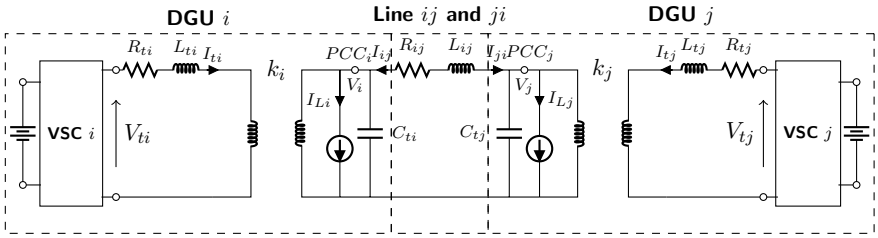

Figure 2.2: Single phase equivalent electrical scheme of an AC ImG composed of two radially connected DGUs with unmodeled loads.

framework, load currents and inverter output voltages may be unbalanced, but they cannot contain any zero-sequence component.

By applying KVL, KCL and constitutive relations, the ImG in Figure 2.2 is described by the following set of equations:

$$\text{DGU } i\text{:} \quad \begin{cases} v_{ti}^{abc} = R_{ti}\, i_{ti}^{abc} + L_{ti}\dfrac{\mathrm{d}}{\mathrm{d}t} i_{ti}^{abc} + \tilde{k}_i\, v_i^{abc} & \text{(2.2a)} \\ \tilde{k}_i^*\, i_{ti}^{abc} = -i_{ij}^{abc} + C_{ti}\dfrac{\mathrm{d}}{\mathrm{d}t} v_i^{abc} + i_{Li}^{abc} & \text{(2.2b)} \end{cases}$$

$$\text{Line } ij\text{:} \quad \begin{cases} v_i^{abc} = -R_{ij}\, i_{ij}^{abc} - L_{ij}\dfrac{\mathrm{d}}{\mathrm{d}t} i_{ij}^{abc} + v_j^{abc} & \text{(2.2c)} \end{cases}$$

$$\text{Line } ji\text{:} \quad \begin{cases} v_j^{abc} = -R_{ji}\, i_{ji}^{abc} - L_{ji}\dfrac{\mathrm{d}}{\mathrm{d}t} i_{ji}^{abc} + v_i^{abc} & \text{(2.2d)} \end{cases}$$

$$\text{DGU } j\text{:} \quad \begin{cases} v_{tj}^{abc} = R_{ji}\, i_{tj}^{abc} + L_{ji}\dfrac{\mathrm{d}}{\mathrm{d}t} i_{tj}^{abc} + \tilde{k}_j v_j^{abc} & \text{(2.2e)} \\ \tilde{k}_j^*\, i_{tj}^{abc} = -i_{ji}^{abc} + C_{tj}\dfrac{\mathrm{d}}{\mathrm{d}t} v_j^{abc} + i_{Lj}^{abc} & \text{(2.2f)} \end{cases}$$

where (i) $\tilde{k}_i$ and $\tilde{k}_j$ are the complex transformation ratios of transformers i and j, respectively, (ii) $\tilde{k}_i^*$ and $\tilde{k}_j^*$ indicate their complex conjugate quantities, and (iii) vectors $v^{abc} = [v_a, v_b, v_c]^T$ and $i^{abc} = [i_a, i_b, i_c]^T$ collect, respectively, three-phase voltages and currents in the *abc* reference frame.

In order to guarantee that $i_{ij}^{abc}(t) = -i_{ji}^{abc}(t)$, $\forall t \geq 0$, the following modeling assumption is introduced [RSFT15].

Assumption 2.2. *Initial states for the line currents fulfill* $i_{ij}^{abc}(0) = -i_{ji}^{abc}(0)$. *Furthermore, it holds* $L_{ij} = L_{ji}$ *and* $R_{ij} = R_{ji}$.

Remark 2.3. *As observed in [RSFT15], systems* (2.2c) *and* (2.2d) *are equivalent to line models described by a single line current associated with a reference direction.*

At this point, we aim to rewrite equations (2.2a)-(2.2f) in $dq0$ coordinates by means of the Park transformation [Par29]. As already anticipated, this change of coordinates allows to represent signals which were originally sinusoidal (in the *abc* reference frame) as constant ones. We will see later in Part II of the thesis, which is dedicated to AC ImGs, how this feature simplifies both control design and analysis. Let ω_0 be the reference angular frequency for the considered ImG. When the Park transformation is applied to equations (2.2a)-(2.2e), the phase angle θ in the transformation matrix $T(\theta)$ [Par29] can be set equal to $\theta = \omega_0 t + \phi$, where ϕ is an angle suitably chosen for eliminating the phase shifts introduced by the complex transformation ratios $\tilde{k}_i$ and $\tilde{k}_j$. We indicate the moduli of complex transformation ratio as k: $k_i = |\tilde{k}_i|$ and $k_j = |\tilde{k}_j|$. The models of DGUs and lines in (2.2) can be then rewritten in the dq reference frame rotating with speed ω_0 as:

$$\text{DGU } i\text{:} \quad \begin{cases} \dfrac{\mathrm{d}}{\mathrm{d}t} V_i^{dq} + \mathrm{i}\omega_0 V_i^{dq} = \dfrac{k_i}{C_{ti}} I_{ti}^{dq} + \dfrac{1}{C_{ti}} I_{ij}^{dq} - \dfrac{1}{C_{ti}} I_{Li}^{dq} & \text{(2.3a)} \\ \dfrac{\mathrm{d}}{\mathrm{d}t} I_{ti}^{dq} + \mathrm{i}\omega_0 I_{ti}^{dq} = -\dfrac{R_{ti}}{L_{ti}} I_{ti}^{dq} - \dfrac{k_i}{L_{ti}} V_i^{dq} + \dfrac{1}{L_{ti}} V_{ti}^{dq} & \text{(2.3b)} \end{cases}$$

$$\text{Line } ij\text{:} \quad \begin{cases} \dfrac{\mathrm{d}}{\mathrm{d}t} I_{ij}^{dq} + \mathrm{i}\omega_0 I_{ij}^{dq} = \dfrac{1}{L_{ij}} V_j^{dq} - \dfrac{R_{ij}}{L_{ij}} I_{ij}^{dq} - \dfrac{1}{L_{ij}} V_i^{dq} & \text{(2.3c)} \end{cases}$$

$$\text{Line } ji\text{:} \quad \begin{cases} \dfrac{\mathrm{d}}{\mathrm{d}t} I_{ji}^{dq} + \mathrm{i}\omega_0 I_{ji}^{dq} = \dfrac{1}{L_{ji}} V_i^{dq} - \dfrac{R_{ji}}{L_{ji}} I_{ji}^{dq} - \dfrac{1}{L_{ji}} V_j^{dq} & \text{(2.3d)} \end{cases}$$

$$\text{DGU } j\text{:} \quad \begin{cases} \dfrac{\mathrm{d}}{\mathrm{d}t} V_j^{dq} + \mathrm{i}\omega_0 V_j^{dq} = \dfrac{k_j}{C_{tj}} I_{tj}^{dq} + \dfrac{1}{C_{tj}} I_{ji}^{dq} - \dfrac{1}{C_{tj}} I_{Lj}^{dq} & \text{(2.3e)} \\ \dfrac{\mathrm{d}}{\mathrm{d}t} I_{tj}^{dq} + \mathrm{i}\omega_0 I_{tj}^{dq} = -\dfrac{R_{tj}}{L_{tj}} I_{tj}^{dq} - \dfrac{k_j}{L_{tj}} V_j^{dq} + \dfrac{1}{L_{tj}} V_{tj}^{dq} & \text{(2.3f)} \end{cases}$$

Remark 2.4. *Models* (2.1) *and* (2.2)-(2.3) *hinge on the following assumption: both Buck and VSC dynamics, that are inherently switching, have been averaged over time. This is, however, a mild approximation for modern DC/DC and DC/AC converters which can operate at very high frequencies. We further notice that these averaged models are widely used in the literature [SDVG14a, RE09, MKKG10, EDI12].*

Part I

Scalable control of DC microgrids

Chapter 3

Line-dependent plug-and-play control of DC microgrids

Contents

3.1 Introduction 30
3.2 DC microgrid model 31
3.2.1 QSL model of a microgrid composed of 2 DGUs . 32
3.2.2 QSL model of a microgrid composed of N DGUs 35
3.3 Plug-and-play decentralized voltage control . . 36
3.3.1 Decentralized control scheme with integrators . . 36
3.3.2 Decentralized plug-and-play control 38
3.3.3 QSL approximations as singular perturbations . 44
3.3.4 Enhancements of local controllers for improving performances 45
3.3.5 Algorithm for the design of local controllers . . . 48
3.3.6 Plug-and-play operations 49
3.3.7 Hot plugging in/out operations 50
3.4 Simulation results 50
3.4.1 Scenario 1 50
3.4.2 Scenario 2 56
3.5 Final comments 60
3.6 Appendix 62
3.6.1 Proof of Theorem 3.1 62
3.6.2 How interactions among DGUs can destabilize a DC mG 65
3.6.3 Bumpless control transfer 67
3.6.4 Overall model of a microgrid composed of N DGUs 69
3.6.5 Electrical and simulation parameters of Scenario 1 and 2 70

3.1 Introduction

In this chapter, we develop a scalable procedure for designing decentralized voltage regulators in DC mGs. We propose a PnP methodology in which the synthesis of a local controller requires only the model of the corresponding DGU and the parameters of power lines connected to it. Most importantly, no specific information about any other DGU in the network is needed. For modeling and mathematical analyses, we exploit Quasi-Stationary Line (QSL) approximations of line dynamics [VSZ95].

Other features of the proposed methodology are summarized hereafter.

1. Local control synthesis exploits the model of the corresponding DGU and the values of power lines connected to it (hence the name *line-dependent* design). As a consequence, whenever a DGU is plugged in or out, only its neighboring subsystems will have to retune their local controllers.

2. We use separable Lyapunov functions for mapping control design into a Linear Matrix Inequality (LMI) problem, thus getting a convex optimization problem which can be efficiently solved by LMI solvers [BEGFB94]. This also allows to automatically deny plugging in/out requests if these operations compromise the stability of the mG.

We recall that primary controllers for DC mGs are mainly based on droop methods [SDVG14b, DLVG16]. So far, however, the stability of the closed-loop systems has been rigorously analyzed only for specific islanded mGs [SDVG14b, DLVG16]. Moreover, the design of stabilizing droop controllers is often performed in a centralized fashion [MDRP$^+$16, MQLD14]. On the contrary, the PnP control design algorithm presented in this chapter is scalable, and collective voltage stability is assessed in a decentralized fashion, independently of the way DGUs[1] are interconnected.

We highlight that a topology-independent stability analysis for DC mGs, where DGUs are assumed to controllable current sources, has been provided [ZD15]; we will comment this work later on in Chapter 5.

The presented control algorithm shares several similarities with the one proposed in [RSFT15] (summarized in Chapter 6), hence showing that the combination of QSL models and separable Lyapunov functions provides a unified framework for addressing voltage stability problems both in AC and DC microgrids. This is a positive feature, given the fundamental differences in microgrid models and control aims in the AC and DC cases.

[1] Modeled as in the dashed box in Figure 2.1.

In order to validate our results, we run several simulations in PSCAD using realistic models of Buck converters and associated filters. As a first test, we consider two radially connected DGUs [SDVG14a] and we show that, in spite of QSL approximations, PnP controllers lead to very good performances in terms of voltage tracking and robustness to unknown load dynamics. We also show how to embed PnP controllers in a bumpless transfer scheme [ÅH06] so as to avoid abrupt changes of the control variables due to controller switching. Then, we consider an mG with 6 DGUs arranged in a meshed topology including loops, and discuss the real-time plugging in and out of a DGU.

The chapter is structured as follows. Starting from the electrical models of DC DGUs and power lines presented in Chapter 2, we derive the state-space QSL model of a network with two radially connected DGUs (see Figure 2.1). The obtained model is then generalized to mGs with N DGUs. In Section 3.3, we describe the procedure for performing PnP operations. In Section 3.4 we assess the performance of PnP controllers through simulation case studies. Section 3.5 is devoted to concluding remarks.

3.2 DC microgrid model

In this section, we present the state-space models of mGs used for control design and mathematical analyses. For clarity, we first focus on the mG shown in Figure 2.1, composed of 2 DGUs and described by the set of equations (2.1). Recalling Assumption 2.1 and the notation introduced in Remark 2.1 (i.e. $I_{ij}(t) = -I_{ji}(t)$), we notice that both the models of DGU i and j in (2.1) have the same structure. In particular, since the load current I_{L*}, $* \in \{i, j\}$, is treated as a disturbance, from (2.1) we obtain the following linear system

$$\begin{aligned} \dot{x}(t) &= Ax(t) + Bu(t) + Md(t) \\ y(t) &= Cx(t) \end{aligned} \tag{3.1}$$

where $x = [V_i, I_{ti}, I_{ij}, I_{ji}, V_{j,}, I_{tj}]^T$ is the state, $u = [V_{ti}, V_{tj}]^T$ the input, $d = [I_{Li}, I_{Lj}]^T$ the disturbance and $y = [V_i, V_j]^T$ the output of the system.

Matrices A, B, C and M are shown below:

$$A = \begin{bmatrix} 0 & \frac{1}{C_{ti}} & \frac{1}{C_{ti}} & 0 & 0 & 0 \\ -\frac{1}{L_{ti}} & -\frac{R_{ti}}{L_{ti}} & 0 & 0 & 0 & 0 \\ -\frac{1}{L_{ij}} & 0 & -\frac{R_{ij}}{L_{ij}} & 0 & \frac{1}{L_{ij}} & 0 \\ \frac{1}{L_{ji}} & 0 & 0 & -\frac{R_{ji}}{L_{ji}} & -\frac{1}{L_{ji}} & 0 \\ 0 & 0 & 0 & \frac{1}{C_{tj}} & 0 & \frac{1}{C_{tj}} \\ 0 & 0 & 0 & 0 & -\frac{1}{L_{tj}} & -\frac{R_{tj}}{L_{tj}} \end{bmatrix}, \tag{3.2}$$

$$B = \begin{bmatrix} 0 & 0 \\ \frac{1}{L_{ti}} & 0 \\ 0 & 0 \\ 0 & 0 \\ 0 & 0 \\ 0 & \frac{1}{L_{tj}} \end{bmatrix}, \qquad C^T = \begin{bmatrix} 1 & 0 \\ 0 & 0 \\ 0 & 0 \\ 0 & 0 \\ 0 & 1 \\ 0 & 0 \end{bmatrix}, \qquad M = \begin{bmatrix} -\frac{1}{C_{ti}} & 0 \\ 0 & 0 \\ 0 & 0 \\ 0 & 0 \\ 0 & -\frac{1}{C_{tj}} \\ 0 & 0 \end{bmatrix}. \tag{3.3}$$

From (3.2) and (3.3), it can be seen that DGUs state variables (i.e. voltages at the PCC and converter output currents) depend on line currents, which are the states of the lines; this may render the system quite difficult to handle. It would be desirable to obtain a simplified model in which DGUs state variables directly depend on each other, without being influenced by states of the lines. In the following, we show how to achieve this goal by means of QSL approximations of line dynamics [VSZ95].

3.2.1 QSL model of a microgrid composed of 2 DGUs

As in [VSZ95] and [AWA07], we assume L_{ij} and L_{ji} small enough so as to replace the left-hand side of (2.1c) and (2.1d) with zero. Consequently, from (2.1c) and (2.1d), one gets:

$$\bar{I}_{ij} = \frac{V_j}{R_{ij}} - \frac{V_i}{R_{ij}} \tag{3.4a}$$

$$\bar{I}_{ji} = \frac{V_i}{R_{ji}} - \frac{V_j}{R_{ji}} \tag{3.4b}$$

By replacing variable I_{ij} in (2.1a) with the right-hand side of (3.4a), we obtain the following QSL model of DGU i

$$\text{DGU } i: \quad \begin{cases} \dfrac{dV_i}{dt} = \dfrac{1}{C_{ti}} I_{ti} + \dfrac{V_j}{C_{ti} R_{ij}} - \dfrac{V_i}{C_{ti} R_{ij}} - \dfrac{1}{C_{ti}} I_{Li} \\ \dfrac{dI_{ti}}{dt} = -\dfrac{1}{L_{ti}} V_i - \dfrac{R_{ti}}{L_{ti}} I_{ti} + \dfrac{1}{L_{ti}} V_{ti} \end{cases} \tag{3.5}$$

Switching indexes i and j in (3.5) gives the model of DGU j. It can be equivalently derived by substituting I_{ji} in (2.1e) with the right-hand side of (3.4b). In a more compact form, the dynamics of DGU i is

$$\Sigma_{[i]}^{DGU}: \begin{cases} \dot{x}_{[i]}(t) = A_{ii} x_{[i]}(t) + B_i u_{[i]}(t) + M_i d_{[i]}(t) + \xi_{[i]}(t) \\ y_{[i]}(t) = C_i x_{[i]}(t) \\ z_{[i]}(t) = H_i y_{[i]}(t) \end{cases} \tag{3.6}$$

where $x_{[i]} = [V_i, I_{ti}]^T$ is the state, $u_{[i]} = V_{ti}$ the control input, $d_{[i]} = I_{Li}$ the exogenous input and $z_{[i]} = V_i$ the controlled variable of the system. Moreover, $y_{[i]}(t)$ is the measurable output and we assume $y_{[i]} = x_{[i]}$, while $\xi_{[i]}(t) = A_{ij} x_{[j]}$ represents the coupling with DGU j.

The matrices of $\Sigma_{[i]}^{DGU}$ are obtained from (3.5) and they are here provided:

$$A_{ii} = \begin{bmatrix} -\frac{1}{R_{ij} C_{ti}} & \frac{1}{C_{ti}} \\ -\frac{1}{L_{ti}} & -\frac{R_{ti}}{L_{ti}} \end{bmatrix}, \qquad A_{ij} = \begin{bmatrix} \frac{1}{R_{ij} C_{ti}} & 0 \\ 0 & 0 \end{bmatrix}, \qquad B_i = \begin{bmatrix} 0 \\ \frac{1}{L_{ti}} \end{bmatrix},$$

$$M_i = \begin{bmatrix} -\frac{1}{C_{ti}} \\ 0 \end{bmatrix}, \qquad C_i = \begin{bmatrix} 1 & 0 \\ 0 & 1 \end{bmatrix}, \qquad H_i = \begin{bmatrix} 1 & 0 \end{bmatrix}.$$

As regards power line ij, we obtain the subsystem

$$\Sigma_{[ij]}^{Line}: \left\{ \dot{x}_{[l,ij]}(t) = A_{ll,ij} x_{[l,ij]}(t) + A_{li,ij} x_{[i]}(t) + A_{lj,ij} x_{[j]}(t) \right. \tag{3.7}$$

where $x_{[l,ij]} = I_{ij}$ is the state of the line. The matrices of (3.7), derived from (2.1c), have the following form:

$$A_{li,ij} = \begin{bmatrix} -\frac{1}{L_{ij}} & 0 \end{bmatrix}, \qquad A_{lj,ij} = \begin{bmatrix} \frac{1}{L_{ij}} & 0 \end{bmatrix}, \qquad A_{ll,ij} = -\frac{R_{ij}}{L_{ij}}.$$

We have now all the ingredients to write the overall model of the mG in Figure 2.1 under QSL approximations of power line dynamics. In particular,

from (3.6) and (3.7), we get

$$\begin{aligned}
\begin{bmatrix} \dot{x}_{[i]} \\ \dot{x}_{[j]} \\ \dot{x}_{[l,ij]} \\ \dot{x}_{[l,ji]} \end{bmatrix} &= \begin{bmatrix} A_{ii} & A_{ij} & 0 & 0 \\ A_{ji} & A_{jj} & 0 & 0 \\ A_{li,ij} & A_{lj,ij} & A_{ll,ij} & 0 \\ A_{li,ji} & A_{lj,ji} & 0 & A_{ll,ji} \end{bmatrix} \begin{bmatrix} x_{[i]} \\ x_{[j]} \\ x_{[l,ij]} \\ x_{[l,ji]} \end{bmatrix} + \begin{bmatrix} B_i & 0 \\ 0 & B_j \\ 0 & 0 \\ 0 & 0 \end{bmatrix} \begin{bmatrix} u_{[i]} \\ u_{[j]} \end{bmatrix} + \\
&\quad + \begin{bmatrix} M_i & 0 \\ 0 & M_j \\ 0 & 0 \\ 0 & 0 \end{bmatrix} \begin{bmatrix} d_{[i]} \\ d_{[j]} \end{bmatrix} \\
\begin{bmatrix} y_{[i]} \\ y_{[j]} \end{bmatrix} &= \begin{bmatrix} C_1 & 0 & 0 & 0 \\ 0 & C_2 & 0 & 0 \end{bmatrix} \begin{bmatrix} x_{[i]} \\ x_{[j]} \\ x_{[l,ij]} \\ x_{[l,ji]} \end{bmatrix} \\
\begin{bmatrix} z_{[i]} \\ z_{[j]} \end{bmatrix} &= \begin{bmatrix} H_i & 0 \\ 0 & H_j \end{bmatrix} \begin{bmatrix} y_{[i]} \\ y_{[j]} \end{bmatrix}.
\end{aligned} \tag{3.8}$$

Remark 3.1. *We notice that matrix A in* (3.8) *has the following block-triangular structure*

$$A = \left[\begin{array}{cc|cc} A_{ii} & A_{ij} & 0 & 0 \\ A_{ji} & A_{jj} & 0 & 0 \\ \hline A_{li,ij} & A_{lj,ij} & A_{ll,ij} & 0 \\ A_{li,ji} & A_{lj,ji} & 0 & A_{ll,ji} \end{array}\right].$$

Consequently, its eigenvalues are given by the union of those of $\begin{bmatrix} A_{ii} & A_{ij} \\ A_{ji} & A_{jj} \end{bmatrix}$, *$A_{ll,ij}$ and $A_{ll,ji}$. Moreover, by construction, $A_{ll,ij} = A_{ll,ji} < 0$. Hence, for stability analysis, line dynamics can be neglected and just the system composed of $\Sigma_{[i]}^{DGU}$ and $\Sigma_{[j]}^{DGU}$ (giving rise to the upper-left block of matrix A) matters. We will refer to it as QSL-mG model.*

Remark 3.2. *We will show in Section 3.3.3 that QSL approximations can be justified in terms of singular perturbation theory [KKO99, Abe86, MVVG15]. In other words, stabilization of* (3.8) *(which, in the light of Remark 3.1, depends exclusively on the stability of* $\begin{bmatrix} A_{ii} & A_{ij} \\ A_{ji} & A_{jj} \end{bmatrix}$*), will imply stabilization of* (2.1) *for sufficiently small line inductances.*

3.2.2 QSL model of a microgrid composed of N DGUs

In this section, we extend the model (3.6) to mGs composed of N DGUs. Let $\mathcal{V} = \{1, \dots, N\}$, we call two DGUs neighbors if there is a power line connecting them, and we denote with $\mathcal{N}_i \subset \mathcal{V}$ the subset of neighbors of DGU i. We highlight that the neighboring relation is symmetric, i.e. $j \in \mathcal{N}_i$ implies $i \in \mathcal{N}_j$. Furthermore, let $\mathcal{E} = \{(i,j) : i \in \mathcal{V},\, j \in \mathcal{N}_i\}$ collect pairs of indices associated with lines[2]. In this setting, the whole mG model is obtained by

1. modeling each DGU i, $i \in \mathcal{V}$, as in (2.1a)-(2.1b) after replacing I_{ij} with $\sum_{j\in\mathcal{N}_i} I_{ij}$;
2. modeling each line $(i,j) \in \mathcal{E}$ as in (2.1c).

However, if QSL approximations of all lines $(i,j) \in \mathcal{E}$ are used, the mG is described only by subsystems in the following form

$$\text{DGU } i: \quad \begin{cases} \dfrac{dV_i}{dt} = \dfrac{1}{C_{ti}} I_{ti} + \displaystyle\sum_{j\in\mathcal{N}_i} \left(\frac{V_j}{C_{ti}R_{ij}} - \frac{V_i}{C_{ti}R_{ij}} \right) - \frac{1}{C_{ti}} I_{Li} \\ \dfrac{dI_{ti}}{dt} = -\dfrac{1}{L_{ti}} V_i - \dfrac{R_{ti}}{L_{ti}} I_{ti} + \dfrac{1}{L_{ti}} V_{ti} \end{cases} \tag{3.9}$$

Model (3.9) can still be written in the more compact form (3.6), where now term $\xi_{[i]}$ equals to $\sum_{j\in\mathcal{N}_i} A_{ij} x_{[j]}(t)$. All matrices appearing in this new model do not change, with the exception of A_{ii} that becomes

$$A_{ii} = \begin{bmatrix} \sum_{j\in\mathcal{N}_i} -\frac{1}{R_{ij}C_{ti}} & \frac{1}{C_{ti}} \\ -\frac{1}{L_{ti}} & -\frac{R_{ti}}{L_{ti}} \end{bmatrix}. \tag{3.10}$$

The overall QSL-mG model can be written as follows

$$\begin{aligned} \dot{\mathbf{x}}(t) &= \mathbf{A}\mathbf{x}(t) + \mathbf{B}\mathbf{u}(t) + \mathbf{M}\mathbf{d}(t) \\ \mathbf{y}(t) &= \mathbf{C}\mathbf{x}(t) \\ \mathbf{z}(t) &= \mathbf{H}\mathbf{y}(t) \end{aligned} \tag{3.11}$$

where $\mathbf{x} = \left[x_{[1]}^T, \dots, x_{[N]}^T\right]^T \in \mathbb{R}^{2N}$, $\mathbf{u} = \left[u_{[1]}, \dots, u_{[N]}\right]^T \in \mathbb{R}^N$, $\mathbf{d} = \left[d_{[1]}, \dots, d_{[N]}\right]^T \in \mathbb{R}^N$, $\mathbf{y} = \left[y_{[1]}^T, \dots, y_{[N]}^T\right]^T \in \mathbb{R}^{2N}$, $\mathbf{z} = \left[z_{[1]}, \dots, z_{[N]}\right]^T \in \mathbb{R}^N$. Matrices $\mathbf{A}$, $\mathbf{B}$, $\mathbf{M}$, $\mathbf{C}$ and $\mathbf{H}$ are reported in Appendix 3.6.4.

[2]Note that we consider (i,j) an ordered pair and therefore, from the symmetry of the neighboring relation, if $(i,j) \in \mathcal{E}$ then also $(j,i) \in \mathcal{E}$.

Comments in Remark 3.2 apply also here: in Section 3.3.3, we will show that the QSL-mG model can be justified treating inductances L_{ij}, $(i,j) \in \mathcal{E}$, as perturbation parameters and resorting to singular perturbation theory.

Remark 3.3. *Models in the form* (3.9) *describe DGUs whose electrical scheme is shown in the dashed box of Figure 2.1. Notably, we notice that loads appear only at the PCC of each DGU. For this reason, in the sequel, mGs composed of DGUs modeled as in* (3.9) *will be referred to as load-connected. In general, however, DGUs and loads can be interconnected according to arbitrary topologies. However, we can still describe DGUs through models* (3.9)*, without loss of generality. Indeed, it has been shown that general interconnections of loads and DGUs can always be mapped into load-connected topologies by means of a network reduction method known as Kron reduction [DB13]. We will exploit this mathematical tool for developing the network reduction procedure presented in Chapter 8.*

3.3 Plug-and-play decentralized voltage control

3.3.1 Decentralized control scheme with integrators

Let $\mathbf{z_{ref}}(t)$ denote the desired reference trajectory for the output $\mathbf{z}(t)$. In order to track constant references $\mathbf{z_{ref}}(t) = \bar{\mathbf{z}}_{\mathbf{ref}}$ when $\mathbf{d}(t) = \bar{\mathbf{d}}$ is constant, we augment the mG model with integrators [SP96]. A necessary condition for steering to zero the error $\mathbf{e}(t) = \mathbf{z_{ref}}(t) - \mathbf{z}(t)$ as $t \to \infty$, is that, for arbitrary $\bar{\mathbf{d}}$ and $\bar{\mathbf{z}}_{\mathbf{ref}}$, there are equilibrium states $\bar{\mathbf{x}}$ and inputs $\bar{\mathbf{u}}$ verifying

$$\begin{aligned} \mathbf{0} &= \mathbf{A}\bar{\mathbf{x}} + \mathbf{B}\bar{\mathbf{u}} + \mathbf{M}\bar{\mathbf{d}} \\ \bar{\mathbf{z}}_{\mathbf{ref}} &= \mathbf{HC}\bar{\mathbf{x}} \end{aligned} \tag{3.12}$$

$$\Gamma \begin{bmatrix} \bar{\mathbf{x}} \\ \bar{\mathbf{u}} \end{bmatrix} = \begin{bmatrix} \mathbf{0} & -\mathbf{M} \\ \mathbf{I} & \mathbf{0} \end{bmatrix} \begin{bmatrix} \bar{\mathbf{z}}_{\mathbf{ref}} \\ \bar{\mathbf{d}} \end{bmatrix}, \quad \Gamma = \begin{bmatrix} \mathbf{A} & \mathbf{B} \\ \mathbf{HC} & \mathbf{0} \end{bmatrix} \in \mathbb{R}^{3N \times 3N}. \tag{3.13}$$

Proposition 3.1. *Given* $\bar{\mathbf{z}}_{\mathbf{ref}}$ *and* $\bar{\mathbf{d}}$*, vectors* $\bar{\mathbf{x}}$ *and* $\bar{\mathbf{u}}$ *satisfying* (3.13) *always exist.*

Proof. From [SP96], we know that there exist $\bar{\mathbf{x}}, \bar{\mathbf{u}}$ verifying (3.13) if and only if the following two conditions are fulfilled:

(i) the number of controlled variables is not greater than the number of control inputs;

(ii) the system under control has no invariant zeros (i.e. $\text{rank}(\Gamma) = 3N$).

Condition (i) is fulfilled since from (3.6) one has that $u_{[i]}$ and $z_{[i]}$ have the same size, $\forall i \in \mathcal{V}$. In order to prove Condition (ii), we exploit the definition of matrices **A**, **B**, **C** and **H** and the fact that electrical parameters are positive. □

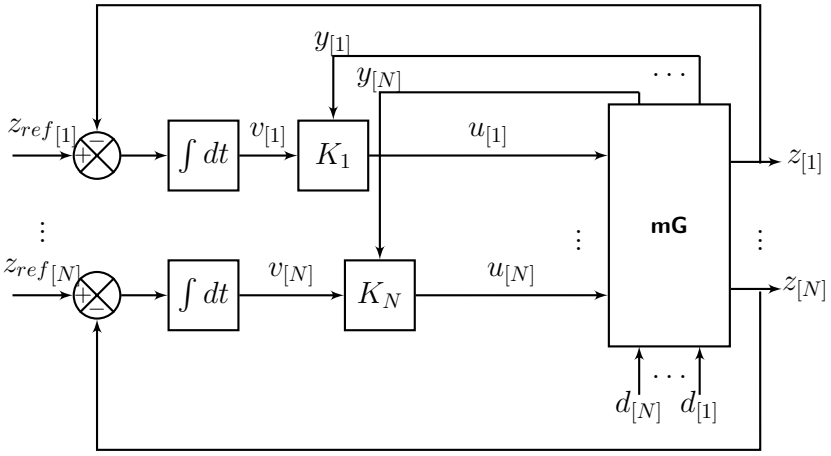

Figure 3.1: Control scheme with integrators for the overall DC mG.

The dynamics of the integrators is (see Figure 3.1)

$$\begin{aligned} \dot{v}_{[i]}(t) = e_{[i]}(t) &= z_{ref\,[i]}(t) - z_{[i]}(t) \\ &= z_{ref\,[i]}(t) - H_i C_i x_{[i]}(t), \end{aligned} \tag{3.14}$$

and hence, the DGU model augmented with integrators is

$$\hat{\Sigma}_{[i]}^{DGU} : \begin{cases} \dot{\hat{x}}_{[i]}(t) = \hat{A}_{ii}\hat{x}_{[i]}(t) + \hat{B}_i u_{[i]}(t) + \hat{M}_i \hat{d}_{[i]}(t) + \hat{\xi}_{[i]}(t) \\ \hat{y}_{[i]}(t) = \hat{C}_i \hat{x}_{[i]}(t) \\ z_{[i]}(t) = \hat{H}_i \hat{y}_{[i]}(t) \end{cases} \tag{3.15}$$

where $\hat{x}_{[i]} = [x^T{}_{[i]}, v_{[i]}]^T \in \mathbb{R}^3$ is the state, $\hat{y}_{[i]} = \hat{x}_{[i]} \in \mathbb{R}^3$ is the measurable output, $\hat{d}_{[i]} = [d_{[i]}, z_{ref\,[i]}]^T \in \mathbb{R}^2$ collects the exogenous signals (both current of the load and reference signals), and $\hat{\xi}_{[i]}(t) = \sum_{j \in \mathcal{N}_i} \hat{A}_{ij}\hat{x}_{[j]}(t)$. Matrices in (3.15) are defined as follows

$$\hat{A}_{ii} = \begin{bmatrix} A_{ii} & 0 \\ -H_i C_i & 0 \end{bmatrix}, \qquad \hat{A}_{ij} = \begin{bmatrix} A_{ij} & 0 \\ 0 & 0 \end{bmatrix}, \qquad \hat{B}_i = \begin{bmatrix} B_i \\ 0 \end{bmatrix}, \qquad \hat{C}_i = \begin{bmatrix} C_i & 0 \\ 0 & 1 \end{bmatrix},$$
$$\hat{M}_i = \begin{bmatrix} M_i & 0 \\ 0 & 1 \end{bmatrix}, \qquad \hat{H}_i = \begin{bmatrix} H_i & 0 \end{bmatrix}.$$

Through the following proposition we make sure that the pair $(\hat{A}_{ii}, \hat{B}_i)$ is controllable, hence system (3.15) can be stabilized.

Proposition 3.2. *The pair $(\hat{A}_{ii}, \hat{B}_i)$ is controllable.*

Proof. Using the definition of controllability matrix, we get

$$\begin{aligned} \hat{M}_i^C &= \begin{bmatrix} \hat{B}_i & \hat{A}_{ii}\hat{B}_i & \hat{A}_{ii}^2\hat{B}_i \end{bmatrix} \\ &= \underbrace{\begin{bmatrix} A_{ii} & B_i \\ -H_i C_i & 0 \end{bmatrix}}_{\hat{M}_{i,1}^C} \underbrace{\begin{bmatrix} 0 & B_i & A_{ii}B_i \\ I & 0 & 0 \end{bmatrix}}_{\hat{M}_{i,2}^C}. \end{aligned} \tag{3.16}$$

Matrices $\hat{M}_{i,1}^C$ and $\hat{M}_{i,2}^C$ have always full rank, since all electrical parameters are positive, hence $\text{rank}(\hat{M}_i^C) = 3$. Therefore the pair $(\hat{A}_{ii}, \hat{B}_i)$ is controllable. □

The overall augmented system is obtained from (3.15) as

$$\begin{cases} \dot{\hat{\mathbf{x}}}(t) = \hat{\mathbf{A}}\hat{\mathbf{x}}(t) + \hat{\mathbf{B}}\mathbf{u}(t) + \hat{\mathbf{M}}\hat{\mathbf{d}}(t) \\ \hat{\mathbf{y}}(t) = \hat{\mathbf{C}}\hat{\mathbf{x}}(t) \\ \mathbf{z}(t) = \hat{\mathbf{H}}\hat{\mathbf{y}}(t) \end{cases} \tag{3.17}$$

where $\hat{\mathbf{x}}$, $\hat{\mathbf{y}}$ and $\hat{\mathbf{d}}$ collect variables $\hat{x}_{[i]}$, $\hat{y}_{[i]}$ and $\hat{d}_{[i]}$ respectively, and matrices $\hat{\mathbf{A}}, \hat{\mathbf{B}}, \hat{\mathbf{C}}, \hat{\mathbf{M}}$ and $\hat{\mathbf{H}}$ are obtained from systems (3.15).

3.3.2 Decentralized plug-and-play control

This section presents the adopted control approach that allows us to design local controllers while guaranteeing asymptotic stability for the augmented system (3.17). Local controllers are synthesized in a decentralized fashion enabling PnP operations. Let us equip each DGU $\hat{\Sigma}_{[i]}^{DGU}$ with the following state-feedback controller

$$\mathcal{C}_{[i]}: \qquad u_{[i]}(t) = K_i \hat{y}_{[i]}(t) = K_i \hat{x}_{[i]}(t) \tag{3.18}$$

where $K_i \in \mathbb{R}^{1\times 3}$. As shown in Figure 3.2, controllers $\mathcal{C}_{[i]}$, $i \in \mathcal{V}$, define a multivariable PI regulator; moreover, they are decentralized, since the computation of $u_{[i]}(t)$ requires the state of $\hat{\Sigma}^{DGU}_{[i]}$ only.

Remark 3.4. *We highlight that, in general, voltage set-points $V_{ref,i}$ are either constant or determined by higher level controller devoted, for instance, to current sharing (see [DLVG16] and Chapter 5 of the thesis) or power flow optimization [BCCZ15]. In particular, both centralized and distributed algorithms for these purposes exist [DLVG16, BCCZ15].*

Let nominal subsystems be given by $\hat{\Sigma}^{DGU}_{[i]}$ without coupling terms $\hat{\xi}_{[i]}(t)$. We aim to design local controllers $\mathcal{C}_{[i]}$ such that the nominal closed-

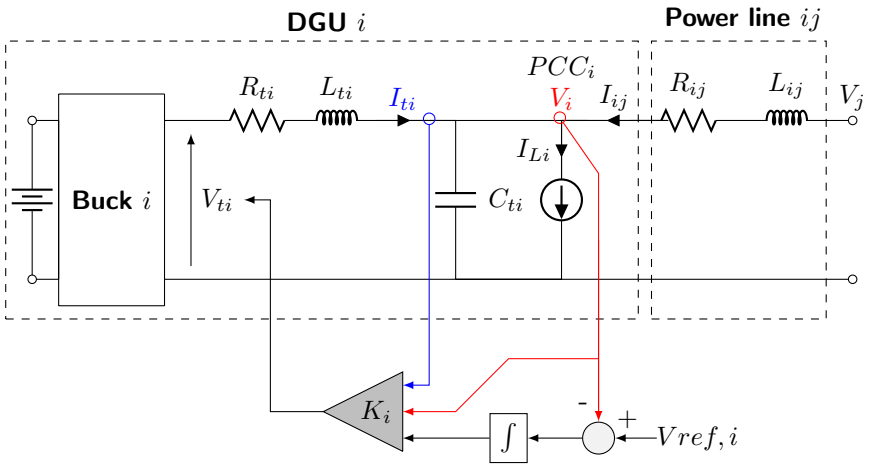

Figure 3.2: DC mG - Electrical scheme of DGU i, power line ij, and local PnP voltage controller.

loop subsystem

$$\begin{cases} \dot{\hat{x}}_{[i]}(t) = (\hat{A}_{ii} + \hat{B}_i K_i)\hat{x}_{[i]}(t) + \hat{M}_i \hat{d}_{[i]}(t) \\ \hat{y}_{[i]}(t) = \hat{C}_i \hat{x}_{[i]}(t) \\ z_{[i]}(t) = \hat{H}_i \hat{y}_{[i]}(t) \end{cases} \tag{3.19}$$

is asymptotically stable. From Lyapunov theory, we know that if there exists a symmetric matrix $P_i \in \mathbb{R}^{3\times 3}, P_i > 0$ such that

$$(\hat{A}_{ii} + \hat{B}_i K_i)^T P_i + P_i(\hat{A}_{ii} + \hat{B}_i K_i) < 0, \tag{3.20}$$

the nominal closed-loop subsystem equipped with controller $\mathcal{C}_{[i]}$ is asymptotically stable. Similarly, consider the following closed-loop QSL-mG model obtained from (3.17) and (3.18)

$$\begin{cases} \dot{\hat{\mathbf{x}}}(t) = (\hat{\mathbf{A}} + \hat{\mathbf{B}}\mathbf{K})\hat{\mathbf{x}}(t) + \hat{\mathbf{M}}\hat{\mathbf{d}}(t) \\ \hat{\mathbf{y}}(t) = \hat{\mathbf{C}}\hat{\mathbf{x}}(t) \\ \mathbf{z}(t) = \hat{\mathbf{H}}\hat{\mathbf{y}}(t) \end{cases} \tag{3.21}$$

where $\hat{\mathbf{A}}$, $\hat{\mathbf{B}}$ and $\mathbf{K}$ collect matrices $\hat{A}_{ij}$, $\hat{B}_i$ and K_i, for all $i,\ j \in \mathcal{V}$. Then, (3.21) is asymptotically stable if matrix $\mathbf{P} = \text{diag}\,[P_1, \ldots, P_N]$ satisfies

$$(\hat{\mathbf{A}} + \hat{\mathbf{B}}\mathbf{K})^T\mathbf{P} + \mathbf{P}(\hat{\mathbf{A}} + \hat{\mathbf{B}}\mathbf{K}) < 0. \tag{3.22}$$

Remark 3.5. *It is important to highlight that, in general,* (3.20) *does not imply* (3.22)*. Indeed, decentralized design of local controllers can fail to guarantee voltage stability of the whole mG, if couplings among DGUs are neglected in the design phase (see the example in Appendix 3.6.2).*

In order to derive conditions such that (3.20) guarantees (3.22), we first define $\hat{\mathbf{A}}_{\mathbf{D}} = \text{diag}\left[\hat{A}_{ii}, \ldots, \hat{A}_{NN}\right]$ and $\hat{\mathbf{A}}_{\mathbf{C}} = \hat{\mathbf{A}} - \hat{\mathbf{A}}_{\mathbf{D}}$. Then, we exploit the following assumptions to ensure asymptotic stability of the closed-loop QSL-mG.

Assumption 3.1. *Decentralized controllers $\mathcal{C}_{[i]}$, $i \in \mathcal{V}$ are designed such that* (3.20) *holds with*

$$P_i = \left[\begin{array}{c|cc} \eta_i & 0 & 0 \\ \hline 0 & \bullet & \bullet \\ 0 & \bullet & \bullet \end{array}\right] \tag{3.23}$$

where $\bullet$ denotes an arbitrary entry and $\eta_i > 0$ is a local parameter.

Regarding Assumption 3.1, we will show later that checking the existence of P_i as in (3.23) and K_i fulfilling (3.20) amounts to solve a convex optimization problem.

The next proposition provides the main stability result.

Proposition 3.3. *There exist $\eta_i > 0$, $i = 1, \ldots, N$ such that, under Assumption 3.1, the overall closed-loop QSL-mG is asymptotically stable.*

Proof. We have to show that (3.22) holds, which is equivalent to prove that

$$\underbrace{(\hat{\mathbf{A}}_\mathbf{D} + \hat{\mathbf{B}}\mathbf{K})^T\mathbf{P} + \mathbf{P}(\hat{\mathbf{A}}_\mathbf{D} + \hat{\mathbf{B}}\mathbf{K})}_{(a)} + \underbrace{\hat{\mathbf{A}}_\mathbf{C}^T\mathbf{P} + \mathbf{P}\hat{\mathbf{A}}_\mathbf{C}}_{(b)} < 0. \tag{3.24}$$

We highlight that term (a) is a block diagonal matrix collecting, on its diagonal, all left-hand sides of (3.20). It follows that term (a) is a negative definite matrix. Moreover, each block (i, j) of term (b) can be written as

$$\begin{cases} P_i\hat{A}_{ij} + \hat{A}_{ji}^T P_j & \text{if } j \in \mathcal{N}_i \\ 0 & \text{otherwise} \end{cases}$$

where

$$P_i\hat{A}_{ij} = \begin{bmatrix} \frac{\eta_i}{R_{ij}C_{ti}} & 0 & 0 \\ 0 & 0 & 0 \\ 0 & 0 & 0 \end{bmatrix} \text{ and } \hat{A}_{ji}^T P_j = \begin{bmatrix} \frac{\eta_j}{R_{ji}C_{tj}} & 0 & 0 \\ 0 & 0 & 0 \\ 0 & 0 & 0 \end{bmatrix}.$$

It turns out that term (b) can be made arbitrarily close to zero by setting coefficients η_i small enough. In view of the fact that term (a) is negative definite, there always exist coefficients η_i satisfying (3.24). □

The proof of Proposition 3.3 highlights that coefficients η_i, which are tuning knobs that can be set by the user, should be chosen such that $\frac{\eta_i}{R_{ij}C_{ti}} \approx 0, \forall i \in \mathcal{V}, \forall j \in \mathcal{N}_i$. Furthermore, controllers K_i should be designed such that inequality

$$(\hat{A}_{ii} + \hat{B}_i K_i)^T P_i + P_i(\hat{A}_{ii} + \hat{B}_i K_i) + \gamma_i^{-1} I \leq 0 \tag{3.25}$$

is fulfilled for $\gamma_i > 0$ large enough and matrix P_i structured as in (3.23). In order to complete the design of the local controller $\mathcal{C}_{[i]}$, we have to solve the following problem.

Problem 3.1. *Compute a vector K_i such that the nominal closed-loop subsystem is asymptotically stable and Assumption 3.1 is verified, i.e.* (3.20) *holds for a matrix P_i structured as in* (3.23).

Consider the following optimization problem

$$\mathcal{O}_i : \min_{Y_i, G_i, \gamma_i, \beta_i, \delta_i} \quad \alpha_{i1}\gamma_i + \alpha_{i2}\beta_i + \alpha_{i3}\delta_i$$

$$Y_i = \begin{bmatrix} \eta_i^{-1} & 0 & 0 \\ 0 & \bullet & \bullet \\ 0 & \bullet & \bullet \end{bmatrix} > 0 \tag{3.26a}$$

$$\begin{bmatrix} Y_i\hat{A}_{ii}^T + G_i^T\hat{B}_i^T + \hat{A}_{ii}Y_i + \hat{B}_iG_i & Y_i \\ Y_i & -\gamma_i I \end{bmatrix} \leq 0 \tag{3.26b}$$

$$\begin{bmatrix} -\beta_i I & G_i^T \\ G_i & -I \end{bmatrix} < 0 \tag{3.26c}$$

$$\begin{bmatrix} Y_i & I \\ I & \delta_i I \end{bmatrix} > 0 \tag{3.26d}$$

$$\gamma_i > 0, \quad \beta_i > 0, \quad \delta_i > 0 \tag{3.26e}$$

where α_{i1}, α_{i2} and α_{i3} represent positive weights and $\bullet$ are arbitrary entries. We also recall that, since all constraints in (3.26) are LMI, the optimization problem is convex and can be solved with efficient (i.e. polynomial-time) LMI solvers [BEGFB94].

Lemma 3.1. *Problem $\mathcal{O}_i$ is feasible if and only if Problem 3.1 has a solution. Moreover, K_i and P_i in* (3.20) *are given by $K_i = G_iY_i^{-1}$, $P_i = Y_i^{-1}$ and*

$$||K_i||_2 < \sqrt{\beta_i}\delta_i. \tag{3.27}$$

Proof. Inequality (3.20) is equivalent to the existence of $\gamma_i > 0$ such that (3.25) holds. By applying the Schur lemma on (3.25), we get the following inequality

$$\begin{bmatrix} (\hat{A}_{ii} + \hat{B}_iK_i)^TP_i + P_i(\hat{A}_{ii} + \hat{B}_iK_i) & I \\ I & -\gamma_i I \end{bmatrix} \leq 0, \tag{3.28}$$

which is nonlinear in P_i and K_i. In order to get rid of the nonlinear terms, we perform the following parametrization trick [BEGFB94]

$$\begin{aligned} Y_i &= P_i^{-1} \\ G_i &= K_iY_i. \end{aligned} \tag{3.29}$$

Notice that Y_i has the same structure as P_i. By pre- and post-multiplying (3.28) with $\begin{bmatrix} Y_i & 0 \\ 0 & I \end{bmatrix}$ and exploiting (3.29), we obtain

$$\begin{bmatrix} Y_i\hat{A}_{ii}^T + G_i^T\hat{B}_i^T + \hat{A}_{ii}Y_i + \hat{B}_iG_i & Y_i \\ Y_i & -\gamma_i I \end{bmatrix} \leq 0. \tag{3.30}$$

Constraint (3.26a) ensures that matrix P_i has the structure required by Assumption 3.1. At the same time, constraint (3.26b) guarantees the stability of the closed-loop subsystem. Further constraints appear in Problem $\mathcal{O}_i$ with the aim of bounding $||K_i||_2$. In particular, we add $||G_i||_2 < \sqrt{\beta_i}$ and $||Y_i^{-1}||_2 < \delta_i$ (which, via Schur complement, correspond to constraints (3.26c) and (3.26d)) to prevent $||K_i||_2$ from becoming too large. These bounds imply $||K_i||_2 < \sqrt{\beta_i}\delta_i$ and then affect the magnitude of control variables. □

Remark 3.6. *From* (3.25)*, the parameter γ_i is the inverse of the quadratic stability margin [BEGFB94], which is a measure of robust stability. Furthermore, from* (3.27)*, small β_i and δ_i prevent the control action from becoming too aggressive. A suitable tuning of weights α_{i1}, α_{i2} and α_{i3} in the cost of problem $\mathcal{O}_i$ allows one to achieve a balance between these performance requirements.*

Next, we discuss the key feature of the proposed decentralized control approach. We first notice that constraints in (3.26) depend upon local fixed matrices ($\hat{A}_{ii}$, $\hat{B}_i$) and local design parameters (α_{i1}, α_{i2}, α_{i3}). It follows that the computation of controller $\mathcal{C}_{[i]}$ is completely independent of the computation of controllers $\mathcal{C}_{[j]}$ when $j \neq i$ since, provided that problem $\mathcal{O}_i$ is feasible, controller $\mathcal{C}_{[i]}$ can be directly obtained through $K_i = G_i Y_i^{-1}$. In addition, it is clear that constraints (3.26c) and (3.26d) affect only the magnitude of control variables as stated in Lemma 3.1. Finally, if problems $\mathcal{O}_i$ are feasible for sufficiently small coefficients η_i, all assumptions in Proposition 3.3 can be verified, thus obtaining that the overall closed-loop QSL-mG is asymptotically stable.

Remark 3.7. *The two main source of conservativeness of our approach are the block-diagonal structure of the Lyapunov matrix* $\mathbf{P}$ *and the structure* (3.23) *of matrices P_i. The former assumption is common in decentralized control [Lun92] and it is mild because, as shown in the proof of Proposition 3.3, DGUs interactions have little impact on the fulfillment of* (3.22) *for sufficiently small η_i. Requiring that the stability of each DGU $\Sigma_{[i]}^{DGU}$ can be certified through the Lyapunov function $\mathscr{V}_{[i]}(x_{[i]}) = x_{[i]}^T P_i x_{[i]}$, with P_i as in* (3.23)*, is more critical. Indeed,* (3.23) *requires that $\mathscr{V}_{[i]}$ is separable, i.e. $\mathscr{V}_{[i]} = \eta_i V_i^2 + \tilde{\mathscr{V}}(I_{ti}, v_i)$, for a suitable function $\tilde{\mathscr{V}}(I_{ti}, v_i)$. This suggests to look at the closed-loop dynamics of $\hat{\Sigma}_{[i]}^{DGU}$ as the interaction of two subsystems with state V_i and $[I_{ti}, v_i]^T$, respectively. Letting $K_i = [k_{i1}, k_{i2}, k_{i3}]$, the*

matrix $\hat{A}_i + \hat{B}_i K_i$ *can be partitioned as*

$$\hat{A}_i + \hat{B}_i K_i = \left[\begin{array}{c|cc} \sum_{j\in\mathcal{N}_i} -\frac{1}{R_{ij}C_{ti}} & \frac{1}{C_{ti}} & 0 \\ \hline \frac{k_{i1}-1}{L_{ti}} & \frac{k_{i2}-R_{ti}}{L_{ti}} & \frac{k_{i3}}{L_{ti}} \\ -1 & 0 & 0 \end{array}\right] = \left[\begin{array}{cc} \hat{A}_{cl,i1} & \hat{A}_{cl,i2} \\ \hat{A}_{cl,i3} & \hat{A}_{cl,i4} \end{array}\right].$$

Basic results in decentralized control [Lun92] show that the possibility of certifying stability of $\hat{A}_i + \hat{B}_i K_i$ *through* $\mathscr{V}_{[i]}$ *(i.e. the fulfillment of* (3.22)*) depends on the magnitude of the interconnection terms* $\hat{A}_{cl,i2}$ *and* $\hat{A}_{cl,i3}$ *(if they were both zero, the structure* (3.23) *would not be conservative). Note also that the local controller can partially modify* $\hat{A}_{cl,i3}$ *but not* $\hat{A}_{cl,i2}$*.*

3.3.3 QSL approximations as singular perturbations

We now discuss stability properties brought about by the proposed PnP decentralized controllers when applied to the mG model obtained without using QSL approximations. In other words, from (2.1a)-(2.1c), (3.14) and (3.18), we study stability of the closed-loop mG given by the controlled DGU models

$$\dot{\hat{x}}_{[i]}(t) = \hat{A}_i^{\circ}\hat{x}_{[i]} + \hat{M}_i\hat{d}_{[i]} + \left[\begin{array}{c} \frac{1}{C_{ti}}\sum_{j\in\mathcal{N}_i} I_{ij} \\ 0 \\ 0 \end{array}\right], \quad i \in \mathcal{V}, \tag{3.31}$$

with

$$\hat{A}_i^{\circ} = \left[\begin{array}{ccc} 0 & \frac{1}{C_{ti}} & 0 \\ \frac{k_{i1}-1}{L_{ti}} & \frac{k_{i2}-R_{ti}}{L_{ti}} & \frac{k_{i3}}{L_{ti}} \\ -1 & 0 & 0 \end{array}\right],$$

and the line dynamics (2.1c), i.e.

$$L_{ij}\dot{I}_{ij} = -R_{ij}I_{ij} + \begin{bmatrix} 1 & 0 & 0 \end{bmatrix}(\hat{x}_{[j]} - \hat{x}_{[i]}), \qquad \forall (i,j) \in \mathcal{E}. \tag{3.32}$$

Theorem 3.1. *If the closed-loop QSL-mG is asymptotically stable, then there is* $\bar{\varepsilon} > 0$ *such that, if* $L_{ij} < \bar{\varepsilon}$*,* $\forall (i,j) \in \mathcal{E}$*, also the system* (3.31)-(3.32) *is asymptotically stable.*

Proof. The proof, that is based on results in [Abe86], is reported in Appendix 3.6.1. □

Remark 3.8. *The estimation of parameter $\bar{\epsilon}$ is a well known problem in singular perturbation theory. Some methods for deriving such bound in our setting (i.e. multi-parameter singular perturbation problem) are discussed in [Abe86].*

3.3.4 Enhancements of local controllers for improving performances

In order to improve transient performances of controllers $\mathcal{C}_{[i]}$, we enhance them with feed-forward terms for

(i) pre-filtering reference signals;

(ii) compensating measurable disturbances.

Pre-filtering of the reference signal

Pre-filtering is a well known technique used to widen the bandwidth so as to speed up the response of the system. For each nominal closed-loop subsystem (3.19), we consider the transfer function $F_{[i]}(s)$ from $z_{ref\,[i]}(t)$ to the controlled variable $z_{[i]}(t)$, i.e.

$$F_{[i]}(s) = (\hat{H}_i \hat{C}_i)(sI - (\hat{A}_{ii} + \hat{B}_i K_i))^{-1} \begin{bmatrix} 0 \\ 1 \end{bmatrix}. \tag{3.33}$$

By virtue of a feedforward compensator $\tilde{C}_{[i]}(s)$, it is possible to filter the reference signal $z_{ref\,[i]}(t)$ (see Figure 3.3). Consequently, the new transfer

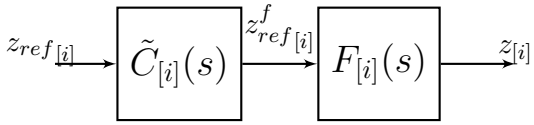

Figure 3.3: Block diagram of closed-loop DGU i with pre-filter.

function from $z_{ref\,[i]}(t)$ to $z_{[i]}(t)$ becomes

$$\tilde{F}_{[i]}(s) = \tilde{C}_{[i]}(s) F_{[i]}(s). \tag{3.34}$$

Now, taking a desired transfer function $\tilde{F}_{[i]}(s)$ for each subsystem, we can compute, from (3.34), the pre-filter $\tilde{C}_{[i]}(s)$ as

$$\tilde{C}_{[i]}(s) = \tilde{F}_{[i]}(s)F_{[i]}(s)^{-1} \tag{3.35}$$

under the following conditions [SP96]:

PF1 $F_{[i]}(s)$ must not have Right-Half-Plane (RHP) zeros that would become RHP poles of $\tilde{C}_{[i]}(s)$, making it unstable;

PF2 $F_{[i]}(s)$ must not contain a time delay, otherwise $\tilde{C}_{[i]}(s)$ would have a predictive action;

PF3 $\tilde{C}_{[i]}(s)$ must be realizable, i.e. it must have more poles than zeros.

Hence, if these conditions are fulfilled, the filter $\tilde{C}_{[i]}(s)$ given by (3.35) is realizable and asymptotically stable (this condition is essential since $\tilde{C}_{[i]}(s)$ works in open-loop). Furthermore, since $F_{[i]}(s)$ is asymptotically stable (controllers $\mathcal{C}_{[i]}$ are, in fact, designed solving the problem $\mathcal{O}_i$), the closed-loop system including filters $\tilde{C}_{[i]}(s)$ is asymptotically stable as well. We highlight that, if not all conditions PF1, PF2 and PF3 are fulfilled, then expression (3.35) cannot be used. Still, the compensator $\tilde{C}_{[i]}(s)$ can be designed for being effective within a given bandwidth, as shown in [SP96].

Compensation of measurable disturbances

Since load dynamics is assumed to be unknown, we have modeled each load current as a measurable disturbance $d_{[i]}(t)$. Let us define new local controllers $\tilde{\mathcal{C}}_{[i]}$ as

$$\tilde{\mathcal{C}}_{[i]}: \quad u_{[i]} = K_i\hat{x}_{[i]}(t) + \tilde{u}_{[i]}(t), \tag{3.36}$$

obtained by adding term $\tilde{u}_{[i]}(t)$ to controllers $\mathcal{C}_{[i]}$ in (3.18). The closed-loop dynamics (3.19) can be rewritten as follows

$$\tilde{\Sigma}^{DGU}_{[i]}: \begin{cases} \dot{\hat{x}}_{[i]}(t) = (\hat{A}_{ii} + \hat{B}_iK_i)\hat{x}_{[i]}(t) + \hat{M}_i\hat{d}_{[i]}(t) + \hat{B}_i\tilde{u}_{[i]}(t) \\ \hat{y}_{[i]}(t) = \hat{C}_i\hat{x}_{[i]}(t) \\ z_{[i]}(t) = \hat{H}_i\hat{y}_{[i]}(t) \end{cases} \tag{3.37}$$

We now use the new input $\tilde{u}_{[i]}(t)$ to compensate the measurable disturbance $d_{[i]}(t)$ (recall that $\hat{d}_{[i]} = [d^T{}_{[i]}\ z^T_{ref\,[i]}]^T$). From (3.37), the transfer function

from the disturbance $d_{[i]}(t)$ to the controlled variable $z_{[i]}(t)$ is

$$G^d_{[i]}(s) = (\hat{H}_i\hat{C}_i)(sI - (\hat{A}_{ii} + \hat{B}_iK_i))^{-1}\begin{bmatrix} M_i \\ 0 \end{bmatrix}. \tag{3.38}$$

Moreover, the transfer function from the new input $\tilde{u}_{[i]}(t)$ to the controlled variable $z_{[i]}(t)$ is

$$G_{[i]}(s) = (\hat{H}_i\hat{C}_i)(sI - (\hat{A}_{ii} + \hat{B}_iK_i))^{-1}\hat{B}_i. \tag{3.39}$$

If we combine (3.38) and (3.39), we obtain

$$z_{[i]}(s) = G_{[i]}(s)\tilde{u}_{[i]}(s) + G^d_{[i]}(s)d_{[i]}(s).$$

In order to zero the effect of the disturbance on the controlled variable, we set

$$\tilde{u}_{[i]}(s) = N_{[i]}(s)d_{[i]}(s).$$

where

$$N_{[i]}(s) = -G_{[i]}(s)^{-1}G^d_{[i]}(s) \tag{3.40}$$

is the transfer function of the compensator. Note that $N_{[i]}(s)$ is well defined under the following conditions [SP96]:

C1 $G_{[i]}(s)$ must not have RHP zeros that would become RHP poles of $N_{[i]}(s)$;

C2 $G_{[i]}(s)$ must not contain a time delay, otherwise $N_{[i]}(s)$ would have a predictive action

C3 $N_{[i]}(s)$ must be realizable, i.e. it must have more poles than zeros.

In this way, we can ensure that the compensator $N_{[i]}(s)$ is asymptotically stable, hence preserving the asymptotic stability of the system. When not all conditions C1, C2 and C3 are fulfilled, formula (3.40) cannot be used and perfect compensation cannot be achieved. Still, the compensator $N_{[i]}(s)$ can be designed to reject disturbances within a given bandwidth, as shown in [SP96]. The overall control scheme with the addition of the compensators is shown in Figure 3.4.

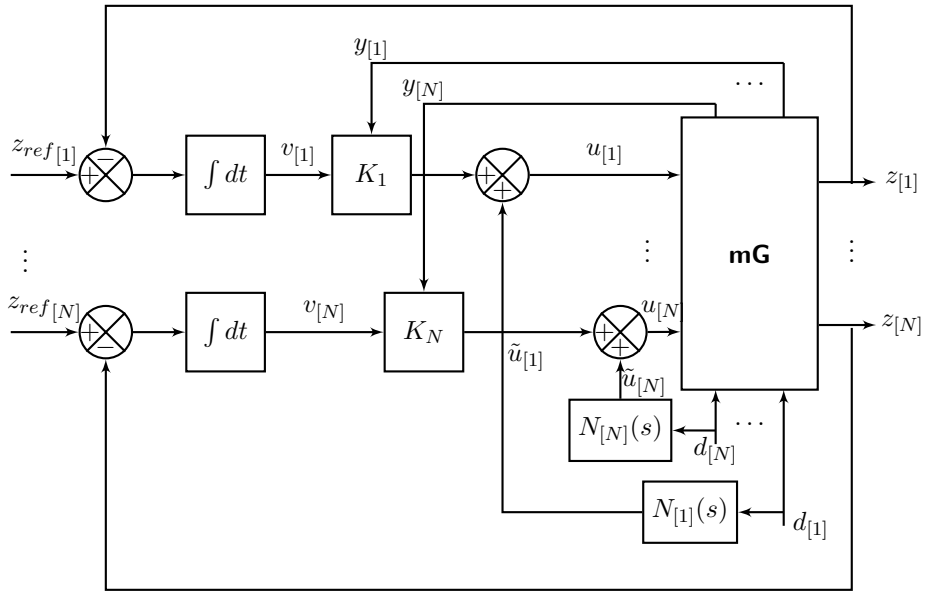

Figure 3.4: Overall DC mG control scheme with compensation of measurable disturbances $d_{[i]}(s)$.

3.3.5 Algorithm for the design of local controllers

Algorithm 3.1 collects the steps of the overall design procedure.

Algorithm 3.1 Design of controller $\mathcal{C}_{[i]}$ and compensators $\tilde{C}_{[i]}$ and $N_{[i]}$ for subsystem $\hat{\Sigma}_{[i]}^{DGU}$

Input: DGU $\hat{\Sigma}_{[i]}^{DGU}$ as in (3.15)

Output: Controller $\mathcal{C}_{[i]}$ and, optionally, pre-filter $\tilde{C}_{[i]}$ and compensator $N_{[i]}$

(A) Find K_i solving the LMI problem (3.26). If it is not feasible **stop** (controller $\mathcal{C}_{[i]}$ cannot be designed).
Optional steps

(B) Design the asymptotically stable local pre-filter $\tilde{C}_{[i]}$ and compensator $N_{[i]}$ as in (3.40).

3.3.6 Plug-and-play operations

In the following, we discuss the operations for updating local controllers when DGUs are added to or removed from an mG. We remind that all these operations are performed with the aim of preserving stability of the new closed-loop system. Consider, as a starting point, an mG composed of subsystems $\hat{\Sigma}_{[i]}^{DGU}, i \in \mathcal{V}$ equipped with local controllers $\mathcal{C}_{[i]}$ and compensators $\tilde{C}_{[i]}$ and $N_{[i]}$, $i \in \mathcal{V}$ produced by Algorithm 3.1.

Plug-in operation. Assume that the plug-in of a new DGU $\hat{\Sigma}_{[N+1]}^{DGU}$ described by matrices, $\hat{A}_{N+1\,N+1}$, $\hat{B}_{N+1}$, $\hat{C}_{N+1}$, $\hat{M}_{N+1}$, $\hat{H}_{N+1}$ and $\{\hat{A}_{N+1\,j}\}_{j\in\mathcal{N}_{N+1}}$ needs to be performed. Let $\mathcal{N}_{N+1}$ be the set of DGUs that are directly coupled with $\hat{\Sigma}_{[N+1]}^{DGU}$ through power lines and let $\{\hat{A}_{N+1\,j}\}_{j\in\mathcal{N}_{N+1}}$ be the matrices containing the corresponding coupling terms. According to our method, the design of controller $\mathcal{C}_{[N+1]}$ and compensators $\tilde{C}_{[N+1]}$ and $N_{[N+i]}$ requires Algorithm 3.1 to be executed. Since DGUs $\hat{\Sigma}_{[j]}^{DGU}$, $j \in \mathcal{N}_{N+1}$, have the new neighbor $\hat{\Sigma}_{[N+1]}^{DGU}$, we need to redesign controllers $\mathcal{C}_{[j]}$ and compensators $\tilde{C}_{[j]}$ and $N_{[j]}$, $\forall j \in \mathcal{N}_{N+1}$ because matrices $\hat{A}_{jj}$, $j \in \mathcal{N}_{N+1}$ change.

Only if Algorithm 3.1 does not stop in Step (A) when computing controllers $\mathcal{C}_{[k]}$ for all $k \in \mathcal{N}_{N+1} \cup \{N+1\}$, we have that the plug-in of $\hat{\Sigma}_{[N+1]}^{DGU}$ is allowed. Moreover, we stress that the redesign is not propagated further in the network and therefore the asymptotic stability of the new overall closed-loop QSL-mG model is preserved for a sufficient small η_{N+1} even without changing controllers $\mathcal{C}_{[i]}$, $\tilde{C}_{[i]}$ and $N_{[i]}$, $i \notin \{N+1\} \cup \mathcal{N}_{N+1}$.

Unplugging operation. Let us now examine the unplugging of DGU $\hat{\Sigma}_{[k]}^{DGU}$, $k \in \mathcal{V}$. The disconnection of $\hat{\Sigma}_{[k]}^{DGU}$ from the network leads to a change in matrix $\hat{A}_{jj}$ of each $\hat{\Sigma}_{[j]}^{DGU}$, $j \in \mathcal{N}_k$. Consequently, for each $j \in \mathcal{N}_k$, we have to redesign controllers $\mathcal{C}_{[j]}$ and compensators $\tilde{C}_{[j]}$ and $N_{[j]}$. As for the plug-in operation, we run Algorithm 3.1. If all operations can be successfully terminated, then the unplugging of $\hat{\Sigma}_{[k]}^{DGU}$ is allowed and stability is preserved without redesigning the local controllers $\mathcal{C}_{[j]}$, $j \notin \mathcal{N}_k$.

Remark 3.9. *From a practical point of view, one can imagine that, whenever a plug-in/-out operation needs to be performed, the neighboring DGUs of the entering/leaving subsystem are alerted by means of a communication network. The communication does not necessarily need to be performed in real-time since, in principle, addition/removal operations of DGUs are*

scheduled in advance. Note also that the communication network can be realized using different technologies (such as SCADA systems or wireless). Furthermore, we highlight that communication channels are needed for implementing secondary control schemes (see, e.g., Chapter 5). Hence, in this framework, the same network can be exploited for announcing plug-in and unplugging events. Finally, we notice that recent studies propose to use the electrical interconnections (i.e. power lines) for transmitting communication signals [DWSM17].

3.3.7 Hot plugging in/out operations

Plugging in/out operations can require to switch local controllers in real-time. In order to avoid jumps in the control variable at switching times, we embedded each local regulator into a bumpless control scheme [ÅH06] that is described in Appendix 3.6.3.

In particular, prior to real-time plugging in operation (*hot plugging in*), it is recommended to keep set points constant for a sufficient amount of time so as to guarantee the control variable in the bumpless control scheme is in steady state. This ensures smooth behaviors of the electrical variables. Similarly, when an unplugging operation is scheduled in advance, it is advisable to follow an *hot unplugging* protocol similar to the one described above for plugging in.

3.4 Simulation results

In this section, we study performance due to PnP controllers described in Section 3.3. As a starting point, we consider the mG depicted in Figure 2.1 with only two DGUs (Scenario 1) and we evaluate performance in terms of (i) tracking step references, (ii) transients after the hot plugging in of the two DGUs and (iii) robustness to unknown load dynamics. Then, we extend the analysis to an mG with 6 DGUs (Scenario 2) and we show that stability of the whole microgrid is guaranteed.

Simulations have been performed in PSCAD, a simulation environment for electric systems that allows to implement the mG model with realistic components.

3.4.1 Scenario 1

In this scenario, we consider the mG shown in Figure 2.1 composed of two identical DC DGUs connected through RL lines supporting 10 Ω and 6 Ω

loads, respectively. The duration of the simulation is 8 seconds and, for the sake of simplicity, we set $i = 1$ and $j = 2$. The output voltage reference has been selected at 48 V and it is equal for both DGUs. Parameters values for all DGUs are given in Table 3.2. Notice that that they are comparable to those used in [SDVG14a]. Figures 3.6 and 3.7 show the voltages at PCC_1 and PCC_2, respectively, for the whole simulation.

Voltage reference tracking at the startup

We assume that at the beginning of the simulation ($t = 0$ s), subsystems $\hat{\Sigma}_{[1]}^{DGU}$ and $\hat{\Sigma}_{[2]}^{DGU}$ are not interconnected. Therefore, stabilizing controllers $\mathcal{C}_i$, $i = 1, 2$ are designed neglecting coupling among DGUs. Moreover, in order to widen the bandwidth of each closed-loop subsystem, we use local pre-filters $\tilde{C}_{[i]}$, $i = 1, 2$ of reference signals. The desired closed-loop transfer functions $\tilde{F}_i(s)$, $i = 1, 2$ have been chosen as low-pass filters with steady-state gain equal to 0 dB and bandwidth equal to 100 Hz. The eigenvalues of the two decoupled closed-loop QSL subsystems are shown in Figure 3.5a. Moreover, by running Step (B) of Algorithm 3.1 we obtain two asymptotically stable local pre-filters $\tilde{C}_i$, $i = 1, 2$ whose Bode magnitude plots are depicted in Figure 3.5b. Notice that through the addition of the pre-filters, the frequency response of the two closed-loop transfer functions $F_i(s)$, $i = 1, 2$ coincide with the frequency response of the desired transfer functions $\tilde{F}_i(s)$, $i = 1, 2$ (see the green line in Figure 3.5c). From Figures 3.6 and 3.7 we notice that, at startup, the controllers ensure excellent tracking of the reference signals in a very short time (both voltages at PCC_1 and PCC_2 are equal to zero at $t = 0$).

Hot plugging in of DGUs 1 and 2

At time $t = 2$ s, we connect DGUs 1 and 2 together. This requires real-time switching of the local controllers which translates into two hot plugging in operations, as described in Section 3.3.7. The new decentralized controllers for subsystems $\hat{\Sigma}_{[1]}^{DGU}$ and $\hat{\Sigma}_{[2]}^{DGU}$ are designed running Algorithm 3.1. As shown in Section 3.3.6, the interconnection of the two subsystems leads to a variation of each DGU dynamics, therefore even compensators $\tilde{C}_{[i]}$ and $N_{[i]}$, $i = 1, 2$ need to be updated. In particular, the new desired closed-loop transfer functions $\tilde{F}_i(s)$, $i = 1, 2$ have been chosen as low-pass filters with steady-state gain equal to 0 dB and bandwidth equal to 100 Hz.

Since Algorithm 3.1 never stops in Step (A), the hot plug-in of the DGUs is allowed and local controllers get replaced by the new ones at

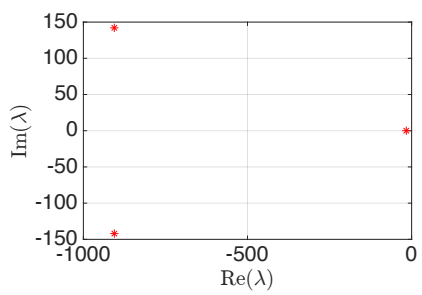

(a) Eigenvalues of each of the two decoupled closed-loop (CL) QSL ImG.

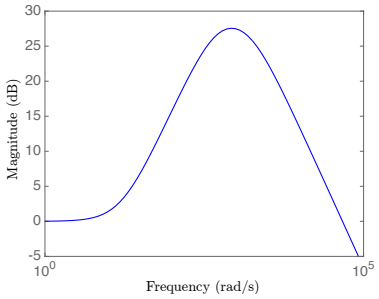

(b) Bode magnitude plot of pre-filters $\tilde{C}_{[i]}$, $i = 1, 2$.

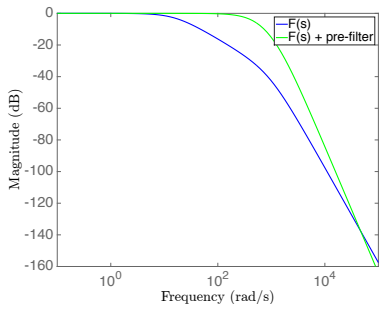

(c) Bode magnitude plot of $F_i(s)$, $i = 1, 2$ with (green) and without (blue) pre-filters.

Figure 3.5: Features of PnP controllers for Scenario 1 when the DGUs are not interconnected.

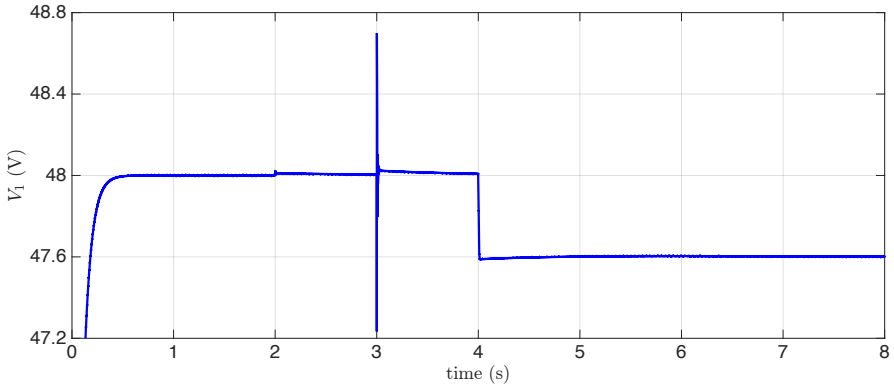

Figure 3.6: Scenario 1 - Voltage at PCC_1.

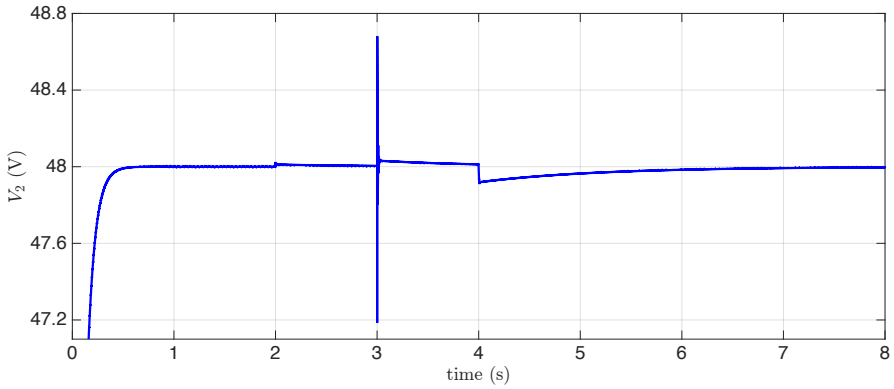

Figure 3.7: Scenario 1 - Voltage at PCC_2.

$t = 2$ s. Figure 3.8a shows the closed-loop eigenvalues of the overall QSL-mG composed of two interconnected DGUs. The Bode magnitude plots of compensators $\tilde{C}_{[i]}$ and $N_{[i]}$, $i = 1, 2$ are depicted in Figure 3.8b and 3.8c, respectively, while the singular values of the overall closed-loop transfer function $F(s)$ with inputs $[z_{ref_{[1]}}, z_{ref_{[2]}}]^T$ and outputs $[z_{[1]}, z_{[2]}]^T$ are shown in Figure 3.8d.

Figures 3.6 and 3.7 show that bumpless control transfer schemes ensure no significant deviations in the output signals when the controller switch is performed at $t = 2$ s.

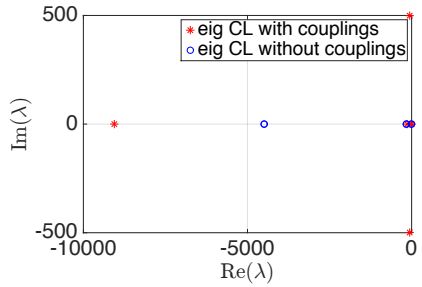

(a) Eigenvalues of the closed-loop (CL) QSL mG.

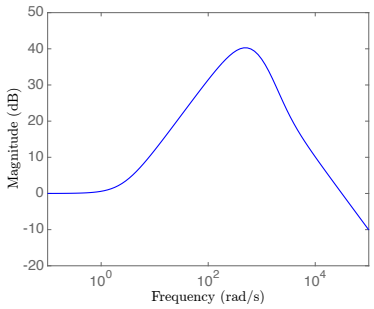

(b) Bode magnitude plot of pre-filters $\tilde{C}_{[i]}$, $i = 1, 2$.

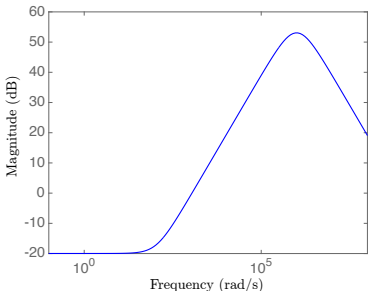

(c) Bode magnitude plot of disturbances compensators $N_{[i]}$, $i = 1, 2$.

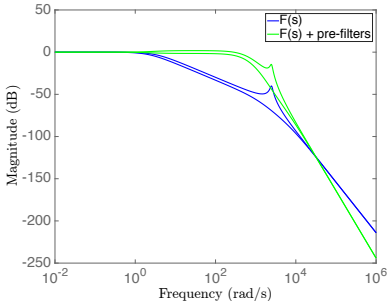

(d) Singular values of $F(s)$ with (green) and without (blue) pre-filters.

Figure 3.8: Features of PnP controllers for Scenario 1 when the DGUs are connected together.

Robustness to unknown load dynamics

Next, we assess the performance of PnP controllers when loads suddenly change. To this purpose, at $t = 3$ s we decrease the load resistances at PCC_1 and PCC_2 to half of their initial values. Oscillations visible in Figures 3.6 and 3.7 are zoomed in in Figures 3.9a and 3.9b, respectively. These plots confirm very good compensation of the current disturbances produced by load changes. The small oscillations of the voltage signals are due to the presence of complex conjugate poles in the transfer function of the overall closed-loop microgrid including couplings (as shown in Figure 3.8a). However, these oscillations disappear after a short transient. We recall that load currents (see Figures 3.9c and 3.9d) are treated as measurable disturbances in our model, and a variation of the load resistance induces step-like changes in the disturbances.

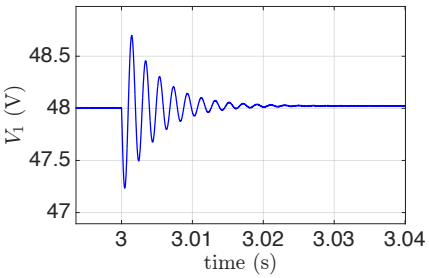

(a) Voltage at PCC_1.

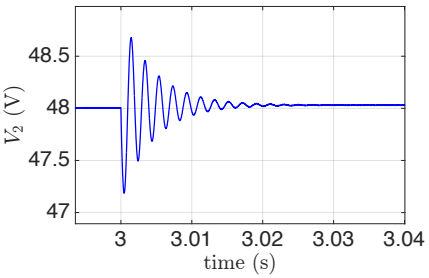

(b) Voltage at PCC_2.

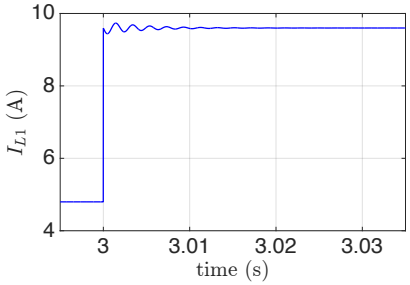

(c) Instantaneous load current I_{L1}.

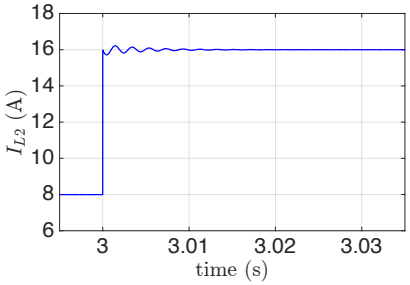

(d) Instantaneous load current I_{L2}.

Figure 3.9: Scenario 1 - Performance of PnP decentralized voltage control in presence of load switches at time $t = 3$ s.

Voltage tracking for DGU 1

Finally, we evaluate the performance in tracking step changes in the voltage reference at one PCC (e.g. PCC_1) when the DGUs are connected together. This test is of particular concern if we look at the concrete implementation of DC mGs. In fact, changes in the voltage references can be required in order to regulate power flow among the DGU, or to control the state-of-charge of batteries possibly embedded in the mG. To this purpose, at $t = 4$ s, we let $v^{\star}_{1,MG}$ (i.e. the reference signal of DGU 1) step down to 47.6 V. Notice that this small variation of the voltage reference at PCC_1 is sufficient to let an appreciable amount of current flow through the line, since the line impedance is quite small. Figure 3.6 shows how PnP controllers are capable to guarantee good tracking performances for DGU 1, when the corresponding voltage reference is changed ($t = 4$ s). Moreover, interactions between the two DGUs are small (see Figure 3.7).

3.4.2 Scenario 2

In this second scenario, we consider the meshed mG shown in black in Figure 3.10 and composed of 5 DGUs. Differently from Scenario 1, some DGU have more than one neighbor. This means that the disturbances influencing their dynamics will be greater. Moreover, the presence of a loop further complicates voltage regulation. While several studies focused on radially interconnected mGs, to the best of our knowledge, control of loop-interconnected DGUs has not been equally investigated yet.

In order to assess the capability of the proposed decentralized approach to cope with heterogeneous dynamics, we consider an mG composed of DGUs with non-identical electrical parameters; they are listed in tables 3.3 and 3.4 in Appendix 3.6.5. Moreover, in order to allow for current flow through the lines, we set slightly different voltage references for the DGUs composing the mG in Figure 3.10 (see Table 3.5 in Appendix 3.6.5). We also assume that DGUs 1-5 supply 10 Ω, 6 Ω, 4 Ω, 2 Ω and 3 Ω

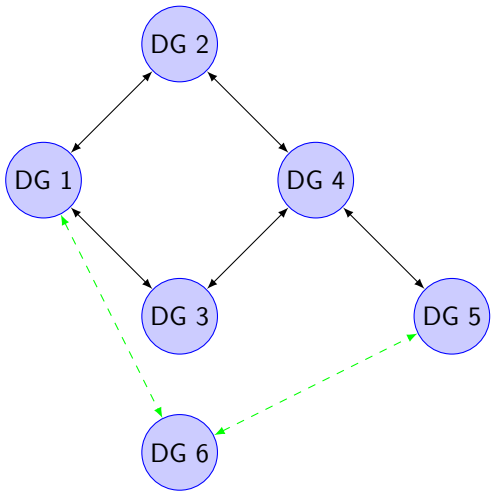

Figure 3.10: Scenario 2 - Scheme of the mG composed of 5 DGUs until $t = 4$ s (in black) and of 6 DGUs after the plugging in of $\hat{\Sigma}_{[6]}^{DGU}$ (in green). Blue nodes represent DGUs modeled as in the dashed box in Figure 3.2, with a local load connected to each PCC. Black arrows identify RL power lines.

loads, respectively. Furthermore, we highlight that, for this scenario, no compensators $\tilde{C}_i$ and N_i have been used. The duration of the simulation is 15 seconds.

At $t = 0$, all the DGUs are assumed to be isolated and not connected to each other. However, we choose to equip each subsystem $\hat{\Sigma}^{DGU}_{[i]}$, $i \in \mathcal{V} = \{1, \ldots, 5\}$, with controller $\mathcal{C}_{[i]}$ designed by running Algorithm 3.1 and taking into account couplings among DGUs. This is possible because, as shown in Section 3.3.2, local controllers stabilize the mG also in absence of couplings.

Because of this choice of local controllers in the startup phase, when the five subsystems are connected together at time $t = 1.5$ s, no bumpless control scheme is required since no real-time switch of controllers is performed. The closed-loop eigenvalues of the overall QSL-mG are depicted in Figure 3.11a while Figure 3.11b shows the closed-loop transfer function of the whole microgrid.

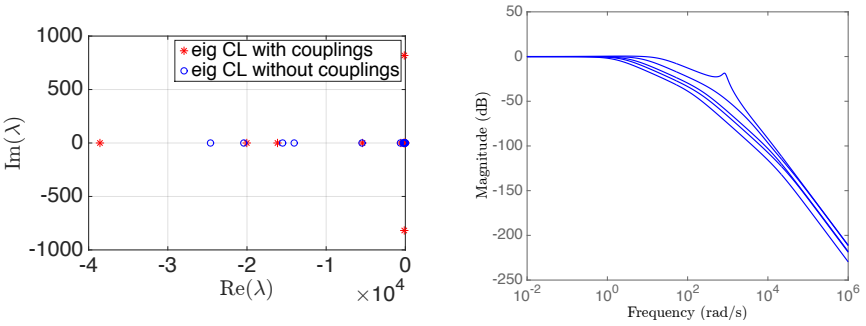

(a) Eigenvalues of the closed-loop (CL) QSL mG.

(b) Singular values of $F(s)$.

Figure 3.11: Features of PnP controllers for Scenario 2 with 5 interconnected DGUs.

Plug-in of a new DGU

For evaluating the PnP capabilities of our control approach, at time $t = 4$ s, we simulate the connection of DGU $\hat{\Sigma}^{DGU}_{[6]}$ with $\hat{\Sigma}^{DGU}_{[1]}$ and $\hat{\Sigma}^{DGU}_{[5]}$, as shown in Figure 3.10. This requires to update in real-time controllers $\mathcal{C}_{[j]}$, $j \in \mathcal{N}_6$, with $\mathcal{N}_6 = \{1, 5\}$ (see Section 3.3.6). Notably, the new controllers for subsystems $\hat{\Sigma}^{DGU}_{[1]}$, $\hat{\Sigma}^{DGU}_{[5]}$ and $\hat{\Sigma}^{DGU}_{[5]}$ are synthesized running Algorithm 3.1 and, since it never stops in Step (A), the hot plug-in of DGU 6 is allowed. At the same time, the local regulators for DGU 1 and 5 get replaced by the new ones at $t = 4$ s. Figures 3.12a and 3.12b show, respectively, the closed-loop eigenvalues and the singular values of the closed-loop $F(s)$ of the overall QSL-mG represented in Figure 3.10 and equipped with the

controllers described above. Moreover, from Figure 3.13, we note that, despite the different voltages at PCCs of DGUs 1, 5 and 6, bumpless control transfer schemes ensure small deviations of the output signals from their references when controller switch is performed. Moreover, these perturbations disappear after short transients.

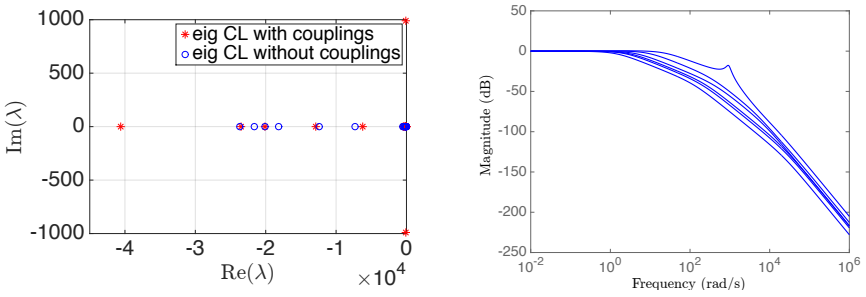

(a) Eigenvalues of the closed-loop (CL) QSL mG.

(b) Singular values of $F(s)$.

Figure 3.12: Features of PnP controllers for Scenario 2 with 6 interconnected DGUs

Robustness to unknown load dynamics

In order to test the robustness of the overall mG to unknown load dynamics, at $t = 8$ s, the load of DGU 6 is decreased from 8 Ω to 4 Ω. Figures 3.14a and 3.14b show that, when the load change of $\hat{\Sigma}_{[6]}^{DGU}$ occurs, the voltages at PCC_1 and PCC_5 exhibit very small variations which last for a short time. Then, load voltages of $\hat{\Sigma}_{[1]}^{DGU}$ and $\hat{\Sigma}_{[5]}^{DGU}$ converge to their reference values. Similar remarks can be done for the new DGU $\hat{\Sigma}_{[6]}^{DGU}$: as shown in Figure 3.14c, there is a short transient at the time of the load change, that is effectively compensated by the control action. These experiments highlight that controllers $\mathcal{C}_{[i]}$, $i = 1, \ldots, 6$ may ensure very good tracking of the reference signal and robustness to unknown load dynamics even without using compensators $\tilde{C}_{[6]}$ and $N_{[6]}$.

Unplugging of a DGU

Next, we simulate the disconnection of $\hat{\Sigma}_{[3]}^{DGU}$ so that the considered mG assumes the topology shown in Figure 3.15. The set of neighbors of DGU 3 is $\mathcal{N}_3 = \{1, 4\}$. Because of the disconnection, there is a change in the local

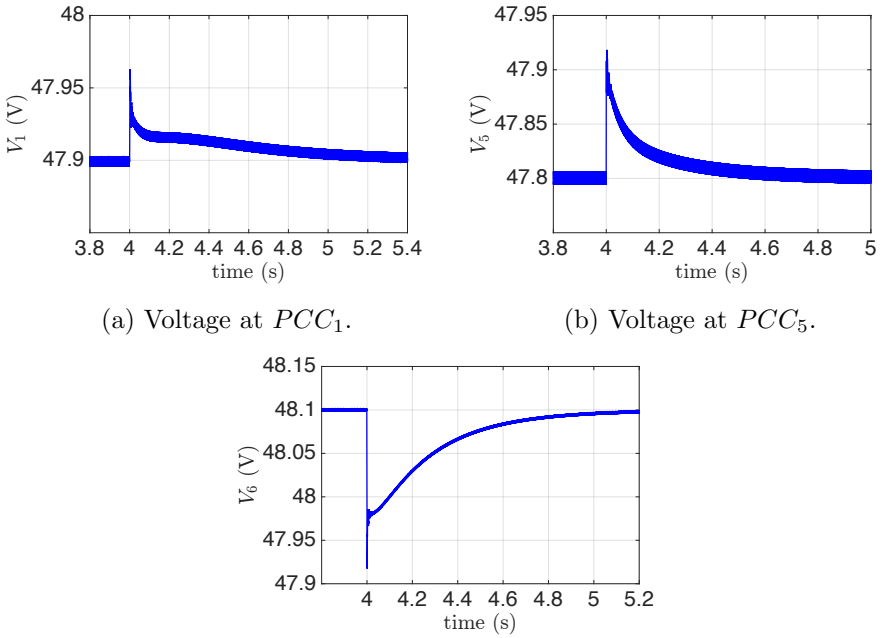

(a) Voltage at PCC_1.

(b) Voltage at PCC_5.

(c) Voltage at PCC_6.

Figure 3.13: Scenario 2 - Performance of PnP decentralized voltage controllers during the hot plug-in of DGU 6 at time $t = 4$ s.

dynamics $\hat{A}_{jj}$ of DGUs $\hat{\Sigma}_{[j]}^{DGU}$, $j \in \mathcal{N}_3$. Then, each controller $\mathcal{C}_{[j]}$, $j \in \mathcal{N}_3$ must be redesigned (see Section 3.3.6). Consequently, we run Algorithm 3.1 for computing the vectors K_1 and K_4 according to the new mG topology. Since Algorithm 3.1 never stops in Step (A), the disconnection of $\hat{\Sigma}_{[3]}^{DGU}$ is allowed. Figure 3.16a shows that the closed-loop model of the new QSL microgrid is still asymptotically stable while Figure 3.16b shows the closed-loop transfer function $F(s)$ of the mG.

Hot-unplugging of $\hat{\Sigma}_{[3]}^{DGU}$ is performed at time $t = 12$ s. Even for the unplugging operation, by means of bumpless control transfer, load voltages of DGUs $\hat{\Sigma}_{[j]}^{DGU}$, $j \in \mathcal{N}_3$ show small deviation from their respective reference values when the hot-unplugging of DGU 3 (and, hence, updating of controllers $\mathcal{C}_{[1]}$ and $\mathcal{C}_{[5]}$) is performed at $t = 12$ s (see Figure 3.17). We stress again that stability of the mG is preserved despite the disconnection of $\hat{\Sigma}_{[3]}^{DGU}$.

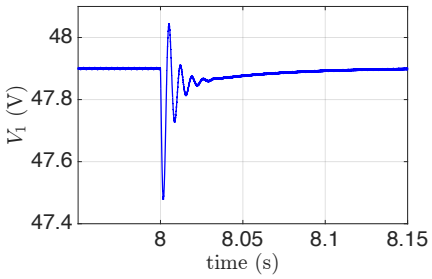

(a) Voltage at PCC_1.

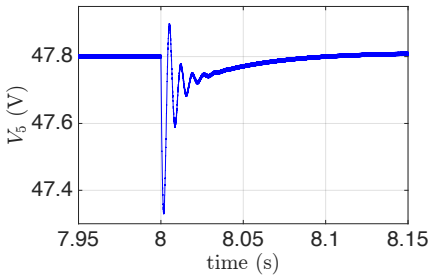

(b) Voltage at PCC_5.

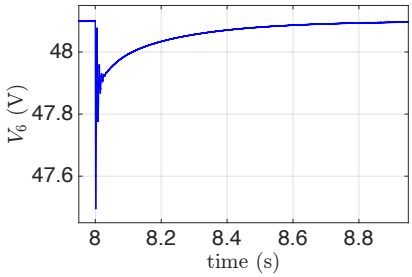

(c) Voltage at PCC_6.

Figure 3.14: Scenario 2 - Performance of PnP decentralized voltage controllers in terms of robustness to an abrupt change of load resistances at time $t = 8$ s.

3.5 Final comments

In this chapter, we presented a scalable control design approach for guaranteeing voltage stability in DC mGs. The main feature of the proposed methodology is that, whenever a DGU is plugged in or out, only a limited number of local controllers must be updated. This is due to the fact that the synthesis of each individual regulator uses only information about the corresponding DGU and lines connected to it.

In the next chapter, an extension of the methodology described in the above sections is provided. Notably, we will present a procedure for designing local stabilizing voltage regulators in a totally decentralized fashion, i.e. exploiting the knowledge of the corresponding DGU model only. Other pieces of information from neighboring subsystems (such as the value of the power lines connected to them) will not be required anymore.

We also observe that primary PnP voltage controllers can be coupled

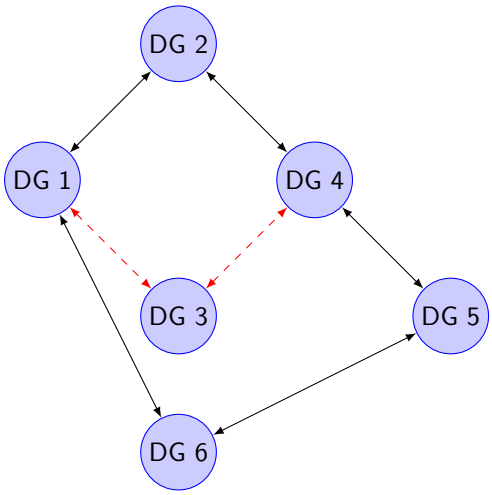

Figure 3.15: Scenario 2 - Scheme of the mG composed of 5 DGUs after the unplugging of $\hat{\Sigma}_{[3]}^{DGU}$ at time $t = 12$ s.

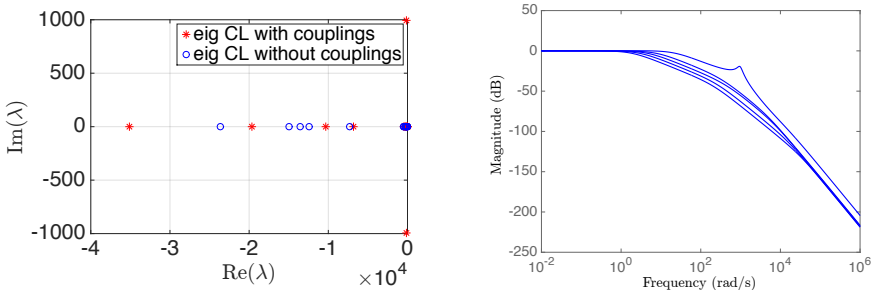

(a) Eigenvalues of the closed-loop (CL) QSL mG.

(b) Singular values of $F(s)$.

Figure 3.16: Features of PnP controllers for Scenario 2 after the unplugging of DGU 3.

with higher level regulators so as to orchestrate mutual coordination among DGUs and achieve advanced behaviors. As discussed in Remark 3.4, these tasks are addressed by letting an higher control layer compute suitable voltage set-points for primary PnP regulators. In Chapter 5, we show how to build a secondary consensus-based control layer on top of a primary voltage regulation scheme, with the aim of guaranteeing stable current sharing and voltage balancing.

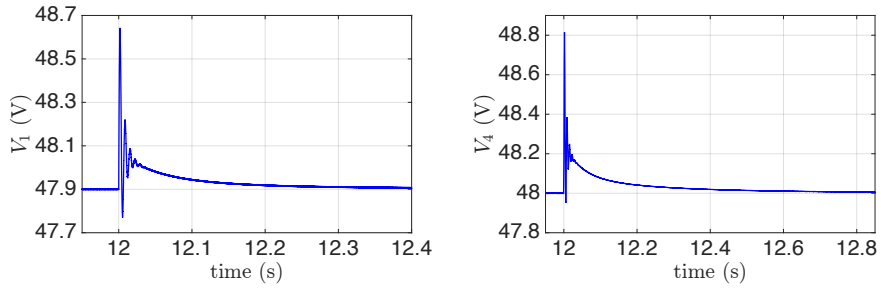

(a) Voltage at PCC_1. (b) Voltage at PCC_4.

Figure 3.17: Scenario 2 - Performance of PnP decentralized voltage controllers during the hot-unplugging of DGU 3 at $t = 12$ s.

3.6 Appendix

3.6.1 Proof of Theorem 3.1

Proof. We treat each impedance L_{ij} in (3.32) as a singular perturbation parameter and exploit results in [Abe86] on multi-parameter singular perturbations. More specifically, we want to apply Theorem 5 in [Abe86]. We denote with $\bar{N}$ the cardinality of $\mathcal{E}$, assign indices $1, \dots, \bar{N}$ to pairs in $\mathcal{E}$, i.e. $\mathcal{E} = \{e_1, e_2, \dots, e_{\bar{N}}\}$, and define $\tilde{x} = [I_{e_1}, \dots, I_{e_{\bar{N}}}]^T$. Let also $\mathcal{I} \in \mathbb{R}^{|\mathcal{V}| \times \bar{N}}$ be the incidence matrix of the directed graph $\mathcal{G}$ with nodes $\mathcal{V}$ and edges $\mathcal{E}$. This means that, assuming $e_j = (k, \ell)$, row j of $\mathcal{I}$ has the elements

$$\mathcal{I} = \begin{cases} -1 & \text{if } i = k \\ 1 & \text{if } i = \ell \\ 0 & \text{otherwise} \end{cases}$$

By neglecting exogenous disturbances $\hat{d}_{[i]}$ in (3.31) (as they do not affect stability properties), model (3.31) and (3.32) can be written as

$$\dot{\hat{\mathbf{x}}} = \hat{\mathbf{A}}^\circ \hat{\mathbf{x}} + \hat{\mathbf{B}}^\circ \tilde{\mathbf{x}} \tag{3.41a}$$

$$\mathbf{E}(\varepsilon)\dot{\tilde{\mathbf{x}}} = \hat{\mathbf{C}}^\circ \hat{\mathbf{x}} + \hat{\mathbf{D}}^\circ \tilde{\mathbf{x}} \tag{3.41b}$$

where

$$\hat{\mathbf{A}}^\circ = \operatorname{diag}\left[\hat{A}_1^\circ, \dots, \hat{A}_N^\circ\right], \quad \hat{\mathbf{B}}^\circ = \operatorname{diag}\left[\hat{B}_1^\circ, \dots, \hat{B}_N^\circ\right], \quad \hat{\mathbf{C}}^\circ = \mathcal{I}^T \otimes \begin{bmatrix} 1 & 0 & 0 \end{bmatrix},$$

$$\hat{\mathbf{D}}^\circ = \operatorname{diag}\left[-R_{e_1}, \dots, -R_{e_{\bar{N}}}\right], \ \varepsilon = [L_{e_1}, \dots, L_{e_{\bar{N}}}], \ \mathbf{E}(\varepsilon) = \operatorname{diag}\left[L_{e_1}, \dots, L_{e_{\bar{N}}}\right].$$

In these matrices, L_e and R_e are the inductance and resistance of line $e \in \mathcal{E}$ (see (3.32)) and, from (3.31), blocks $\hat{B}_i^\circ$, $i, \dots, N$ are defined as

$$\hat{B}_i^\circ = \frac{1}{C_{ti}} \begin{bmatrix} 1_{\mathcal{N}_i} \\ 0_{\bar{N}} \\ 0_{\bar{N}} \end{bmatrix},$$

where $0_{\bar{N}}$ is a row vector composed of $\bar{N}$ zeros and the vector $1_{\mathcal{N}_i} \in \mathbb{R}^{1\times\bar{N}}$ has all zero entries, except those in positions $j \in \mathcal{N}_i$, which are equal to one.

We now verify assumptions of Theorem 5 in [Abe86]. First, we check that matrix $\hat{\mathbf{D}}^\circ$ is strongly block D-stable relative to the multi index $(1, \dots, 1)$ made of $\bar{N}$ elements. From Definitions 1 and 3 in [Abe86], characterizing strong block D-stability amounts to verify that there exists $\mu > 0$ such that, for all matrices $Q \in \mathbb{R}^{\bar{N}\times\bar{N}}$ verifying

$$||Q||_F = \left(\sum_{i=1}^{\bar{N}} \sum_{j=1}^{\bar{N}} (Q_{ij})^2 \right)^{\frac{1}{2}} < \mu$$

($||\cdot||_F$ denotes the Frobenius norm) and for all $\theta_i > 0$, $i = 1, \dots, \bar{N}$, the matrices $\Theta(\hat{\mathbf{D}}^\circ + Q)$, $\Theta = \operatorname{diag}[\theta_1, \dots, \theta_{\bar{N}}]$ are Hurwitz (i.e. their eigenvalues have strictly negative real part). To prove this property, we use the Gershgorin circle theorem [GVL12]. Note that

$$\Theta(\hat{\mathbf{D}}^\circ + Q) = \\ = \begin{bmatrix} \theta_1(-R_{e_1} + Q_{11}) & \theta_1 Q_{12} & \dots & \theta_1 Q_{1\bar{N}} \\ \theta_2 Q_{21} & \theta_2(-R_{e_2} + Q_{22}) & \dots & \theta_2 Q_{2\bar{N}} \\ \vdots & \ddots & \ddots & \vdots \\ \theta_{\bar{N}} Q_{\bar{N}1} & \theta_{\bar{N}} Q_{\bar{N}2} & \dots & \theta_{\bar{N}}(-R_{e_{\bar{N}}} + Q_{\bar{N}\bar{N}}) \end{bmatrix}.$$

Let $\mathcal{B}(c, \rho) \subset \mathbb{C}$ be the closed ball of center c and radius ρ. Then, all eigenvalues of $\Theta(\hat{\mathbf{D}}^\circ + Q)$ are in the set $\bigcup_{i=1}^{\bar{N}} \mathcal{B}(c_i, \rho_i)$ where $c_i = \theta_i(-R_{e_i} + Q_{ii})$ and $\rho_i = \sum_{\substack{j=1 \\ j\neq i}}^{\bar{N}} |\theta_i Q_{ij}|$. Each ball $\mathcal{B}(c_i, \rho_i)$ collects only complex numbers with strictly negative real parts if

$$\theta_i(-R_{e_i} + Q_{ii}) < -\rho_i. \tag{3.42}$$

Since $\theta_i > 0$, condition (3.42) is equivalent to $\theta_i(-R_{e_i} + Q_{ii}) < \theta_i \sum_{\substack{j=1 \\ j\neq i}}^{\bar{N}} |Q_{ij}|$ and hence

$$\sum_{\substack{j=1 \\ j\neq i}}^{\bar{N}} |Q_{ij}| < R_{e_i} - Q_{ii}. \tag{3.43}$$

We show now that all conditions (3.43) for $i \in \mathcal{V}$ are fulfilled if $\mu = \frac{1}{\sqrt{\bar{N}}} \min_{e_i \in \mathcal{E}} R_{e_i}$. Indeed, if $\mu > ||Q||_F$, then

$$\min_{e_i \in \mathcal{E}} R_{e_i} > \sqrt{\bar{N}}||Q||_F \geq \sqrt{\bar{N}}||Q_{i,\bullet}||_2, \tag{3.44}$$

where $Q_{i,\bullet}$ is row i of matrix Q and $||Q_{i,\bullet}||_2 = (\sum_{j=1}^{\bar{N}} \left(Q_{i,j}\right)^2)^{\frac{1}{2}}$ is its Euclidean norm. Denoting with $||Q_{i,\bullet}||_1 = \sum_{j=1}^{\bar{N}} |Q_{i,j}|$ the 1-norm of $Q_{i,\bullet}$, we have

$$\sqrt{\bar{N}}||Q_{i,\bullet}||_2 \geq ||Q_{i,\bullet}||_1 \geq Q_{ii} + \sum_{\substack{j=1 \\ j\neq i}}^{\bar{N}} |Q_{ij}|. \tag{3.45}$$

From (3.44) and (3.45) we have

$$\min_{e_i \in \mathcal{E}} R_{e_i} - Q_{ii} > \sum_{\substack{j=1 \\ j\neq i}}^{\bar{N}} |Q_{ij}|.$$

that implies (3.43) for all $i \in \mathcal{V}$.

The last assumption of Theorem 5 in [Abe86] that has to be verified is that the quasi-stationary model given by (3.41a) and

$$\hat{\mathbf{C}}^\circ \hat{\mathbf{x}} + \hat{\mathbf{D}}^\circ \tilde{\mathbf{x}} = 0 \tag{3.46}$$

is asymptotically stable, i.e. the matrix $\hat{\mathbf{A}}^\circ - \hat{\mathbf{B}}^\circ (\hat{\mathbf{D}}^\circ)^{-1} \hat{\mathbf{C}}^\circ$ is Hurwitz. Note that (3.46) is the system of scalar equations

$$R_{e_j} I_{e_j} = V_\ell - V_k, \qquad \text{if } e_j = (k, \ell) \tag{3.47}$$

for all $e_j \in \mathcal{E}$.

Since (3.47) are the QSL conditions (3.4a), the model given by (3.41a) and (3.46) is the closed-loop QSL-mG model, which is asymptotically stable by assumption. Then, the application of Theorem 5 of [Abe86] completes the proof. □

3.6.2 How interactions among DGUs can destabilize a DC mG

In this appendix, we show why designing decentralized stabilizing controllers without counteracting the contribution of coupling terms on the total system energy computation may lead to mG instability when DGUs are interconnected.

We consider two DGUs with dynamics

$$\begin{aligned}\hat{\Sigma}_{[1]}: &\begin{cases}\dot{\hat{x}}_{[1]}(t) = \hat{A}_{11}\hat{x}_{[1]}(t) + \hat{A}_{12}\hat{x}_{[2]}(t) + \hat{B}_1 u_{[1]}(t) + \hat{M}_1\hat{d}_{[1]}(t)\\ y_{[1]}(t) = \hat{C}_1\hat{x}_{[1]}(t)\end{cases}\\ \hat{\Sigma}_{[2]}: &\begin{cases}\dot{\hat{x}}_{[2]}(t) = \hat{A}_{22}\hat{x}_{[2]}(t) + \hat{A}_{21}\hat{x}_{[1]}(t) + \hat{B}_2 u_{[2]}(t) + \hat{M}_2\hat{d}_{[2]}(t)\\ y_{[2]}(t) = \hat{C}_2\hat{x}_{[2]}(t)\end{cases}\end{aligned} \tag{3.48}$$

where $\hat{x}_{[i]} = [V_i, I_{ti}, v_i]^T$, $u_{[i]} = V_{ti}$, $y_{[i]} = V_i$, $\hat{d}_{[i]} = [I_{Li}, V_{ref,i}]^T$, $i = 1, 2$, are, respectively, the state, the control input, the controlled variable and the exogenous input. Matrices in (3.48) have the same structure as in Section 3.2.1; hence, since in this example $\mathcal{N}_1 = \{2\}$ and $\mathcal{N}_2 = \{1\}$, one has

$$A_{ii} = \begin{bmatrix} -\frac{1}{R_{ij}C_{ti}} & \frac{1}{C_{ti}} \\ -\frac{1}{L_{ti}} & -\frac{R_{ti}}{L_{ti}} \end{bmatrix}, \qquad i = 1, 2. \tag{3.49}$$

Electrical parameters, which are similar to those in [SDVG14a], are reported in Table 3.1.

In the sequel, we separately analyze the impact of couplings on the mG stability when DGUs are locally stabilized via either Linear Quadratic Regulators (LQRs) or through pole placement design.

Linear Quadratic Regulators

We design decentralized controllers for each DGU assuming that they are dynamically decoupled, hence $\hat{A}_{12} = \hat{A}_{21} = 0$. Since the state $\hat{x}_{[i]}$ is measured, we can design the following state-feedback decentralized controllers

$$\begin{aligned} u_{[1]}(t) &= K_1\hat{x}_{[1]}(t)\\ u_{[2]}(t) &= K_2\hat{x}_{[2]}(t)\end{aligned} \tag{3.50}$$

where K_1 and K_2 are LQRs computed using the weights $Q_1 = \text{diag}[10^{-3}, 10^{-2}, 10^3]$, $R_1 = 0.1$ and $Q_2 = \text{diag}[10^{-2}, 10^{-2}, 10^4]$, $R_2 = 10^{-2}$, respectively. Control laws (3.50) guarantee that the closed-loop decoupled DGUs

$$\begin{aligned}\begin{bmatrix}\dot{\hat{x}}_{[1]}(t)\\ \dot{\hat{x}}_{[2]}(t)\end{bmatrix} &= \begin{bmatrix}\hat{A}_{11} & 0\\ 0 & \hat{A}_{22}\end{bmatrix}\begin{bmatrix}\hat{x}_{[1]}(t)\\ \hat{x}_{[2]}(t)\end{bmatrix} + \begin{bmatrix}\hat{B}_1K_1 & 0\\ 0 & \hat{B}_2K_2\end{bmatrix}\begin{bmatrix}\hat{x}_{[1]}(t)\\ \hat{x}_{[2]}(t)\end{bmatrix} =\\ &= \underbrace{\begin{bmatrix}\hat{A}_{11}+\hat{B}_1K_1 & 0\\ 0 & \hat{A}_{22}+\hat{B}_2K_2\end{bmatrix}}_{\mathbf{\hat{A}^D_{CL}}}\begin{bmatrix}\hat{x}_{[1]}(t)\\ \hat{x}_{[2]}(t)\end{bmatrix}\end{aligned} \tag{3.51}$$

are asymptotically stable. Indeed, $\text{eig}(\mathbf{\hat{A}^D_{CL}}) = \text{eig}(\hat{A}_{11}+\hat{B}_1K_1) \cup \text{eig}(\hat{A}_{22}+\hat{B}_2K_2)$ is the set

$$\{-9.0629{\cdot}10^3, -0.0143{\cdot}10^3, -0.1945{\cdot}10^3\}\cup\{-9.9717{\cdot}10^3, -0.0486{\cdot}10^3, -0.6064{\cdot}10^3\}.$$

Considering coupling terms, the closed-loop system becomes

$$\begin{aligned}\begin{bmatrix}\dot{\hat{x}}_{[1]}(t)\\ \dot{\hat{x}}_{[2]}(t)\end{bmatrix} &= \begin{bmatrix}\hat{A}_{11} & \hat{A}_{12}\\ \hat{A}_{21} & \hat{A}_{22}\end{bmatrix}\begin{bmatrix}\hat{x}_{[1]}(t)\\ \hat{x}_{[2]}(t)\end{bmatrix} + \begin{bmatrix}\hat{B}_1K_1 & 0\\ 0 & \hat{B}_2K_2\end{bmatrix}\begin{bmatrix}\hat{x}_{[1]}(t)\\ \hat{x}_{[2]}(t)\end{bmatrix} =\\ &= \begin{bmatrix}\dot{\hat{x}}_{[1]}(t)\\ \dot{\hat{x}}_{[2]}(t)\end{bmatrix}\underbrace{\begin{bmatrix}\hat{A}_{11}+\hat{B}_1K_1 & \hat{A}_{12}\\ \hat{A}_{21} & \hat{A}_{22}+\hat{B}_1K_1\end{bmatrix}}_{\mathbf{\hat{A}^C_{CL}}}\begin{bmatrix}\dot{\hat{x}}_{[1]}(t)\\ \dot{\hat{x}}_{[2]}(t)\end{bmatrix}.\end{aligned} \tag{3.52}$$

Since the controllers have been designed without taking into account interactions among DGUs, we cannot ensure that system (3.52) is asymptotically stable. In fact, for the proposed example, we have

$$\text{eig}(\mathbf{\hat{A}^C_{CL}}) = \{-19077, \mathbf{20+560}\text{i}, \mathbf{20-560}\text{i}, -690, -161, -11\}.$$

Pole placement design

An alternative method for designing decentralized stabilizing controllers (3.50), is to assume again $\hat{A}_{12} = \hat{A}_{21} = 0$ and place the closed-loop poles of subsystems $\hat{\Sigma}_{[1]}$ and $\hat{\Sigma}_{[2]}$ (i.e. the eigenvalues of $\mathbf{\hat{A}^D_{CL}}$) in the left half plane. In particular, since the pair $(\hat{A}_{ii}, \hat{B}_i)$ is controllable (see Proposition 3.2), we can set

$$\begin{aligned}\text{eig}(\hat{A}_{11}+\hat{B}_1K_1) &= \{-8.5190\cdot10^3, -530.4, -1.46\}\\ \text{eig}(\hat{A}_{22}+\hat{B}_2K_2) &= \{-9.3734\cdot10^3, -571.9, -1.44\}\end{aligned} \tag{3.53}$$

and derive gains K_1 and K_2 satisfying (3.53) by using the algorithm in [KNVD85]. Obviously, the obtained controllers stabilize the closed-loop decoupled subsystems (3.51). However, they cannot guarantee that the interconnection of DGUs 1 and 2 (i.e. system (3.52)) is asymptotically stable. Indeed, we get

$$\text{eig}(\hat{\mathbf{A}}_{\mathbf{CL}}^{\mathbf{C}}) = \{-18803, \mathbf{23} + \mathbf{2319}\text{i}, \mathbf{23} - \mathbf{2319}\text{i}, -237, -0.16, -0.13\}.$$

Converter parameters			
DGU	R_t (Ω)	L_t (mH)	C_t (mF)
$\hat{\Sigma}_{[1]}$	0.1	1.8	2.2
$\hat{\Sigma}_{[2]}$	0.2	1.7	2
Power line parameters			
R_{12} (Ω)		L_{12} (μH)	
0.05		1.8	

Table 3.1: Electrical parameters of the mG with dynamics (3.48).

3.6.3 Bumpless control transfer

Since the controller $\mathcal{C}_{[i]}$ and the compensators $\tilde{C}_{[i]}$ and $N_{[i]}$ are dynamic systems, it is necessary to make sure that their states are correctly initialized when a switch of the controller (i.e. a plugging in or unplugging operation) is required. Assuming that the control switch is made at time $\bar{t}$, we call $u_{prec,i}$ the control signal produced by the controller $\mathcal{C}_{[i]}$ up to time $\bar{t}$. It might happen that the updated controller will provide a control variable $u_i(\bar{t})$ different from $u_{prec,i}(\bar{t})$. Therefore, it is necessary to ensure there is no substantial difference in the two values. This property is called *bumpless control transfer* and it has been first studied when switching between manual and Proportional Integral Derivative (PID) control [ÅH06].

A bumpless control transfer implementation of PnP local controller for system $\hat{\Sigma}_{[i]}^{DGU}$ is illustrated in Figure 3.18.

For the sake of simplicity, from now on, we drop the index i of the subsystem. Moreover, we assume all switches are in the position shown in Figure 3.18 at times $t < \bar{t}$ (so that the input $u^{prec}(t)$ is supplied to the system $\hat{\Sigma}^{DGU}$) and they close simultaneously at time $\bar{t}$ (hence providing

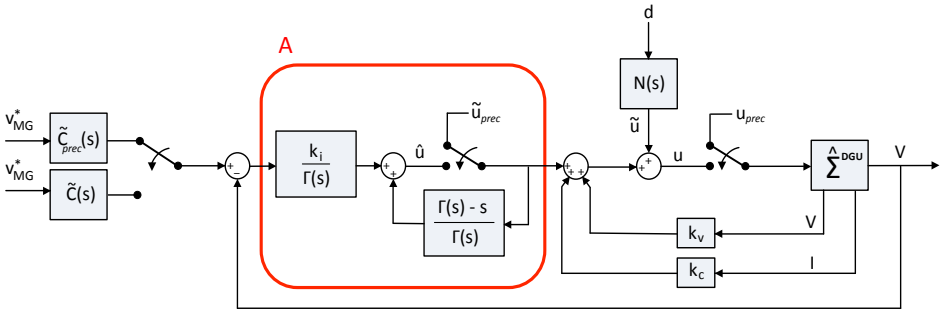

Figure 3.18: Bumpless control transfer scheme. The three switches close simultaneously at time $\bar{t}$.

the new input $u(t)$ to $\hat{\Sigma}^{DGU}$ from $t = \bar{t}$ on). The PnP controller activated at time $\bar{t}$ is given by

$$K = [k_v \ k_c \ k_i].$$

Notice that the integrator embedded in the DGU model for zeroing the steady-state error is replaced by block A (highlighted in red in Figure 3.18), where the polynomial $\Gamma(s)$ has to be chosen such that $\frac{k_i}{\Gamma(0)} > 0$ and such that the transfer function

$$\Psi(s) = \frac{\Gamma(s) - s}{\Gamma(s)}$$

is asymptotically stable and realizable. Indeed, under these assumptions, the transfer function from the input to the output of block A is $\frac{k_i}{s}$ when the switch is closed.

In block A, a switch is present so that the signal is either $\tilde{u}_{prec}$ (up to time $\bar{t}$) or $\hat{u}$ (right after $\bar{t}$). The variable $\tilde{u}_{prec}$ is given by

$$\tilde{u}_{prec} = u_{prec} - k_v V - k_c I_t - \tilde{u}, \tag{3.54}$$

where $\tilde{u}$ is the additional input produced by compensator $N(s)$, computed with respect to the dynamics of the system after the commutation ($N(s) = 0$ if such a compensation is not implemented). Notice that, choosing $\tilde{u}_{prec}$ as in (3.54) guarantees $u = u_{prec}$ right before the commutation. Moreover, we highlight that since there could be a transient in the $\hat{u}$ response to track signal $\tilde{u}_{prec}$, it is fundamental to wait for the two signals to become similar[3]

[3]This eventually happens because, by construction, $\Psi(s)$ is an asymptotically stable transfer function with unit gain.

before proceeding with the commutation. In this way, we avoid jumps in the control variable. Furthermore, if an optional pre-filter of the reference is implemented, at time $\bar{t}$, it is also necessary to commute from transfer function $\tilde{C}_{prec}(s)$ to $\tilde{C}(s)$, since each plugging in or unplugging operation of other DGU in the overall mG lead to a variation of the local dynamics of the considered subsystem $\hat{\Sigma}_i^{DGU}$ (see the term $\sum_{j\in\mathcal{N}_i} -\frac{1}{R_{ij}C_{ti}}$ in (3.10)).

3.6.4 Overall model of a microgrid composed of N DGUs

$$\begin{bmatrix} \dot{x}_{[1]} \\ \dot{x}_{[2]} \\ \dot{x}_{[3]} \\ \vdots \\ \dot{x}_{[N]} \end{bmatrix} = \underbrace{\begin{bmatrix} A_{11} & A_{12} & A_{13} & \dots & A_{1N} \\ A_{21} & A_{22} & A_{23} & \dots & A_{2N} \\ A_{31} & A_{32} & A_{3l} & \dots & A_{3N} \\ \vdots & \vdots & \vdots & \ddots & \vdots \\ A_{N1} & A_{N2} & A_{N3} & \dots & A_{NN} \end{bmatrix}}_{\mathbf{A}} \begin{bmatrix} x_{[1]} \\ x_{[2]} \\ x_{[3]} \\ \vdots \\ x_{[N]} \end{bmatrix} +$$

$$+ \underbrace{\begin{bmatrix} B_1 & 0 & \dots & 0 \\ 0 & B_2 & \ddots & \vdots \\ \vdots & \ddots & \ddots & 0 \\ 0 & \dots & 0 & B_N \end{bmatrix}}_{\mathbf{B}} \begin{bmatrix} u_{[1]} \\ u_{[2]} \\ \vdots \\ u_{[N]} \end{bmatrix} + \underbrace{\begin{bmatrix} M_1 & 0 & \dots & 0 \\ 0 & M_2 & \ddots & \vdots \\ \vdots & \ddots & \ddots & 0 \\ 0 & \dots & 0 & M_N \end{bmatrix}}_{\mathbf{M}} \begin{bmatrix} d_{[1]} \\ d_{[2]} \\ \vdots \\ d_{[N]} \end{bmatrix}$$

$$\begin{bmatrix} y_{[1]} \\ y_{[2]} \\ y_{[3]} \\ \vdots \\ y_{[N]} \end{bmatrix} = \underbrace{\begin{bmatrix} C_1 & 0 & 0 & \dots & 0 \\ 0 & C_2 & 0 & \ddots & \vdots \\ 0 & 0 & C_3 & \ddots & 0 \\ \vdots & \ddots & \ddots & \ddots & 0 \\ 0 & \dots & 0 & 0 & C_N \end{bmatrix}}_{\mathbf{C}} \begin{bmatrix} x_{[1]} \\ x_{[2]} \\ x_{[3]} \\ \vdots \\ x_{[N]} \end{bmatrix}$$

$$\begin{bmatrix} z_{[1]} \\ z_{[2]} \\ z_{[3]} \\ \vdots \\ z_{[N]} \end{bmatrix} = \underbrace{\begin{bmatrix} H_1 & 0 & 0 & \dots & 0 \\ 0 & H_2 & 0 & \ddots & \vdots \\ 0 & 0 & H_3 & \ddots & 0 \\ \vdots & \ddots & \ddots & \ddots & 0 \\ 0 & \dots & 0 & 0 & H_N \end{bmatrix}}_{\mathbf{H}} \begin{bmatrix} y_{[1]} \\ y_{[2]} \\ y_{[3]} \\ \vdots \\ y_{[N]} \end{bmatrix}.$$

3.6.5 Electrical and simulation parameters of Scenario 1 and 2

We provide all the electrical and simulation parameters of scenarios 1 and 2 (described in Sections 3.4.1 and 3.4.2, respectively).

Parameter	Symbol	Value
DC power supply	V_{DC}	100 V
Output capacitance	C_{t*}	2.2 mF
Converter inductance	L_{t*}	1.8 mH
Inductor + switch loss resistance	R_{t*}	0.2 Ω
Switching frequency	f_{sw}	10 kHz
Power line inductance	L_{12}	1.8 μH
Power line resistance	R_{12}	0.05 Ω

Table 3.2: Scenario 1 - Electrical setup of DGU $* \in \{1, 2\}$ and line parameters.

DGU	Resistance R_t (Ω)	Capacitance C_t (mF)	Inductance L_t (mH)
$\hat{\Sigma}^{DGU}_{[1]}$	0.2	2.2	1.8
$\hat{\Sigma}^{DGU}_{[2]}$	0.3	1.9	2.0
$\hat{\Sigma}^{DGU}_{[3]}$	0.1	1.7	2.2
$\hat{\Sigma}^{DGU}_{[4]}$	0.5	2.5	3.0
$\hat{\Sigma}^{DGU}_{[5]}$	0.4	2.0	1.2
$\hat{\Sigma}^{DGU}_{[6]}$	0.6	3.0	2.5

Table 3.3: Scenario 2 - Buck filter parameters for DGU $\hat{\Sigma}^{DGU}_{[i]}$, $i = \{1, \ldots, 6\}$.

Connected DGUs (i, j)	Resistance R_{ij} (Ω)	Inductance L_{ij} (μH)
$(1, 2)$	0.05	2.1
$(1, 3)$	0.07	1.8
$(3, 4)$	0.06	1.0
$(2, 4)$	0.04	2.3
$(4, 5)$	0.08	1.8
$(1, 6)$	0.1	2.5
$(5, 6)$	0.08	3.0

Table 3.4: Scenario 2 - Power line parameters.

DGU	Voltage reference (V)
$\hat{\Sigma}^{DGU}_{[1]}$	47.9
$\hat{\Sigma}^{DGU}_{[2]}$	48
$\hat{\Sigma}^{DGU}_{[3]}$	47.7
$\hat{\Sigma}^{DGU}_{[4]}$	48
$\hat{\Sigma}^{DGU}_{[5]}$	47.8
$\hat{\Sigma}^{DGU}_{[6]}$	48.1

Table 3.5: Scenario 2 - Voltage references for DGUs $\hat{\Sigma}^{DGU}_{[i]}$, $i = \{1, \ldots, 6\}$.

Parameter	Symbol	Value
DC power supply	V_{DC}	100 V
Switching frequency	f_{sw}	10 kHz

Table 3.6: Scenario 2 - Common parameters of DGU $\hat{\Sigma}^{DGU}_{[i]}$, $i = \{1, \ldots, 6\}$.

Chapter 4

Line-independent plug-and-play control of DC microgrids

Contents

4.1 Introduction 73
4.2 DC microgrid model 74
4.3 Design of stabilizing voltage controllers 75
4.3.1 Structure of local controllers 75
4.3.2 Conditions for stability of the closed-loop microgrid 76
4.3.3 Line-independent controller computation through LMIs 79
4.3.4 Plug-and-play operations 81
4.4 Simulation results 82
4.5 Final comments 85
4.6 Appendix 87
4.6.1 Proof of Proposition 4.2 87
4.6.2 Proof of Theorem 4.1 90
4.6.3 Feasibility of the LMI test (4.16) 96

4.1 Introduction

In this chapter, we propose a variant of the PnP design algorithm presented in Chapter 3. The main difference is that the computation of local controllers does not require anymore the knowledge of power line parameters (hence the name *line-independent* design), and the only global quantity used in the synthesis algorithm is a scalar parameter. This feature leads to the following advantages.

1. If a DGU wants to plug -in or -out, its neighboring subsystems do not have to update their local controllers. This considerably simplifies the plug-in/-out protocol described in Section 3.3.6. In fact, switching of local regulators and bumpless control architectures (for avoiding abrupt changes in the control variables) are now unnecessary.

2. The design procedure proposed in this chapter allows to better comply with privacy requirements of energy markets where DGUs can have different owners. Indeed, the addition of new DGUs does not require other stakeholders to disclose models of their own DGUs or change their operation.

For the presented design procedure, the structure of each local controller is identical to the one proposed in Section 3.3.2. Also LMI problems associated with control design are similar to those in Chapter 3. However, the proof of asymptotic stability of the closed-loop system is substantially different and more involved. In particular, it is based on the fact that, under QSL approximations, electrical coupling among DGUs can be described by graph Laplacians [DB13]. This feature, together with the use of structured Lyapunov functions and the LaSalle Invariance principle [Kha01], allows us to derive the desired result.

The chapter is structured as follows. Results from Chapter 3 about the DGU model and the structure of PnP controllers are summarized in Sections 4.2 and 4.3.1. The new PnP approach for designing local voltage regulators is described in Sections 4.3.2, 4.3.3 and 4.3.4, along with the stability analysis of the closed-loop system. Simulations in PSCAD using a 6-DGUs mG and validating the PnP capabilities of the proposed controllers are discussed in Section 4.4.

4.2 DC microgrid model

We start by considering the same DGU model described in Section 3.2, whose electrical scheme is depicted in Figure 3.2. Sets $\mathcal{V}$, $\mathcal{N}_i$ ($i \subset \mathcal{V}$) and $\mathcal{E}$ are defined as in Chapter 3 (see Section 3.2.2). The topology of the mG is described by the undirected graph[1] $\mathcal{G}_{el}$ with nodes $\mathcal{V}$ and edges $\mathcal{E}$.

Under QSL approximations of power lines, the dynamics of DGU i in

[1]See Appendix A.2 for basic definitions in graph theory.

(3.9) can be written in terms of state-space variables as follows

$$\Sigma_{[i]}^{DGU}: \begin{cases} \dot{x}_{[i]}(t) = A_{ii}x_{[i]}(t) + B_i u_{[i]}(t) + M_i d_{[i]}(t) + \xi_{[i]}(t) \\ y_{[i]}(t) = C_i x_{[i]}(t) \\ z_{[i]}(t) = H_i x_{[i]}(t) \end{cases} \tag{4.1}$$

We recall that $x_{[i]} = [V_i, I_{ti}]^T$ is the state, $u_{[i]} = V_{ti}$ the control input, $d_{[i]} = I_{Li}$ the exogenous input, and $z_{[i]} = V_i$ the controlled variable of the system. Moreover, $y_{[i]}(t) = x_{[i]}$ is the measurable output, whereas the term $\xi_{[i]} = \sum_{j\in\mathcal{N}_i} A_{ij}(x_{[j]} - x_{[i]})$ accounts for the couplings with each DGU $j \in \mathcal{N}_i$.

Remark 4.1. *Model* (4.1) *is identical to the one provided in Chapter 3 (see* (3.6)*), except that all coupling terms have been now embedded in variables* $\xi_{[i]}$.

The matrices of $\Sigma_{[i]}^{DGU}$ are obtained from (3.9) as

$$A_{ii} = \begin{bmatrix} 0 & \frac{1}{C_{ti}} \\ -\frac{1}{L_{ti}} & -\frac{R_{ti}}{L_{ti}} \end{bmatrix}, \qquad A_{ij} = \begin{bmatrix} \frac{1}{R_{ij}C_{ti}} & 0 \\ 0 & 0 \end{bmatrix}, \qquad B_i = \begin{bmatrix} 0 \\ \frac{1}{L_{ti}} \end{bmatrix},$$

$$M_i = \begin{bmatrix} -\frac{1}{C_{ti}} \\ 0 \end{bmatrix}, \qquad C_i = \begin{bmatrix} 1 & 0 \\ 0 & 1 \end{bmatrix}, \qquad H_i = \begin{bmatrix} 1 & 0 \end{bmatrix},$$

and the overall QSL-mG model is given by (3.11).

4.3 Design of stabilizing voltage controllers

4.3.1 Structure of local controllers

Following the approach described in Section 3.3.1, in order to track constant references $\mathbf{z_{ref}}(t) = \bar{\mathbf{z}}_{\mathbf{ref}}$ (when $\mathbf{d}(t) = \bar{\mathbf{d}}$ is constant), we augment the mG model with integrators, thus obtaining the following DGU model

$$\hat{\Sigma}_{[i]}^{DGU}: \begin{cases} \dot{\hat{x}}_{[i]}(t) = \hat{A}_{ii}\hat{x}_{[i]}(t) + \hat{B}_i u_{[i]}(t) + \hat{M}_i \hat{d}_{[i]}(t) + \hat{\xi}_{[i]}(t) \\ \hat{y}_{[i]}(t) = \hat{C}_i \hat{x}_{[i]}(t) \\ z_{[i]}(t) = \hat{H}_i \hat{x}_{[i]}(t) \end{cases} \tag{4.2}$$

where $\hat{x}_{[i]} = [x^T{}_{[i]}, v_{[i]}]^T \in \mathbb{R}^3$ is the state, $\hat{d}_{[i]} = [d_{[i]}, z_{ref}{}_{[i]}]^T \in \mathbb{R}^2$ collects the exogenous signals, and

$$\hat{\xi}_{[i]} = \sum_{j\in\mathcal{N}_i} \hat{A}_{ij}(\hat{x}_{[j]} - \hat{x}_{[i]}).$$

Matrices in (4.2) are defined as follows

$$\hat{A}_{ii} = \begin{bmatrix} A_{ii} & 0 \\ -H_i C_i & 0 \end{bmatrix}, \qquad \hat{A}_{ij} = \begin{bmatrix} A_{ij} & 0 \\ 0 & 0 \end{bmatrix}, \qquad \hat{B}_i = \begin{bmatrix} B_i \\ 0 \end{bmatrix},$$
$$\hat{C}_i = \begin{bmatrix} C_i & 0 \\ 0 & 1 \end{bmatrix}, \qquad \hat{M}_i = \begin{bmatrix} M_i & 0 \\ 0 & 1 \end{bmatrix}, \qquad \hat{H}_i = \begin{bmatrix} H_i & 0 \end{bmatrix}.$$

As in Proposition 3.2, one can show that the positivity of the electrical parameters guarantees that the pair $(\hat{A}_{ii}, \hat{B}_i)$ is controllable. Therefore, system (4.2) can be stabilized.

The overall augmented system, obtained from (4.2), has the form (3.17).

We equip each DGU $\hat{\Sigma}_{[i]}^{DGU}$ with the same decentralized state-feedback controller described in Section 3.3.2 and shown in Figure 3.2, i.e.

$$\mathcal{C}_{[i]}: \qquad u_{[i]}(t) = K_i \hat{x}_{[i]}(t). \tag{4.3}$$

Once again, we stress that, in general, decentralized design of local regulators can fail to guarantee voltage stability of the whole mG, if couplings among DGUs are neglected during the design phase (see the examples in Appendix 3.6.2).

In the sequel, we show how structured Lyapunov functions can be used to ensure asymptotic stability of the whole mG, when DGUs are equipped with controllers (4.3).

4.3.2 Conditions for stability of the closed-loop microgrid

In absence of coupling terms $\hat{\xi}_{[i]}(t)$, one would like to guarantee asymptotic stability of the nominal closed-loop subsystem

$$\dot{\hat{x}}_{[i]}(t) = \underbrace{(\hat{A}_{ii} + \hat{B}_i K_i)}_{F_i} \hat{x}_{[i]}(t) + \hat{M}_i \hat{d}_{[i]}(t). \tag{4.4}$$

By direct calculation, it can be shown that F_i has the following structure

$$\begin{aligned} F_i &= \left[\begin{array}{c|cc} 0 & f_{12,i} & 0 \\ \hline f_{21,i} & f_{22,i} & f_{23,i} \\ f_{13,i} & 0 & 0 \end{array}\right] = \\ &= \left[\begin{array}{c|cc} 0 & \frac{1}{C_{ti}} & 0 \\ \hline \frac{(k_{i,1}-1)}{L_{ti}} & \frac{(k_{i,2}-R_{ti})}{L_{ti}} & \frac{k_{i,3}}{L_{ti}} \\ -1 & 0 & 0 \end{array}\right] = \left[\begin{array}{c|c} 0 & \mathcal{F}_{12,i} \\ \hline \mathcal{F}_{21,i} & \mathcal{F}_{22,i} \end{array}\right]. \end{aligned} \tag{4.5}$$

From Lyapunov theory, asymptotic stability of (4.4) is equivalent to the existence of a Lyapunov function $\mathscr{V}_i(\hat{x}_{[i]}) = \hat{x}_{[i]}^T P_i \hat{x}_{[i]}$, where $P_i \in \mathbb{R}^{3\times 3}$, $P = P^T > 0$ and

$$Q_i = F_i^T P_i + P_i F_i \tag{4.6}$$

is negative definite. In presence of nonzero coupling terms, we will show that asymptotic stability can be achieved under two additional conditions. The first one is the use of the following separable Lyapunov functions

$$\mathscr{V}_i(\hat{x}_{[i]}) = \eta_i \hat{x}_{[i],1}^2 + [\hat{x}_{[i],2}\ \hat{x}_{[i],3}]\mathcal{P}_{22,i}[\hat{x}_{[i],2}\ \hat{x}_{[i],3}]^T,$$

where

$$\mathcal{P}_{22,i} = \begin{bmatrix} p_{22,i} & p_{23,i} \\ p_{23,i} & p_{33,i} \end{bmatrix}. \tag{4.7}$$

This requirement is summarized in the next assumption.

Assumption 4.1. *Gains K_i, $i \in \mathcal{V}$ are designed such that, in (4.6), the positive definite matrix P_i has the structure*

$$P_i = \left[\begin{array}{c|c} \eta_i & \mathbf{0}_{1\times 2} \\ \hline \mathbf{0}_{2\times 1} & \mathcal{P}_{22,i} \end{array}\right], \tag{4.8}$$

where the entries of $\mathcal{P}_{22,i}$ are arbitrary and $\eta_i > 0$ is a local parameter.

The second condition concerns the values of parameters η_i.

Assumption 4.2. *Given a constant $\bar{\sigma} > 0$ (a parameter common to all DGUs), parameters η_i in (4.8) are given by*

$$\eta_i = \bar{\sigma} C_{ti}, \qquad \forall i \in \mathcal{V}. \tag{4.9}$$

The next result shows that, under Assumption 4.1, Lyapunov theory certifies, at most, marginal stability of (4.4).

Proposition 4.1. *Under Assumption 4.1, the matrix Q_i cannot be negative definite. Moreover, if*

$$Q_i \leq 0, \tag{4.10}$$

then Q_i has the following structure:

$$Q_i = \left[\begin{array}{c|cc} 0 & 0 & 0 \\ \hline 0 & q_{22,i} & q_{23,i} \\ 0 & q_{23,i} & q_{33,i} \end{array}\right] = \left[\begin{array}{c|c} 0 & \mathbf{0}_{1\times 2} \\ \hline \mathbf{0}_{2\times 1} & \mathcal{Q}_{22,i} \end{array}\right]. \tag{4.11}$$

Proof. By direct computation, from (4.5) and (4.8) one has $q_{11,i} = 0$, showing that Q_i cannot be negative definite, as its first minor is not negative. Moreover, it is known that, if a negative semidefinite matrix has a zero element on its diagonal, then the corresponding row and column have zero entries. This basic property can be shown as follows. If $\mathcal{Q} \in \mathbb{R}^{n\times n}$ is symmetric and negative semidefinite, then $x^T\mathcal{Q}x \leq 0$, $\forall x \in \mathbb{R}^n$. Partitioning $\mathcal{Q}$ and x as

$$\mathcal{Q} = \left[\begin{array}{c|c} \mathcal{Q}_{11} & \widetilde{\mathcal{Q}}^T \\ \hline \widetilde{\mathcal{Q}} & \widehat{\mathcal{Q}} \end{array}\right] \qquad \text{and} \qquad x = \begin{bmatrix} x_{11} \\ \\ \tilde{x} \end{bmatrix},$$

one obtains

$$x^T\mathcal{Q}x = x_{11}^2\mathcal{Q}_{11} + 2x_{11}\widetilde{\mathcal{Q}}^T\tilde{x} + \tilde{x}^T\widehat{\mathcal{Q}}\tilde{x}.$$

Without loss of generality, assume $\mathcal{Q}_{11} = 0$. Then, for any x with $\tilde{x} = 0$ and $x_{11} \neq 0$, one has $x^T\mathcal{Q}x = 0$, i.e. x is a maximizer of $x^T\mathcal{Q}x$. Consequently, it must hold $\frac{\mathrm{d}}{\mathrm{d}x}\left(x^T\mathcal{Q}x\right) = 0$, i.e. $2\mathcal{Q}x = 0$, yielding

$$\begin{cases} \mathcal{Q}_{11}x_{11} + \widetilde{\mathcal{Q}}^T\tilde{x} = 0 \\ \quad \widetilde{\mathcal{Q}}x_{11} + \widehat{\mathcal{Q}}\tilde{x} = 0 \end{cases}$$

Using $\mathcal{Q}_{11} = 0$ and $\tilde{x} = 0$, the previous linear system reduces to $\widetilde{\mathcal{Q}}x_{11} = 0$, that implies $\widetilde{\mathcal{Q}} = 0$. Concluding, (4.10) implies (4.11). □

Consider now the overall closed-loop mG model

$$\begin{cases} \dot{\hat{\mathbf{x}}}(t) = (\hat{\mathbf{A}} + \hat{\mathbf{B}}\mathbf{K})\hat{\mathbf{x}}(t) + \hat{\mathbf{M}}\hat{\mathbf{d}}(t) \\ \hat{\mathbf{y}}(t) = \hat{\mathbf{C}}\hat{\mathbf{x}}(t) \\ \mathbf{z}(t) = \hat{\mathbf{H}}\hat{\mathbf{x}}(t) \end{cases} \tag{4.12}$$

obtained by combining (3.17) and (4.3), with $\mathbf{K} = \mathrm{diag}\,[K_1, \ldots, K_N]$. Consider also the collective Lyapunov function

$$\mathscr{V}(\hat{\mathbf{x}}) = \sum_{i=1}^{N} \mathscr{V}_i(\hat{x}_{[i]}) = \hat{\mathbf{x}}^T\mathbf{P}\hat{\mathbf{x}}, \tag{4.13}$$

where $\mathbf{P} = \mathrm{diag}\,[P_1, \ldots, P_N]$. One has $\dot{\mathscr{V}}(\hat{\mathbf{x}}) = \hat{\mathbf{x}}^T\mathbf{Q}\hat{\mathbf{x}}$, with

$$\mathbf{Q} = (\hat{\mathbf{A}} + \hat{\mathbf{B}}\mathbf{K})^T\mathbf{P} + \mathbf{P}(\hat{\mathbf{A}} + \hat{\mathbf{B}}\mathbf{K}).$$

A consequence of Proposition 4.1 is that, under Assumption 4.1, the matrix $\mathbf{Q}$ cannot be negative definite. At most, one has

$$\mathbf{Q} \leq 0. \tag{4.14}$$

Moreover, even if (4.10) holds for all $i \in \mathcal{V}$, the inequality (4.14) might be violated because of the nonzero coupling terms $\hat{A}_{ij}$ in matrix $\hat{\mathbf{A}}$. The next result shows that this cannot happen under Assumption 4.2.

Proposition 4.2. *Under Assumptions 4.1 and 4.2, if gains K_i are computed in order to fulfill* (4.10) *for all $i \in \mathcal{V}$, then* (4.14) *holds.*

Proof. The proof is given in Appendix 4.6.1. □

Remark 4.2. *The proof of Proposition 4.2 reveals that, under Assumption 4.2, interactions between local Lyapunov functions $\mathscr{V}_i(\hat{x}_{[i]})$ due to terms $\hat{A}_{ij}$, $i \neq j$, take the form of a weighted Laplacian matrix [GR01] associated with the graph $\mathcal{G}_{el}$. Furthermore, differently from the idea in Section 3.3.2 of nullifying interactions by choosing $\eta_i > 0$ in* (4.8) *sufficiently small, here* (4.14) *holds true even if parameters η_i are large.*

The next goal is to show asymptotic stability of the mG using the marginal stability result in Proposition 4.2 together with LaSalle invariance theorem. The main result is then given in the next theorem.

Theorem 4.1. *If Assumptions 4.1 and 4.2 are fulfilled, the graph $\mathcal{G}_{el}$ is connected,* (4.10) *holds, and $k_{3,i} \neq 0$, $\forall i \in \mathcal{V}$, then the origin of* (4.12) *is asymptotically stable.*

Proof. The proof is presented in Appendix 4.6.2. □

4.3.3 Line-independent controller computation through LMIs

We now show how to compute matrices K_i and P_i via numerical optimization so as to comply with assumptions of Theorem 4.1. In order to enforce, when possible, a margin of robustness, controllers K_i should be designed such that inequality

$$(\hat{A}_{ii} + \hat{B}_i K_i)^T P_i + P_i(\hat{A}_{ii} + \hat{B}_i K_i) + \Gamma_i^{-1} \leq 0, \tag{4.15}$$

with $\Gamma_i = \text{diag}\,[\gamma_{1i}, \gamma_{2i}, \gamma_{3i}]$, is verified for $\gamma_{ki} \geq 0$, $k = 1, 2, 3$, and matrix P_i structured as in (4.8). The design of the local controller $\mathcal{C}_{[i]}$ is performed solving the following problem.

Problem 4.1. *For parameters η_i chosen as in* (4.9)*, compute a vector K_i such that Assumption 4.1 is verified and* (4.10) *holds.*

Consider the following optimization problem

$$\mathcal{O}_i : \min_{\substack{Y_i, G_i, \gamma_{1i}, \\ \gamma_{2i}, \gamma_{3i}, \beta_i, \zeta_i}} \quad \alpha_{1i}\gamma_{1i} + \alpha_{2i}\gamma_{2i} + \alpha_{3i}\gamma_{3i} + \alpha_{4i}\beta_i + \alpha_{5i}\zeta_i$$

$$Y_i = \begin{bmatrix} \eta_i^{-1} & 0 & 0 \\ 0 & \bullet & \bullet \\ 0 & \bullet & \bullet \end{bmatrix} > 0 \tag{4.16a}$$

$$\begin{bmatrix} Y_i\hat{A}_{ii}^T + G_i^T\hat{B}_i^T + \hat{A}_{ii}Y_i + \hat{B}_iG_i & Y_i \\ Y_i & -\Gamma_i \end{bmatrix} \leq 0 \tag{4.16b}$$

$$\begin{bmatrix} -\beta_i I & G_i^T \\ G_i & -I \end{bmatrix} < 0 \tag{4.16c}$$

$$\begin{bmatrix} Y_i & I \\ I & \zeta_i I \end{bmatrix} > 0 \tag{4.16d}$$

$$\gamma_{1i}, \gamma_{2i}, \gamma_{3i} \geq 0, \quad \beta_i > 0, \quad \zeta_i > 0 \tag{4.16e}$$

where α_{ji}, $j = 1\ldots, 5$ represent positive weights and $\bullet$ are arbitrary entries. We notice that all constraints in (4.16) are LMIs. Therefore, the optimization problem $\mathcal{O}_i$ is convex and can be solved in polynomial time [BEGFB94]. The next Lemma, already proved in Section 3.3.2, establishes the relations between problem $\mathcal{O}_i$ and matrices K_i and P_i.

Lemma 4.1. *Problem $\mathcal{O}_i$ is feasible if and only if Problem 4.1 has a solution. Moreover, K_i and P_i in* (4.6) *are given by $K_i = G_iY_i^{-1}$, $P_i = Y_i^{-1}$ and*

$$||K_i||_2 < \sqrt{\beta_i}\zeta_i.$$

Next, we discuss the key features of the proposed decentralized control approach. We first notice that constraints in (4.16) depend upon local fixed matrices ($\hat{A}_{ii}$, $\hat{B}_i$) and local design parameters (α_{1i}, α_{2i}, α_{3i}, α_{4i}, α_{5i}). It follows that the computation of controller $\mathcal{C}_{[i]}$ is completely independent from the computation of controllers $\mathcal{C}_{[j]}$, $j \neq i$, up to the knowledge of the common parameter $\bar{\sigma}$ in (4.9). Secondly, (4.16) is independent of parameters of electrical lines connecting DGUs. Thirdly, as discussed after Proposition 4.2, differently from the method discussed in Chapter 3, the design procedure does not require that parameters η_i are sufficiently small, so as to reduce the coupling among DGUs (see term (b) in (3.24)). Finally, if problems $\mathcal{O}_i$, $i \in \mathcal{V}$, are feasible, then the overall closed-loop mG

is asymptotically stable, provided that $k_{3,i} \neq 0$, $i \in \mathcal{V}$ (see Theorem 4.1). The latter condition was always fulfilled in all numerical experiments we performed. Algorithm 4.1 collects the steps of the overall design procedure. For improving the closed-loop bandwidth of each controlled DGU and the rejection of current disturbances I_{Li}, it also includes the optional design of pre-filters $\tilde{C}_{[i]}$ and disturbance compensators $N_{[i]}$ (see Section 3.3.4).

Algorithm 4.1 Design of controller $\mathcal{C}_{[i]}$ and compensators $\tilde{C}_{[i]}$ and $N_{[i]}$ for subsystem $\hat{\Sigma}_{[i]}^{DGU}$

Input: DGU $\hat{\Sigma}_{[i]}^{DGU}$ as in (4.2)

Output: Controller $\mathcal{C}_{[i]}$ and, optionally, pre-filter $\tilde{C}_{[i]}$ and compensator $N_{[i]}$

(A) Find K_i solving the LMI problem (4.16). If it is not feasible, or $k_{3,i} \neq 0$ cannot be obtained, **stop** (the controller $\mathcal{C}_{[i]}$ cannot be designed).
Optional step

(B) Design an asymptotically stable local pre-filter $\tilde{C}_{[i]}$ and compensator $N_{[i]}$ (see Section 3.3.4).

Remark 4.3. *In order to assess the conservativeness of the LMIs* (4.16)*, we solved it for* $\bar{\sigma} = 10$ *and for various combinations of parameters* (R_t, L_t, C_t) *characterizing the DGUs, checking when they are infeasible. In particular, we derived from the literature meaningful parameter ranges for converters typically used in LV DC mGs [SDVG14b, HGK+16, DGVS14]. Numerical results, provided in Appendix 4.6.3, show that the LMIs are always feasible. Furthermore, in the same Appendix, we compare the presented method with the one in Chapter 3 in terms of feasibility of the corresponding problems. Notably, we provide an example where LMIs* (4.16) *are feasible while the design procedure in described in Chapter 3 is not.*

4.3.4 Plug-and-play operations

We describe the operations that are required for adding and removing DGUs, while preserving the stability of the mG. As a starting point, we consider an mG composed of subsystems $\hat{\Sigma}_{[i]}^{DGU}, i \in \mathcal{V}$, equipped with local controllers $\mathcal{C}_{[i]}$ and compensators $\tilde{C}_{[i]}$ and $N_{[i]}$, $i \in \mathcal{V}$ produced by Algorithm 4.1. We also assume that the graph $\mathcal{G}_{el}$ is connected.

Plug-in operation. Assume that a new DGU $\hat{\Sigma}^{DGU}_{[N+1]}$ sends a plug-in request. Let $\mathcal{N}_{N+1}$ be the set of DGUs that will be connected to $\hat{\Sigma}^{DGU}_{[N+1]}$. The design of controller $\mathcal{C}_{[N+1]}$ and compensators $\tilde{C}_{[N+1]}$ and $N_{[N+1]}$ requires Algorithm 4.1 to be executed. Differently from the plugging in protocol described in Chapter 3, there is no need to redesign controllers $\mathcal{C}_{[j]}$ and compensators $\tilde{C}_{[j]}$ and $N_{[j]}$, $\forall j \in \mathcal{N}_{N+1}$, because matrices $\hat{A}_{jj}$, $j \in \mathcal{N}_{N+1}$ do not change. Therefore, if Algorithm 4.1 does not stop in Step (A) when computing controllers $\mathcal{C}_{[N+1]}$, the plug-in of $\hat{\Sigma}^{DGU}_{[N+1]}$ is allowed.

Unplugging operation. Assume now that DGU $k \in \mathcal{V}$, needs to be disconnected from the network. Differently from the method in Chapter 3, since the unplugging of subsystem $\hat{\Sigma}^{DGU}_{[k]}$ does not change the matrix $\hat{A}_{jj}$ of each $\hat{\Sigma}^{DGU}_{[j]}$, $j \in \mathcal{N}_k$, DGU k can be removed without redesigning the local controllers $\mathcal{C}_{[j]}$, $j \notin \mathcal{N}_k$. in view of Theorem 4.1, stability is preserved as long as the new graph $\mathcal{G}_{el}$ is still connected.

Remark 4.4. *According to the above PnP operations, whenever a DGU i wants to be plugged in or out, no updating of controllers of neighboring DGU j, $j \in \mathcal{N}_i$ is required. As a consequence, there is no need to equip each local controller with bumpless control scheme described in Chapter 3 for ensuring smooth behaviors of the control variable when controllers are switched in real-time.*

4.4 Simulation results

In order to compare the new PnP design methodology with the one described in Chapter 3, we performed the same simulation discussed in Scenario 2 in Section 3.4.2. Notably, we consider the meshed mG in Figure 3.10 composed of 6 DGUs, which have non-identical electrical parameters (reported in Table 3.3). As in Section 3.4.2, voltage references for the DGUs are set to slightly different values (see Table 3.5 in Appendix 3.6.5), so as to make the case study more realistic, whereas the constant ratio $\bar{\sigma}$ in (4.9) has been chosen equal to 10.

We assume that DGUs 1-5 supply 10 Ω, 6 Ω, 4 Ω, 2 Ω and 3 Ω resistive loads, respectively. In PnP controllers $\mathcal{C}_{[i]}$, no compensators $\tilde{C}_i$ and N_i have been used.

At $t = 0$, DGUs 1-5 are interconnected and equipped with controllers $\mathcal{C}_{[i]}$, $i = 1, \ldots, 5$, produced by Algorithm 4.1.

Plug-in of a new DGU

At time $t = 4$ s, we simulate the connection of DGU $\hat{\Sigma}_{[6]}^{DGU}$ with $\hat{\Sigma}_{[1]}^{DGU}$ and $\hat{\Sigma}_{[5]}^{DGU}$ (see Figure 3.10). According to the plug-in protocol described in Section 4.3.4, one must run Algorithm 4.1 only for designing $\mathcal{C}_{[6]}$. As the Algorithm does not stop in Step (A), the plug-in of DGU 6 is performed and, most importantly, no update of the controllers $\mathcal{C}_{[j]}$, $j \in \mathcal{N}_6$, with $\mathcal{N}_6 = \{1, 5\}$ is required. Figure 4.1 illustrates voltages at PCCs 1, 5 and 6 around the plug-in time. We notice very small deviations of the output signals of DGUs 1, 5 and 6 from their references when DGU 6 is plugged-in. Moreover, since no switch of controller is performed, these perturbations are much smaller than those in the corresponding simulations in Chapter 3 (see the comparison in Figure 4.4).

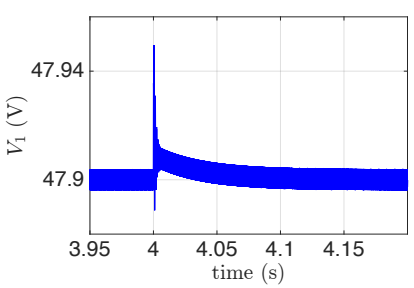

(a) Voltage at PCC_1.

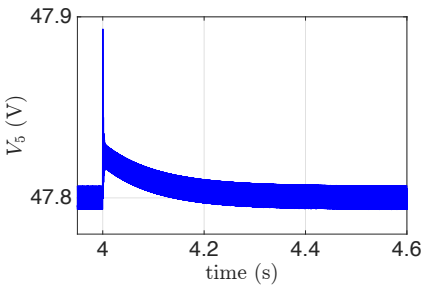

(b) Voltage at PCC_5.

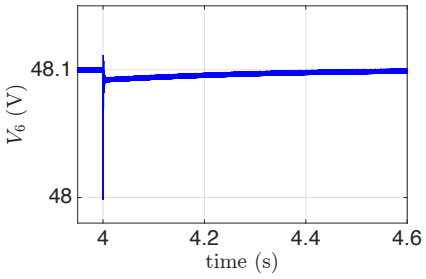

(c) Voltage at PCC_6.

Figure 4.1: Performance of PnP decentralized voltage controllers during the plug-in of DGU 6 at time $t = 4$ s.

Robustness to unknown load changes

At $t = 8$ s, the load of DGU 6 is decreased from 8 Ω to 4 Ω. As shown in Figures 4.2a-4.2b, right after $t = 8$ s the voltages at PCC_1 and PCC_5 exhibit oscillations that disappear after very short transients. A visual comparison with the voltages in Figure 20 of [SDVG14b], where primary droop controllers have been used to compensate load changes, shows that transients in Figure 4.2 are very short.

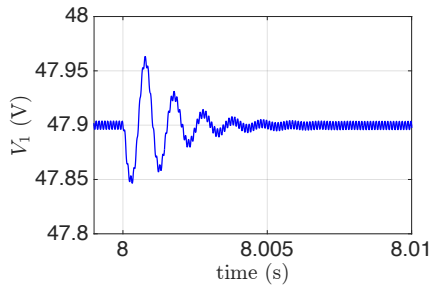

(a) Voltage at PCC_1.

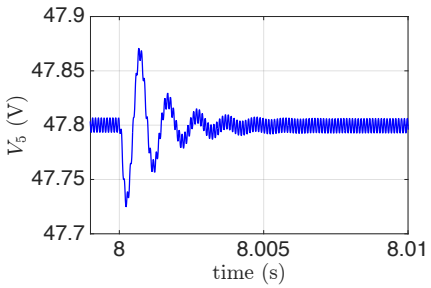

(b) Voltage at PCC_5.

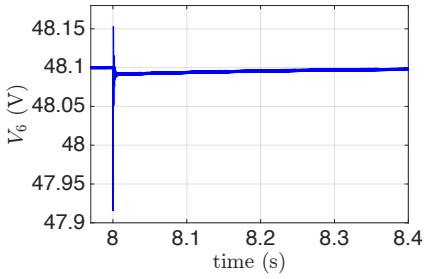

(c) Voltage at PCC_6.

Figure 4.2: Performance of PnP decentralized voltage controllers in terms of robustness to an abrupt change of load resistances at time $t = 8$ s.

Unplugging of a DGU

At time $t = 12$ s, we perform the disconnection of $\hat{\Sigma}_{[3]}^{DGU}$ (see Figure 3.15). As described in Section 4.3.4, no controller update is required for the DGUs that were connected to it (i.e. DGUs 1 and 4). Figure 4.3 shows the voltages at PCCs 1 and 4 around the unplugging event. Since controllers $\mathcal{C}_{[1]}$ and $\mathcal{C}_{[4]}$ do not need to be updated, subsystems $\hat{\Sigma}_{[j]}^{DGU}$, $j \in \mathcal{N}_3$, show

deviations from their respective references which are smaller than those shown in Figure 3.17 (see the comparison in Figure 4.5).

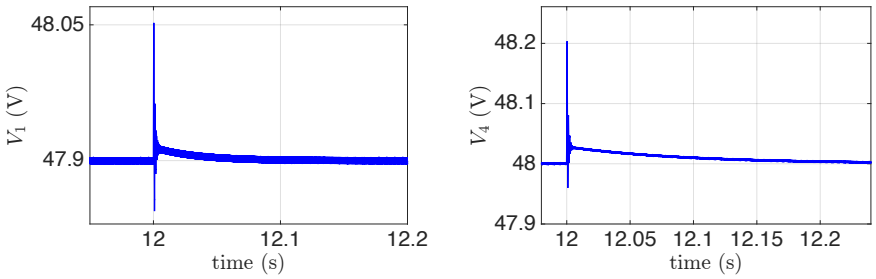

(a) Voltage at PCC_1. (b) Voltage at PCC_4.

Figure 4.3: Performance of PnP decentralized voltage controllers during the unplugging of DGU 3 at $t = 12$ s.

4.5 Final comments

In this chapter, we presented a totally decentralized control design approach for voltage stabilization in DC mG. Differently from the PnP methodology discussed in Chapter 3, the synthesis of local regulators does not require the knowledge of power line parameters. Compared to the line-dependent approach described in the previous chapter, line-independent design has several advantages, in terms of practical implementation, performance, and feasibility of the LMI tests providing stabilizing controllers K_i. In fact, we have seen that, since the computation of each regulator requires the model of the corresponding DGU only, there is no need anymore to update neighboring controllers (and to implement bumpless architectures for avoiding abrupt changes in the control variables) when subsystems are plugged in-/out. Consequently, we have smaller voltage deviations with respect to those shown by PnP line-dependent regulators, in correspondence of addition/removal operations of DGUs. As regards the advantages at the design stage, they are detailed in Appendix 4.6.3.

In the next chapter, we show how to couple the primary control layers presented in Chapters 3 and 4 with a secondary control layer ensuring stable current sharing and voltage balancing.

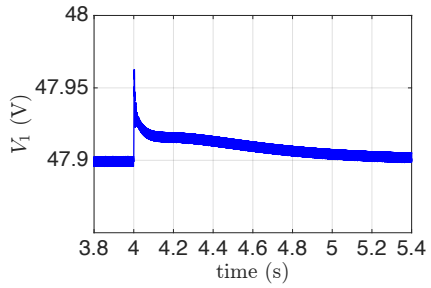

(a) Line-dependent approach: voltage at PCC_1.

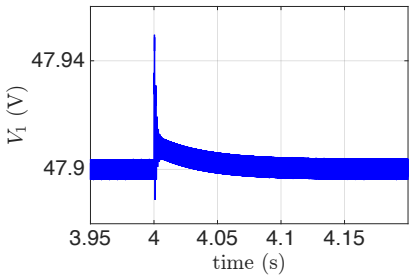

(b) Line-independent approach: voltage at PCC_1.

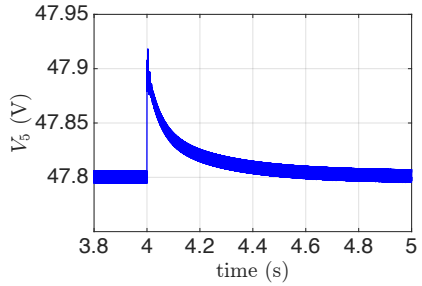

(c) Line-dependent approach: voltage at PCC_4.

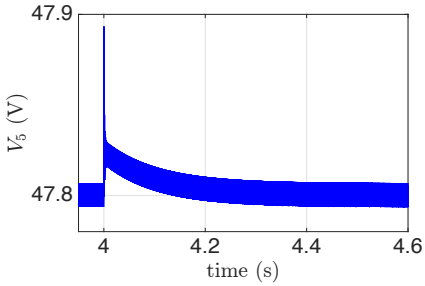

(d) Line-independent approach: voltage at PCC_4.

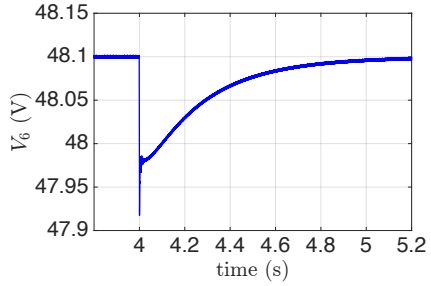

(e) Line-dependent approach: voltage at PCC_6.

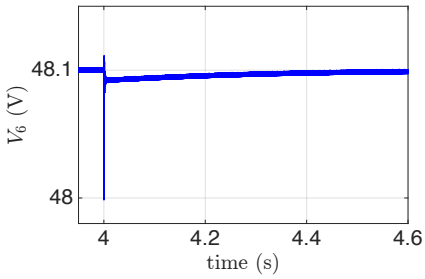

(f) Line-independent approach: voltage at PCC_6.

Figure 4.4: Visual comparison between the performance of the line-dependent and the line-independent approach when the plug-in of a DGU is performed.

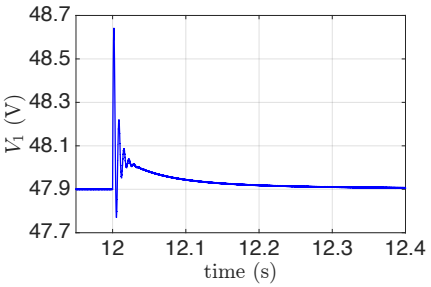

(a) Line-dependent approach: voltage at PCC_4.

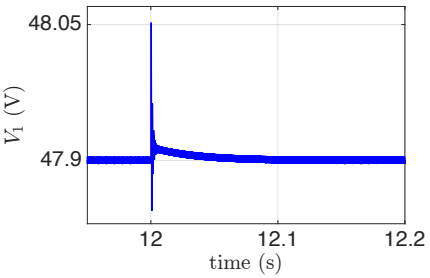

(b) Line-independent approach: voltage at PCC_1.

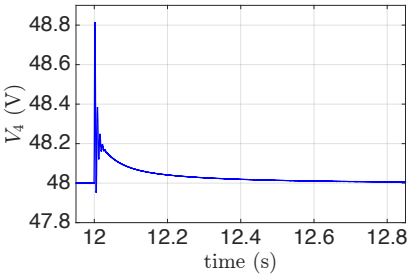

(c) Line-dependent approach: voltage at PCC_4.

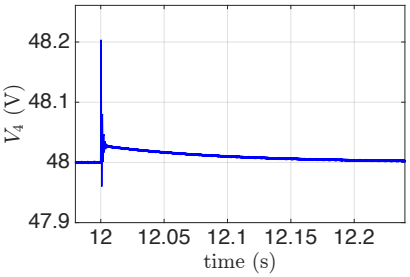

(d) Line-independent approach: voltage at PCC_4.

Figure 4.5: Visual comparison between the performance of the line-dependent and the line-independent approach when the unplugging of a DGU is performed.

4.6 Appendix

4.6.1 Proof of Proposition 4.2

Proof. Consider the following decomposition of matrix $\hat{\mathbf{A}}$

$$\hat{\mathbf{A}} = \hat{\mathbf{A}}_{\mathbf{D}} + \hat{\mathbf{A}}_{\mathbf{\Xi}} + \hat{\mathbf{A}}_{\mathbf{C}}, \tag{4.17}$$

where $\hat{\mathbf{A}}_{\mathbf{D}} = \text{diag}\left[\hat{A}_{ii}, \ldots, \hat{A}_{NN}\right]$ collects the local dynamics only, while $\hat{\mathbf{A}}_{\mathbf{\Xi}} = \text{diag}\left[\hat{A}_{\xi 1}, \ldots, \hat{A}_{\xi N}\right]$ with

$$\hat{A}_{\xi i} = \begin{bmatrix} -\sum\limits_{j \in \mathcal{N}_i} \frac{1}{R_{ij} C_{ti}} & 0 & 0 \\ 0 & 0 & 0 \\ 0 & 0 & 0 \end{bmatrix},$$

takes into account the dependence of each local state on the neighboring DGUs. We want to prove (4.14), that, according to the decomposition (4.17), is equivalent to show that

$$\underbrace{(\hat{\mathbf{A}}_{\mathbf{D}} + \hat{\mathbf{B}}\mathbf{K})^{\mathbf{T}}\mathbf{P} + \mathbf{P}(\hat{\mathbf{A}}_{\mathbf{D}} + \hat{\mathbf{B}}\mathbf{K})}_{(a)} + \underbrace{\mathbf{2}\hat{\mathbf{A}}_{\mathbf{\Xi}}\mathbf{P}}_{(b)} + \underbrace{\hat{\mathbf{A}}_{\mathbf{C}}^{T}\mathbf{P} + \mathbf{P}\hat{\mathbf{A}}_{\mathbf{C}}}_{(c)} \leq 0. \quad (4.18)$$

By means of (4.10), matrix $(a) = \text{diag}\left[Q_1, \ldots, Q_N\right]$ is negative semidefinite. Now, let us study the contribution of $(b) + (c)$ in (4.18). Matrix (b), by construction, is block diagonal and collects on its diagonal blocks in the form

$$2\hat{A}_{\xi i} P_i = \begin{bmatrix} -2\sum\limits_{j \in \mathcal{N}_i} \tilde{\eta}_{ij} & 0 & 0 \\ 0 & 0 & 0 \\ 0 & 0 & 0 \end{bmatrix}, \quad (4.19)$$

where

$$\tilde{\eta}_{ij} = \frac{\eta_i}{R_{ij} C_{ti}}. \quad (4.20)$$

As regards matrix (c), we have that each the block in position (i, j) is equal to

$$\begin{cases} P_i \hat{A}_{ij} + \hat{A}_{ji}^T P_j & \text{if } j \in \mathcal{N}_i \\ 0 & \text{otherwise} \end{cases}$$

where

$$P_i \hat{A}_{ij} + \hat{A}_{ji}^T P_j = \begin{bmatrix} \tilde{\eta}_{ij} + \tilde{\eta}_{ji} & 0 & 0 \\ 0 & 0 & 0 \\ 0 & 0 & 0 \end{bmatrix}. \quad (4.21)$$

From (4.19) and (4.21), we notice that only the elements in position $(1,1)$ of each 3×3 block of $(b)+(c)$ can be different from zero. Hence, in order to evaluate the positive/negative definiteness of the $3N\times 3N$ matrix $(b)+(c)$, we can equivalently consider the $N\times N$ matrix

$$\mathcal{L}=\begin{bmatrix} -2\sum\limits_{j\in\mathcal{N}_1}\tilde{\eta}_{1j} & \bar{\eta}_{12} & \dots & \bar{\eta}_{1N} \\ \bar{\eta}_{21} & \ddots & \ddots & \vdots \\ \vdots & \ddots & -2\sum\limits_{j\in\mathcal{N}_{N-1}}\tilde{\eta}_{N-1j} & \bar{\eta}_{N-1N} \\ \bar{\eta}_{N1} & \dots & \bar{\eta}_{NN-1} & -2\sum\limits_{j\in\mathcal{N}_N}\tilde{\eta}_{Nj} \end{bmatrix}, \tag{4.22}$$

obtained by deleting the second and third row and column in each block of $(b)+(c)$. One has $\mathcal{L}=\mathcal{M}+\mathcal{G}$, where

$$\mathcal{M}=\begin{bmatrix} -2\sum\limits_{j\in\mathcal{N}_1}\tilde{\eta}_{1j} & 0 & \dots & 0 \\ 0 & -2\sum\limits_{j\in\mathcal{N}_2}\tilde{\eta}_{2j} & \ddots & \vdots \\ \vdots & \ddots & \ddots & 0 \\ 0 & \dots & 0 & -2\sum\limits_{j\in\mathcal{N}_N}\tilde{\eta}_{Nj} \end{bmatrix}$$

and

$$\mathcal{G}=\begin{bmatrix} 0 & \bar{\eta}_{12} & \dots & \bar{\eta}_{1N} \\ \bar{\eta}_{21} & 0 & \ddots & \vdots \\ \vdots & \ddots & \ddots & \bar{\eta}_{N-1N} \\ \bar{\eta}_{N1} & \dots & \bar{\eta}_{NN-1} & 0 \end{bmatrix}. \tag{4.23}$$

Notice that each off-diagonal element $\bar{\eta}_{ij}$ in (4.23) is equal to

$$\bar{\eta}_{ij}=\begin{cases} (\tilde{\eta}_{ij}+\tilde{\eta}_{ji}) & \text{if } j\in\mathcal{N}_i \\ 0 & \text{otherwise} \end{cases} \tag{4.24}$$

At this point, from Assumption 4.2, one obtains that $\tilde{\eta}_{ij}=\tilde{\eta}_{ji}$ (see (4.20)) and, consequently, $\bar{\eta}_{ij}=\bar{\eta}_{ji}=2\tilde{\eta}_{ij}$ (see (4.24)). Hence, $\mathcal{L}$ is symmetric and has non negative off-diagonal elements and zero row and column sum. It follows that $-\mathcal{L}$ is a Laplacian matrix [GR01]. As such, it verifies $\mathcal{L}\leq 0$ by construction. Concluding, we have shown that (4.18) holds. □

4.6.2 Proof of Theorem 4.1

The proof of Theorem 4.1 exploits some preliminary results (derived in the next two propositions) that characterize the states $\hat{\mathbf{x}}$ yielding $\dot{\mathscr{V}}(\hat{\mathbf{x}}) = 0$.

Proposition 4.3. *Let Assumptions 4.1 and 4.2 hold and let us define* $h_i(v_i) = v_i^T \mathcal{Q}_{22,i} v_i$, *where* $\mathcal{Q}_{22,i}$ *is defined in* (4.11) *and* $v_i \in \mathbb{R}^2$. *If* (4.10) *is guaranteed, and* $k_{3,i} \neq 0$, *then*

$$h_i(\bar{v}_i) = 0 \Longleftrightarrow \bar{v}_i \in \mathrm{Ker}(\mathcal{F}_{22,i}).$$

Proof. For the sake of simplicity, in the sequel we omit the subscript i. We start by proving that

$$\bar{v} \in \mathrm{Ker}(\mathcal{F}_{22}) \Longrightarrow h(\bar{v}) = 0. \tag{4.25}$$

To this aim, we first replace (4.5) and (4.8) in (4.6), thus obtaining

$$\mathcal{Q}_{22} = \mathcal{F}_{22}^T \mathcal{P}_{22} + \mathcal{P}_{22} \mathcal{F}_{22}. \tag{4.26}$$

Then, we write

$$h(\bar{v}) = \bar{v}^T \mathcal{Q}_{22} \bar{v} = 2\bar{v}^T \mathcal{P}_{22} \underbrace{\mathcal{F}_{22}\bar{v}}_{=\mathbf{0}_{2\times 1}} = 0.$$

Next, we show that

$$h(\bar{v}) = 0 \Longrightarrow \bar{v} \in \mathrm{Ker}(\mathcal{F}_{22}). \tag{4.27}$$

We start by reformulating the condition $h(\bar{v}) = 0$ in (4.27). In particular, from basic linear algebra, we have the following orthogonal decomposition induced by $\mathcal{F}_{22}$: $\mathbb{R}^4 = \mathrm{Im}(\mathcal{F}_{22}^T) \oplus \mathrm{Ker}(\mathcal{F}_{22})$, which allows us to write any vector $v \in \mathbb{R}^4$ as

$$v = \hat{v} + \tilde{v}, \quad \hat{v} \in \mathrm{Im}(\mathcal{F}_{22}^T), \tilde{v} \in \mathrm{Ker}(\mathcal{F}_{22}). \tag{4.28}$$

Since we are assuming that Q is negative semidefinite and structured as in (4.11), vectors $\bar{v}$ satisfying $h(\bar{v}) = 0$ also maximize $h(\cdot)$. Hence,

$$h(\bar{v}) = 0 \Longleftrightarrow \frac{\mathrm{d}h}{\mathrm{d}v}(\bar{v}) = \mathcal{Q}_{22}\bar{v} = \mathbf{0}_{2\times 1}, \tag{4.29}$$

which, decomposing $\bar{v}$ as in (4.28), provides

$$h(\bar{v}) = 0 \Longleftrightarrow \mathcal{Q}_{22}\hat{v} + \underbrace{\mathcal{Q}_{22}\tilde{v}}_{=\mathbf{0}_{2\times 1}} = \mathbf{0}_{2\times 1}. \tag{4.30}$$

Notice that $\mathcal{Q}_{22}\tilde{v} = \mathbf{0}_{2\times 1}$ in (4.30) follows from the fact that $\tilde{v} \in \mathrm{Ker}(\mathcal{F}_{22})$. In particular, from (4.25), we know that $h(\tilde{v}) = 0$, and hence condition (4.29) must hold for $\bar{v} = \tilde{v}$. At this point, using (4.30), we can rewrite (4.27) as

$$\mathcal{Q}_{22}\hat{v} = \mathbf{0}_{2\times 1} \Longrightarrow \bar{v} \in \mathrm{Ker}(\mathcal{F}_{22}),$$

which, since $\bar{v} \in \mathrm{Ker}(\mathcal{F}_{22}) \Longleftrightarrow \hat{v} = \mathbf{0}_{2\times 1}$, finally becomes

$$\mathcal{Q}_{22}\hat{v} = \mathbf{0}_{2\times 1} \Longrightarrow \hat{v} = \mathbf{0}_{2\times 1}. \tag{4.31}$$

In summary, we have shown that, in order to prove (4.27), one can equivalently demonstrate (4.31). To this aim, we parametrize $\hat{v} \in \mathrm{Im}(\mathcal{F}_{22}^T)$ as

$$\mathrm{Im}(\mathcal{F}_{22}^T) = \left\{ \mathcal{F}_{22}^T \begin{bmatrix} y_1 \\ y_2 \end{bmatrix}, y_1, y_2 \in \mathbb{R} \right\}$$

which, recalling (4.5), becomes

$$\mathrm{Im}(\mathcal{F}_{22}^T) = \left\{ \begin{bmatrix} f_{22} & 0 \\ f_{23} & 0 \end{bmatrix} \begin{bmatrix} y_1 \\ y_2 \end{bmatrix}, y_1, y_2 \in \mathbb{R} \right\} = \left\{ \begin{bmatrix} f_{22} \\ f_{23} \end{bmatrix} y_1, y_1 \in \mathbb{R} \right\}.$$

Hence, we rewrite $\mathcal{Q}_{22}\hat{v} = \mathbf{0}_{2\times 1}$ in (4.31) as $\mathcal{Q}_{22}[f_{22}\ f_{23}]^T y_1 = \mathbf{0}_{2\times 1}$, that, by means of (4.26), implies

$$\mathcal{P}_{22}\mathcal{F}_{22} \begin{bmatrix} f_{22} \\ f_{23} \end{bmatrix} y_1 = -\mathcal{F}_{22}^T \mathcal{P}_{22} \begin{bmatrix} f_{22} \\ f_{23} \end{bmatrix} y_1. \tag{4.32}$$

Replacing (4.5) and (4.7) in (4.32), we get

$$\begin{cases} p_{22}\left(f_{22}^2 + f_{23}^2\right) y_1 = -f_{22}^2 p_{22} y_1 - f_{22} f_{23} p_{23} y_1 \\ p_{23}\left(f_{22}^2 + f_{23}^2\right) y_1 = -f_{22} f_{23} p_{22} y_1 - f_{23}^2 p_{23} y_1 \end{cases} \tag{4.33}$$

Notice that (4.33) is verified if $y_1 = 0$ (i.e. if $\hat{v} = \mathbf{0}_{2\times 1}$). To conclude the proof, we just need to show that $y_1 = 0$ is the only solution of (4.33). To this purpose, we proceed by contradiction and assume that there exists a $y_1 \neq 0$ fulfilling (4.33). This leads to

$$\begin{cases} p_{22}\left(2f_{22}^2 + f_{23}^2\right) = -f_{22} f_{23} p_{23} & \text{(4.34a)} \\ p_{23}\left(f_{22}^2 + f_{23}^2\right) = -f_{22} f_{23} p_{22} - f_{23}^2 p_{23} & \text{(4.34b)} \end{cases}$$

Let us consider (4.34a) and let us assume, for the time being,

$$f_{22} \neq 0 \text{ and } f_{23} \neq 0. \tag{4.35}$$

We will show later that these two conditions are satisfied if $k_3 \neq 0$. Since it also holds $p_{22} > 0$[2], we have $-f_{22}f_{23}p_{23} > 0$, which implies $p_{23} \neq 0$. Then, we derive

$$p_{22} = -\frac{f_{22}f_{23}p_{23}}{2f_{22}^2 + f_{23}^2}$$

and replace it in (4.34b), obtaining

$$2p_{23}f_{23}^2 + p_{23}f_{22}^2 = \frac{f_{22}^2 f_{23}^2 p_{23}}{2f_{22}^2 + f_{23}^2}. \tag{4.36}$$

Finally, by direct calculation, (4.36) amounts to

$$4f_{22}^2 f_{23}^2 + 2f_{23}^4 + 2f_{22}^4 = 0,$$

which is true if and only if $f_{22} = f_{23} = 0$. However, from (4.35), these conditions are never verified.

The last step is to show that (4.35) holds. Recalling that electrical parameters are positive, one has $k_3 \neq 0 \implies f_{23} \neq 0$ (see (4.5)). Moreover, $Q \leq 0$, implies $\mathcal{Q}_{22} \leq 0$ (in fact, as the last row of $\mathcal{F}_{22}$ is zero, $\mathcal{Q}_{22}$ cannot be negative definite). Now, if $f_{22} = 0$ holds, we would have $q_{22} = 0$, which implies $q_{23} = q_{32} = 0$. However, by construction, we have $q_{23} = q_{32} = f_{23}p_{22} + f_{22}p_{23}$ (see (4.11)), which is never zero if $f_{22,i} = 0$, because $f_{23} \neq 0$ and $p_{22} \neq 0$. □

Proposition 4.4. *Let $g_i(w_i) = w_i^T Q_i w_i$. Under the same assumptions of Proposition 4.3, only vectors $\bar{w}_i$ in the form*

$$\bar{w}_i = \begin{bmatrix} \alpha_i & \beta_i & \delta_i\beta_i \end{bmatrix}^T$$

with α_i, $\beta_i \in \mathbb{R}$, and $\delta_i = -\frac{k_{2,i} - R_{ti}}{k_{3,i}}$, fulfill

$$g_i(\bar{w}_i) = \bar{w}_i^T Q_i \bar{w}_i = 0. \tag{4.37}$$

Proof. In the sequel, we omit the subscript i. From (4.11), $g(w)$ is equal to

$$\left[\begin{array}{c|c} w_1 & w_2^T \end{array}\right] \left[\begin{array}{c|c} 0 & \mathbf{0}_{1\times 2} \\ \hline \mathbf{0}_{2\times 1} & \mathcal{Q}_{22} \end{array}\right] \left[\begin{array}{c} w_1 \\ \hline w_2 \end{array}\right], \tag{4.38}$$

[2]Matrix P is structured as in (4.8) and it is positive definite. Therefore, $\mathcal{P}_{22} > 0$, which implies that the first minor of $\mathcal{P}_{22}$ (i.e. p_{22}) must be strictly positive.

where $w_2 \in \mathbb{R}^2$. Since Q is negative semidefinite, the vectors $\bar{w}$ satisfying (4.37) also maximize $g(\cdot)$. Hence, it must hold $\frac{\mathrm{d}g}{\mathrm{d}w}(\bar{w}) = Q\bar{w} = \mathbf{0}_{3\times 1}$, i.e.

$$\left[\begin{array}{c|c} 0 & \mathbf{0}_{1\times 2} \\ \hline \mathbf{0}_{2\times 1} & \mathcal{Q}_{22} \end{array}\right] \left[\begin{array}{c} \bar{w}_1 \\ \hline \bar{w}_2 \end{array}\right] = \mathbf{0}_{3\times 1}. \tag{4.39}$$

It is easy to show that, by direct calculation, a set of solutions to (4.37) and (4.39) is composed of vectors in the form

$$\bar{w} = \left[\begin{array}{ccc} \alpha & 0 & 0 \end{array}\right]^T, \quad \alpha \in \mathbb{R}. \tag{4.40}$$

Moreover, from (4.38), we have that (4.37) is also verified if there exist vectors

$$\tilde{w} = \left[\begin{array}{c|c} w_1 & \underline{w}_2^T \end{array}\right]^T, \qquad \underline{w}_2 \neq [0\ 0]^T, \tag{4.41}$$

such that $w_1 \in \mathbb{R}$ and

$$\underline{w}_2^T \mathcal{Q}_{22} \underline{w}_2 = 0. \tag{4.42}$$

From Proposition 4.3, we know that vectors $\underline{w}_2$ fulfilling (4.42) belong to $\mathrm{Ker}(F_{22})$, which, recalling (4.5), can be explicitly computed as follows

$$\begin{aligned} \mathrm{Ker}(\mathcal{F}_{22}) &= \left\{ x \in \mathbb{R}^2 : \left[\begin{array}{cc} f_{22} & f_{23} \\ 0 & 0 \end{array}\right] x = \mathbf{0}_{2\times 1} \right\} = \\ &= \left\{ x \in \mathbb{R}^2 : x = \left[\begin{array}{cc} \beta & \delta\beta \end{array}\right]^T, \beta \in \mathbb{R}, \delta = -\frac{k_2 - R_t}{k_3} \right\}. \end{aligned} \tag{4.43}$$

The proof ends by merging (4.40) and (4.41), with $\underline{w}_2$ as in (4.43). □

Proof of Theorem 4.1. From Proposition 4.2, $\dot{\mathscr{V}}(\hat{\mathbf{x}})$ is negative semidefinite (i.e. (4.14) holds). We want to show that the origin of the mG is also attractive using the LaSalle invariance Theorem [Kha01]. For this purpose, we first compute the set $R = \{\mathbf{x} \in \mathbb{R}^{3N} : \mathbf{x}^T \mathbf{Q} \mathbf{x} = 0\}$, which, by means of the decomposition in (4.18), coincides with

$$\begin{aligned} R &= \{\mathbf{x} : \mathbf{x}^T \left((a) + (b) + (c)\right) \mathbf{x} = 0\} \\ &= \underbrace{\{\mathbf{x} : \mathbf{x}^T (a) \mathbf{x} = 0\}}_{X_1} \cap \underbrace{\{\mathbf{x} : \mathbf{x}^T \left[(b) + (c)\right] \mathbf{x} = 0\}}_{X_2}. \end{aligned} \tag{4.44}$$

In particular, the last equality follows from the fact that (a) and $(b) + (c)$ are negative semidefinite matrices (see the proof of Proposition 4.2). We

first focus on the elements of set X_2. Since matrix $(b)+(c)$ can be seen as an "expansion" of the Laplacian (4.22), with zero entries on the second and third row of each 3×3 block, we have that, by construction, vectors in the form

$$\tilde{\mathbf{x}} = [\ 0\ \tilde{x}_{12}\ \tilde{x}_{13}\ |\ \cdots\ |\ 0\ \tilde{x}_{N2}\ \tilde{x}_{N3}\ ]^T, \quad \tilde{x}_{i2}, \tilde{x}_{i3} \in \mathbb{R}, \forall i \in \mathcal{V}, \tag{4.45}$$

belong to X_2. Moreover, since the kernel of the Laplacian matrix of a connected graph contains only vectors with identical entries [GR01], it also holds

$$\{\bar{\mathbf{x}} = \bar{x}\,[\ 1\ 0\ 0\ |\ \cdots\ |\ 1\ 0\ 0\ ]^T,\ \bar{x} \in \mathbb{R}\} \subset X_2, \tag{4.46}$$

with $\bar{x} \in \mathbb{R}$. Hence, by merging (4.45) and (4.46), we have that

$$X_2 = \{\mathbf{x} : \mathbf{x} = [\ \bar{x}\ \tilde{x}_{12}\ \tilde{x}_{13}\ |\ \cdots\ |\ \bar{x}\ \tilde{x}_{N2}\ \tilde{x}_{N3}\ ]^T, \bar{x}, \tilde{x}_{i2}, \tilde{x}_{i3} \in \mathbb{R}\}.$$

Next, we characterize the set X_1. By exploiting Proposition 4.4, it follows that

$$X_1 = \{\mathbf{x} : \mathbf{x} = [\ \alpha_1\ \beta_1\ \delta_1\beta_1\ |\ \cdots\ |\ \alpha_N\ \beta_N\ \delta_N\beta_N\ ]^T, \alpha_i, \beta_i \in \mathbb{R}\}, \tag{4.47}$$

and, from (4.44),

$$R = \{\mathbf{x} : \mathbf{x} = [\ \bar{\alpha}\ \beta_1\ \delta_1\beta_1\ |\ \cdots\ |\ \bar{\alpha}\ \beta_N\ \delta_N\beta_N\ ]^T, \bar{\alpha}, \beta_i \in \mathbb{R}\}. \tag{4.48}$$

At this point, in order to conclude the proof, we need to show that the largest invariant set $M \subseteq R$ is the origin. To this purpose, we consider (4.4), include coupling terms $\hat{\xi}_{[i]}$, set $\hat{d}_{[i]} = 0$ and choose as initial state $\hat{\mathbf{x}}(0) = [\hat{x}_1(0)|\dots|\hat{x}_N(0)]^T \in R$. We aim to find conditions on the elements of $\hat{\mathbf{x}}(0)$ that must hold for having $\dot{\hat{\mathbf{x}}} \in R$. One has, using (4.5)

$$\begin{aligned}\dot{\hat{x}}_i(0) &= F_i\hat{x}_i(0) + \sum_{j\in\mathcal{N}_i} \underbrace{\hat{A}_{ij}\left(\hat{x}_j(0) - \hat{x}_i(0)\right)}_{=\mathbf{0}_{3\times 1}} = \\ &= \begin{bmatrix} \frac{\beta_i}{C_{ti}} \\ \frac{k_{1,i}-1}{L_{ti}}\bar{\alpha} + \underbrace{\frac{k_{2,i}-R_{ti}}{L_{ti}}\beta_i + \frac{k_{3,i}}{L_{ti}}\delta_i\beta_i}_{=0} \\ -\bar{\alpha} \end{bmatrix} = \begin{bmatrix} \frac{\beta_i}{C_{ti}} \\ \frac{k_{1,i}-1}{L_{ti}}\bar{\alpha} \\ -\bar{\alpha} \end{bmatrix},\end{aligned}$$

for all $i \in \mathcal{V}$. From (4.48), $\dot{\tilde{\mathbf{x}}}(0) \in R$ if and only if, it holds

$$\begin{cases} \dfrac{\beta_i}{C_{ti}} = \bar{\rho} & \text{(4.49a)} \\ \dfrac{k_{1,i}-1}{L_{ti}}\delta_i\bar{\alpha} = -\bar{\alpha}, & \text{(4.49b)} \end{cases}$$

for $i \in \mathcal{V}$ and $\bar{\rho} \in \mathbb{R}$. Condition (4.49b) is fulfilled if either

$$\bar{\alpha} = 0 \tag{4.50}$$

or

$$\delta_i = -\frac{L_{ti}}{k_{1,i}-1}. \tag{4.51}$$

Let us first focus on (4.51). From Proposition 4.1, we have that $q_{12,i} = q_{13,i} = 0$. By direct computation, one has that

$$q_{12,i} = \frac{(k_{1,i}-1)}{L_{ti}}p_{22,i} - p_{23,i} + \frac{\eta_i}{C_{ti}}. \tag{4.52}$$

Moreover, we show that

$$p_{22,i} = -\delta_i p_{23,i}. \tag{4.53}$$

Notably, since (4.10) and (4.11) hold, vectors $\bar{v}_i$ satisfying $h_i(\bar{v}_i) = \bar{v}_i^T \mathcal{Q}_{22,i}\bar{v}_i = 0$ also maximize $h_i(\cdot)$, i.e.

$$h_i(\bar{v}_i) = 0 \iff \frac{\mathrm{d}h}{\mathrm{d}v}(\bar{v}_i) = \mathcal{Q}_{22,i}\bar{v}_i = \mathbf{0}_{2\times 1}. \tag{4.54}$$

From Proposition 4.3, we know that only vectors $v \in \mathrm{Ker}(\mathcal{F}_{22})$ verify (4.54). Hence, (4.53) can be obtained by solving (4.54) with vectors defined as in (4.43).

By exploiting (4.53), substituting (4.9) in (4.52), and setting $q_{12,i} = 0$, we get

$$k_{1,i} = 1 - \frac{L_{ti}}{\delta_i} - \bar{\sigma}\frac{L_{ti}}{p_{22,i}}. \tag{4.55}$$

Then, if we replace (4.55) in (4.51), we obtain

$$\delta_i = \frac{\delta_i p_{22,i}}{p_{22,i} + \bar{\sigma}\delta_i} = \frac{\delta_i}{1 + \bar{\sigma}\frac{\delta_i}{p_{22,i}}},$$

which is true if $\bar{\sigma}\frac{\delta_i}{p_{22,i}} = 0$. This latter condition, however, is never verified since L_{ti} in (4.51) is always positive, as well as $p_{22,i}$ and $\bar{\sigma}$. It follows that (4.49b) has only one solution, which is (4.50). Therefore, by considering also the solutions of (4.49a), we find that $\dot{\hat{\mathbf{x}}}(0) \in R$ only if $\hat{\mathbf{x}}(0) \in S$, where

$$S = \{\mathbf{x} = [\ 0\ \bar{\rho}C_{t1}\ \bar{\rho}\delta_1 C_{t1}\ |\ \dots\ |\ 0\ \bar{\rho}C_{tN}\ \bar{\rho}\delta_N C_{tN}\ ]^T, \bar{\rho} \in \mathbb{R}\}. \quad (4.56)$$

Furthermore, it must hold $M \subseteq S$. Then, in order to characterize M, we pick an initial state $\tilde{\mathbf{x}}(0) = [\tilde{x}_1(0)|\dots|\tilde{x}_N(0)]^T \in S$ and impose $\dot{\tilde{\mathbf{x}}}(0) \in S$. This translates into the equations

$$\dot{\tilde{x}}_i(0) = (\hat{A}_{ii} + \hat{B}_i K_i)\tilde{x}_i(0) + \sum_{j\in\mathcal{N}_i} \underbrace{\hat{A}_{ij}\,(\tilde{x}_j(0) - \tilde{x}_i(0))}_{=0} =$$

$$= (\hat{A}_{ii} + \hat{B}_i K_i) \begin{bmatrix} 0 \\ \bar{\rho}C_{ti} \\ \bar{\rho}\delta_i C_{ti} \end{bmatrix} = \begin{bmatrix} \bar{\rho} \\ 0 \\ 0 \end{bmatrix},$$

for all $i \in \mathcal{V}$. It follows that $\dot{\tilde{\mathbf{x}}}(0) \in S$ only if $\bar{\rho} = 0$. Since $M \subseteq S$, from (4.56) one has $M = \{0\}$. □

4.6.3 Feasibility of the LMI test (4.16)

This Appendix summarizes the studies we performed in order to (i) evaluate the applicability of our *line-independent* control design procedure, and (ii) provide a proper comparison between the proposed approach and the method discussed in Chapter 3. For both the analyses, LMIs have been solved in MatLab/Yalmip, using SeDuMi solver.

Line-independent design: conservativity of the plug-in test (4.16)

In order to better assess the applicability of the line-independent control design procedure (and to provide a guideline to the choice of $\bar{\sigma}$ in (4.9)), we performed the following extensive analysis. For $\bar{\sigma} = 10$, we solved LMI (4.16) considering different values of the DGU converter parameters (R_t, L_t, C_t), and check when LMIs are infeasible.

Figure 4.6 shows combinations of these parameters for which the LMI are feasible (blue circles), and infeasible (red stars). Although we used wide ranges for converters parameters, numerical results reveal that, for values

typically found in the literature for LV DC mGs[3] (i.e. the points within the green box in Figure 4.6), LMI are always feasible. This confirms the validity of the proposed control design methodology.

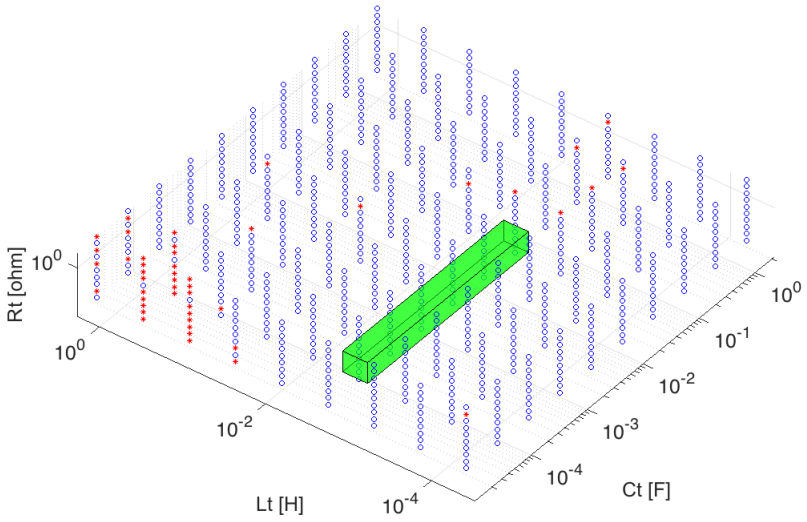

Figure 4.6: LMI results for combinations of R_t, L_t and C_t. Blue circles indicate feasible LMIs while red stars correspond to infeasible ones. The green box encloses typical DGU parameters for LV DC mGs.

Comparison with the line-dependent approach in Chapter 3

In order to compare the proposed design methodology with the one in Chapter 3, we show the existence of a limit on the maximum number of subsystems which can be connected to the PCC of a given DGU (say DGU i), before obtaining the infeasibility of the i-th local *line-dependent* plug-in test (i.e. the LMI (3.26)).

We start by considering the interconnection of DGUs 1 and 2 at stage $k = 1$ (see Figure 4.7a). Then, at each stage $k > 1$, we solve the LMI (3.26) for DGU 1 (using $\eta = 10^{-4}$), connecting one DGU at a time to PCC_1, thus creating the star topology shown in Figure 4.7b. Electrical and optimization parameters used for this analysis are reported in Table 4.1.

Numerical results reveal that the feasibility test for DGU 1 fails when the plug-in of DGU 4 is requested. This is due to the fact that the design of

[3]See, e.g., [HGK+16], [SDVG14a] and [DGVS14].

each local controller depends on the parameters of power lines connecting the corresponding unit to its neighbors. On the other hand, in the previous paragraph we have shown that, for $\bar{\sigma} = 10$, the *line-independent* LMIs (4.16) are always feasible.

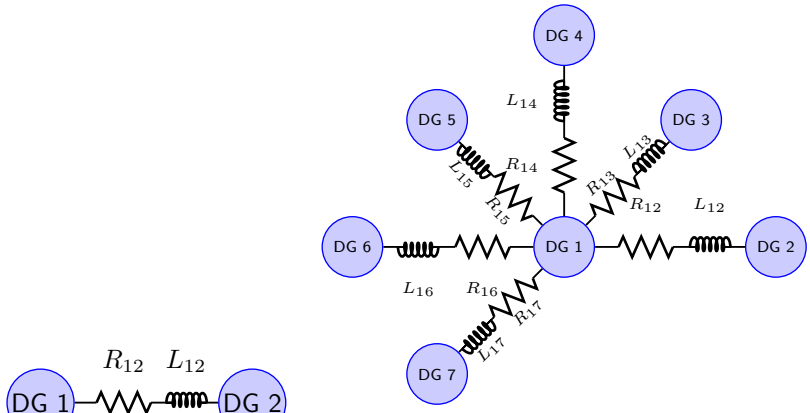

(a) Starting mG ($k = 1$).

(b) Example of star-connected mG after 6 stages ($k = 6$).

Figure 4.7: Finding the maximum number of DGUs which can be connected to PCC_1 before obtaining a plug-in request failure.

Converter parameters			
DGU	R_t (Ω)	L_t (mH)	C_t (mF)
$\hat{\Sigma}_{[1]}$	0.2	1.8	2.2
$\hat{\Sigma}_{[2]}$	0.3	2	2.2
$\hat{\Sigma}_{[3]}$	0.1	2.2	2.2
$\hat{\Sigma}_{[4]}$	0.5	3	2.2
Power line parameters			
Connected DGUs (i, j)		Resistance R_{ij} (Ω)	Inductance $L_{ij}(\mu$H)
$(1, 2)$		0.05	2.1
$(1, 3)$		0.07	1.8
$(1, 4)$		0.03	2.5
Optimization parameters			
α_1	α_2		α_3
10^{-6}	10^{-2}		10^{-3}

Table 4.1: Electrical and optimization parameters.

Chapter 5

Consensus-based secondary control layer for stable current sharing and voltage balancing in DC microgrids

Contents

5.1 Introduction 102

5.1.1 Microgrid modeling and primary control 105

5.2 Secondary control based on consensus algorithms 106

5.3 Modeling and analysis of the complete system . 108

5.3.1 Unit-gain approximation of primary control loops 108

5.3.2 First-order approximation of primary control loops 115

5.3.3 Plug-and-play design of secondary control 119

5.4 Validation of secondary controllers 120

5.4.1 Simulation results 120

5.4.2 Experimental results 122

5.5 Final comments 125

5.6 Appendix 127

5.6.1 Proof of Proposition 5.3 127

5.6.2 Proof of Theorem 5.1 128

5.6.3 Proof of Theorem 5.2 130

5.6.4 On the eigenvalues of $\mathbb{Q} = \mathbb{L}D\mathbb{M}$ 132

5.6.5 Electrical and simulation parameters 135

5.1 Introduction

In this chapter, we present a secondary consensus-based control layer for achieving advanced behaviors in DC mGs. As discussed in Section 1.2, besides voltage stability, other challenges must be addressed. The first desirable goal is current sharing, i.e. to make DGUs compensate constant load currents proportionally to given parameters (e.g., the converter ratings) and independently of the mG topology and line impedances. We recall that current sharing prevents the circulation of unregulated currents, which, in turn, may overload generators and lead to failures or system blackout.

Another objective is voltage balancing, i.e. to keep the average output voltage of DGUs close to a prescribed level. Indeed, load devices are designed to be supplied by a nominal reference voltage: it is therefore important to ensure that the voltages at the load buses are spread around this value.

Current sharing is often realized through secondary-level consensus algorithms, tightly coupled with primary controllers; therefore, stability of the overall closed-loop system cannot be given for granted. In [BDL14, MNLD15], a secondary-level consensus scheme is employed to guarantee current sharing while allowing for safe addition/removal of DGUs in mGs with a specific topology (i.e. with a common load, supplied by all the sources). However, the design of local regulators ensuring overall closed-loop stability is not scalable, since it requires to be performed in a centralized fashion. Consensus-based secondary controllers for mGs with more general topologies have been presented in [SDA$^+$14]; also in this case, however, stability of the closed-loop mG equipped with primary and secondary control layers is studied through centralized analysis (i.e. root locus), or via simulations.
Synthesis algorithms of this kind become prohibitive for large mGs. Moreover, they are unsuitable for mGs with flexible structure because, to preserve voltage stability, the plugging in or out of DGUs might require to update all local controllers in the mG. This motivated the development of scalable design procedures for local controllers as the ones presented in Chapters 3, 4 and in [ZD15].

In the following, a systematic method for the scalable design of secondary controllers in DC mGs with general topologies is presented. We assume that the proposed higher-level scheme is built on top of a primary stabilizing voltage control layer and we aim to achieve current sharing and voltage balancing in a stable fashion. Similarly to [ZD15], at the secondary

level we exploit consensus filters requiring DGUs to communicate in real-time over a connected network. There is, however, a key difference between our approach and the one presented in [ZD15]. In the latter work, authors assume distributed sources to be controllable *current* sources; on the contrary, we aim to make primary-controlled DGUs behave as ideal *voltage* generators. The main advantage of our assumption is that, in principle, by properly choosing the reference values for the output voltages of each DGU, one can always regulate the currents that flow through the power lines, even when internal load conditions change. In this way, unwanted circulating currents (which may open the safety breakers in order to prevent damages on the devices) can be avoided. On the other hand, if all the DGUs in the mG are treated as ideal current sources, the primary regulation scheme alone cannot guarantee such control on the flowing currents [ZD15].

At the modeling level, we propose two abstractions for the DGUs controlled with primary voltage regulators: unit-gain and first-order transfer function approximation. The first one is used only for tutorial purposes and for developing basic mathematical tools that will allow us to extend the key results to the second (more realistic) approximation of the primary loops.

Another contribution of this chapter is the study of the eigenstructure of the product of three matrices ($\mathbb{L}D\mathbb{M}$), where (i) $\mathbb{L}$ and $\mathbb{M}$ are the graph Laplacians associated with the electrical and the communication graphs, respectively, and (ii) D is a diagonal positive definite matrix defining the desired ratios between balanced currents. While several studies focused on the properties of the product of stochastic matrices (see e.g. [JLM03]), which are central in discrete-time consensus, to our knowledge weighted products of Laplacians received much less attention. In particular, we show that, under two different conditions, $\mathbb{L}D\mathbb{M}$ preserves some key features of Laplacian matrices. In this case, the asymptotic achievement of current sharing and voltage balancing in a globally exponentially stable fashion is proved.

The chapter is organized as follows. In Section 5.1.1, we briefly summarize the adopted electrical model of DGUs and PnP primary controllers. The secondary control layer is developed and analyzed in Sections 5.2 and 5.3. In particular, Section 5.3.3 shows that, similarly to the regulators in Chapters 3 and 4, secondary controllers can be designed in a PnP fashion. Section 5.4.1 demonstrates current sharing and voltage balancing through simulations in Simulink/PLECS, where non-idealities of real converters and lines have been taken into account. Finally, in Section 5.4.2 we present ex-

perimental tests performed on a real DC mG.

Preliminary notation and definitions. The average of a vector $v \in \mathbb{R}^n$ is $\langle v \rangle = \frac{1}{n}\sum_{i=1}^{n} v_i$. We denote with H^1 the subspace composed of all vectors with zero average [BM05, FTBG06] i.e. $H^1 = \{v \in \mathbb{R}^n : \langle v \rangle = 0\}$. The space orthogonal to H^1 is $H^1_\perp$. It holds $H^1_\perp = \{\alpha \mathbf{1}_n,\ \alpha \in \mathbb{R}\}$ and $\dim(H^1_\perp) = 1$. Moreover, the decomposition $\mathbb{R}^n = H^1 \oplus H^1_\perp$ is direct, i.e. each vector $v \in \mathbb{R}^n$ can always be written in a unique way as

$$v = \hat{v} + \bar{v} \qquad \text{with } \hat{v} \in H^1 \text{ and } \bar{v} \in H^1_\perp. \tag{5.1}$$

Consider the matrix $A \in \mathbb{R}^{n\times n}$. With $A(H^1|H^1)$ we indicate the linear map $A : H^1 \to H^1$ (i.e. the restriction of the map $A : \mathbb{R}^n \to \mathbb{R}^n$ to the subspace H^1). For a subspace $\mathscr{M} \subset \mathbb{R}^n$, we denote with $P_{\mathscr{M}}(v)$ the projection of $v \in \mathbb{R}^n$ on $\mathscr{M}$. The subspace $\mathscr{M} \subset \mathbb{R}^n$ is said to be *A-invariant* if $v \in \mathscr{M} \Rightarrow Av \in \mathscr{M}$.

Let $A \in \mathbb{R}^{n\times n}$ be a matrix with real eigenvalues. The *inertia* of A is the triple $i(A) = (i_+(A), i_-(A), i_0(A))$, where $i_+(A)$ is the number of positive eigenvalues of A, $i_-(A)$ is the number of negative eigenvalues of A, and $i_0(A)$ is the number of zero eigenvalues of A, all counted with their algebraic multiplicity [HH91].

Laplacian matrices[1] have the key properties summarized in the next proposition [AC05, GR01, BM05].

Proposition 5.1. *For a weakly connected graph*[2] $\mathcal{G}$ *with weights* $w_i > 0$*, the associated Laplacian matrix* $L \in \mathbb{R}^{n\times n}$ *has the following properties:*

(i) it has non positive off-diagonal elements;

(ii) $\lambda_1(L) \geq \cdots \geq \lambda_{n-1}(L) \geq 0 = \lambda_n$*;*

(iii) $\mathrm{Ker}(L) = H^1_\perp$ *and* $\mathrm{Im}(L) = H^1$*;*

(iv) $L(H^1|H^1)$ *is invertible.*

Proof. Points (i)-(iii) are shown, e.g. in [AC05, GR01]. Point (iv) has been shown in [BM05] with the framework of partial difference equations. Next, we provide a proof based on linear algebra only. We start noticing that the linear map $L(H^1|H^1)$ invertible if it is surjective and injective [Lan87].

[1] See Appendix A.2 for the definition of Laplacian matrix of a graph.
[2] See Appendix A.2 for basic definitions in graph theory.

First, we show the surjectivity of L on H^1. By construction, $\text{rank}(L) = n-1$ because

$$\text{rank}(L) = \dim(\text{Im}(L)) = \dim(\mathbb{R}^n) - \dim(H^1_\perp) = n - 1.$$

Moreover, since L is symmetric, each column of L has zero sum and hence is a vector in H^1. Since $\text{Im}(L)$ is the column span, then $\text{Im}(L) \subseteq H^1$. Since $\dim(H^1) = n - 1$, one obtains $\text{Im}(L) = H^1$. This proves that the map $L(H^1|H^1)$ is surjective.
Next, we prove that $L(H^1|H^1)$ is also injective. By definition, this holds if

$$\forall b \in H^1 \qquad \forall x, y \in H^1 \qquad (Lx = b \text{ and } Ly = b) \Rightarrow x = y.$$

Now, $Lx = Ly = b$ implies that $L(x-y) = 0$. It means that $x-y \in \text{Ker}(L)$, therefore $\exists \alpha \in \mathbb{R}$ such that $x - y = \alpha \mathbf{1}_n$. However, since $x - y \in H^1$, $x - y = \alpha \mathbf{1}_n$ is verified only for $\alpha = 0$; this leads to $x = y$. □

5.1.1 Microgrid modeling and primary control

As in Chapters 3 and 4, we consider a DC mG composed of N DGUs. Each DGU has the electrical scheme is shown in Figure 3.2 and is modeled by the set of equations 3.9. All the state, input and output variables are defined as in Section 3.2.

In the sequel, we will assume that DGUs are equipped with decentralized primary controllers guaranteeing voltage stability. This goal can be achieved using, for instance, PnP regulators presented in Chapters 3 and 4.

For modeling the interaction of multiple DGUs, we represent the mG with a digraph $\mathcal{G}_{el} = (\mathcal{V}, \mathcal{E}_{el}, W_{el})$ (see the example in Figure 5.1), where (i) each node is a DGU with a decentralized primary voltage controller and local current load, (ii) edges $e^{el}_1, \ldots, e^{el}_M$ ($M = |\mathcal{E}_{el}|$) are power lines whose orientation define a reference direction for positive currents, (iii) the weight w^{el}_i of each edge e^{el}_i connecting nodes j and k is equal to the line conductance[3] $\frac{1}{R_{jk}}$, and (iv) $N = |\mathcal{V}|$. Moreover, we indicate with $\mathcal{N}^{el}_i$ and $\mathcal{N}^c_i$ the sets of neighbors of node $i \in \mathcal{V}$ in the electrical and communication graph, respectively.

Remark 5.1. *We recall that local PnP controllers can be enhanced with pre-filters so as to shape in a desired way the transfer function $F_{[i]}(s)$ between voltages $V_{ref,i}$ and V_i represented in Figure 3.2 (see Section 3.3.4).*

[3]Line inductances L_{ij} are neglected as we assume QSL approximations.

The closed-loop transfer function $F_{[i]}(s)$ has 3 poles and in the sequel it will be approximated by a unit gain and a first-order system. The first approximation will be used mainly for tutorial reasons. The second one is very mild at low and medium frequencies, as it can be noticed, e.g., from the Bode plots of $F_{[i]}(s)$ in Figure 3.8d.

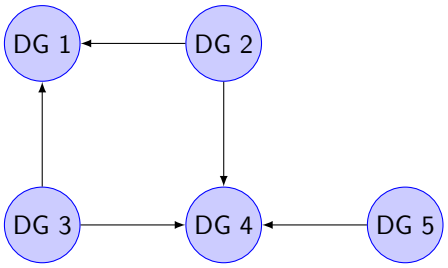

Figure 5.1: Graph representation of an mG.

5.2 Secondary control based on consensus algorithms

Most of the existing primary stabilizing controllers (including the PnP regulators proposed in Chapters 3 and 4), have the goal of turning DGUs into controlled voltage generators, i.e. to approximate, as well as possible, the identity $V_i = V_{ref,i}$. As such, they do not ensure current sharing and voltage balancing, defined in the sequel.

Definition 5.1. *For constant load currents $I_{Li}, i = 1, \dots, N$, current sharing is achieved if, at steady state, the overall load current is proportionally shared among DGUs, i.e. if*

$$\frac{I_{ti}}{I_{ti}^s} = \frac{I_{tj}}{I_{tj}^s} \quad \text{for all } i, j \in \mathcal{V}, \tag{5.2}$$

where $I_{ti}^s > 0$ are scaling factors.

We recall that current sharing is desirable in order to avoid situations in which some DGUs are not able to supply local loads, thus requiring power from other DGUs. A very common goal is to make DGUs share the total load current proportionally to their generation capacity. This can be obtained by measuring the output currents in per-unit (pu), i.e. setting

each scaling factor I_{ti}^s in (5.2) equal to the corresponding DGU rated current (see Section 5.4.1 for an example). On the other hand, if the scaling factors are all identical, the current sharing condition becomes

$$I_{ti} = \langle \mathbf{I_L} \rangle \qquad i = 1, \ldots, N, \tag{5.3}$$

where $\mathbf{I_L} = [I_{L1}, I_{L2}, \ldots, I_{LN}]^T$ is the vector of the local load currents.

Assumption 5.1. *Voltage references are identical for all DGUs, i.e.* $V_{ref,i} = V_{ref}$, $\forall i \in \mathcal{V}$.

Definition 5.2. *Under Assumption 5.1, voltage balancing is achieved if*

$$\langle \mathbf{V} \rangle = V_{ref}. \tag{5.4}$$

where vector $\mathbf{V} = [V_1, V_2, \ldots, V_N]^T$ *collects the PCC voltages.*

In order to guarantee current sharing and voltage balancing, we use a consensus-based secondary control layer. Consensus filters are commonly employed for achieving global information sharing or coordination through distributed computations [OSM04, Bulns]. In our case, as shown in Figure 5.2, we adopt the following consensus scheme for adjusting the references of each primary voltage regulator

$$\Delta \dot{V}_i(t) = -k_I \sum_{j=1, j\neq i}^{N} a_{ij} \left(\frac{I_{ti}(t)}{I_{ti}^s} - \frac{I_{tj}(t)}{I_{tj}^s} \right), \tag{5.5}$$

where $a_{ij} > 0$ if DGUs i and j are connected by a communication link ($a_{ij} = 0$, otherwise), and the coefficient $k_I > 0$ is common to all DGUs. The use of consensus protocols has been thoroughly studied for networks of agents with simple dynamics, e.g. simple integrators [OSM04, Bulns], with the goal of proving convergence of individual states to a common value. In our case, however, (5.5) is interfaced with the mG dynamics and convergence of currents I_{ti} to the same value does not trivially follow from standard consensus theory. This property will be rigorously analyzed in Section 5.3.

In the sequel, we assume bidirectional communication, i.e. $a_{ij} = a_{ji}$. The corresponding communication digraph is $\mathcal{G}_c = (\mathcal{V}, \mathcal{E}_c, W_c)$, where $(i, j) \in \mathcal{E}_c \iff a_{ij} > 0$, and the i-th diagonal element of W_c coincides with the weight of edge e_i^c, i.e. a_{jk} if e_i^c links nodes j and k. Considerations on the topologies of $\mathcal{G}_c$ and $\mathcal{G}_{el}$ guaranteeing stable current sharing and voltage balancing are detailed in Section 5.3.1. In all cases, however, the following standing assumption must hold.

Assumption 5.2. *The graphs $\mathcal{G}_{el}$ and $\mathcal{G}_c$ are weakly connected*[4].

From a system point of view, the collective dynamics of the group of DGUs following (5.5) can be expressed as

$$\dot{\boldsymbol{\Delta}\mathbf{V}} = -\underbrace{k_I L}_{\mathbb{L}} D\mathbf{I_t}, \tag{5.6}$$

where $\boldsymbol{\Delta}\mathbf{V} = [\Delta V_1, \ldots, \Delta V_N]^T = \mathbf{V} - \mathbf{V_{ref}}$, $\mathbf{V_{ref}} = [V_{ref,1}, V_{ref,2}, \ldots, V_{ref,N}]^T$, $\mathbf{I_t} = [I_{t1}, I_{t2}, \ldots, I_{tN}]^T$, $D = \text{diag}\left[\frac{1}{I^s_{t1}}, \ldots, \frac{1}{I^s_{tN}}\right] = \text{diag}\left[d_1, \ldots, d_N\right]$ and L is Laplacian matrix of $\mathcal{G}_c$. Note that $\mathbb{L}$ is the Laplacian matrix of $\mathcal{G}_c$ with W_c replaced by $k_I W_c$.

5.3 Modeling and analysis of the complete system

The hierarchical control scheme of a DGU equipped with primary and secondary regulators is shown in Figure 5.2. For studying the behavior of the closed-loop mG, we first approximate DGUs under the effect of primary controllers by unit gains (Section 5.3.1) and prove that current sharing is achieved in a stable way. We also provide conditions for voltage balancing. Results derived in this simple setting will be instrumental in studying the more complex scheme where primary control loops are abstracted into first-order transfer functions (Section 5.3.2).

5.3.1 Unit-gain approximation of primary control loops

By approximating primary loops with ideal unit gains, we have the relations $V_i = V_{ref,i} + \Delta V_i$, $\forall i \in \mathcal{V}$.

Figures 5.3a-5.3b show the resulting control scheme, used for deriving the dynamics of the overall mG as a function of the inputs $\mathbf{I_L}$ and $\mathbf{V_{ref}}$. Starting from the left-hand side of Figure 5.3a, we have, in order, (5.6) and

$$\mathbf{V} = \boldsymbol{\Delta}\mathbf{V} + \mathbf{V_{ref}}. \tag{5.7}$$

Then, from basic circuit theory, we derive the relation between the vector of voltages $\mathbf{V}$ and the vector of line currents $\mathbf{I}_\ell = [I_{\ell 1}, \ldots, I_{\ell M}]^T$ as

$$\mathbf{I}_\ell = -WB^T\mathbf{V}, \tag{5.8}$$

[4]See Appendix A.2 for the definition of weakly connected digraph.

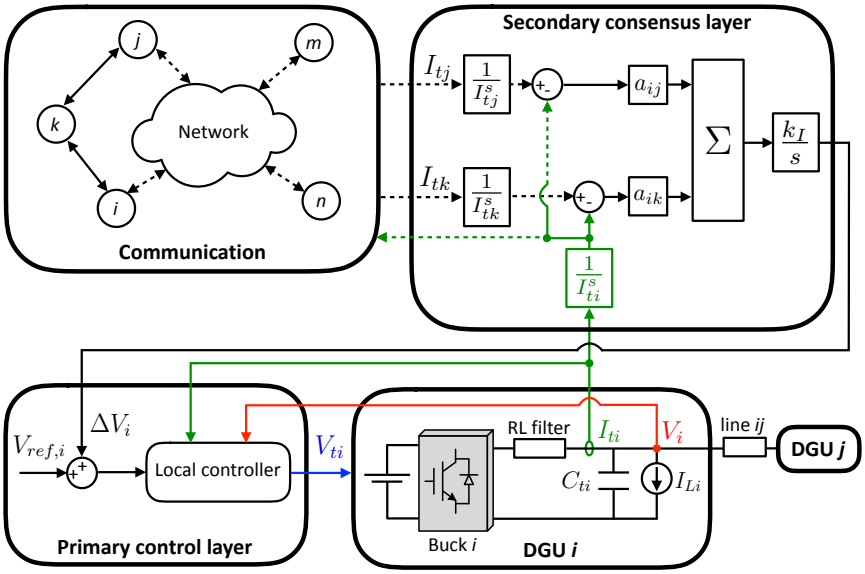

Figure 5.2: Complete hierarchical control scheme of DGU i.

where W and B are the weight and the incidence matrix of $\mathcal{G}_{el}$, respectively. Next, we get

$$\mathbf{I_t} = \mathbf{I_L} - B\mathbf{I}_\ell \tag{5.9}$$

and, merging equations (5.6)-(5.9), we finally obtain

$$\begin{aligned} \Sigma: \ \dot{\boldsymbol{\Delta}}\mathbf{V} &= -\mathbb{L}D\underbrace{BWB^T}_{\mathbb{M}}\boldsymbol{\Delta}\mathbf{V} - \mathbb{L}D\mathbf{I_L} - \mathbb{L}D\underbrace{BWB^T}_{\mathbb{M}}\mathbf{V_{ref}} \\ &= -\mathbb{Q}\boldsymbol{\Delta}\mathbf{V} - \mathbb{L}D\mathbf{I_L} - \mathbb{Q}\mathbf{V_{ref}} \end{aligned} \tag{5.10}$$

where $\mathbb{M} = \mathcal{L}(\mathcal{G}_{el}) = BWB^T$ is the Laplacian matrix of the electrical network and $\mathbb{Q} = \mathbb{L}D\mathbb{M}$.

Properties of the matrix $\mathbb{Q}$

The matrix $\mathbb{Q}$ in (5.10) captures the interaction of electric couplings and communication. From (5.10), it governs the voltage dynamics and hence the achievement of current sharing and voltage balancing. Notice that $\mathbb{Q}$ is obtained pre- and post- multiplying a diagonal matrix by two Laplacians ($\mathbb{L}$ and $\mathbb{M}$, respectively). It follows that $\mathbb{Q}$ is not a Laplacian matrix itself because it might fail to be symmetric and have positive off-diagonal entries, even if weights of $\mathcal{G}_{el}$ and $\mathcal{G}_c$ are positive. Nevertheless, in the sequel

we provide two distinct conditions under which $\mathbb{Q}$ preserves some key features of Laplacian matrices. Before proceeding, we introduce the following preliminary result.

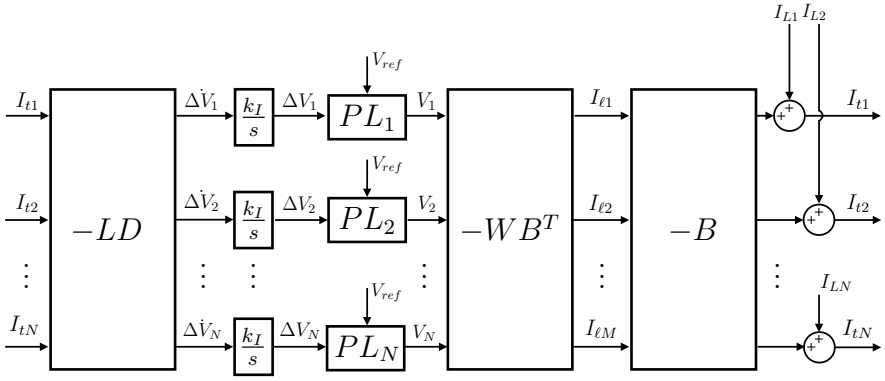

(a) Hierarchical control scheme.

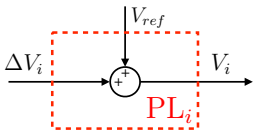

(b) i-th ideal primary loop.

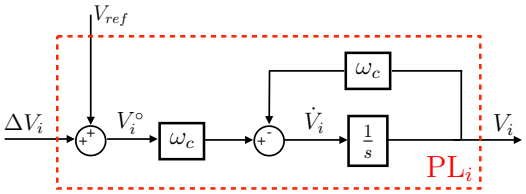

(c) First-order approximation of the i-th primary loop.

Figure 5.3: Hierarchical control scheme and Primary Loop (PL) approximations.

Proposition 5.2. *It holds* $P_{H^1}(D\mathbb{M}H^1) = H^1$.

Proof. From Proposition 5.1-(iv), we know that $\mathbb{M}(H^1|H^1)$ is invertible, hence surjective. Then,

$$D\mathbb{M}H^1 = DH^1.$$

We now study the projection map $P_{H^1} : DH^1 \to H^1$. Since D is invertible, we have that $\dim(DH^1) = \dim(H^1) = N - 1$. Therefore, one has

$$\dim\left(\mathrm{Im}(P_{H^1})\right) + \dim\left(\mathrm{Ker}(P_{H^1})\right) = N - 1. \tag{5.11}$$

The next step is to show that

$$\mathrm{Ker}(P_{H^1}) = \{0\}, \tag{5.12}$$

so that, from (5.11), P_{H^1} is surjective. Let $u \in DH^1$ and set $u = \bar{u} + \hat{u}$, where $\bar{u} \in H^1_\perp$ and $\hat{u} \in H^1$. Hence, $P_{H^1} u = P_{H^1} \hat{u} = \hat{u}$ and, if $u \in \mathrm{Ker}(P_{H^1})$, then $\hat{u} = 0$. In other words, $u \in \mathrm{Ker}(P_{H^1})$ verifies

$$\begin{cases} u = \alpha_u \mathbf{1} & \text{for some } \alpha_u \in \mathbb{R} \\ u = Dv & \text{for some } v \in H^1 \end{cases}$$

One has

$$||u||^2_{D^{-1}} = u^T D^{-1} u = \alpha_u \mathbf{1}^T D^{-1} D v = \alpha_u \mathbf{1}^T v = 0$$

where the last identity follows from the fact that $v \in H^1$ has zero average. But, since $||\cdot||_{D^{-1}}$ is a norm, $||u||^2_{D^{-1}} = 0$ implies $u = 0$. This shows (5.12). □

At this point, we can introduce two assumptions which allow us to characterize the eigenstructure of matrix $\mathbb{Q}$; then, we discuss their impact on the choice of the communication graph topology as well as on the value of coefficients a_{ij} in (5.5).

Assumption 5.3. *The diagonal matrix containing the scaling factors for the output currents coincides with the identity, i.e.* $D = I$.

Assumption 5.4. *It holds* $D \neq I$, $D > 0$ *and the product* $\mathbb{L}D\mathbb{M}$ *commutes (i.e.* $\mathbb{L}D\mathbb{M} = \mathbb{M}D\mathbb{L}$*).*

Remark 5.2. *Under Assumption 5.3, the desired goal is that all converters in the mG produce the same current (measured in Ampere and not in p.u.), i.e. that* (5.3) *holds. This can be desirable, for instance, when all the converters in the network have the same generation capacity. We notice that Assumption 5.3 does not enforce constraints on the graphs* $\mathcal{G}_{el}$ *and* $\mathcal{G}_c$*, which must fulfill Assumption 5.2 only.*

Remark 5.3. *Assumption 5.4 is suited to the case of converters with different ratings. However, it requires matrix* $\mathbb{Q}$ *to be symmetric. An interesting case where this condition is verified is given by*

$$\mathbb{L} = \mu \mathbb{M}, \tag{5.13}$$

where $\mu > 0$ *is a global parameter, common to all the DGUs*[5]*. Relation* (5.13) *holds if the following conditions are simultaneously guaranteed:*

[5]From (5.13), $\mathbb{Q} = \mathbb{L}D\mathbb{M} = \mu \mathbb{M}D\mathbb{M}$, which commutes since $\mathbb{M}$ and D are symmetric and μ is a scalar.

(a) $\mathcal{G}_{el}$ *and* $\mathcal{G}_c$ *have the same topology;*

(b) coefficients in (5.5) *are chosen as* $a_{ij} = \mu\frac{1}{R_{ij}}$ *if DGUs* i *and* j *are connected by a communication link.*

Condition (b) *has an impact on the design of local Laplacian control laws* (5.5)*. Notably, each agent (say DGU* i*) needs to know the global parameter* μ *and the value of the conductances* $\frac{1}{R_{ij}}$ *connecting it to its electrical neighbors* j *belonging to set* $\mathcal{N}_i^{el}$ *(which, in this particular case, coincides with* $\mathcal{N}_i^c$*).*

Remark 5.4. *Assumptions 5.3 or 5.4 are instrumental in guaranteeing asymptotic stability of the hierarchical control architecture in Figure 5.2. Indeed, as will be shown in the following proposition, the above conditions imply that the eigenvalues of* $\mathbb{Q}$ *are nonnegative. Note that, if neither Assumption 5.3 nor 5.4 are verified,* $\mathbb{Q}$ *can have negative eigenvalues (see the example in Appendix 5.6.4).*

Proposition 5.3. *The matrix* $\mathbb{Q} = \mathbb{L}D\mathbb{M}$ *has the following properties:*

(i) $\mathrm{Ker}(\mathbb{Q}) = H^1_\perp$*;*

(ii) $\mathrm{Range}(\mathbb{Q}) = H^1$*;*

(iii) the linear transformation $\mathbb{Q}(H^1|H^1)$ *is invertible;*

(iv) under Assumption 5.3 or 5.4, $\mathbb{Q}$ *is diagonalizable and has real nonnegative eigenvalues;*

(v) under Assumption 5.3 or 5.4, the zero eigenvalue of $\mathbb{Q}$ *has algebraic multiplicity equal to one.*

Proof. The proof of Proposition 5.3 is given in Appendix 5.6.1. □

Analysis of equilibria

In order to evaluate the steady-state behavior of the electrical signals appearing in Figure 5.3a-5.3b, we study the equilibria of system (5.10). Hence, for given constant inputs $(\mathbf{I}^*_{\mathbf{L}}, \mathbf{V}^*_{\mathbf{ref}})$, we characterize the solutions $\boldsymbol{\Delta}\mathbf{V}^*$ of equation

$$\mathbb{Q}\boldsymbol{\Delta}\mathbf{V}^* = -\mathbb{L}D\mathbf{I}^*_{\mathbf{L}} - \mathbb{Q}\mathbf{V}^*_{\mathbf{ref}} \tag{5.14}$$

through the following Proposition.

Proposition 5.4. *For equation* (5.14)*,*

(i) there is only one solution $\widetilde{\boldsymbol{\Delta}\mathbf{V}}^* \in H^1$*;*

(ii) all solutions $\boldsymbol{\Delta}\mathbf{V}^* \in \mathbb{R}^N$ *can be written as*

$$\boldsymbol{\Delta}\mathbf{V}^* = \widetilde{\boldsymbol{\Delta}\mathbf{V}}^* + \alpha \mathbf{1}_N \qquad \alpha \in \mathbb{R}. \tag{5.15}$$

Proof. Proposition 5.3-(ii) shows that (5.14) has solutions only if $-\mathbb{L}D\mathbf{I}^*_{\mathbf{L}} - \mathbb{Q}\mathbf{V}^*_{\mathbf{ref}} \in H^1$. From Propositions 5.1-(iii) and 5.3-(ii) this is always true. Statement (i) directly follows from Proposition 5.3-(iii).

For the proof of statement (ii), we split $\boldsymbol{\Delta}\mathbf{V}^* \in \mathbb{R}^N$ as in (5.1), i.e. $\boldsymbol{\Delta}\mathbf{V}^* = \widehat{\boldsymbol{\Delta}\mathbf{V}}^* + \overline{\boldsymbol{\Delta}\mathbf{V}}^*$. From (5.14) and Proposition 5.3-(i), one has that, irrespectively of $\overline{\boldsymbol{\Delta}\mathbf{V}}^* = \alpha\mathbf{1}_N \in H^1_\perp$, $\mathbb{Q}\widehat{\boldsymbol{\Delta}\mathbf{V}}^* = -\mathbb{L}D\mathbf{I}^*_{\mathbf{L}} - \mathbb{Q}\mathbf{V}^*_{\mathbf{ref}}$. Moreover, from the first part of the proof, it holds $\widehat{\boldsymbol{\Delta}\mathbf{V}}^* = \widetilde{\boldsymbol{\Delta}\mathbf{V}}^*$. □

Next, we relate properties of the equilibria of (5.10) to current sharing and voltage balancing.

Proposition 5.5. *Consider system* (5.10) *with constant inputs* $(\mathbf{I}^*_{\mathbf{L}}, \mathbf{V}^*_{\mathbf{ref}})$*. Then, current sharing is achieved at steady state. Moreover, if* $\mathbf{V}^*_{\mathbf{ref}} = V_{ref}\mathbf{1}_N$ *(i.e. if Assumption 5.1 holds) and* α *in* (5.15) *is equal to zero, then the equilibrium* $\mathbf{V}^*$ *verifies the voltage balancing condition* (5.4)*.*

Proof. At the equilibrium, since $\mathrm{Ker}(\mathbb{L}) = H^1_\perp$ (see Proposition 5.1-(iii)), from (5.6) we have that

$$\begin{aligned} -\mathbb{L}D\mathbf{I}^*_{\mathbf{t}} = \mathbf{0}_N &\Leftrightarrow D\mathbf{I}^*_{\mathbf{t}} = \bar{I}_t\mathbf{1}_N \\ &\Leftrightarrow \left[\frac{I^*_{t1}}{I^s_{t1}}, \ldots, \frac{I^*_{tN}}{I^s_{tN}}\right]^T = \bar{I}_t\mathbf{1}_N, \end{aligned} \tag{5.16}$$

which is (5.2). Let now $\boldsymbol{\Delta}\mathbf{V}^*$ be an equilibrium for system (5.10). Replacing (5.15) in (5.7) and averaging the resulting vector, we get

$$\langle \mathbf{V}^* \rangle = \underbrace{\langle \widetilde{\boldsymbol{\Delta}\mathbf{V}}^* \rangle}_{=0} + \underbrace{N\alpha}_{=0} + V_{ref},$$

which is (5.4). □

Stability analysis

The similarities established in Proposition 5.3 between the spectral properties of graph Laplacians and the matrix $\mathbb{Q}$ will allow us to study the stability properties of (5.10) using methods similar to the ones adopted for analysis of classical consensus dynamics. Results in this section follow the approach in [FTBG06], where stability of consensus is analyzed through the use of invariant subspaces. An advantage of this rationale is that it carries over almost invariably to the case of more complex models of primary loops (Section 5.3.2).

In the sequel, we prove exponentially stable convergence of $\boldsymbol{\Delta}\mathbf{V}$ in (5.10) to an equilibrium ensuring both current sharing and voltage balancing for constant ${\mathbf{I_L}}^*$ and $\mathbf{V}^*_{\mathbf{ref}} = V_{ref}\mathbf{1}_N$. We first show that projections $P_{H^1_\perp}(\boldsymbol{\Delta}\mathbf{V}) = \overline{\boldsymbol{\Delta}\mathbf{V}}$ and $P_{H^1}(\boldsymbol{\Delta}\mathbf{V}) = \widehat{\boldsymbol{\Delta}\mathbf{V}}$ have non-interacting dynamics (or, equivalently, that subspaces H^1 and $H^1_\perp$ are invariant for (5.10)).

Proposition 5.6. *If* $\boldsymbol{\Delta}\mathbf{V}$ *is given by system* Σ *in* (5.10) *for* $\boldsymbol{\Delta}\mathbf{V}(0) = \boldsymbol{\Delta}\mathbf{V}_0$*, then* $\boldsymbol{\Delta}\mathbf{V} = \overline{\boldsymbol{\Delta}\mathbf{V}} + \widehat{\boldsymbol{\Delta}\mathbf{V}}$*, where* $\overline{\boldsymbol{\Delta}\mathbf{V}} \in H^1_\perp$ *and* $\widehat{\boldsymbol{\Delta}\mathbf{V}} \in H^1$ *fulfill*

$$\overline{\Sigma}: \begin{cases} \dot{\overline{\boldsymbol{\Delta}\mathbf{V}}} = \mathbf{0}_N \\ \overline{\boldsymbol{\Delta}\mathbf{V}}(0) = \langle \boldsymbol{\Delta}\mathbf{V_0} \rangle \mathbf{1}_N \end{cases} \tag{5.17}$$

and

$$\widehat{\Sigma}: \begin{cases} \dot{\widehat{\boldsymbol{\Delta}\mathbf{V}}} = -\mathbb{Q}\widehat{\boldsymbol{\Delta}\mathbf{V}} - \mathbb{L}D\mathbf{I_L} - \mathbb{Q}\mathbf{V_{ref}} \\ \widehat{\boldsymbol{\Delta}\mathbf{V}}(0) = \boldsymbol{\Delta}\mathbf{V}_0 - \overline{\boldsymbol{\Delta}\mathbf{V}}_0. \end{cases} \tag{5.18}$$

Proof. We write vectors $\boldsymbol{\Delta}\mathbf{V}(0)$, $\mathbf{I_L}$ and $\mathbf{V_{ref}}$ according to the decomposition (5.1), i.e. using "$\widehat{\ }$" and "$\overline{\ }$" for denoting their H^1 and $H^1_\perp$ components, respectively. As described in [FTBG06], we analyze the dynamics of $\overline{\boldsymbol{\Delta}\mathbf{V}}$ by averaging both sides of (5.10) and $\boldsymbol{\Delta}\mathbf{V}(0) = \boldsymbol{\Delta}\mathbf{V}_0$, respectively. From points (i)-(ii) of Proposition 5.3, we have $\langle -\mathbb{Q}\boldsymbol{\Delta}\mathbf{V}\rangle = 0$ and $\langle -\mathbb{Q}\mathbf{V_{ref}}\rangle = 0$. Since $\mathrm{Im}(\mathbb{L}) = H^1$ (see Proposition 5.1-(iii)), we also have $\langle -\mathbb{L}D\mathbf{I_L}\rangle = 0$, hence obtaining $\frac{d}{dt}\langle \boldsymbol{\Delta}\mathbf{V}\rangle = 0$. Recalling that $\overline{\boldsymbol{\Delta}\mathbf{V_0}} = \langle \boldsymbol{\Delta}\mathbf{V_0}\rangle \mathbf{1}_N$, we obtain (5.17).

Next, we analyze $\widehat{\boldsymbol{\Delta}\mathbf{V}} = \boldsymbol{\Delta}\mathbf{V} - \overline{\boldsymbol{\Delta}\mathbf{V}}$. We have

$$\dot{\widehat{\boldsymbol{\Delta}\mathbf{V}}} = \dot{\boldsymbol{\Delta}\mathbf{V}} - \underbrace{\dot{\overline{\boldsymbol{\Delta}\mathbf{V}}}}_{=\mathbf{0}_N} = -\mathbb{Q}\boldsymbol{\Delta}\mathbf{V} - \mathbb{L}D\mathbf{I_L} - \mathbb{Q}\mathbf{V_{ref}}$$

and $\widehat{\boldsymbol{\Delta}\mathbf{V}}(0) = \boldsymbol{\Delta}\mathbf{V}_0 - \overline{\boldsymbol{\Delta}\mathbf{V}}_0$. From Proposition 5.3-(i), $\mathbb{Q}\boldsymbol{\Delta}\mathbf{V} = \mathbb{Q}\widehat{\boldsymbol{\Delta}\mathbf{V}}$ and then we have (5.18). □

Remark 5.5. *The splitting of* Σ *into systems* $\overline{\Sigma}$ *and* $\widehat{\Sigma}$ *implies that, if* $\mathbf{\Delta V_0}$ *has zero average, then* $\mathbf{\Delta V}(t)$ *has the same property,* $\forall t \geq 0$ *and irrespectively of inputs* $(\mathbf{I_L}, \mathbf{V_{ref}})$*. This behavior can be realized by suitable initialization of the integrators appearing in Figure 5.3a.*

According to system $\overline{\Sigma}$, the value of $P_{H^1_\perp}(\mathbf{\Delta V}) = \overline{\mathbf{\Delta V}}$ remains constant over time and equal to $\overline{\mathbf{\Delta V_0}}$. Hence, in order to characterize the stability of equilibria (5.15), it is sufficient to study the dynamics (5.18). In an equivalent way, one can consider system (5.10) and the following definition of stability on a subspace.

Definition 5.3. *Let* $\mathscr{M}$ *be a subspace of* $\mathbb{R}^n$*. The origin of* $\dot{x} = \mathcal{A}x$*,* $x(t) \in \mathbb{R}^n$ *is Globally Exponentially Stable (GES) on* $\mathscr{M}$ *if* $\exists \kappa, \eta > 0 : \|P_{\mathscr{M}} x(t)\| \leq \kappa e^{-\eta t} \|P_{\mathscr{M}} x(0)\|$*. The parameter* η *is termed rate of convergence.*

Note that Σ is a linear system and, for stability analysis, we can neglect inputs, hence obtaining

$$\begin{cases} \dot{\mathbf{\Delta V}} = -\mathbb{Q}\mathbf{\Delta V} \\ \mathbf{\Delta V}(0) = \mathbf{\Delta V}_0. \end{cases} \tag{5.19}$$

Theorem 5.1. *Under Assumption 5.3 or 5.4, the origin of* (5.19) *is GES on* H^1*. Moreover, the rate of convergence is the smallest strictly positive eigenvalue of* $\mathbb{Q}$*.*

Proof. The proof of Theorem 5.1 is presented in Appendix 5.6. □

The above results reveal that, given an initial condition $\mathbf{\Delta V}(0) = \mathbf{\Delta V_0}$ for system (5.10) and constant inputs $\mathbf{I_L^*}$ and $\mathbf{V_{ref}^*} = V_{ref}\mathbf{1}_N$, the state $\mathbf{\Delta V}$ converges to the equilibrium (5.15) with $\alpha = \langle \mathbf{\Delta V_0} \rangle$.
Summarizing the main results of this section, we have that the consensus scheme described by (5.5), Assumption 5.1 and

$$\langle \mathbf{\Delta V_0} \rangle = 0 \tag{5.20}$$

guarantee the asymptotic achievement of current sharing and voltage balancing in a GES fashion.

5.3.2 First-order approximation of primary control loops

Figure 5.3a and Figure 5.3c show the overall closed-loop scheme of an mG equipped with (i) consensus current loops and (ii) primary control loops

modeled as first-order transfer functions. Differently from the case analyzed in Section 5.3.1, each local dynamics is now described by means of two states which are the state of the consensus current loop (ΔV_i) and the state of the controlled DGU (V_i in Figure 5.3c). We highlight that relations (5.6) and (5.7) still hold, while the additional state equation is

$$\dot{\mathbf{V}} = \Omega \mathbf{V}^\circ - \Omega \mathbf{V}, \tag{5.21}$$

where vectors $\mathbf{V}^\circ = [V_1^\circ, V_2^\circ, \dots, V_N^\circ]^T$ and $\mathbf{V}$ belong to $\mathbb{R}^N$, and the diagonal matrix $\Omega = \omega_c I \in \mathbb{R}^{N \times N}$, $\omega_c > 0$, collects on its diagonal the approximate bandwidth of each controlled DGU. In view of Remark 5.1, assuming equal approximate bandwidths for all the controlled DGU is a mild constraint.

As in Section 5.3.1, in order to find the dynamics of the closed-loop scheme, we write relations among mG variables. From Figure 5.3a, we notice that (5.6) holds, and

$$\mathbf{V}^\circ = \boldsymbol{\Delta}\mathbf{V} + \mathbf{V}_{\mathbf{ref}}. \tag{5.22}$$

Always from Figure 5.3a, we have that, for line and output currents, equations (5.8) and (5.9) are still valid. By merging relations (5.6), (5.22), (5.21), (5.8) and (5.9), we can write the dynamics of the overall mG as

$$\begin{cases} \dot{\boldsymbol{\Delta}\mathbf{V}} = -\mathbb{Q}\mathbf{V} - \mathbb{L}D\mathbf{I}_{\mathbf{L}} & \text{(5.23a)} \\ \dot{\mathbf{V}} = \Omega\boldsymbol{\Delta}\mathbf{V} - \Omega\mathbf{V} + \Omega\mathbf{V}_{\mathbf{ref}}, & \text{(5.23b)} \end{cases}$$

or, equivalently, in compact form,

$$\begin{bmatrix} \dot{\boldsymbol{\Delta}\mathbf{V}} \\ \dot{\mathbf{V}} \end{bmatrix} = \underbrace{\begin{bmatrix} \mathbf{0}_N & -\mathbb{Q} \\ \Omega & -\Omega \end{bmatrix}}_{\mathcal{Q}} \begin{bmatrix} \boldsymbol{\Delta}\mathbf{V} \\ \mathbf{V} \end{bmatrix} + \begin{bmatrix} \mathbf{0}_N & -\mathbb{L}D \\ \Omega & -\Omega \end{bmatrix} \begin{bmatrix} \mathbf{V}_{\mathbf{ref}} \\ \mathbf{I}_{\mathbf{L}} \end{bmatrix},$$

with $\mathcal{Q} \in \mathbb{R}^{2N \times 2N}$ and $[\boldsymbol{\Delta}\mathbf{V}^T \mathbf{V}^T]^T \in \mathbb{R}^N \times \mathbb{R}^N$.

Analysis of equilibria

The equilibria of system (5.23) for constant inputs $(\mathbf{I}_{\mathbf{L}}^*, \mathbf{V}_{\mathbf{ref}}^*)$, are obtained by computing the solutions $[\boldsymbol{\Delta}\mathbf{V}^{*T}, \mathbf{V}^{*T}]^T$ to the system

$$\begin{cases} \mathbb{Q}\mathbf{V}^* = -\mathbb{L}D\mathbf{I}_{\mathbf{L}}^* & \text{(5.24a)} \\ \mathbf{0}_N = \Omega\boldsymbol{\Delta}\mathbf{V}^* - \Omega\mathbf{V}^* + \Omega\mathbf{V}_{\mathbf{ref}}^*. & \text{(5.24b)} \end{cases}$$

Since matrix Ω is invertible, equation (5.24b) becomes

$$\mathbf{V}^* = \boldsymbol{\Delta}\mathbf{V}^* + \mathbf{V}^*_{\mathbf{ref}}. \tag{5.25}$$

By substituting (5.25) in (5.24a), we get

$$\mathbb{Q}\boldsymbol{\Delta}\mathbf{V}^* = -\mathbb{L}D\mathbf{I}^*_{\mathbf{L}} - \mathbb{Q}\mathbf{V}^*_{\mathbf{ref}}.$$

that is exactly (5.14). We can then exploit Proposition 5.4 for concluding that there are infinitely many solutions $\boldsymbol{\Delta}\mathbf{V}^* \in \mathbb{R}^N$ in the form (5.15). Replacing (5.15) in (5.25), we can write equilibria of system (5.23) as

$$\begin{bmatrix} \boldsymbol{\Delta}\mathbf{V}^* \\ \mathbf{V}^* \end{bmatrix} = \begin{bmatrix} \widehat{\boldsymbol{\Delta}\mathbf{V}}^* + \alpha\mathbf{1}_N \\ \widehat{\boldsymbol{\Delta}\mathbf{V}}^* + \alpha\mathbf{1}_N + \mathbf{V}^*_{\mathbf{ref}} \end{bmatrix}. \tag{5.26}$$

Relations between the equilibria and current sharing/voltage balancing are given in the next proposition.

Proposition 5.7. *Consider the system* (5.23) *with constant inputs* $\mathbf{I}^*_{\mathbf{L}}$ *and* $\mathbf{V}^*_{\mathbf{ref}}$*. At the equilibrium, current sharing is achieved. Moreover, if* $\mathbf{V}^*_{\mathbf{ref}} = V_{ref}\mathbf{1}_N$ *(i.e. if Assumption 5.1 holds) and* α *in* (5.26) *is equal to zero, then the equilibrium* $[\boldsymbol{\Delta}\mathbf{V}^{*T}, \mathbf{V}^{*T}]^T$ *verifies the voltage balancing.*

Proof. Since equation (5.6) holds, one has that, at the equilibrium, relation (5.16) is verified. Then, the proof is identical to the one of Proposition 5.5. □

Next, similarly to the simplified case described in Section 5.3.1, we evaluate the stability properties of the closed-loop system (5.23) so as to show the convergence of state $[\boldsymbol{\Delta}\mathbf{V}^T\mathbf{V}^T]^T$ to an equilibrium which guarantees current sharing and voltage balancing.

Stability analysis

Proposition 5.8. *If* $[\boldsymbol{\Delta}\mathbf{V}^T\mathbf{V}^T]^T$ *verifies* (5.23)*, then*

$$\underbrace{\begin{bmatrix} \boldsymbol{\Delta}\mathbf{V} \\ \mathbf{V} \end{bmatrix}}_{\mathbf{v}} = \underbrace{\begin{bmatrix} \overline{\boldsymbol{\Delta}\mathbf{V}} \\ \overline{\mathbf{V}} \end{bmatrix}}_{\bar{\mathbf{v}}} + \underbrace{\begin{bmatrix} \widehat{\boldsymbol{\Delta}\mathbf{V}} \\ \widehat{\mathbf{V}} \end{bmatrix}}_{\hat{\mathbf{v}}},$$

where $\bar{\mathbf{v}} \in H^1_\perp \times H^1_\perp$ *and* $\hat{\mathbf{v}} \in H^1 \times H^1$ *fulfill*

$$\widetilde{\Sigma}^1_\perp : \begin{cases} \dot{\overline{\boldsymbol{\Delta}\mathbf{V}}} = \mathbf{0}_N & \text{(5.27a)} \\ \dot{\overline{\mathbf{V}}} = \Omega\overline{\boldsymbol{\Delta}\mathbf{V}} - \Omega\overline{\mathbf{V}} + \Omega\overline{\mathbf{V}_{\mathbf{ref}}} & \text{(5.27b)} \end{cases}$$

and

$$\widetilde{\Sigma}^1 : \begin{cases} \dot{\widehat{\boldsymbol{\Delta}\mathbf{V}}} = -\mathbb{Q}\widehat{\mathbf{V}} - \mathbb{L}D\mathbf{I_L} & (5.28a) \\ \dot{\widehat{\mathbf{V}}} = \Omega\widehat{\boldsymbol{\Delta}\mathbf{V}} - \Omega\widehat{\mathbf{V}} + \Omega\widehat{\mathbf{V}_{\mathbf{ref}}}, & (5.28b) \end{cases}$$

respectively.

Proof. The dynamics of $\overline{\boldsymbol{\Delta}\mathbf{V}}$ and $\widehat{\boldsymbol{\Delta}\mathbf{V}}$ can be derived proceeding as in the proof of Proposition 5.6. In a similar way, by averaging both sides of (5.23b), one derives the (independent) dynamics of $\overline{\mathbf{V}}$ and $\widehat{\mathbf{V}}$. □

The above decomposition allows us to evaluate the evolution of state $\mathbf{v}$ on $\mathbb{R}^{N\times N}$ by separately analyzing dynamics (5.27) and (5.28), i.e. studying the behavior of projections $\bar{\mathbf{v}} = P_{\mathscr{M}_1}(\mathbf{v})$ and $\hat{\mathbf{v}} = P_{\mathscr{M}_2}(\mathbf{v})$, with $\mathscr{M}_1 = H^1_\perp \times H^1_\perp$ and $\mathscr{M}_2 = H^1 \times H^1$.

First we focus on $\tilde{\Sigma}^1_\perp$. Without loss of generality, for stability analysis we can neglect the input vector $\overline{\mathbf{V}_{\mathbf{ref}}}$ in (5.27b), thus having:

$$\begin{cases} \dot{\overline{\boldsymbol{\Delta}\mathbf{V}}} = \mathbf{0}_N & (5.29a) \\ \dot{\overline{\mathbf{V}}} = \Omega\overline{\boldsymbol{\Delta}\mathbf{V}} - \Omega\overline{\mathbf{V}}. & (5.29b) \end{cases}$$

By construction, (5.29b) collects the decoupled equations

$$\dot{\overline{V}}_i = \omega_c\overline{\Delta V_i} - \omega_c\overline{V}_i \quad \forall i = 1,\dots,N, \tag{5.30}$$

where, according to (5.27a), each term $\overline{\Delta V_i}$ in can be treated as an exogenous input (thus not affecting stability properties). It follows that dynamics (5.30) is asymptotically stable, since $\omega_c > 0$. In summary, system (5.27) tells us that the average $\overline{\boldsymbol{\Delta}\mathbf{V}}$ will remain constant in time (and equal to $\langle\boldsymbol{\Delta}\mathbf{V_0}\rangle$), while $\overline{\mathbf{V}}$ will converge to the origin. For studying stability properties of system $\widetilde{\Sigma}^1$, we consider (5.23) without inputs, i.e.

$$\begin{cases} \dot{\boldsymbol{\Delta}\mathbf{V}} = -\mathbb{Q}\mathbf{V} \\ \dot{\mathbf{V}} = \Omega\boldsymbol{\Delta}\mathbf{V} - \Omega\mathbf{V} \end{cases} \tag{5.31}$$

and analyze stability on $H^1 \times H^1$. We have the following result.

Theorem 5.2. *Under Assumption 5.3 or 5.4, the origin of* (5.31) *is GES on $H^1 \times H^1$. Furthermore, matrix $\mathcal{Q}$ has a simple zero eigenvalue and the rate of convergence is the maximum among real parts of all other eigenvalues.*

Proof. The proof is given in Appendix 5.6.3. □

By means of Theorem 5.2, we have that, given an initial condition $[\boldsymbol{\Delta V_0}^T \mathbf{V_0}^T]^T$ for system (5.23), the state $[\boldsymbol{\Delta V}^T \mathbf{V}^T]^T$ will converge to the equilibrium in (5.26), with $\alpha = \langle \boldsymbol{\Delta V_0} \rangle$.

The results above show that, for system (5.23), current sharing is achieved in a GES fashion. In a similar way, asymptotic voltage balancing is ensured if Assumption 5.1 and (5.20) are fulfilled.

5.3.3 Plug-and-play design of secondary control

We now describe the procedure for designing secondary controllers in a PnP fashion. We will show that, as for the PnP design of primary regulators, when a DGU is added or removed, the secondary control layer can be updated only locally for preserving current sharing and voltage balancing.

Plug-in operation. Under Assumption 5.3, when a DGU (say DGU i) sends a plug-in request at a time $\bar{t}$, it choses a set $\mathcal{N}_i^c$ of communication neighbors (which must not necessarily coincide with $\mathcal{N}_i^{el}$) and fixes parameters $a_{ij} > 0, \forall j \in \mathcal{N}_i^c$, in order to design the local consensus filter (5.5). At the same time, each DGU j, $j \in \mathcal{N}_i^c$, updates its consensus filter by setting $a_{ji} = a_{ij}$ in (5.5). If, instead, $D \neq I$, one can fulfill Assumption 5.4 by allowing the entering DGU to receive the value of conductances $\frac{1}{R_{ij}}$ from the neighboring DGUs $j \in \mathcal{N}_i^{el}$ and by setting $\mathcal{N}_i^c = \mathcal{N}_i^{el}$ (see Remark 5.3). By doing so, DGU i can choose parameters $a_{ij} = \mu \frac{1}{R_{ij}}$, and each DGU $j \in \mathcal{N}_i^c$ sets $a_{ji} = a_{ij}$, thus updating its consensus filter (5.5). Overall, Theorems 5.1 and 5.2 ensure that the disagreement dynamics of the mG states is GES. Let Assumption 5.1 hold for all the interconnected DGUs in the mG before $\bar{t}$ and let us denote the common reference voltage by V_{ref}. If DGU i sets $V_{ref,i} = V_{ref}$ and if we choose $\Delta V_i(\bar{t}) = 0$ (thus having $\langle \begin{bmatrix} \boldsymbol{\Delta V'}(\bar{t}) \\ \Delta V_i(\bar{t}) \end{bmatrix} \rangle = 0$, where $\boldsymbol{\Delta V'}(\bar{t})$ is the vector $\boldsymbol{\Delta V}$ prior the plugging-in of DGU i), both current sharing and voltage balancing are preserved in the asymptotic régime (see Propositions 5.5 and 5.7).

Unplugging operation. Under Assumption 5.3 or 5.4, when a DGU (say DGU j) is unplugged at time $\bar{t}$, provided that the new graphs $\mathcal{G}_{el}$ and $\mathcal{G}_c$ fulfill Assumption 5.2, the key condition that must be guaranteed is that the vector $\boldsymbol{\Delta V}_{-j}$ (i.e. $\boldsymbol{\Delta V}$ without element j) verifies $\langle \boldsymbol{\Delta V}_{-j}(\bar{t}) \rangle = 0$. If

$\langle \mathbf{\Delta V}(\bar{t}^-)\rangle = 0$, this can be achieved by re-setting

$$\Delta V_i(\bar{t}) = \Delta V_i(\bar{t}^-) + \frac{\Delta V_j(\bar{t}^-)}{|\mathcal{N}_j^c|}$$

for all $i \in \mathcal{N}_j^c$, and keeping $\Delta V_i(\bar{t}) = \Delta V_i(\bar{t}^-)$ for all $i \notin \mathcal{N}_j^c \cup \{j\}$. Indeed, this yields

$$\begin{aligned}
\langle \mathbf{\Delta V}_{-j}(\bar{t})\rangle &= \frac{1}{N-1}\sum_{i\in\mathcal{N}_j^c}\Delta V_i(\bar{t}) + \frac{1}{N-1}\sum_{i\notin\mathcal{N}_j^c\cup\{j\}}\Delta V_i(\bar{t}) = \\
&= \frac{1}{N-1}\left(\sum_{i\in\mathcal{N}_j^c}\Delta V_i(\bar{t}^-) + \frac{1}{|\mathcal{N}_j^c|}\sum_{i\in\mathcal{N}_j^c}\Delta V_j(\bar{t}^-) + \sum_{i\notin\mathcal{N}_j^c\cup\{j\}}\Delta V_i(\bar{t}^-)\right) = \\
&= \frac{1}{N-1}\left(N\langle \mathbf{\Delta V}(\bar{t}^-)\rangle\right) = 0.
\end{aligned}$$

5.4 Validation of secondary controllers

5.4.1 Simulation results

In this section, we aim to demonstrate the capability of the proposed control scheme to guarantee current sharing and voltage balancing when DGUs are plugged in/out and load changes occur. Simulations have been performed in Simulink/PLECS. We consider an mG composed of 7 DGUs, interconnected as in Figure 5.4, with non-identical electrical parameters and power lines. Notice that some DGUs have more than one neighbor, hence the impact of couplings on their dynamics will be larger. Moreover, the presence of loops in the electrical network further complicates the voltage regulation. Primary PnP voltage regulators are designed according to the line-dependent method in Chapter 3, whereas, as regards the secondary control layer, we choose k_I in (5.6) equal to 1. DGUs have rated currents $I_{ti}^r = 10$ A, $i = 1,2,3$, $I_{t4}^r = I_{t5}^r = 5$ A and $I_{t6}^r = I_{t7}^r = 3.33$ A. Since, in this scenario, we aim to achieve the current sharing condition in (5.2), we set $I_{ti}^s = I_{ti}^r$, $i = 1,\dots,7$, thus having, in (5.6), $D \neq I$. Then, in order to guarantee the asymptotic stability of the hierarchical control scheme, we fulfill Assumption 5.4 by (i) letting $\mathcal{G}_c$ have the same topology of $\mathcal{G}_{el}$, and (ii) picking $a_{ij} = \frac{1}{R_{ij}}$, if DGUs i and j are connected by a communication link (see Remark 5.3). Furthermore, the voltage reference in Assumption 5.1 is $V_{ref} = 48$ V, and the electrical parameters are given in Appendix 5.6.5.

In the following, we describe Figure 5.5, which illustrates the evolution of the main electrical quantities (i.e. measured DGU output currents in Amperes, DGU output currents in p.u., PCC voltages and average PCCs voltage) during the consecutive simulation stages shown in Figure 5.4.

Stage 1. At time $t_0 = 0$, all the DGUs are assumed to be isolated and only the primary PnP voltage regulators, designed using the method described in Chapter 3, are active. Therefore, as shown in Figure 5.5, (i) each DGU supplies its local load while keeping the corresponding PCC voltage at 48 V, and (ii) the DGU output currents in p.u. are different. We further highlight that primary controllers have been designed assuming that all the switches in Figure 5.4 connecting DGUs 1-6 are closed. From Chapter 3, however, they also stabilize the mG when all switches are open.

Stage 2. Subsystems 1-6 are connected together at time $t_1 = 2$ s and, according to the previous observation, no update of primary controllers is needed. As shown in the plot of V_{PCC} in Figure 5.5, voltage stability and fast transients after the plug-in operations are ensured by PnP primary regulators. The secondary control layer is still disabled at this stage.

Stage 3. At time $t_2 = 5$ s, we activate the secondary control layer for DGUs 1-6, thus ensuring asymptotic current sharing among them (see the plot of the currents in p.u.). This is achieved by automatically adjusting the voltages at PCC (as shown in the plot of V_{PCC}). Moreover, the top plot of Figure 5.5 reveals that, as expected, DGUs 4 and 5 share half of the current of DGUs 1-3, while the output current of DGUs 6 is one third of the ones of DGUs 1-3. We further highlight that, by setting $\Delta V_i(t_2) = 0$, $i = 1, \ldots, 6$, as described in Section 5.3.3, condition (5.20) is fulfilled and asymptotic voltage balancing is guaranteed (see the plot of V_{av}).

Stage 4. For evaluating the PnP capabilities of our control scheme, at $t_3 = 15$ s, DGU 7 sends a plug-in request to DGUs 4 and 5. Previous primary controllers of DGUs 4 and 5 still fulfill the plug-in conditions in Chapter 3: they are therefore maintained and the plug-in of DGU 7 is performed. In the light of Assumption 5.3, at t_3 also the secondary controller of DGU 7 is activated, thus enabling the DGU to contribute to current sharing. This can be noticed in Figure 5.5, as all PCC voltages change in order to let all the output currents in p.u. converge to a common value. We also notice that the measured output currents (top plot of Figure 5.5) are

still shared accordingly (i.e. $I_{t1} = I_{t2} = I_{t3} = 2I_{t4} = 2I_{t5} = 3I_{t6} = 3I_{t7}$). Furthermore, choosing $\Delta V_7(t_3) = 0$ (as described in Section 5.3.3), we maintain the average PCCs voltage at 48 V (see V_{av}, stage 4).

Stage 5. At $t_4 = 25$ s, we halve the load of DGU 1, thus increasing the corresponding load current I_{L1} and causing a peak in the corresponding output current. However, after few seconds, all the DGUs share again the total load current, while the averaged PCC voltage converges to the reference value.

Stage 6. Finally, we assess the performance of the proposed hierarchical scheme when the sudden disconnection of a DGU occurs. To this aim, at time $t_5 = 35$ s, we disconnect DGU 3. Figure 5.5 (stage 6) shows that voltage stability, current sharing and voltage balancing are preserved in the mG composed of DGUs 1-2 and 4-7.

5.4.2 Experimental results

Performance brought about by the presented hierarchical scheme been also validated via experimental tests based on the mG platform in the top-left panel of Figure 5.6, which consists of three *Danfoss* inverters, a dSPACE1103 control board and LEM sensors. In order to properly emulate DC/DC converters (i.e. Buck converters), only the first phase of each inverter has been used. Buck converters operate in parallel to emulate DGUs while different local load conditions have been obtained by connecting each PCC to a resistive load. All the converters are supplied by DC source generators. For this scenario, primary PnP voltage controllers are designed using the line-independent approach in presented in Chapter 4, and Assumption 5.3 holds. Hence, since $D = I$, $I^s_{t1} = I^s_{t2} = I^s_{t3} = \bar{I}_t$, i.e. we aim to achieve the asymptotic current sharing condition (5.3). Moreover, we set k_I in (5.6) equal to 0.5, while coefficients a_{ij} in (5.5) are equal to 1 if DGUs i and j are connected by a communication link, 0 otherwise. We also recall that, under Assumption 5.3, the stability of the mG equipped with our hierarchical scheme is preserved even if the topologies of $\mathcal{G}_c$ and $\mathcal{G}_{el}$ differ. Notably, we consider the mG in Figure 5.6, where $\mathcal{G}_{el}$ and $\mathcal{G}_c$ are highlighted in blue and red, respectively, and the edges of $\mathcal{G}_{el}$ are RL lines. The controllers have been implemented in Simulink and compiled to the dSPACE system in order to command the Buck switches at a frequency of 10 kHz. Although the dSPACE platform is unique, separate local PnP volt-

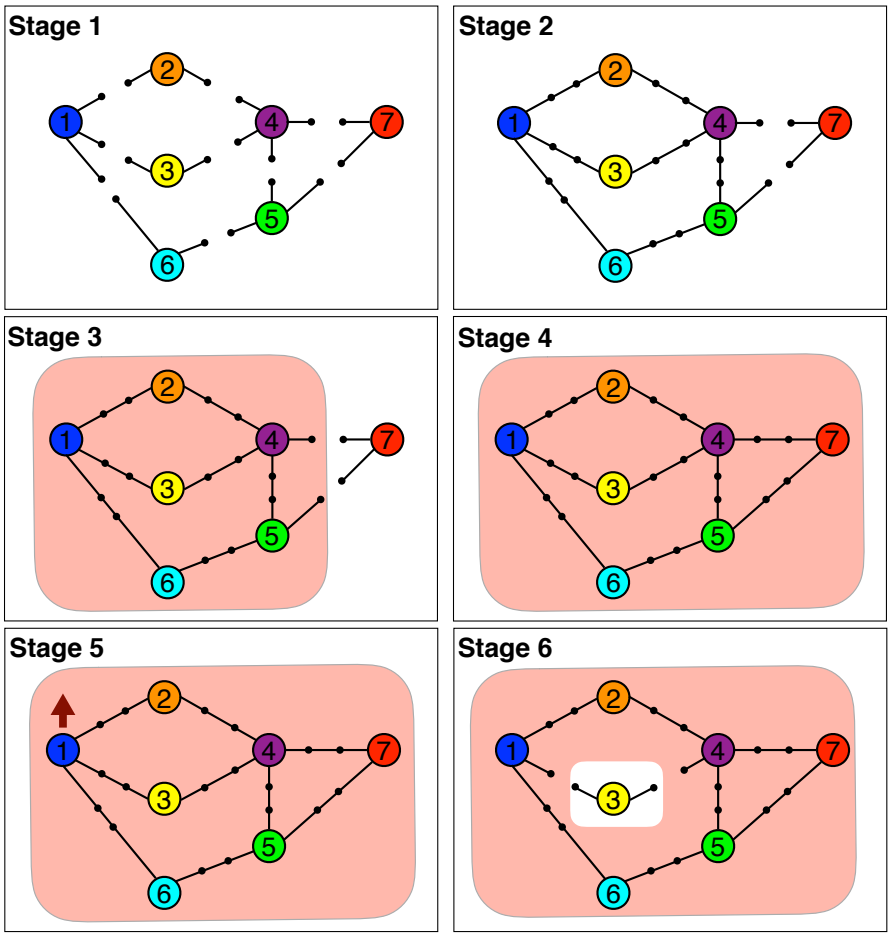

Figure 5.4: Simulation stages: numbered nodes represent DGUs, while black lines denote power lines. The secondary control layer is activated for the DGUs contained in the red area. Open switches in stages 1, 2, 3 and 6 denote disconnected DGUs. The arrow in stage 5 represents a step up in the load current of DGU 1.

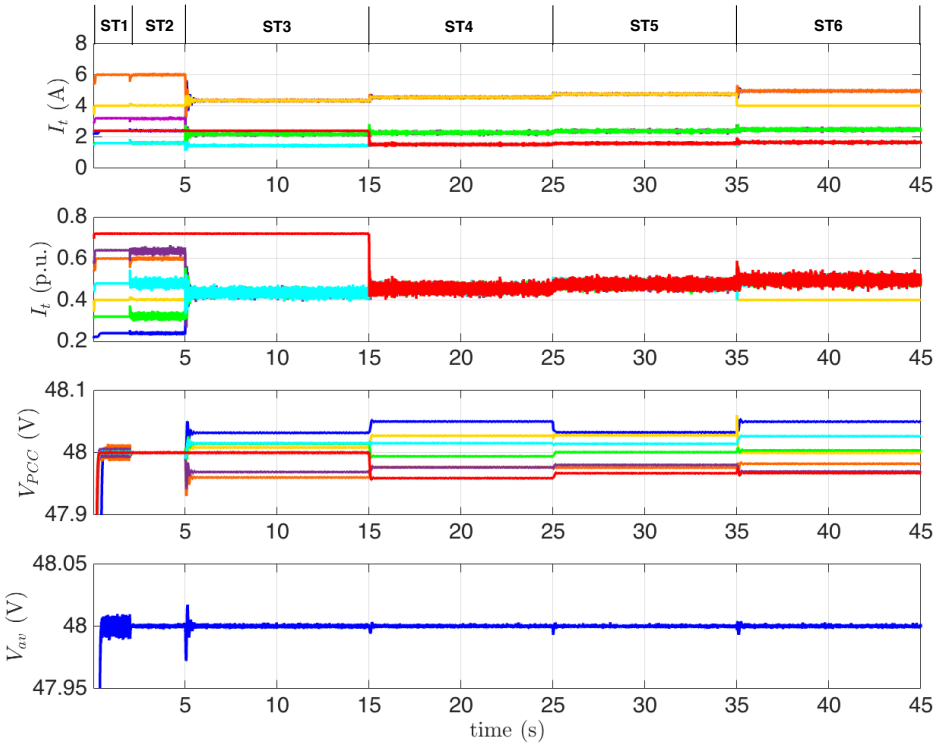

Figure 5.5: Simulation results: evolution of measured output currents, output currents in p.u., voltages at PCCs and average PCCs voltage. Lines in the plots are associated with different DGUs and they are color-coded as in Figure 5.4. Simulation stages are those shown in Figure 5.4.

age regulators have been implemented for each converter, so as to preserve the decentralized nature of the primary control layer.

We consider the mG in Figure 5.6, where $\mathcal{G}_{el}$ and $\mathcal{G}_c$ are highlighted in blue and red, respectively. The edges of $\mathcal{G}_{el}$ are RL lines. In the sequel, we provide a detailed description of the evolution of the main electrical quantities, which are shown in Figure 5.7.

At time $t_0 = 0$ s, all the DGUs are isolated and not connected to each other.

At times $t_1 \approx 2.5$ s, $t_2 \approx 5$ s and $t_3 \approx 10$ s, we connect DGU 1 to 2, 2 to 3 and 1 to 3, respectively, thus obtaining a loop in the electrical topology. We recall that, since DGUs are equipped with PnP stabilizing regulators designed following the line-independent synthesis procedure presented in Chapter 4, no controller update is required when units are connected together. As shown in the plot of the PCC voltages in Figure 5.7, PnP primary voltage regulators ensure smooth transitions and stability. We also highlight that, since for $t < t_3$ the secondary layer is not active, the output currents are not equally shared and the PCC voltages coincide with the reference (notably, Assumption 5.1 holds, with $V_{ref} = 48$ V).

Next, at time $t_4 \approx 15$ s, we set $\Delta V_i(t_4) = 0$, $i = 1, 2, 3$ and enable the secondary current layer. Since we choose the same scaling factor for all the DGUs, we have that the three output currents converge to the same measured value (see I_t in Figure 5.7). Furthermore, similarly to the simulation example, the fulfillment of condition (5.20) guarantees asymptotic voltage balancing (see V_{av} in Figure 5.7).

Finally, in order to assess the robustness of the proposed control scheme to unknown load dynamics, at time $t_5 \approx 25$ s we decrease the load of DGU 3, causing an increment in the corresponding load current. As a consequence, the value of $\bar{I}_t = \langle \mathbf{I}_\mathbf{L}^* \rangle$ increases as well. Also in this case, we have that the total load current is equally shared among DGUs while V_{av} does not deviate from 48 V.

5.5 Final comments

In this chapter, we presented a secondary consensus-based control layer for current sharing and voltage balancing in DC mGs. Under the assumption that DGUs are equipped with decentralized primary controllers guaranteeing voltage stability in the mG (e.g., PnP regulators), we proved stability of the hierarchical control scheme, current sharing and voltage balancing in the asymptotic régime. Moreover, a method for designing secondary con-

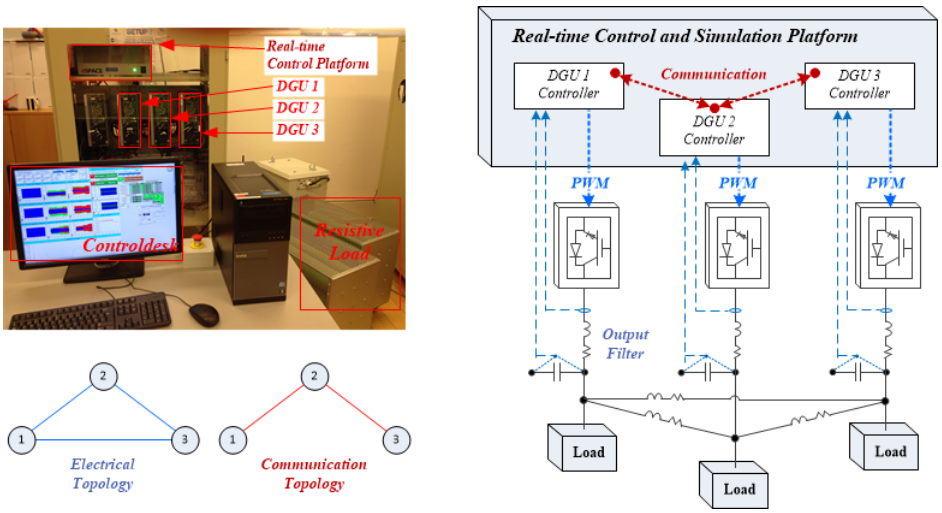

Figure 5.6: Experimental validation: mG setup (top-left), topologies of the electrical and communication graphs (bottom-left), and implemented control architecture (on the right).

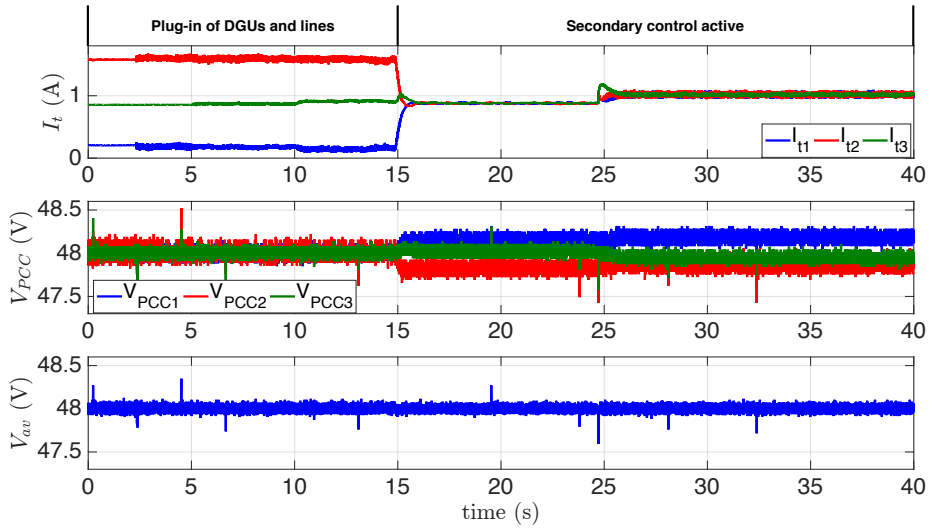

Figure 5.7: Experimental results for the mG in Figure 5.6. In the time interval from 2.5 s to 15 s, DGUs are connected together and primary PnP voltage regulators are enabled. From time 15 s onwards, also the secondary control layer is active. At time 25 s, the local load of DGU 3 is halved.

trollers in a PnP fashion for handling plugging in/out of DGUs has been presented.

In future research, communication delays [BFT08, MDGV14], will be included in the mathematical analysis. Furthermore, we will consider complex consensus controllers (e.g. PI regulators) for enhancing the convergence speed.

5.6 Appendix

5.6.1 Proof of Proposition 5.3

Proof. We start by proving point (ii). Since, from Proposition 5.1-(iii), $\mathrm{Ker}(\mathbb{M}) = H^1_\perp$, one has $\mathbb{M}\mathbb{R}^N = \mathbb{M}(H^1_\perp \oplus H^1) = \mathbb{M}H^1$. Furthermore, from Proposition 5.2, $P_{H^1}(D\mathbb{M}H^1) = H^1$. Proposition 5.1-(iv) applied to the Laplacian $\mathbb{L}$ shows that $\mathbb{L}(D\mathbb{M}\mathbb{R}^N) = H^1$, which is (ii).

For proving point (i), we recall that $\mathrm{Ker}(\mathbb{M}) = H^1_\perp$ and then $\mathrm{Ker}(\mathbb{L}D\mathbb{M}) \supseteq H^1_\perp$. From (ii) we have that $\dim(\mathrm{Im}(\mathbb{Q})) = N-1$. The equation $\dim(\mathrm{Im}(\mathbb{Q}))+\dim(\mathrm{Ker}(\mathbb{Q})) = N$ implies that $\dim(\mathrm{Ker}(\mathbb{Q})) = 1$. Since $\dim(H^1_\perp) = 1$, we have $\mathrm{Ker}(\mathbb{Q}) = H^1_\perp$.
In order to prove point (iii), we show that $\mathbb{Q}(H^1|H^1)$ is both surjective and injective [Lan87]. The surjectivity of $\mathbb{Q}$ on H^1 has been shown above when proving point (ii). For proving the injectivity, we need to check if it holds

$$\forall b \in H^1 \qquad \forall x, y \in H^1 \qquad (\mathbb{Q}x = b \text{ and } \mathbb{Q}y = b) \Rightarrow x = y.$$

Now, $\mathbb{Q}x = \mathbb{Q}y = b$ implies that $\mathbb{Q}(x - y) = 0$. It means that $x - y \in \mathrm{Ker}(\mathbb{Q}) = H^1_\perp$, therefore $\exists \alpha \in \mathbb{R}$ such that $x - y = \alpha \mathbf{1}_n$. However, since $x - y \in H^1$, $x - y = \alpha \mathbf{1}_n$ is verified only for $\alpha = 0$; this leads to $x = y$.

As regards statement (iv), we first consider the case in which Assumption 5.3 holds. Since $D = I$, we have that $\mathbb{Q} = \mathbb{L}\mathbb{M}$. Hence, $\mathbb{Q}$ is the product of two matrices, both positive semidefinite in the real sense. Moreover, since $\mathbb{L}$ and $\mathbb{M}$ are symmetric, they are positive semidefinite also in the complex sense [Pea65]. The proof concludes by applying Corollary 2.3 in [HH91], which states that the product of two complex positive semidefinite matrices is diagonalizable and has nonnegative real eigenvalues.

We now prove statement (iv) when Assumption 5.4 holds. Since D is diagonal with positive elements, the matrix $D^{\frac{1}{2}}$ verifying $D = D^{\frac{1}{2}}D^{\frac{1}{2}}$ exists and is invertible. Then, $\mathbb{Q}$ can be written as follows

$$\mathbb{Q} = D^{-\frac{1}{2}} \underbrace{D^{\frac{1}{2}}\mathbb{L}D^{\frac{1}{2}}}_{\mathcal{L}} \underbrace{D^{\frac{1}{2}}\mathbb{M}D^{\frac{1}{2}}}_{\mathcal{M}} D^{-\frac{1}{2}}. \tag{5.32}$$

Matrices $\mathcal{L}$ and $\mathcal{M}$ in (5.32) are positive semidefinite in the real sense and symmetric; hence, they are positive semidefinite also in the complex sense. Therefore, also in this case, we can use Corollary 2.3 in [HH91] to state that $\mathcal{LM}$ is has nonnegative real eigenvalues. Now, since $D^{-\frac{1}{2}}$ in (5.32) is symmetric, matrix $\mathcal{LM}$ is congruent to $\mathbb{Q}$. Thus, since under Assumption 5.4 $\mathcal{LM}$ is symmetric[6], by Sylvester's law of inertia [HJ12], the inertia of $\mathbb{Q}$ and $\mathcal{LM}$ coincide, i.e.

$$(i_+(\mathcal{LM}), 0, i_0(\mathcal{LM})) = (i_+(\mathbb{Q}), 0, i_0(\mathbb{Q})).$$

This concludes the proof of statement (iv) under Assumption 5.4.

Finally, point (v) follows from points (i) and (iv). Indeed, since $\mathbb{Q}$ is diagonalizable, the algebraic and geometric multiplicity of null eigenvalues coincide. From point (i), since $\dim(H_\perp^1) = 1$, we conclude that the zero eigenvalue of $\mathbb{Q}$ is unique. □

5.6.2 Proof of Theorem 5.1

We introduce a preliminary Lemma, partly taken from Theorem 19 in [CD12].

Lemma 5.1. *For $\mathcal{A} \in \mathbb{R}^{n\times n}$, let $\mathscr{M}_1$ and $\mathscr{M}_2$ be $\mathcal{A}$-invariant subspaces of $\mathbb{R}^n$ such that $dim(\mathscr{M}_1) = k$, $dim(\mathscr{M}_2) = n-k$ and $\mathbb{R}^n = \mathscr{M}_1 \oplus \mathscr{M}_2$. Then:*

(I) there is a matrix $T \in \mathbb{R}^{n\times n}$ such that $A = T^{-1}\mathcal{A}T$ has the block-diagonal structure

$$A = \left[\begin{array}{c|c} A_{11} & \mathbf{0}_{k\times(n-k)} \\ \hline \mathbf{0}_{(n-k)\times k} & A_{22} \end{array}\right], \tag{5.33}$$

with $A_{11} \in \mathbb{R}^{k\times k}$ and $A_{22} \in \mathbb{R}^{(n-k)\times(n-k)}$. In particular, if $\{b_1, \dots, b_k\}$ and $\{b_{k+1}, \dots, b_n\}$ are basis for $\mathscr{M}_1$ and $\mathscr{M}_2$, respectively, the transformation matrix T has the block structure

$$T = [b_1|\cdots|b_k|b_{k+1}|\cdots|b_n]. \tag{5.34}$$

Therefore, if $x \in \mathscr{M}_1$, then $T^{-1}x = \left[\begin{array}{c} \tilde{x}_1 \\ \hline 0 \end{array}\right]$ with $\tilde{x}_1 \in \mathbb{R}^k$. Similarly, if $x \in \mathscr{M}_2$, then $T^{-1}x = \left[\begin{array}{c} 0 \\ \hline \tilde{x}_2 \end{array}\right]$ with $\tilde{x}_2 \in \mathbb{R}^{n-k}$.

[6]Indeed, $(\mathcal{LM})^T = \mathcal{ML} = D^{\frac{1}{2}} \underbrace{\mathbb{M}D^{\frac{1}{2}}D^{\frac{1}{2}}\mathbb{L}}_{\mathbb{M}D\mathbb{L}=\mathbb{L}D\mathbb{M}} D^{\frac{1}{2}} = \mathcal{LM}$.

(II) The origin of $\dot{x} = \mathcal{A}x$ is GES on $\mathscr{M}_1$ if and only if the origin of $\dot{\tilde{x}}_1 = A_{11}\tilde{x}_1$ is GES. Moreover, parameters $\kappa, \eta > 0$ verifying $\|\tilde{x}_1(t)\| \leq \kappa e^{-\eta t}\|\tilde{x}_1(0)\|$, also guarantee $\|P_{\mathscr{M}_1}x(t)\| \leq \kappa e^{-\eta t}\|P_{\mathscr{M}_1}x(0)\|$.

Proof. For the proof of point (I), we defer the reader to the proof of Theorem 19 in [CD12].

The proof of point (II) directly follows from the block-diagonal structure of matrix A in (5.33). Indeed,

$$\dot{x} = \mathcal{A}x \Leftrightarrow \dot{\tilde{x}} = A\begin{bmatrix}\tilde{x}_1\\ \hline \tilde{x}_2\end{bmatrix} \Leftrightarrow \quad \begin{cases}\dot{\tilde{x}}_1 = A_{11}\tilde{x}_1\\ \dot{\tilde{x}}_2 = A_{22}\tilde{x}_2,\end{cases}$$

i.e. A_{11} is the matrix representation of the map $\mathcal{A}(\mathscr{M}_1|\mathscr{M}_2)$. In other words, studying the stability of $\mathcal{A}$ on $\mathscr{M}_1$ is equivalent to study the stability of A_{11}. Moreover, by construction, $P_{\mathscr{M}_1}(x) = T\begin{bmatrix}\tilde{x}_1\\ \hline 0\end{bmatrix}$. Then,

$$\|P_{\mathscr{M}_1}(x(t))\| \leq \|T\|\|\tilde{x}_1(t)\| \leq \|T\|\kappa e^{-\eta t}\|\tilde{x}_1(0)\|. \tag{5.35}$$

Since $\|\tilde{x}_1(0)\| \leq \|T^{-1}\|\|P_{\mathscr{M}_1}(x(0))\|$, inequality (5.35) becomes

$$\|P_{\mathscr{M}_1}(x)\| \leq \|T\|\kappa e^{-\eta t}\|\tilde{x}_1(0)\| \leq \kappa e^{-\eta t}\|P_{\mathscr{M}_1}(x(0))\|.$$

□

Proof of Theorem 5.1. Points (i) and (ii) of Proposition 5.3 show that subspaces H^1 and $H^1_\perp$ are $\mathbb{Q}$-invariant. Moreover, $\mathbb{R}^N = H^1 \oplus H^1_\perp$. It follows that Lemma 5.1 can be applied with $\mathscr{M}_1 = H^1$ and $\mathscr{M}_2 = H^1_\perp$. In particular, by means of point (I), we know that there exists a transformation matrix $T \in \mathbb{R}^{N\times N}$ such that the linear map $\mathbb{Q}$ can be represented as in (5.33). Denoting with $B^1 = \{b_1, \ldots, b_{N-1}\}$ and $B^1_\perp = \mathbf{1}_N$ the basis for H^1 and $H^1_\perp$, respectively, from (5.34), we have

$$T = [b_1|\cdots|b_{N-1}|\mathbf{1}_N].$$

Matrix $Q = T^{-1}\mathbb{Q}T$ is given by

$$Q = \begin{bmatrix}Q_{11} & \mathbf{0}\\ \mathbf{0} & q_{22}\end{bmatrix} \tag{5.36}$$

where $Q_{11} \in \mathbb{R}^{(N-1)\times(N-1)}$. Moreover, scalar $q_{22} = 0$ since, by construction, it represents the map $\mathbb{Q}(H^1_\perp|H^1_\perp)$ (see Proposition 5.3-(i)). We notice

that the representations of $\widehat{\mathbf{\Delta V}}$ and $\overline{\mathbf{\Delta V}}$ with respect to the basis $\mathcal{B}$ are $\tilde{v}_1 = T^{-1}\widehat{\mathbf{\Delta V}} = [\xi_1, \dots, \xi_{N-1}, 0]^T$ and $\tilde{v}_\perp = T^{-1}\overline{\mathbf{\Delta V}} = [0, \dots, 0, \xi_N]^T$, respectively. Now we prove that the origin of

$$\dot{\tilde{v}}_1 = -Q_{11}\tilde{v}_1 \tag{5.37}$$

is GES. Since Q and $\mathbb{Q}$ are similar matrices, they have the same eigenvalues. Therefore, by exploiting points (iv) and (v) of Proposition 5.3, one has that all the eigenvalues of Q_{11} are strictly positive. This proves that (5.37) is GES and, as shown in [CD12], the convergence rate is $-\lambda$, where λ is the minimal eigenvalue of Q_{11}. The remainder of the proof follows directly from point (II) of Lemma 5.1.

5.6.3 Proof of Theorem 5.2

We first present two Propositions which provide preliminary results that will be used to prove Theorem 5.2.

Proposition 5.9. *Subspaces $H^1 \times H^1$ and $H^1_\perp \times H^1_\perp$ are $\mathcal{Q}$-invariant.*

Proof. We first show that, for any vector $\hat{\mathbf{v}} = [\hat{\mathbf{v}}_\mathbf{1}^T \hat{\mathbf{v}}_\mathbf{2}^T]^T$, it holds $\mathcal{Q}\hat{\mathbf{v}} \in H^1 \times H^1$. Indeed,

$$\mathcal{Q}\hat{\mathbf{v}} = \begin{bmatrix} \mathbf{0}_N & -\mathbb{Q} \\ \Omega & -\Omega \end{bmatrix} \begin{bmatrix} \hat{\mathbf{v}}_\mathbf{1} \\ \hat{\mathbf{v}}_\mathbf{2} \end{bmatrix} = \begin{bmatrix} -\mathbb{Q}\hat{\mathbf{v}}_\mathbf{2} \\ \Omega(\hat{\mathbf{v}}_\mathbf{1} - \hat{\mathbf{v}}_\mathbf{2}) \end{bmatrix},$$

and, from Proposition 5.3-(iii), the rightmost vector belongs to $H^1 \times H^1$.

Similarly, for any vector $\bar{\mathbf{v}} = [\bar{\mathbf{v}}_\mathbf{1}^T \bar{\mathbf{v}}_\mathbf{2}^T]^T \in H^1_\perp \times H^1_\perp$, we have that

$$\mathcal{Q}\hat{\mathbf{v}} = \begin{bmatrix} \mathbf{0}_N & -\mathbb{Q} \\ \Omega & -\Omega \end{bmatrix} \begin{bmatrix} \bar{\mathbf{v}}_\mathbf{1} \\ \bar{\mathbf{v}}_\mathbf{2} \end{bmatrix} = \begin{bmatrix} \mathbf{0}_N \\ \Omega(\bar{\mathbf{v}}_\mathbf{1} - \bar{\mathbf{v}}_\mathbf{2}) \end{bmatrix}$$

and then $\mathcal{Q}\bar{\mathbf{v}} \in H^1_\perp \times H^1_\perp$. □

Proposition 5.10. *Matrix $\mathcal{Q}$ has two eigenvalues equal to zero and $-\omega_c$, respectively. All other eigenvalues have strictly negative real part.*

Proof. By definition, vector $[\mathbf{\Delta V}^T \mathbf{V}^T]^T \neq \mathbf{0}_{2N}$ is an eigenvector of $\mathcal{Q}$, if there exists λ_i such that

$$\begin{bmatrix} \mathbf{0} & -\mathbb{Q} \\ \Omega & -\Omega \end{bmatrix} \begin{bmatrix} \mathbf{\Delta V} \\ \mathbf{V} \end{bmatrix} = \lambda_i \begin{bmatrix} \mathbf{\Delta V} \\ \mathbf{V} \end{bmatrix}. \tag{5.38}$$

From (5.38), one gets:

$$-\mathbb{Q}\mathbf{V} = \lambda_i \boldsymbol{\Delta}\mathbf{V} \tag{5.39a}$$

$$\omega_c(\boldsymbol{\Delta}\mathbf{V} - \mathbf{V}) = \lambda_i \mathbf{V}. \tag{5.39b}$$

By isolating $\boldsymbol{\Delta}\mathbf{V}$ in (5.39b) and substituting it in (5.39a), we obtain

$$-\mathbb{Q}\mathbf{V} = \underbrace{\frac{\lambda_i(\lambda_i + \omega_c)}{\omega_c}}_{\hat{\lambda}_i} \mathbf{V}. \tag{5.40}$$

where $\hat{\lambda}_i$ are, by construction, eigenvalues of $-\mathbb{Q}$. From points (iv) and (v) of Proposition 5.3, we have

$$\hat{\lambda}_N = 0 \tag{5.41a}$$

$$\hat{\lambda}_i = -\gamma_i, \;\; \gamma_i > 0 \qquad i = 1, \ldots, N-1. \tag{5.41b}$$

From (5.41a) and (5.40), one has

$$\lambda_i(\lambda_i + \omega_c) = 0$$

and hence $\mathcal{Q}$ has a single eigenvalue equal to zero and an eigenvalue equal to $-\omega_c$. By substituting in (5.41b) the expression of $\hat{\lambda}_i$ in (5.40), one gets:

$$\frac{\lambda_i^2}{\omega_c} + \lambda_i + \gamma_i = 0 \quad i = 1, \ldots, N-1. \tag{5.42}$$

Since all the coefficients of the polynomial in (5.42) are strictly positive, we can conclude that matrix $\mathcal{Q}$ has $2(N-1)$ eigenvalues with $\mathrm{Re}(\lambda_i) < 0$. □

Proof of Theorem 5.2. Similarly to the proof of Theorem 5.1, we can exploit Lemma 5.1 with $\mathscr{M}_1 = H^1 \times H^1$ and $\mathscr{M}_2 = H^1_\perp \times H^1_\perp$. In fact, we know that (i) subspaces $H^1 \times H^1$ and $H^1_\perp \times H^1_\perp$ are $\mathcal{Q}$-invariant (see Proposition 5.9) and (ii) $\mathbb{R}^N \times \mathbb{R}^N = \mathscr{M}_1 \oplus \mathscr{M}_2$. Hence, there exists a transformation matrix $T \in \mathbb{R}^{2N \times 2N}$ such that the linear map $\mathcal{Q}$ has an equivalent block-diagonal representation of the form (5.33), i.e.

$$T^{-1}\mathcal{Q}T = Q = \left[\begin{array}{c|c} Q_{11} & \mathbf{0}_{2(N-1)\times 2} \\ \hline \mathbf{0}_{2\times 2(N-1)} & Q_{22} \end{array}\right], \tag{5.43}$$

with $Q_{11} \in \mathbb{R}^{2(N-1)\times 2(N-1)}$ and $Q_{22} \in \mathbb{R}^{2\times 2}$. By construction, matrices Q_{11} and Q_{22} in (5.43) represent the maps $\mathcal{Q}(\mathscr{M}_1|\mathscr{M}_1)$ and $\mathcal{Q}(\mathscr{M}_2|\mathscr{M}_2)$, respectively. In particular, in the light on the consideration made for system (5.27), we have that the eigenvalues of Q_{22} are zero and $-\omega_c$. Moreover, by construction, the eigenvalues of Q_{11} are the $2(N-1)$ eigenvalues of $\mathcal{Q}$ with strictly negative real part (see Proposition 5.10). □

5.6.4 On the eigenvalues of $\mathbb{Q} = \mathbb{L}D\mathbb{M}$

In this appendix, we provide an example which shows that, by pre- and post- multiplying a generic positive definite diagonal matrix by two positive semidefinite Laplacians (associated with graphs having different topologies), one can obtain a matrix with some negative eigenvalues.

Let us consider the graphs depicted in Figures 5.8 and 5.9.

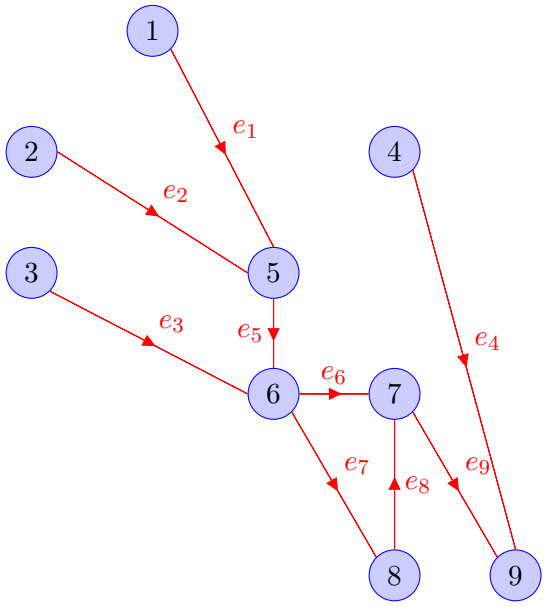

Figure 5.8: Topology of $\mathcal{G}_1$.

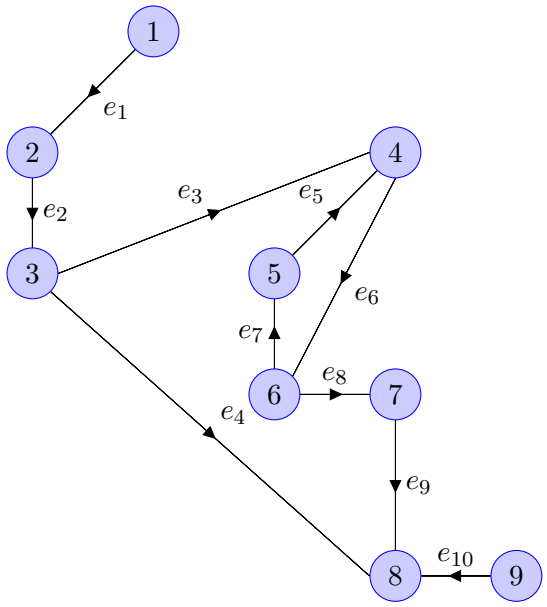

Figure 5.9: Topology of $\mathcal{G}_2$.

According to the assigned edge directions, the incidence matrices associated with $\mathcal{G}_1$ and $\mathcal{G}_2$ have the form

$$B_1 = \begin{bmatrix} -1 & 0 & 0 & 0 & 0 & 0 & 0 & 0 & 0 \\ 0 & -1 & 0 & 0 & 0 & 0 & 0 & 0 & 0 \\ 0 & 0 & -1 & 0 & 0 & 0 & 0 & 0 & 0 \\ 0 & 0 & 0 & -1 & 0 & 0 & 0 & 0 & 0 \\ 1 & 1 & 0 & 0 & -1 & 0 & 0 & 0 & 0 \\ 0 & 0 & 1 & 0 & 1 & -1 & -1 & 0 & 0 \\ 0 & 0 & 0 & 0 & 0 & 1 & 0 & 1 & -1 \\ 0 & 0 & 0 & 0 & 0 & 0 & 1 & -1 & 0 \\ 0 & 0 & 0 & 1 & 0 & 0 & 0 & 0 & 1 \end{bmatrix}$$

and

$$B_2 = \begin{bmatrix} -1 & 0 & 0 & 0 & 0 & 0 & 0 & 0 & 0 & 0 \\ 1 & -1 & 0 & 0 & 0 & 0 & 0 & 0 & 0 & 0 \\ 0 & 1 & -1 & -1 & 0 & 0 & 0 & 0 & 0 & 0 \\ 0 & 0 & 1 & 0 & 1 & -1 & 0 & 0 & 0 & 0 \\ 0 & 0 & 0 & 0 & -1 & 0 & 1 & 0 & 0 & 0 \\ 0 & 0 & 0 & 0 & 0 & 1 & -1 & -1 & 0 & 0 \\ 0 & 0 & 0 & 0 & 0 & 0 & 0 & 1 & -1 & 0 \\ 0 & 0 & 0 & 1 & 0 & 0 & 0 & 0 & 1 & 1 \\ 0 & 0 & 0 & 0 & 0 & 0 & 0 & 0 & 0 & -1 \end{bmatrix},$$

respectively. As regards the (positive) weights of the edges of $\mathcal{G}_1$ and $\mathcal{G}_2$, they are collected in the following diagonal matrices

$$W_1 = \text{diag}[0.8842, 0.8676, 0.9167, 0.8456, 0.2113, 0.0038, 0.4139, 0.1918, 0.9815]$$

and

$$W_2 = \text{diag}[0.6074, 0.9785, 0.8275, 0.3907, 0.4405, 0.2719, 0.1663, 0.8310, 0.3885, 0.8292].$$

At this point, we have all the ingredients for computing the Laplacians of $\mathcal{G}_1$ and $\mathcal{G}_2$ (called $\mathbb{L}$ and $\mathbb{M}$, respectively) as

$$\mathbb{L} = B_1 W_1 B_1^T =$$

$$\begin{bmatrix} 0.8842 & 0 & 0 & 0 & -0.8842 & 0 & 0 & 0 & 0 \\ 0 & 0.8676 & 0 & 0 & -0.8676 & 0 & 0 & 0 & 0 \\ 0 & 0 & 0.9167 & 0 & 0 & -0.9167 & 0 & 0 & 0 \\ 0 & 0 & 0 & 0.8456 & 0 & 0 & 0 & 0 & -0.8456 \\ -0.8842 & -0.8676 & 0 & 0 & 1.9631 & -0.2113 & 0 & 0 & 0 \\ 0 & 0 & -0.9167 & 0 & -0.2113 & 1.5458 & -0.0038 & -0.4139 & 0 \\ 0 & 0 & 0 & 0 & 0 & -0.0038 & 1.1771 & -0.1918 & -0.9815 \\ 0 & 0 & 0 & 0 & 0 & -0.4139 & -0.1918 & 0.6057 & 0 \\ 0 & 0 & 0 & -0.8456 & 0 & 0 & -0.9815 & 0 & 1.8271 \end{bmatrix}$$

and

$$\mathbb{M} = B_2 W_2 B_2^T =$$

$$\begin{bmatrix} 0.6074 & -0.6074 & 0 & 0 & 0 & 0 & 0 & 0 & 0 \\ -0.6074 & 1.5859 & -0.9785 & 0 & 0 & 0 & 0 & 0 & 0 \\ 0 & -0.9785 & 2.1967 & -0.8275 & 0 & 0 & 0 & -0.3907 & 0 \\ 0 & 0 & -0.8275 & 1.5399 & -0.4405 & -0.2719 & 0 & 0 & 0 \\ 0 & 0 & 0 & -0.4405 & 0.6068 & -0.1663 & 0 & 0 & 0 \\ 0 & 0 & 0 & -0.2719 & -0.1663 & 1.2691 & -0.8310 & 0 & 0 \\ 0 & 0 & 0 & 0 & 0 & -0.8310 & 1.2195 & -0.3885 & 0 \\ 0 & 0 & -0.3907 & 0 & 0 & 0 & -0.3885 & 1.6085 & -0.8292 \\ 0 & 0 & 0 & 0 & 0 & 0 & 0 & -0.8292 & 0.8292 \end{bmatrix}.$$

Next, we pick the positive definite diagonal matrix

$$D = \text{diag}[0.5977, 0.4297, 0.4937, 0.0058, 0.4643, 0.0005, 0.6299, 0.8209, 0.3597]$$

and pre- and post- multiply it by $\mathbb{L}$ and $\mathbb{M}$, respectively, thus obtaining

$$\mathbb{Q} = \mathbb{L}D\mathbb{M} =$$

$$\begin{bmatrix}
0.3210 & -0.3210 & 0 & 0.1808 & -0.2491 & 0.0683 & 0 & 0 & 0 \\
-0.2264 & 0.5912 & -0.3647 & 0.1774 & -0.2444 & 0.0670 & 0 & 0 & 0 \\
0 & -0.4428 & 0.9941 & -0.3744 & 0.0001 & -0.0006 & 0.0004 & -0.1768 & 0 \\
0 & 0 & -0.0040 & 0.0075 & -0.0021 & -0.0013 & 0 & 0.2522 & -0.2522 \\
-0.0946 & -0.2701 & 0.3647 & -0.4015 & 0.5531 & -0.1517 & 0.0001 & 0 & 0 \\
0 & 0.4428 & -0.8614 & 0.4175 & -0.0597 & 0.0193 & 0.1284 & -0.3688 & 0.2817 \\
0 & 0 & 0.0615 & 0.0000 & 0.0000 & -0.6161 & 0.9653 & -0.2485 & -0.1622 \\
0 & 0 & -0.1943 & 0.0001 & 0.0000 & 0.1001 & -0.3403 & 0.8467 & -0.4123 \\
0 & 0 & 0.0040 & -0.0075 & 0.0021 & 0.5150 & -0.7539 & -0.3048 & 0.5450
\end{bmatrix}.$$

Now, if we compute the eigenvalues of $\mathbb{Q}$, we get

$$\begin{aligned}
\text{eig}(\mathbb{Q}) = \{&1.3891 + 0.1564\text{i}, 1.3891 - 0.1564\text{i}, 0.9210 + 0.0000\text{i}, 0.5879 + 0.0000\text{i}, \\
&0.4509 + 0.0000\text{i}, 0.1057 + 0.0000\text{i}, \mathbf{-0.0002 + 0.0039}\text{i}, \\
&\mathbf{-0.0002 - 0.0039}\text{i}, 0.0000 + 0.0000\text{i}\}
\end{aligned}$$

that proves the desired result. This example led us to introduce Assumptions 5.3 and 5.4, which define conditions under which the eigenvalues of $\mathbb{Q}$ are always real and nonnegative.

5.6.5 Electrical and simulation parameters

In this appendix, we provide the electrical parameters of the simulation scenario described in Section 5.4.1.

Converter parameters			
DGU	R_t (Ω)	L_t (mH)	C_t (mF)
$\hat{\Sigma}_{[1]}$	0.2	1.8	2.2
$\hat{\Sigma}_{[2]}$	0.3	2	1.9
$\hat{\Sigma}_{[3]}$	0.1	2.2	1.7
$\hat{\Sigma}_{[4]}$	0.5	3	2.5
$\hat{\Sigma}_{[5]}$	0.4	1.2	2
$\hat{\Sigma}_{[6]}$	0.6	2.5	3
$\hat{\Sigma}_{[7]}$	0.3	2	2.1
Power line parameters			
Connected DGUs (i, j)	Resistance R_{ij} (Ω)	Inductance $L_{ij}(\mu$H)	
$(1, 2)$	0.05	2.1	
$(1, 3)$	0.07	1.8	
$(3, 4)$	0.06	1	
$(2, 4)$	0.04	2.3	
$(4, 5)$	0.08	1.8	
$(1, 6)$	0.1	2.5	
$(5, 6)$	0.08	3	
$(4, 7)$	0.09	2.3	
$(7, 5)$	0.05	2.4	

Table 5.1: Electrical parameters.

Part II

Scalable control of AC islanded microgrids

Chapter 6

Line-dependent plug-and-play control of AC islanded microgrids

Contents

6.1 Introduction 139
6.2 AC microgrid model 140
6.2.1 QSL model of a microgrid composed of 2 DGUs . 142
6.2.2 QSL model of a microgrid composed of N DGUs 145
6.3 Plug-and-play voltage and frequency control . . 146
6.3.1 Decentralized control scheme with integrators . . 146
6.3.2 Design of plug-and-play controllers 148
6.3.3 Plug-and-play operations 153

6.1 Introduction

In this chapter, we summarize the PnP control design approach for AC ImGs proposed in [RSFT15]. This review will be instrumental in describing the extensions proposed in Chapters 7, 8 and 9.

Authors of [RSFT15] developed a decentralized control schemes capable to guarantee voltage and frequency stability in ImGs with meshed topologies. The main features of this control design approach are reported hereafter.

1. It is decentralized; indeed, besides two global scalar quantities, the computation of a local controller uses only information about the corresponding DGU and lines connected to it (hence the name *line-dependent* design).

2. PnP operations are enabled, i.e. when a DGU wants to join/leave an existing network, only DGUs physically connected to it have to retune their local controllers.

3. The notions of (i) neutral interactions among DGUs [Lun92], and (ii) QSL approximations of power lines are exploited at the design stage in order to ensure collective ImG stability in spite of physical couplings between subsystems. Moreover, the synthesis of local regulators amounts to solve an LMI problem.

The chapter is organized as follows. The considered QSL-ImG model is discussed Section 6.2. In Section 6.3, we summarize the PnP design methodology and describe how PnP operations can be performed without spoiling the stability of the ImG.

In the remainder of this chapter, we use the same notations as in [RSFT15].

6.2 AC microgrid model

Following the approach in [RSFT15], we start by focusing on the ImG composed of two parallel DGUs and described by the set of equations (2.3) (see Figure 2.2). Recalling Assumption 2.2 (which ensures $i_{ij}^{abc}(t) = -i_{ji}^{abc}(t)$, $\forall t \geq 0$), from (2.3), one obtains the following linear system

$$\begin{aligned} \dot{x}(t) &= Ax(t) + Bu(t) + Md(t) \\ y(t) &= Cx(t) \end{aligned}$$

where $x = [V_i^d, V_i^q, I_{ti}^d, I_{ti}^q, I_{ij}^d, I_{ij}^q, I_{ji}^d, I_{ji}^q, V_j^d, V_j^q, I_{tj}^d, I_{tj}^q]^T$, $u = [V_{ti}^d, V_{ti}^q, V_{tj}^d, V_{tj}^q]^T$, $d = [I_{Li}^d, I_{Li}^q, I_{Lj}^d, I_{Lj}^q]^T$, $y = [V_i^d, V_i^q, V_j^d, V_j^q]^T$ represent the state, input, disturbance and output of the system, respectively. Matrices A, B, M and

C are shown in the following.

$$A = \begin{bmatrix}
0 & \omega_0 & \frac{k_i}{C_{ti}} & 0 & \frac{1}{C_{ti}} & 0 & 0 & 0 & 0 & 0 & 0 & 0 \\
-\omega_0 & 0 & 0 & \frac{k_i}{C_{ti}} & 0 & \frac{1}{C_{ti}} & 0 & 0 & 0 & 0 & 0 & 0 \\
-\frac{k_i}{L_{ti}} & 0 & -\frac{R_{ti}}{L_{ti}} & \omega_0 & 0 & 0 & 0 & 0 & 0 & 0 & 0 & 0 \\
0 & -\frac{k_i}{L_{ti}} & -\omega_0 & -\frac{R_{ti}}{L_{ti}} & 0 & 0 & 0 & 0 & 0 & 0 & 0 & 0 \\
-\frac{1}{L_{ij}} & 0 & 0 & 0 & -\frac{R_{ij}}{L_{ij}} & \omega_0 & 0 & 0 & \frac{1}{L_{ij}} & 0 & 0 & 0 \\
0 & -\frac{1}{L_{ij}} & 0 & 0 & -\omega_0 & -\frac{R_{ij}}{L_{ij}} & 0 & 0 & 0 & \frac{1}{L_{ij}} & 0 & 0 \\
\frac{1}{L_{ji}} & 0 & 0 & 0 & -\frac{R_{ji}}{L_{ji}} & \omega_0 & 0 & 0 & -\frac{1}{L_{ji}} & 0 & 0 & 0 \\
0 & \frac{1}{L_{ji}} & 0 & 0 & -\omega_0 & -\frac{R_{ji}}{L_{ji}} & 0 & 0 & 0 & -\frac{1}{L_{ji}} & 0 & 0 \\
0 & 0 & 0 & 0 & 0 & 0 & \frac{1}{C_{tj}} & 0 & 0 & \omega_0 & \frac{k_j}{C_{tj}} & 0 \\
0 & 0 & 0 & 0 & 0 & 0 & 0 & \frac{1}{C_{tj}} & -\omega_0 & 0 & 0 & \frac{k_j}{C_{tj}} \\
0 & 0 & 0 & 0 & 0 & 0 & 0 & 0 & -\frac{k_j}{L_{tj}} & 0 & -\frac{R_{tj}}{L_{tj}} & \omega_0 \\
0 & 0 & 0 & 0 & 0 & 0 & 0 & 0 & 0 & -\frac{k_j}{L_{tj}} & -\omega_0 & -\frac{R_{tj}}{L_{tj}}
\end{bmatrix}, \tag{6.1}$$

$$B = \begin{bmatrix}
0 & 0 & 0 & 0 \\
0 & 0 & 0 & 0 \\
\frac{1}{L_{ti}} & 0 & 0 & 0 \\
0 & \frac{1}{L_{ti}} & 0 & 0 \\
0 & 0 & 0 & 0 \\
0 & 0 & 0 & 0 \\
0 & 0 & 0 & 0 \\
0 & 0 & 0 & 0 \\
0 & 0 & 0 & 0 \\
0 & 0 & 0 & 0 \\
0 & 0 & \frac{1}{L_{tj}} & 0 \\
0 & 0 & 0 & \frac{1}{L_{tj}}
\end{bmatrix}, C^T = \begin{bmatrix}
1 & 0 & 0 & 0 \\
0 & 1 & 0 & 0 \\
0 & 0 & 0 & 0 \\
0 & 0 & 0 & 0 \\
0 & 0 & 0 & 0 \\
0 & 0 & 0 & 0 \\
0 & 0 & 0 & 0 \\
0 & 0 & 0 & 0 \\
0 & 0 & 1 & 0 \\
0 & 0 & 0 & 1 \\
0 & 0 & 0 & 0 \\
0 & 0 & 0 & 0
\end{bmatrix}, M = \begin{bmatrix}
\frac{1}{C_{ti}} & 0 & 0 & 0 \\
0 & \frac{1}{C_{ti}} & 0 & 0 \\
0 & 0 & 0 & 0 \\
0 & 0 & 0 & 0 \\
0 & 0 & 0 & 0 \\
0 & 0 & 0 & 0 \\
0 & 0 & 0 & 0 \\
0 & 0 & 0 & 0 \\
0 & 0 & \frac{1}{C_{tj}} & 0 \\
0 & 0 & 0 & \frac{1}{C_{tj}} \\
0 & 0 & 0 & 0 \\
0 & 0 & 0 & 0
\end{bmatrix}. \tag{6.2}$$

From (6.1) and (6.2), it can be seen that DGUs state variables (i.e. inverter output currents and PCC voltages) depend on line currents (i.e. the states of the lines), thus making the system quite difficult to handle. As discussed in Chapter 3 for the case of DC mGs, it is desirable to obtain a simplified model in which DGUs states depend exclusively on each other, without being influenced by states of the lines. To this aim, QSL approximations are exploited.

6.2.1 QSL model of a microgrid composed of 2 DGUs

We recall that assuming QSL approximations for power line dynamics amounts to set, in (2.3a)-(2.3f) [RSFT15]

$$\frac{\mathrm{d}}{\mathrm{d}t}I_{ij}^{d}=0,\qquad \frac{\mathrm{d}}{\mathrm{d}t}I_{ij}^{q}=0,\qquad \frac{\mathrm{d}}{\mathrm{d}t}I_{ji}^{d}=0,\qquad \frac{\mathrm{d}}{\mathrm{d}t}I_{ji}^{q}=0.$$

At this point, lines dynamics can be disregarded and (2.3c)-(2.3d) yield

$$I_{ij}^{dq}=\frac{V_{j}^{dq}}{(R_{ij}+\mathrm{i}\omega_0 L_{ij})}-\frac{V_{i}^{dq}}{(R_{ij}+\mathrm{i}\omega_0 L_{ij})} \tag{6.3a}$$

$$I_{ji}^{dq}=\frac{V_{i}^{dq}}{(R_{ji}+\mathrm{i}\omega_0 L_{ji})}-\frac{V_{j}^{dq}}{(R_{ji}+\mathrm{i}\omega_0 L_{ji})} \tag{6.3b}$$

Remark 6.1. *From a practical point of view, QSL approximation assumes lines are at AC steady state, even if their currents and voltages are not sinusoidal. This is evident from* (6.3)*, which express that voltage drops on lines are directly proportional to currents via line impedances* $Z_{ij}=R_{ij}+\mathrm{i}\omega_0 L_{ij}$ *and* $Z_{ji}=Z_{ij}$ *evaluated at* ω_0*, as in the AC steady state case.*

By replacing (6.3) in (2.3a)-(2.3b) and (2.3e)-(2.3f), one gets the following QSL model for DGU i:

$$\text{DGU } i:\begin{cases}\dfrac{\mathrm{d}}{\mathrm{d}t}V_{i}^{dq}=-\mathrm{i}\omega_0 V_{i}^{dq}+\dfrac{I_{ti}^{dq}}{C_{ti}}-\dfrac{I_{Li}^{dq}}{C_{ti}}+\dfrac{1}{C_{ti}}\left(\dfrac{V_{j}^{dq}}{R_{ij}+\mathrm{i}\omega_0 L_{ij}}-\dfrac{V_{i}^{dq}}{R_{ij}+\mathrm{i}\omega_0 L_{ij}}\right)\\ \dfrac{\mathrm{d}}{\mathrm{d}t}I_{i}^{dq}=-\left(\dfrac{R_{ti}}{L_{ti}}+\mathrm{i}\omega_0\right)I_{ti}^{dq}-\dfrac{V_{i}^{dq}}{L_{ti}}+\dfrac{V_{ti}^{dq}}{L_{ti}}\end{cases} \tag{6.4}$$

Notice that the model of DGU j is obtained by switching indices i and j.

Now, model (6.4) can be rewritten in the following compact form

$$\Sigma_{[i]}^{\mathrm{DGU}}:\begin{cases}\dot{x}_{[i]}(t)=A_{ii}x_{[i]}(t)+B_i u_{[i]}(t)+M_i d_{[i]}(t)+\xi_{[i]}(t)\\ y_{[i]}(t)=C_i x_{[i]}(t)\\ z_{[i]}(t)=H_i y_{[i]}(t)\end{cases} \tag{6.5}$$

where $x_{[i]}=[V_i^d,V_i^q,I_{ti}^d,I_{ti}^q]^T$, $u_{[i]}=[V_{ti}^d,V_{ti}^q]^T$, $d_{[i]}=[I_{Li}^d,I_{Li}^q]^T$, $z_{[i]}=[V_i^d,V_i^q]^T$ are, respectively, the state, the control input, the exogenous input

and the controlled variables. The measurable output $y_{[i]}$ is chosen equal to the state, i.e. $y_{[i]} = x_{[i]}$. Moreover, we highlight that the contribution $\xi_{[i]}(t) = A_{ij}x_{[j]}$ represents the coupling term with DGU j.

As regards the power lines dynamics, they are still described by equations (2.3c)-(2.3d). Hence, line ij is represented by the system:

$$\Sigma^{\text{Line}}_{[ij]} : \left\{ \dot{x}_{[l,ij]}(t) = A_{ll,ij}\, x_{[l,ij]}(t) + A_{li,ij}\, x_{[i]}(t) + A_{lj,ij}\, x_{[j]}(t) \right. \tag{6.6}$$

where $x_{[l,ij]} = [I^d_{ij}, I^q_{ij}]^T$ is the state of line ij.

We highlight that the systems associated with DGU j and line ji can be obtained from (6.5) and (6.6), by switching indices i and j.

At this point, one can write the overall QSL model of the ImG shown in Figure 2.2, that is

$$\begin{aligned}
\begin{bmatrix} \dot{x}_{[i]} \\ \dot{x}_{[j]} \\ \dot{x}_{[l,ij]} \\ \dot{x}_{[l,ji]} \end{bmatrix} &= \begin{bmatrix} A_{ii} & A_{ij} & 0 & 0 \\ A_{ji} & A_{jj} & 0 & 0 \\ A_{li,ij} & A_{lj,ij} & A_{ll,ij} & 0 \\ A_{li,ji} & A_{lj,ji} & 0 & A_{ll,ji} \end{bmatrix} \begin{bmatrix} x_{[i]} \\ x_{[j]} \\ x_{[l,ij]} \\ x_{[l,ji]} \end{bmatrix} + \begin{bmatrix} B_i & 0 \\ 0 & B_j \\ 0 & 0 \end{bmatrix} \begin{bmatrix} u_{[i]} \\ u_{[j]} \end{bmatrix} + \\
&\quad + \begin{bmatrix} M_i & 0 \\ 0 & M_j \\ 0 & 0 \end{bmatrix} \begin{bmatrix} d_{[i]} \\ d_{[j]} \end{bmatrix} \\
\begin{bmatrix} y_{[i]} \\ y_{[j]} \end{bmatrix} &= \begin{bmatrix} C_i & 0 & 0 & 0 \\ 0 & C_j & 0 & 0 \end{bmatrix} \begin{bmatrix} x_{[i]} \\ x_{[j]} \\ x_{[l,ij]} \\ x_{[l,ji]} \end{bmatrix} \\
\begin{bmatrix} z_{[i]} \\ z_{[j]} \end{bmatrix} &= \begin{bmatrix} H_i & 0 \\ 0 & H_j \end{bmatrix} \begin{bmatrix} y_{[i]} \\ y_{[j]} \end{bmatrix}
\end{aligned} \tag{6.7}$$

The blocks of (6.7) are shown in the following ($i \in \{1, 2\}$, $i \neq j$)

$$A_{ii} = \begin{bmatrix} -\frac{1}{C_{ti}} \left(\frac{R_{ij}}{|Z_{ij}|^2} \right) & \omega_0 - \frac{1}{C_{ti}} \left(\frac{X_{ij}}{|Z_{ij}|^2} \right) & \frac{k_i}{C_{ti}} & 0 \\ -\omega_0 + \frac{1}{C_{ti}} \left(\frac{X_{ij}}{|Z_{ij}|^2} \right) & -\frac{1}{C_{ti}} \left(\frac{R_{ij}}{|Z_{ij}|^2} \right) & 0 & \frac{k_i}{C_{ti}} \\ -\frac{k_i}{L_{ti}} & 0 & -\frac{R_{ti}}{L_{ti}} & \omega_0 \\ 0 & -\frac{k_i}{L_{ti}} & -\omega_0 & -\frac{R_{ti}}{L_{ti}} \end{bmatrix},$$

$$A_{ij} = \frac{1}{C_{ti}} \begin{bmatrix} \frac{R_{ij}}{|Z_{ij}|^2} & \frac{X_{ij}}{|Z_{ij}|^2} & 0 & 0 \\ -\frac{X_{ij}}{|Z_{ij}|^2} & \frac{R_{ij}}{|Z_{ij}|^2} & 0 & 0 \\ 0 & 0 & 0 & 0 \\ 0 & 0 & 0 & 0 \end{bmatrix}, \quad B_i = \begin{bmatrix} 0 & 0 \\ 0 & 0 \\ \frac{1}{L_{ti}} & 0 \\ 0 & \frac{1}{L_{ti}} \end{bmatrix},$$

$$M_i = \begin{bmatrix} -\frac{1}{C_{ti}} & 0 \\ 0 & -\frac{1}{C_{ti}} \\ 0 & 0 \\ 0 & 0 \end{bmatrix}, \quad C_i = \begin{bmatrix} 1 & 0 & 0 & 0 \\ 0 & 1 & 0 & 0 \\ 0 & 0 & 1 & 0 \\ 0 & 0 & 0 & 1 \end{bmatrix}, \quad H_i = \begin{bmatrix} 1 & 0 & 0 & 0 \\ 0 & 1 & 0 & 0 \end{bmatrix},$$

$$A_{li,ij} = \begin{bmatrix} -\frac{1}{L_{ij}} & 0 & 0 & 0 \\ 0 & -\frac{1}{L_{ij}} & 0 & 0 \end{bmatrix}, \quad A_{lj,ij} = \begin{bmatrix} \frac{1}{L_{ij}} & 0 & 0 & 0 \\ 0 & \frac{1}{L_{ij}} & 0 & 0 \end{bmatrix},$$

$$A_{ll,ij} = \begin{bmatrix} -\frac{R_{ij}}{L_{ij}} & \omega_0 \\ -\omega_0 & -\frac{R_{ij}}{L_{ij}} \end{bmatrix},$$

where $X_{ij} = \omega_0 L_{ij}$, and $|Z_{ij}|$ denotes the modulus of Z_{ij}, i.e. $|Z_{ij}| = \sqrt{R_{ij}^2 + X_{ij}^2}$.

Remark 6.2. *Similarly to what we observed in Remark 3.1 for DC mGs, one has that, since matrix A has the following block lower triangular form*

$$A = \left[\begin{array}{cc|cc} A_{ii} & A_{ij} & 0 & 0 \\ A_{ji} & A_{jj} & 0 & 0 \\ \hline A_{li,ij} & A_{lj,ij} & A_{ll,ij} & 0 \\ A_{li,ji} & A_{lj,ji} & 0 & A_{ll,ji} \end{array}\right], \tag{6.8}$$

its eigenvalues are given by the union of the eigenvalues of the diagonal blocks. In other words,

$$\begin{aligned} \mathrm{eig}(A) &= \mathrm{eig}\begin{pmatrix} A_{ii} & A_{ij} \\ A_{ji} & A_{jj} \end{pmatrix} \bigcup \mathrm{eig}\begin{pmatrix} A_{ll,ij} & 0 \\ 0 & A_{ll,ji} \end{pmatrix} = \\ &= \mathrm{eig}\begin{pmatrix} A_{ii} & A_{ij} \\ A_{ji} & A_{jj} \end{pmatrix} \bigcup \mathrm{eig}(A_{ll,ij}) \bigcup \mathrm{eig}(A_{ll,ji}), \end{aligned}$$

where $A_{ll,ij} = A_{ll,ji}$. Since lines parameters are positive, the line dynamics is always asymptotically stable. As a consequence, asymptotic stability

of the overall system (6.8) *depends on the stability of local DGUs interconnected through the QSL model* (6.3)*. Hence, if decentralized controllers* $u_{[\star]} = k_{[\star]}(y_{[\star]})$*,* $\star \in \{i, j\}$ *are designed so as to stabilize the connection of the DGUs, then the overall closed-loop model of the ImG is asymptotically stable as well.*

6.2.2 QSL model of a microgrid composed of N DGUs

At this point, the dynamic system developed for an ImG with two DGUs can be generalized to a network composed of an arbitrary number (say N) of subsystems. To this aim, we introduce the set $\mathcal{V} = \{1, ..., N\}$, and call two DGUs neighbors if there is a power line connecting their PCCs. Moreover, we define $\mathcal{N}_i \subset \mathcal{V}$ as the set of neighbors of the i-th DGU.

The dynamic system associated with DGU i can be simply retrieved from model (6.4), replacing I_{ij}^{dq} with $\sum_{j\in\mathcal{N}_i} I_{ij}^{dq}$, i.e.

$$\text{DGU } i\text{:} \begin{cases} \dfrac{\mathrm{d}}{\mathrm{d}t} V_i^{dq} = -\mathrm{i}\omega_0 V_i^{dq} + \dfrac{I_{ti}^{dq}}{C_{ti}} - \dfrac{I_{Li}^{dq}}{C_{ti}} + \displaystyle\sum_{j\in\mathcal{N}_i} \frac{1}{C_{ti}} \left(\frac{V_j^{dq} - V_i^{dq}}{Z_{ij}} \right) & \text{(6.9a)} \\ \dfrac{\mathrm{d}}{\mathrm{d}t} I_i^{dq} = -\left(\dfrac{R_{ti}}{L_{ti}} + \mathrm{i}\omega_0 \right) I_{ti}^{dq} - \dfrac{V_i^{dq}}{L_{ti}} + \dfrac{V_{ti}^{dq}}{L_{ti}} & \text{(6.9b)} \end{cases}$$

Model (6.9) can still be written in the more compact form (6.5), inserting $\sum_{j\in\mathcal{N}_i} A_{ij} x_{[j]}(t)$ instead of $\xi_{[i]} = A_{ij} x_{[j]}(t)$. All matrices appearing in this new model do not change, with the exception of A_{ii} that becomes

$$A_{ii} = \begin{bmatrix} -\frac{1}{C_{ti}} \left(\sum_{j\in\mathcal{N}_i} \frac{R_{ij}}{|Z_{ij}|^2} \right) & \omega_0 - \frac{1}{C_{ti}} \left(\sum_{j\in\mathcal{N}_i} \frac{X_{ij}}{|Z_{ij}|^2} \right) & \frac{k_i}{C_{ti}} & 0 \\ -\omega_0 + \frac{1}{C_{ti}} \left(\sum_{j\in\mathcal{N}_i} \frac{X_{ij}}{|Z_{ij}|^2} \right) & -\frac{1}{C_{ti}} \left(\sum_{j\in\mathcal{N}_i} \frac{R_{ij}}{|Z_{ij}|^2} \right) & 0 & \frac{k_i}{C_{ti}} \\ -\frac{k_i}{L_{ti}} & 0 & -\frac{R_{ti}}{L_{ti}} & \omega_0 \\ 0 & -\frac{k_i}{L_{ti}} & -\omega_0 & -\frac{R_{ti}}{L_{ti}} \end{bmatrix} \tag{6.10}$$

Next, we can write the overall QSL-ImG model as follows

$$\begin{aligned}\dot{\mathbf{x}}(t) &= \mathbf{A}\mathbf{x}(t) + \mathbf{B}\mathbf{u}(t) + \mathbf{M}\mathbf{d}(t)\\ \mathbf{y}(t) &= \mathbf{C}\mathbf{x}(t)\\ \mathbf{z}(t) &= \mathbf{H}\mathbf{y}(t)\end{aligned} \tag{6.11}$$

where $\mathbf{x} = [x_{[1]}^T, \dots, x_{[N]}^T]^T \in \mathbb{R}^{4N}$, $\mathbf{u} = [u_{[1]}^T, \dots, u_{[N]}^T]^T \in \mathbb{R}^{2N}$, $\mathbf{d} = [d_{[1]}^T, \dots, d_{[N]}^T]^T \in \mathbb{R}^{2N}$, $\mathbf{y} = [y_{[1]}^T, \dots, y_{[N]}^T]^T \in \mathbb{R}^{4N}$ and $\mathbf{z} = [z_{[1]}^T, \dots, z_{[N]}^T]^T \in \mathbb{R}^{2N}$ are the state, the control input, the exogenous input, the measured variables and the controlled variables of the overall system of DGUs. Matrices $\mathbf{A}$, $\mathbf{B}$, $\mathbf{M}$, $\mathbf{C}$ and $\mathbf{H}$ are reported in Appendix A.3 of [RSFT14].

Remark 6.3. *Models in the form* (6.9) *represent DGUs whose electrical scheme is shown in the dashed box of Figure 2.2. In this scheme, local loads appear only at the PCC of each DGU. For this reason, as for the case of DC mGs (see Remark 3.3), also ImGs composed of DGUs modeled as in* (6.9) *will be referred to as load-connected. We recall that methods for mapping different interconnections of DGUs and load into load-connected networks have been proposed, e.g., in [DB13]. In Chapter 8 we propose a novel approximate network reduction method based on Kron reduction.*

6.3 Plug-and-play voltage and frequency control

6.3.1 Decentralized control scheme with integrators

PCC voltages, collected in vector $\mathbf{z}$, track their set-point $\mathbf{z_{ref}}$, when disturbance $\mathbf{d}(t)$ is constant, if it is guaranteed

$$\lim_{t\to\infty} (\mathbf{z_{ref}}(t) - \mathbf{z}(t)) = \mathbf{0}$$

To this aim, the QSL-ImG model (6.11) is augmented with integrators (see Figure 6.1). Steady state error $\mathbf{z_{ref}} - \mathbf{z}$ is zeroed if the following condition is verified

$$\begin{aligned}\mathbf{0} &= \mathbf{A}\bar{\mathbf{x}} + \mathbf{B}\bar{\mathbf{u}} + \mathbf{M}\bar{\mathbf{d}}\\ \mathbf{z_{ref}} &= \mathbf{H}\mathbf{C}\bar{\mathbf{x}}\end{aligned} \tag{6.12}$$

$$\Gamma \begin{bmatrix}\bar{\mathbf{x}}\\ \bar{\mathbf{u}}\end{bmatrix} = \begin{bmatrix}\mathbf{0} & -\mathbf{M}\\ \mathbf{I} & \mathbf{0}\end{bmatrix} \begin{bmatrix}\mathbf{z_{ref}}\\ \bar{\mathbf{d}}\end{bmatrix}, \qquad \Gamma = \begin{bmatrix}\mathbf{A} & \mathbf{B}\\ \mathbf{HC} & \mathbf{0}\end{bmatrix} \in \mathbb{R}^{6N\times 6N}, \tag{6.13}$$

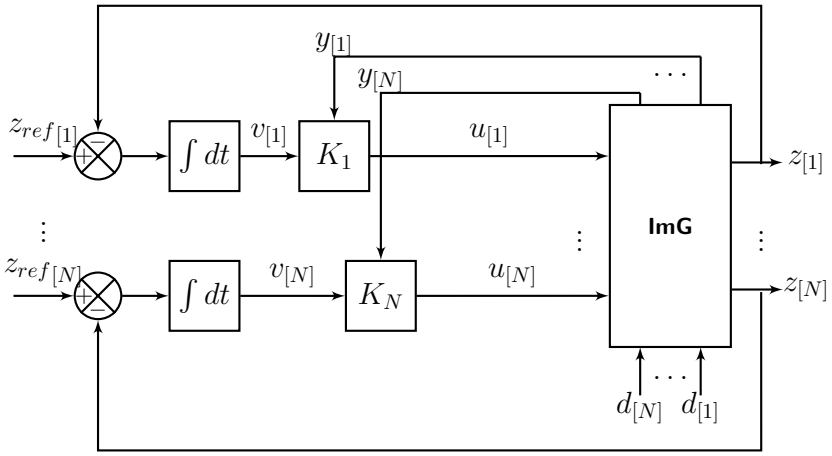

Figure 6.1: Control scheme with integrators for the overall AC ImG.

where $\bar{\mathbf{x}}$ and $\bar{\mathbf{u}}$ denotes equilibrium states and inputs, and $\bar{\mathbf{d}}$ is a constant disturbance. From [RSFT15], given a constant set-point $\mathbf{z_{ref}}$ and a constant disturbance $\bar{\mathbf{d}}$, equilibrium vectors $\bar{\mathbf{x}}$ and $\bar{\mathbf{u}}$ satisfying (6.13) always exist[1].

As shown by Figure 6.1, the dynamics of the integrator of DGU i is

$$\dot{v}_{[i]}(t) = e_{[i]}(t) = z_{ref\,[i]}(t) - z_{[i]}(t) = z_{ref\,[i]}(t) - H_i C_i\, x_{[i]}(t).$$

Consequently, the DGU model augmented with integrators has the form

$$\hat{\Sigma}^{\text{DGU}}_{[i]} : \begin{cases} \dot{\hat{x}}_{[i]}(t) = \hat{A}_{ii}\hat{x}_{[i]}(t) + \hat{B}_i u_{[i]}(t) + \hat{M}_i \hat{d}_{[i]}(t) + \xi_{[i]}(t) \\ \hat{y}_{[i]}(t) = \hat{C}_i \hat{x}_{[i]}(t) \\ z_{[i]}(t) = \hat{H}_i \hat{y}_{[i]}(t) \end{cases} \tag{6.14}$$

where $\hat{x}_{[i]} = [x^T{}_{[i]}, v_i^d, v_i^q]^T \in \mathbb{R}^6$, and $\hat{y}_{[i]} = \hat{x}_{[i]} \in \mathbb{R}^6$ are, respectively, the state and the measurable output; $\hat{d}_{[i]} = [d_{[i]}^T, z_{ref}{}_{[i]}^T]^T \in \mathbb{R}^4$ represents the augmented exogenous signals (load current and set-point, in dq reference frame), and term $\xi_{[i]}(t) = \sum_{j\in\mathcal{N}_i} \hat{A}_{ij}\hat{x}_{[j]}(t)$ accounts for the couplings with neighboring DGUs. The matrices of (6.14) are shown below

$$\hat{A}_{ii} = \begin{bmatrix} A_{ii} & 0 \\ -H_i C_i & 0 \end{bmatrix}, \qquad \hat{A}_{ij} = \begin{bmatrix} A_{ij} & 0 \\ 0 & 0 \end{bmatrix}, \qquad \hat{B}_i = \begin{bmatrix} B_i \\ 0 \end{bmatrix},$$

$$\hat{C}_i = \begin{bmatrix} C_i & 0 \\ 0 & I \end{bmatrix}, \qquad \hat{M}_i = \begin{bmatrix} M_i & 0 \\ 0 & I_2 \end{bmatrix}, \qquad \hat{H}_i = \begin{bmatrix} H_i & 0 \end{bmatrix}. \tag{6.15}$$

[1]The proof, provided in [RSFT15], exploits positivity of line parameters R_{ij} and L_{ij}.

In [RSFT15] it is shown that the pair $(\hat{A}_{ii}, \hat{B}_i)$ is controllable; this is proved exploiting once more positivity of line parameters. Therefore, it is possible to stabilize the augmented model (6.14), through the action of a control scheme.

The overall augmented system, obtained from (6.14), is

$$\begin{cases} \dot{\hat{\mathbf{x}}}(t) = \hat{\mathbf{A}}\hat{\mathbf{x}}(t) + \hat{\mathbf{B}}\mathbf{u}(t) + \hat{\mathbf{M}}\hat{\mathbf{d}}(t) \\ \hat{\mathbf{y}}(t) = \hat{\mathbf{C}}\hat{\mathbf{x}}(t) \\ \mathbf{z}(t) = \hat{\mathbf{H}}\hat{\mathbf{y}}(t) \end{cases} \tag{6.16}$$

where $\hat{\mathbf{x}} = [\hat{x}_{[1]}^T, ..., \hat{x}_{[N]}^T]^T$, $\hat{\mathbf{y}} = [\hat{y}_{[1]}^T, ..., \hat{y}_{[N]}^T]^T$ and $\hat{\mathbf{d}} = [\hat{d}_{[1]}^T, ..., \hat{d}_{[N]}^T]^T$, while matrices $\hat{\mathbf{A}}$, $\hat{\mathbf{B}}$, $\hat{\mathbf{C}}$, $\hat{\mathbf{M}}$, and $\hat{\mathbf{H}}$ are obtained from systems (6.14).

6.3.2 Design of plug-and-play controllers

This section is devoted to the description of the decentralized PnP control scheme ensuring asymptotic stability for the augmented system (6.16). Local controllers $\mathcal{C}_{[i]}$ for each DGU $\hat{\Sigma}_{[i]}^{\text{DGU}}$ are defined as follows:

$$\mathcal{C}_{[i]}: \qquad u_{[i]}(t) = K_i\hat{y}_{[i]}(t) = K_i\hat{x}_{[i]}(t), \tag{6.17}$$

where $K_i \in \mathbb{R}^{2\times 6}$. As shown in Figure 6.2, controllers $\mathcal{C}_{[i]}$, $i \in \mathcal{V}$ are decentralized because their outputs $u_{[i]}$ depend exclusively on the states of the corresponding systems $\hat{\Sigma}_{[i]}^{\text{DGU}}$.

The closed-loop model of each subsystem $\hat{\Sigma}_{[i]}^{\text{DGU}}$ is obtained from (6.14) with the substitution $u_{[i]} = K_i\hat{x}_{[i]}$.

If we neglect coupling terms with other DGUs, we get the following subsystem

$$\begin{cases} \dot{\hat{x}}_{[i]}(t) = (\hat{A}_{ii} + \hat{B}_iK_i)\hat{x}_{[i]}(t) + \hat{M}_i\hat{d}_i(t) \\ \hat{y}_{[i]}(t) = \hat{C}_i\hat{x}_{[i]}(t) \\ z_{[i]}(t) = \hat{H}_i\hat{y}_{[i]}(t) \end{cases} \tag{6.18}$$

From Lyapunov theory, the asymptotic stability of subsystem (6.18) is ensured if there exists a symmetric matrix $P_i \in \mathbb{R}^{6\times 6}, P_i \geq 0$ such that

$$(\hat{A}_{ii} + \hat{B}_iK_i)^TP_i + P_i(\hat{A}_{ii} + \hat{B}_iK_i) < 0. \tag{6.19}$$

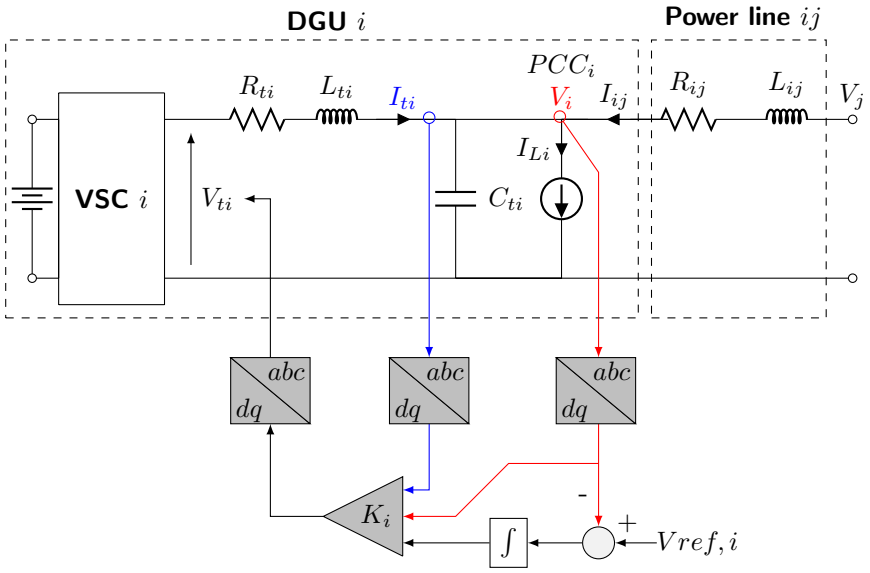

Figure 6.2: AC ImG - Single-phase equivalent scheme of DGU i, power line ij, and local PnP voltage and frequency controller.

From (6.16) and (6.17), one gets the overall closed-loop system with couplings

$$\begin{cases} \dot{\hat{\mathbf{x}}}(t) = (\hat{\mathbf{A}} + \hat{\mathbf{B}}\mathbf{K})\hat{\mathbf{x}}(t) + \hat{\mathbf{M}}\hat{\mathbf{d}}(t) \\ \hat{\mathbf{y}}(t) = \hat{\mathbf{C}}\hat{\mathbf{x}}(t) \\ \mathbf{z}(t) = \hat{\mathbf{H}}\hat{\mathbf{y}}(t) \end{cases} \tag{6.20}$$

where $\hat{\mathbf{A}}$, $\hat{\mathbf{B}}$ and $\mathbf{K}$ collect matrices $\hat{A}_{ij}$, $\hat{B}_i$ and K_i, for all $i,\ j \in \mathcal{V}$.

Asymptotic stability is guaranteed for system (6.20) if there exists a matrix $\mathbf{P} = \text{diag}[P_1, \ldots, P_N]$ so that

$$(\hat{\mathbf{A}} + \hat{\mathbf{B}}\mathbf{K})^T\mathbf{P} + \mathbf{P}(\hat{\mathbf{A}} + \hat{\mathbf{B}}\mathbf{K}) < 0. \tag{6.21}$$

Remark 6.4. *As observed in Remark 3.5 for the case of DC networks, also in AC ImGs, in general,* (6.19) *does not imply* (6.21)*. This is due to the fact that in subsystem* (6.18)*, used to synthesize matrices K_i, couplings were disregarded, while they are accounted for in the overall closed-loop system* (6.20) *(see the example in Appendix B of [RSFT14]).*

In order to ensure that (6.19) implies (6.21), in [RSFT15] the authors exploit the concept of neutral interactions between subsystems. Let us

define matrices $\hat{\mathbf{A}}_\mathbf{D}$ and $\hat{\mathbf{A}}_\mathbf{C}$ as

$$\hat{\mathbf{A}}_\mathbf{D} = \text{diag}[\hat{A}_{ii}, \ldots, \hat{A}_{NN}] \qquad \text{and} \qquad \hat{\mathbf{A}}_\mathbf{C} = \hat{\mathbf{A}} - \hat{\mathbf{A}}_\mathbf{D}.$$

According to the definition provided in [RSFT15], interactions among DGUs are neutral if matrix $\hat{\mathbf{A}}_\mathbf{C}$ can be factorized as:

$$\hat{\mathbf{A}}_\mathbf{C} = \mathbf{SP}, \tag{6.22}$$

where $\mathbf{S}$ is a skew-symmetric matrix (i.e. $\mathbf{S} = -\mathbf{S}^\mathbf{T}$). Next, we introduce the following assumptions.

Assumption 6.1. *(i) Shunt capacitances have the same values at all PCCs: $C_{ti} = C_s$, $\forall i \in \mathcal{V}$.*

(ii) Decentralized controllers $\mathcal{C}_{[i]}$, $i \in \mathcal{V}$ are designed such that (6.19) holds with:

$$P_i = \left[\begin{array}{cc|cccc} \eta & 0 & 0 & 0 & 0 & 0 \\ 0 & \eta & 0 & 0 & 0 & 0 \\ \hline 0 & 0 & \bullet & \bullet & \bullet & \bullet \\ 0 & 0 & \bullet & \bullet & \bullet & \bullet \\ 0 & 0 & \bullet & \bullet & \bullet & \bullet \\ 0 & 0 & \bullet & \bullet & \bullet & \bullet \end{array}\right] \tag{6.23}$$

where $\bullet$ denotes arbitrary entries and $\eta > 0$ is a parameter common to all matrices P_i, $i \in \mathcal{V}$.

(iii) It is verified that $\frac{\eta R_{ij}}{C_s |Z_{ij}|^2} \approx 0$, $\forall i \in \mathcal{V}$, $\forall j \in \mathcal{N}_i$, where $|Z_{ij}| = |R_{ij} + \mathrm{i}\omega_0 L_{ij}|$.

Assumption (i) is not critical; in fact, if capacitances C_{ti} are not all identical, then they can be rewritten as

$$C_{ti} = C_s + \Delta C_i.$$

The current absorbed by each C_{ti}, $i \in \mathcal{V}$, can be split into a current component drawn by nominal capacitance C_s, and a component due to ΔC_i. Currents associated with ΔC_i can be treated as disturbances. In [RSFT15] it is shown, through experiments, that PnP controllers are robust enough so as to provide an effective rejection of disturbances due to ΔC_i, when these terms are sufficiently small.

As regards Assumption (ii), checking the existence of K_i satisfying (6.19) and P_i as in (6.23) amounts to solve an LMI optimization problem.

Assumption (iii) can be fulfilled in different ways. When it is known an upper bound to all ratios $R_{ij}/|Z_{ij}|^2$, then we simply have to choose a sufficiently small value for η. Conversely, if $R_{ij}/|Z_{ij}|^2 \approx 0$, which is the case of mainly inductive lines, η can assume larger values. We underline that $C_s > 0$ and $\eta > 0$ are the only global parameters that must be known to synthesize local controllers.

In [RSFT15], it is shown that under Assumptions (i)-(iii), DGU interactions are neutral and the closed-loop QSL-ImG (6.20) is asymptotically stable.

Each matrix K_i, satisfying Assumption (ii) and ensuring asymptotic stability of (6.18), is so as to fulfill inequality

$$(\hat{A}_{ii} + \hat{B}_i K_i)^T P_i + P_i(\hat{A}_{ii} + \hat{B}_i K_i) + \gamma_i^{-1} I \leq 0, \tag{6.24}$$

in which P_i have the structure in (6.23) and $\gamma_i > 0$ provides a certain degree of robust stability for the origin of (6.18).

The left-hand side of (6.24) can be seen as the Schur complement of a 2×2 block matrix, whose off-diagonal blocks are identity matrices I and whose diagonal blocks are $(\hat{A}_{ii} + \hat{B}_i K_i)^T P_i + P_i(\hat{A}_{ii} + \hat{B}_i K_i)$ and $-\gamma_i I$. Hence, using Schur complement, problem (6.24) becomes

$$\begin{bmatrix} (\hat{A}_{ii} + \hat{B}_i K_i)^T P_i + P_i(\hat{A}_{ii} + \hat{B}_i K_i) & I \\ I & -\gamma_i I \end{bmatrix} \leq 0 \tag{6.25}$$

Since inequality is nonlinear in P_i and K_i, authors in [RSFT15] introduce two matrices

$$\begin{aligned} Y_i &= P_i^{-1} \\ G_i &= K_i Y_i \end{aligned} \tag{6.26}$$

We underline that Y_i and P_i have the identical structure. After that, we pre- and post-multiply (6.25) by $\left[\begin{smallmatrix} Y_i & 0 \\ 0 & I \end{smallmatrix}\right]$ and, by use of (6.26), one gets

$$\begin{bmatrix} Y_i \hat{A}_{ii}^T + G_i^T \hat{B}_i^T + \hat{A}_{ii} Y_i + \hat{B}_i G_i & Y_i \\ Y_i & -\gamma_i I \end{bmatrix} \leq 0. \tag{6.27}$$

Now, consider the following optimization problem:

$$\mathcal{O}_i : \min_{Y_i, G_i, \gamma_i, \beta_i, \delta_i} \quad \alpha_{i1}\gamma_i + \alpha_{i2}\beta_i + \alpha_{i3}\delta_i$$

$$Y_i = \begin{bmatrix} \eta^{-1} & 0 & 0 & 0 & 0 & 0 \\ 0 & \eta^{-1} & 0 & 0 & 0 & 0 \\ 0 & 0 & \bullet & \bullet & \bullet & \bullet \\ 0 & 0 & \bullet & \bullet & \bullet & \bullet \\ 0 & 0 & \bullet & \bullet & \bullet & \bullet \\ 0 & 0 & \bullet & \bullet & \bullet & \bullet \end{bmatrix} > 0 \tag{6.28a}$$

$$\begin{bmatrix} Y_i \hat{A}_{ii}^T + G_i^T \hat{B}_i^T + \hat{A}_{ii} Y_i + \hat{B}_i G_i & Y_i \\ Y_i & -\gamma_i I \end{bmatrix} \leq 0 \tag{6.28b}$$

$$\begin{bmatrix} -\beta_i I & G_i^T \\ G_i & -I \end{bmatrix} < 0 \tag{6.28c}$$

$$\begin{bmatrix} Y_i & I \\ I & \delta_i I \end{bmatrix} > 0 \tag{6.28d}$$

$$\gamma_i > 0, \quad \beta_i > 0, \quad \delta_i > 0 \tag{6.28e}$$

where α_{i1}, α_{i2} and α_{i3} are positive weights and $\bullet$ denotes arbitrary entries. All constraints in (6.28) are LMIs, hence we get a convex optimization problem, which can be efficiently solved by LMI solvers [BEGFB94].

Remark 6.5. *We highlight that constraint* (6.28a)*, imposing the structure of P_i, ensures that Assumption 2 holds. The stability of subsystem* (6.18) *is guaranteed by* (6.28b)*. Constraints* (6.28c) *and* (6.28d) *represent respectively conditions $||G_i||_2 < \sqrt{\beta_i}$ and $||Y_i^{-1}||_2 < \delta_i$, which are introduced to bound $||K_i||_2$. Indeed, with* (6.28c) *and* (6.28d)*, we have $||K_i||_2 < \delta_i\sqrt{\beta_i}$.*

Finally, we observe that problem (6.28) depends upon local design parameters (α_{i1}, α_{i2}, α_{i3}) and local electrical parameters, contained in matrices $\hat{A}_{ii}$ and $\hat{B}_i$. Consequently, once global parameters $\eta > 0$ and $C_s > 0$ have been fixed, the computation of each controller $C_{[i]}$ is not influenced by the synthesis of the other controllers $C_{[j]}$, $j \neq i$. After having solved problem (6.28), matrix K_i is obtained as $K_i = G_i Y_i^{-1}$. Moreover, since Assumptions (i)-(iii) are verified, the closed-loop QSL-ImG (6.18) is asymptotically stable.

Remark 6.6. *Performance of controllers $\mathcal{C}_{[i]}$ can be enhanced by designing pre-filters of reference signals ($\tilde{C}_{[i]}$) and local compensator of measurable disturbances ($N_{[i]}$). For details, we refer the reader to [RSFT14].*

6.3.3 Plug-and-play operations

Once global parameters $C_s > 0$ and $\eta > 0$ are fixed, each controller $\mathcal{C}_{[i]}$ is designed using the following algorithm.

Algorithm 6.1 Design of controller $\mathcal{C}_{[i]}$ and compensators $\tilde{C}_{[i]}$ and $N_{[i]}$ for subsystem $\hat{\Sigma}_{[i]}^{DGU}$

Input: DGU $\hat{\Sigma}_{[i]}^{DGU}$ as in (6.14)

Output: Controller $\mathcal{C}_{[i]}$ and, optionally, pre-filter $\tilde{C}_{[i]}$ and compensator $N_{[i]}$

(A) Find K_i solving the LMI problem (6.28). If it is not feasible **stop** (the controller $\mathcal{C}_{[i]}$ cannot be designed).
Optional steps

(B) Design the asymptotically stable local pre-filter $\tilde{C}_{[i]}$ and compensator $N_{[i]}$ as in Section 3.3. of [RSFT14].

When a new DGU is plugged in, or an already connected DGU is unplugged, matrices A_{ii} of neighboring subsystems change. Hence, their controllers must be redesigned in order to guarantee asymptotic stability of the overall closed-loop system. In [RSFT15], it is described the sequence of operations needed after the plug-in or unplugging of a DGU.

Plug-in operation. Consider an ImG with N DGUs. We want to plug-in a new DGU, denoted as DGU $N+1$, whose associated subsystem is $\hat{\Sigma}_{[N+1]}^{\text{DGU}}$, composed of matrices $\hat{A}_{N+1\,N+1}$, $\hat{B}_{N+1}$, $\hat{C}_{N+1}$, $\hat{M}_{N+1}$, $\hat{H}_{N+1}$ and $\{\hat{A}_{N+1\,j}\}_{j\in\mathcal{N}_{N+1}}$. The set $\mathcal{N}_{N+1}$ identifies the neighbors of DGU $N+1$. One must follow Algorithm 6.1 in order to design controller $\mathcal{C}_{[N+1]}$, pre-filter $\tilde{C}_{[N+1]}$ and compensator $N_{[N+1]}$. Notably, controllers $\mathcal{C}_{[j]}$ and compensators $\tilde{C}_{[j]}$ and $N_{[j]}$, $\forall j \in \mathcal{N}_{N+1}$ of the neighboring DGUs $\hat{\Sigma}_{[j]}^{\text{DGU}}$, $j \in \mathcal{N}_{N+1}$ must be updated. In fact, matrices $\hat{A}_{jj}$, $j \in \mathcal{N}_{N+1}$ change after the connection of DGU $N+1$. In conclusion, plug-in of DGU $N+1$ is allowed if Algorithm 6.1 does not stop in Step (A). We recall that only controllers of neighboring DGUs must be redesigned; all the other controllers are not updated.

Unplugging operation Consider the unplugging of DGU k, whose associated subsystem is $\hat{\Sigma}_{[k]}^{\text{DGU}}$. Matrix $\hat{A}_{jj}$ of each neighboring DGU $\hat{\Sigma}_{[j]}^{\text{DGU}}$,

$j \in \mathcal{N}_k$ changes after DGU k is removed. Consequently, controllers $\mathcal{C}_{[j]}$, pre-filters $\tilde{C}_{[j]}$ and compensators $N_{[j]}$, $j \in \mathcal{N}_k$ must be updated. Unplugging operation of DGU k is allowed if Algorithm 6.1 does not stop in Step (A). All the other controllers $\mathcal{C}_{[j]}$, $j \notin \mathcal{N}_k$ must not to be redesigned.

Chapter 7

A hierarchical control architecture for bus-connected AC islanded microgrids

Contents

7.1 Introduction 156
7.2 Model of a bus-connected microgrid 157
7.3 Plug-and-play primary control layer 159
7.3.1 Control structure 159
7.3.2 Plug-and-play design of local controllers 161
7.3.3 Clock synchronization for primary control 162
7.3.4 Harmonic compensation by tuning the plug-and-play control bandwidth 162
7.4 Coordinated control 163
7.4.1 Voltage tracking at the PoL 164
7.4.2 Sharing of reactive power 167
7.5 Experimental results 167
7.5.1 Microgrid setup 167
7.5.2 Primary control layer validation 169
7.5.3 Primary and secondary layers validation 172
7.6 Final comments 172
7.7 Appendix 173
7.7.1 Proof of Lemma 7.1 173
7.7.2 Derivation of the approximate model (7.10) . . . 174
7.7.3 Electrical and control parameters of the experimental tests 175

7.1 Introduction

In this chapter, we propose a distributed hierarchical control architecture for voltage and frequency stabilization and reactive power sharing in AC ImGs with specific topologies.

At the primary control layer, each DGU is equipped with a local regulator for voltage and frequency stability acting on the corresponding VSC. Following the PnP design approach proposed in [RSFT15] (and summarized in Chapter 6), whenever the addition/removal of a subsystem is required, the feasibility of the operation is automatically checked by designing local controllers through convex optimization. As a consequence, the update of primary regulators, when DGUs plug-in/-out, is automatized and stability of the ImG is always preserved.

At the secondary level, we develop a distributed control scheme for achieving advanced coordinated behaviors, such as reactive power sharing.

The main contributions presented in this chapter are detailed in the following.

1. We provide an extension of the scalable algorithm in Chapter 6 which allows to compute local stabilizing controllers for ImGs arranged in *load-connected* topology only (i.e. networks with local loads appearing at the output terminals of each DGU). Notably, in order to generalize the PnP control methodology in [RSFT15] to a wider class of ImGs, we propose a simple and effective procedure for mapping *bus-connected* topologies[1] (i.e. networks with a common load, supplied by all the DGUs) into their equivalent load-connected models. We highlight that bus-connected ImGs are frequently found in several applications [VGS$^+$13, CGS$^+$16].

2. We demonstrate that *virtual impedance*, a key tool in power electronics developed especially for droop controlled ImGs [HL10, VGS$^+$13], can be likewise extended to basic PnP controllers. This result is useful since virtual impedance loops are needed for setting the output impedance of bus-connected VSCs, thus lowering the unwanted circulating currents between DGUs created by mismatches in lines and inverters parameters.

3. On top of the stabilizing PnP primary layer, we develop a distributed secondary control scheme for voltage tracking at the load bus and reactive power sharing. Unlike other works considering droop-controlled

[1] In the literature, bus-connected topologies are also called *parallel* topologies.

ImGs [EDI12, SSRS16], we show how these objectives of practical interest can be ensured by coupling secondary controllers with low-level PnP regulators. In particular, secondary controllers bring performance improvements without compromising the stability of the ImG.

4. The proposed hierarchical control architecture is validated through experiments on a realistic bus-connected ImG facility. We assess the capability of PnP controllers to track set-point voltages, and show the negligible impact of transients on stability when DGUs join/leave the network. Furthermore, the good behavior of the closed-loop ImG equipped with the secondary control layer is demonstrated in presence of both linear and nonlinear loads. Experimental results prove the feasibility of the proposed control design framework, which guarantees seamless addition/removal of generation units, thus promoting the deployment of autonomous electrical networks with flexible topology.

The chapter is organized as follows. In Section 7.2, we derive the formulae for computing the equivalent load-connected network of a bus-connected one. In Section 7.3, we show how to extend the PnP design procedure presented in Chapter 6 to the case of bus-connected ImGs. In Section 7.4, the secondary coordinated control layer is presented. Section 7.5 is devoted to the assessment, through experiments, of PnP control alone and in combination with the secondary coordinated control layer. Concluding remarks are reported in Section 7.6.

7.2 Model of a bus-connected microgrid

The fact that the method in Chapter 6 allows to design stabilizing PnP controllers for load-connected ImGs only, does not represent a limitation. In fact, as shown in [DB13] and recalled in Remarks 3.3, 6.3, arbitrary interconnections of loads and DGUs can always be mapped into their equivalent load-connected topologies by means of Kron reduction [Kro39]. This mathematical tool, which will be extensively described in Chapter 8, can be exploited for computing (i) the corresponding load-connected topology (where only DGUs are interconnected) of the original, arbitrarily connected ImG, (ii) the admittances of the new power lines and (iii) the equivalent currents injected at the PCCs, accounting for the effect of the eliminated nodes (i.e. the loads that do not appear at the output terminals of DGUs) in the original network[2]. An example of the transformation is provided in

[2]Kron reduction will be discussed in details in Chapter 8.

Figure 7.1.

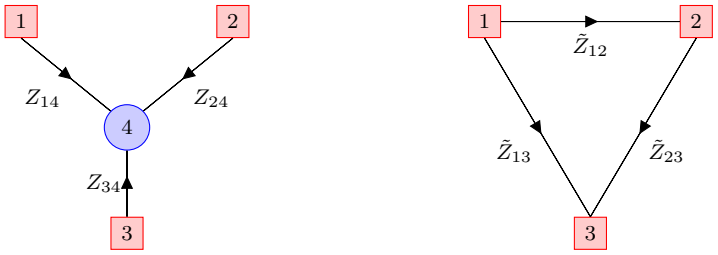

(a) Bus-connected ImG. (b) Equivalent load-connected ImG.

Figure 7.1: Example of network transformation. Red squares indicate DGUs with corresponding local loads I_{Li} (appearing, e.g., in Figure 6.2), while the blue circle in Figure 7.1a denotes the unique load at the common bus. Black arrows identify balanced power lines.

Since several works from the literature consider ImGs arranged in bus-connected topology [SHK+17, HHY+16, VGS+13], we are interested in mapping these topologies into the corresponding load-connected ones. While it goes without saying that Kron reduction can also be applied to this aim (by eliminating the node representing the load bus[3]), it requires the inversion of an admittance matrix. In the following, instead, we provide an equivalent procedure, leading to explicit formulae, for computing the admittances of the power lines of the corresponding load-connected network (e.g. the inverse of the impedances Z_{12}, Z_{13} and Z_{23} in Figure 7.1a). This method relies on KCL, KVL and QSL approximation.

As a starting point, let us consider a bus-connected ImG with N DGUs feeding a common load (I_L) connected to the Point of Load (PoL). Figure 7.2 provides an example with $N = 3$ and shows parameters R_i, L_i and currents I_i characterizing each DGU. As usual, we assume balanced lines. Moreover, sets $\mathcal{V}$ and $\mathcal{N}_i$ ($i \subset \mathcal{V}$) are defined as in Chapter 6 (see Section 6.2.2).

By applying KCL and KVL in the *abc*-frame and performing the Park's transformation [Par29], we have that the dynamics of DGU i in *dq*-coordinates,

[3]Node 4 in the example in Figure 7.1a.

with reference angular frequency $\omega = \omega_0$, are described by

$$\text{DGU}i: \quad \begin{cases} \dfrac{\mathrm{d}}{\mathrm{d}t} V_i^{dq} = \dfrac{I_{ti}^{dq}}{C_{ti}} - \dfrac{I_i^{dq}}{C_{ti}} - \mathrm{i}\omega_0 V_i^{dq} & \text{(7.1a)} \\ \dfrac{\mathrm{d}}{\mathrm{d}t} I_{ti}^{dq} = -\left(\dfrac{R_{ti}}{L_{ti}} + \mathrm{i}\omega_0\right) I_{ti}^{dq} - \dfrac{V_i^{dq}}{L_{ti}} + \dfrac{V_{ti}^{dq}}{L_{ti}} & \text{(7.1b)} \end{cases}$$

The network reduction method is summarized in the following Lemma.

Lemma 7.1. *Consider a bus-connected ImG with complex power lines admittances $1/Z_i$, where $Z_i = R_i + \mathrm{i}\omega_0 L_i$, $i = 1, ..., N$, and common load current I_L. Under QSL approximations of line dynamics, voltages and currents in* (7.1) *coincide with model* (6.9)*, provided that $1/Z_{ij}$ and I_{Li} in* (6.9a) *are defined as*

$$\frac{1}{Z_{ij}} = \frac{1}{Z_j Z_i \sum_{k=1}^{N} \frac{1}{Z_k}}, \quad \forall j \neq i \tag{7.2}$$

and

$$I_{Li}^{dq} = \frac{I_L^{dq}}{\left(Z_i \sum_{k=1}^{N} \frac{1}{Z_k}\right)}, \tag{7.3}$$

respectively.

Proof. The proof of Lemma 7.1 is given in Appendix 7.7.1. □

We highlight that, since admittances $1/Z_{ij}$ $i, j = 1, ..., N$, $i \neq j$ are all nonzero, the described transformation always returns a fully connected reduced network (see the example in Figure 7.1b, where each pair of distinct DGUs is connected by one power line).

7.3 Plug-and-play primary control layer

7.3.1 Control structure

Figure 7.3 shows a bus-connected DGU, equipped with a decentralized PnP controller for voltage and frequency regulation. It can be seen that the structure of the local regulator is the same as the one depicted in Figure 6.2 for load-connected DGU. Notably, each controller exploits measurements of the voltage V_i^{dq} at the PCC and the current I_{ti}^{dq}, in order to control the

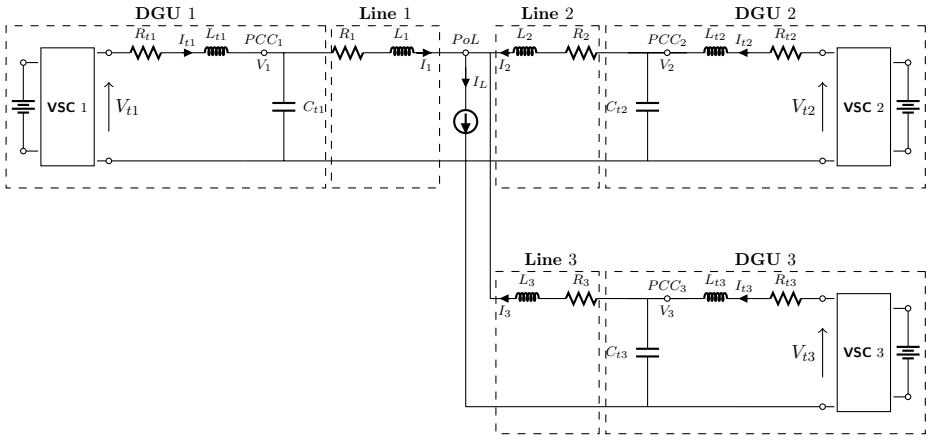

Figure 7.2: Electrical scheme of a bus-connected ImG composed of three DGUs and a common unmodeled load.

voltage V_{ti}^{dq} at the VSC i and make V_i^{dq} track a reference signal. Moreover, the considered controller is multivariable, and the only tunable parameter is the matrix gain K_i in Figure 7.3. Finally, the presence of the integrators guarantees tracking of constant set-point references in the dq-frame, and hence of three-phase sinusoidal quantities in the abc-frame.

In addition to the scheme described in Chapter 6, Figure 7.3 reveals the presence of a virtual impedance loop, i.e. a widely used tool in control of parallel interconnected VSCs [HL10, VGS+13]. Its employment is instrumental for lowering the circulating currents between DGUs generated by line-impedance unbalance and mismatch in inverter parameters. In practice, as shown in Figure 7.3, the virtual impedance reduces the voltage reference by a term proportional to the line current, thus mimicking an RL impedance connected in series to the output filter of the inverter. We also highlight that virtual resistances and inductances should be chosen sufficiently large so as to outnumber such uncertainties in the electrical parameters. In contrast with a physical device, a virtual impedance has no power losses. In [HL10, VGS+13], the virtual impedance is expressed in $\alpha\beta$-coordinates. Similarly, we can model it in dq-coordinates as follows:

$$\begin{aligned} V_{i,v}^d &= R_{i,v} I_i^d + L_{i,v} \frac{\mathrm{d}I_i^d}{\mathrm{d}t} - \omega_0 L_{i,v} I_i^q \\ V_{i,v}^q &= R_{i,v} I_i^q + L_{i,v} \frac{\mathrm{d}I_i^q}{\mathrm{d}t} + \omega_0 L_{i,v} I_i^d \end{aligned} \tag{7.4}$$

where $R_{i,v}$ and $L_{i,v}$ are the virtual resistance and inductance parameters

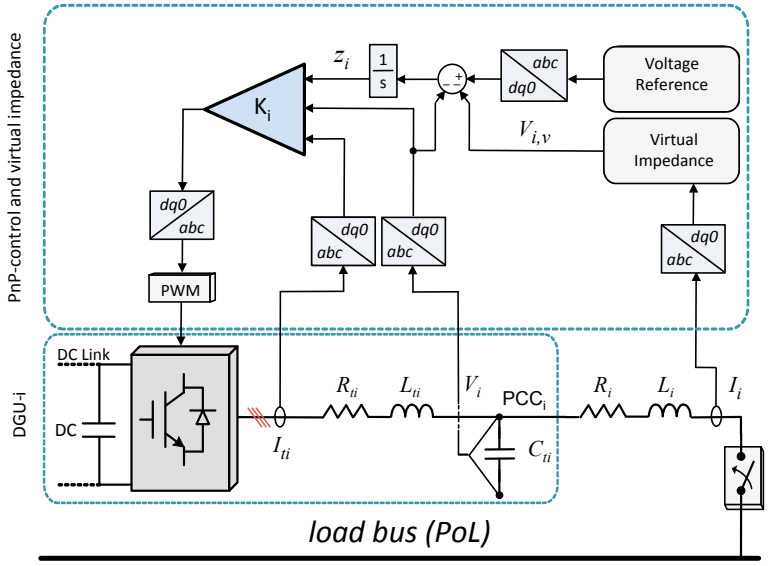

Figure 7.3: Bus-connected DGU equipped with local PnP regulator and virtual impedance loop.

and $V_{i,v}$ and I_i are the voltage and current in the dq-frame shown in Figure 7.3.

7.3.2 Plug-and-play design of local controllers

In this section, we show how to extend the PnP control design procedure described in Chapter 6 (which assumes load-connected ImGs) to bus-connected networks.

Whenever we want to plug-in a new DGU (say DGU i) to an existing ImG, the first step is to compute the line impedances between DGU i and each DGU j, $j \in \mathcal{V} \setminus \{i\}$, using (7.2). Subsequently, the LMI test (6.28) must be successfully solved for all the DGUs, in order to allow the safe connection of DGU i. On the other hand, if only one of these LMIs is infeasible, the plug-in of DGU i is denied. Unplugging of a DGU can be performed in a similar way.

Remark 7.1. *The procedure for handling plug-in/-out operations when the original network is arranged either in a load- or bus-connected topology can be simplified as follows. Let us assume that the hot plug-in (i.e. the plug-in in real-time) of DGU i has been allowed and scheduled at a future time $\bar{t}$. At the same time instant, DGUs j (with $j \in \mathcal{N}_i$ if the ImG is load-connected,*

or $j \in \mathcal{V} \setminus \{i\}$ if the ImG is bus-connected) will start using the new gains. Retuning of gains K_j, however, could be avoided if previous gains are still feasible for the corresponding LMI test. In other words, for such DGUs j, one can check if matrix gains K_j working for $t < \bar{t}$ still fulfill the constraints of their corresponding optimization problem (6.28)*. Preserving previously designed controllers, in fact, has the advantage of reducing perturbations on electrical signals right after $\bar{t}$, which might be caused by controller switching.*

In a similar way, if DGU m is disconnected, the retuning of controllers of DGUs k (with $k \in \mathcal{N}_m$ or $k \in \mathcal{V} \setminus \{m\}$ if the ImG is load- or bus-connected, respectively) can be avoided if the LMI (6.28) *is feasible for previously designed matrix gains K_k.*

7.3.3 Clock synchronization for primary control

The computation of VSC commands assumes that all clocks of local controllers, used for performing *abc* to *dq* transformations, are synchronized. As also highlighted in [EDI12], each DGU can include a crystal oscillator that generates the angular phase $\theta(t) = \int_0^t \omega_0 \, d\tau$. However, if the local oscillators are not synchronized, the local angular phase is given by $\theta_i(t) = \theta(t) + \theta_{i,0}$, where $\theta_{i,0}$ is the initial offset. In [EDI12], the authors propose a synchronization using Global Positioning System (GPS) radio clock, which could achieve an accuracy higher than 1μs [PTP08].

An alternative solution is to synchronize clocks using communication between controllers. This operation can be performed quite rarely because, as noted in [EDI12], currently available crystal oscillators are characterized by high accuracy (from 2 μs to 20 ps in a year [Vig09]). Moreover, synchronization can be done through packet networks, using either a distributed protocol (e.g. Berkeley algorithm [GZ89]) or approaches based on all-to-all communication, such as instantaneous averaging [IEE17].

If an ImG is equipped with primary PnP regulators, prior to allowing the plug-in of a new DGU, it is mandatory to synchronize it with all the ones already connected to the PoL. Therefore, in the experiments described in Section 7.5, we let each new DGU estimate $\theta_{i,0}$ by computing the average angular phases of all the other DGUs.

7.3.4 Harmonic compensation by tuning the plug-and-play control bandwidth

Besides collective voltage and frequency stability, PnP design can guarantee good harmonic compensation, even in absence of low-level resonant con-

trollers (described, e.g., in [VGS+13]). In fact, as explained in [RSFT15], one can also shape, in a desired fashion, the singular values of the overall closed-loop ImG. More specifically, in order to provide suitable attenuation of the 5-th, 7-th and 11-th harmonics in *abc*-frame, we design primary PnP controllers that attenuate the 4-th, 6-th and 10-th harmonics in the rotating *dq*-frame. An example is provided in Figure 7.4 for an ImG with two DGUs. The singular values of closed-loop ImG transfer function from voltage references to the voltages at the PCCs are represented in Figure 7.4a. Similarly, the singular values of the transfer function from voltage references to the currents in the filters are given in Figure 7.4b. Notice that good attenuation can be obtained also when couplings between DGUs are accounted for. In fact, assuming $f_0 = 50$ Hz, from Figure 7.4a, the attenuation of the 5-th, 7-th and 11-th voltage harmonics is 50 dB, 60 dB and 70 dB, respectively.

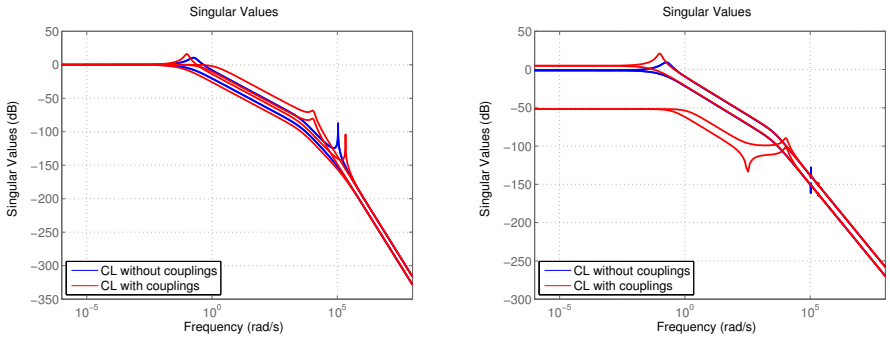

(a) Singular values of the transfer function matrix from *dq* voltage references to *dq* voltages at the PCCs.

(b) Singular values of the transfer function matrix from *dq* voltage references to *dq* currents in the filters.

Figure 7.4: Singular values for the closed-loop ImG with two DGUs.

7.4 Coordinated control

Using PnP controllers described in Sections 7.3.1-7.3.2, we are able to guarantee voltage and frequency stability for the overall ImG. Notably, each local controller regulates the voltage at the corresponding PCC, according to the following reference in the *abc*-frame

$$V_{i_\bullet}^*(t) = V_i^* \sin\left(\omega_0 t + \phi_i^* + \Delta\phi_{i,\bullet}^*\right), \quad \bullet = \{a, b, c\}, \tag{7.5a}$$

$$\Delta\phi^*_{i,a} = 0,\ \Delta\phi^*_{i,b} = -\frac{2\pi}{3},\ \Delta\phi^*_{i,c} = \frac{2\pi}{3}. \tag{7.5b}$$

In bus-connected ImGs, one can indirectly control voltage and frequency at the PoL by choosing voltages V_i^*, $i = 1, \ldots, N$ in (7.5). In several control architectures, the use of a Power-Management System (PMS) has been proposed for this purpose (see, e.g., [EDI12]). The basic idea is to compute voltage references such that each DGU injects prescribed active and reactive power. The PMS must be run in real-time in order to maintain a prescribed power flow, even if loads change. In the following, we propose a distributed secondary control layer capable to guarantee (i) a desired voltage at the PoL, and (ii) sharing of reactive power injections among DGUs.

7.4.1 Voltage tracking at the PoL

Let us indicate the desired PoL voltage with $V^*_{PoL}\angle 0$[4]. In absence of loads, in order to guarantee the reference at the PoL, we could set, in (7.5), $V_i^* = V^*_{PoL}$ and $\phi_i^* = 0$. However, due to the presence of time-varying loads, V_i^* and ϕ_i^* must be adapted over time. We propose that each DGU changes its set-point according to

$$V^*_{i\bullet}(t) = (V^*_{PoL} + \Delta V_{PoL}) \sin\left(\omega_0 t + \Delta\phi_{PoL} + \Delta\phi^*_{i,\bullet}\right), \tag{7.6}$$

with $\bullet = \{a, b, c\}$, and $\Delta\phi^*_{i,\bullet}$ as in (7.5b), instead of (7.5). The next aim is to compute ΔV_{PoL} and $\Delta\phi_{PoL}$ in order to keep PoL voltage close to its reference. Since we can not measure the voltage at the PoL, we estimate its amplitude and phase averaging local measurements

$$V_{PoL} = \sum_{i=1}^{N} \frac{V_{PoL,i}}{N} \qquad \phi_{PoL} = \sum_{i=1}^{N} \frac{\phi_{PoL,i}}{N} \tag{7.7}$$

where $V_{PoL,i}$ and $\phi_{PoL,i}$ are computed by each DGU from V_i and I_i (shown in Figure 7.3) as follows

$$V_{PoL,i} = \sqrt{(V^d_{PoL,i})^2 + (V^q_{PoL,i})^2} \qquad \phi_{PoL,i} = \frac{V^q_{PoL,i}}{V^d_{PoL,i}}, \tag{7.8}$$

[4]Without loss of generality, the phase has been assumed equal to zero.

where

$$V^d_{PoL,i} = V^d_i + \omega_0 L_i I^q_i$$
$$V^q_{PoL,i} = V^q_i - \omega_0 L_i I^d_i.$$

We equip each DGUwith the local controller in Figure 7.5 for computing ΔV_{PoL} and $\Delta\phi_{PoL}$ in (7.6). We note that the controller in Figure 7.5 is replicated in each DGU instead of being unique for the whole ImG. As shown in [SGV14], replicating the controller has several advantages when the communication latency increases. Differently from the PnP control

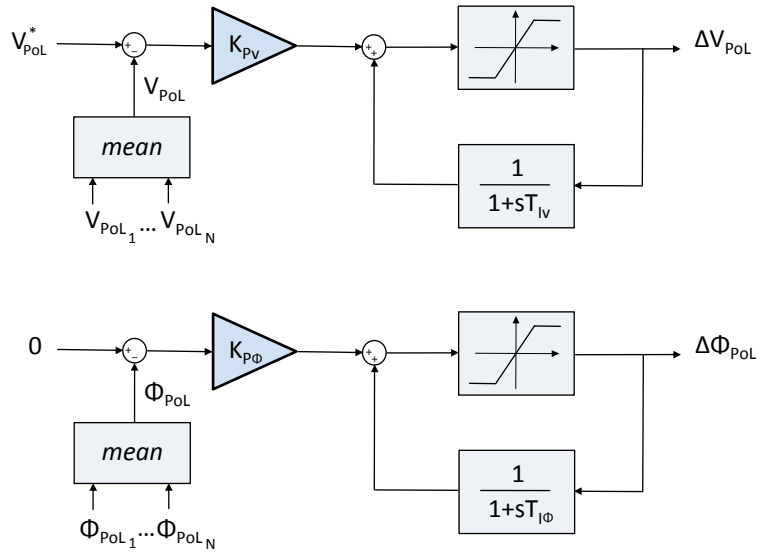

Figure 7.5: Coordinated control layer: computation of correction terms ΔV_{PoL} and $\Delta\phi_{PoL}$. Parameters K_{PV} and $K_{P\phi}$ are the voltage and phase proportional coefficients, while T_{IV} and $T_{I\phi}$ are the voltage and phase integral time constants.

architecture (that is completely decentralized), the secondary layer of controllers is distributed as it needs a communication network in order to exchange values $V_{PoL,i}$ and $\phi_{PoL,i}$, and then to compute locally the averages (7.7). Formula (7.7) requires a fully connected communication network, as all measurements $V_{PoL,i}$ and $\phi_{PoL,i}$ have to be broadcasted to all DGUs. However, this limitation could be avoided by resorting to distributed algorithms, based on consensus strategies, for tracking the average of time-varying signals [Buln s]. Indeed, these methods only require sparse, yet connected, networks. In Figure 7.6 we show the flow of information

for the proposed coordinated controller. Each controller in Figure 7.5 is

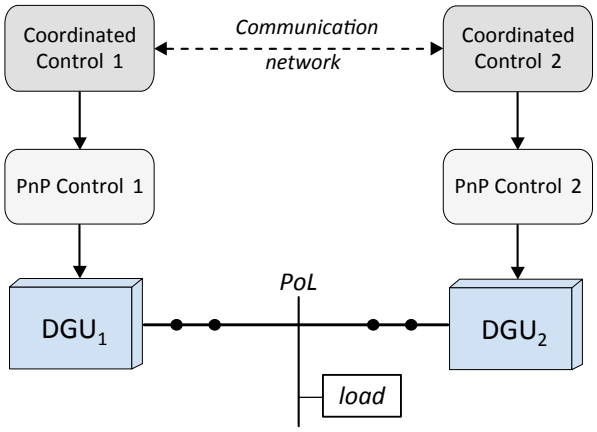

Figure 7.6: Scheme of the coordinated control.

a PI regulator with an anti-windup scheme accounting for saturations on ΔV_{PoL} and $\Delta\phi_{PoL}$. These saturations are needed to limit the amplitude and phase deviations, thus preventing the opening of breakers connecting inverters to the PoL. When saturations are not active, ΔV_{PoL} and $\Delta\phi_{PoL}$ are computed through the standard PI formulae

$$\Delta V_{PoL}(t) = K_{PV}(V^*_{PoL} - V_{PoL}(t)) + K_{IV}\int_0^t (V^*_{PoL} - V_{PoL}(\tau))\, d\tau \quad (7.9a)$$

$$\Delta\phi_{PoL}(t) = K_{P\phi}(0 - \phi_{PoL}(t)) + K_{I\phi}\int_0^t (0 - \phi_{PoL}(\tau))\, d\tau. \quad (7.9b)$$

At this point, we aim to select the integral time constants $T_{IV} = K_{PV}/K_{IV}$ and $T_{I\phi} = K_{P\phi}/K_{I\phi}$ in Figure 7.5 so as to make the corresponding PI control loop sufficiently slower than the inner PnP control loop. In order to properly design the PI parameters in (7.9), one can follow standard design procedures by assuming that the system under control (i.e. the transfer function describing the relation between ΔV_{PoL} and V_{PoL}) has the following form:

$$\frac{V_{PoL}}{\Delta V_{PoL}} = \frac{\mu e^{-s\tau_{PoL}}}{1 + sT_{PoL}}. \quad (7.10)$$

This approximation in justified in Appendix 7.7.2, where explicit formulae for τ_{PoL} and T_{PoL} are also given.

7.4.2 Sharing of reactive power

Inner PnP regulators complemented with coordinated controllers for voltage tracking at the PoL cannot alone guarantee accurate reactive power sharing among DGUs. For this reason, we propose an additional coordinated controller dedicated to this aim. We assume that DGUs are connected to the PoL through mostly inductive lines[5]. In this case, the sharing of the reactive power is due to the amplitude of the voltages [YI10, TLR11]. Therefore, we propose to change the amplitude of the set-point for each DGU as

$$V_i^* = V_{PoL}^* + \Delta V_{PoL} + \Delta V_i^Q, \tag{7.11}$$

where V_{PoL}^* is the reference for voltage at PoL, ΔV_{PoL} is computed as in (7.9a) and ΔV_i^Q is a voltage correction to guarantee reactive power sharing. Voltage ΔV_i^Q is computed by the PI controller equipped with anti-windup shown in Figure 7.7. In particular, when the saturation on ΔV_i^Q is not active, one has:

$$\Delta V_i^Q(t) = K_{PQ}(Q(t) - Q_i(t)) + K_{IQ} \int_0^t (Q(\tau) - Q_i(\tau))\, d\tau,$$

where Q_i is the reactive power injected by the local DGU and $Q(t)$ is the average of the injected reactive powers. The PI regulator in Figure 7.7 is replicated in each DGU. Moreover, the whole control layer requires the communication network displayed in Figure 7.6 since all units must exchange the values of reactive power $Q_i(t)$ for computing locally average $Q(t)$.

Similarly to what we have done for the PI regulators in Figure 7.5, each integral time constant T_{IQ} is designed to make the corresponding PI controller slower than the inner PnP ones.

7.5 Experimental results

7.5.1 Microgrid setup

We tested the performance of the proposed approach using the ImG platform in Figure 5.6; it consists of three *Danfoss* inverters (2.2kVA with *LC* filters), a dSPACE1103 control board and LEM sensors. Inverters operate in parallel to emulate DGUs while different load conditions are obtained

[5]Results can be easily adapted to the case of lines that are mostly resistive.

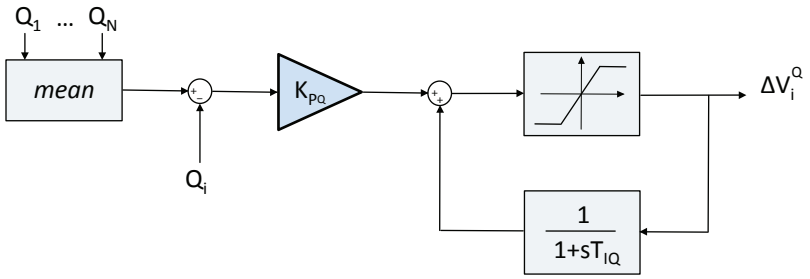

Figure 7.7: Control scheme for the computation of ΔV_i^Q. Parameters K_{PQ} and T_{IQ} are the reactive power proportional term and the reactive power time constant, respectively.

by connecting to the bus resistive loads and/or a diode rectifier. All the inverters are supplied by a DC source generator, therefore neither renewable sources nor energy storage devices are present in the experimental setup. Although this does not allow to study the effect of power fluctuations from renewable sources, the reliability of our experimental validation is guaranteed by the fact that, in general, changes in the power supplied by renewables take place at a timescale that is slower than the one we are interested in for stability analysis.

The controllers have been implemented in Simulink and compiled to the dSPACE system in order to command the inverter switches at a frequency of 10 kHz. Although the dSPACE platform is unique (see also Figure 7.8a), separate local controllers for each inverter were implemented so as to guarantee the control architecture can be implemented in a real distributed inverter system. The scheme of the experimental setup is depicted in Figure 5.6.

In the performed experiments, we make sure that, at time $t = 0$ s, all the controllers are already activated so that all the voltages at the PCCs start from their reference value (230 V).

The control and electrical parameters are reported in Appendix 7.7.3.

In the following sections, we validate primary PnP controllers under linear and nonlinear load conditions, as well as the combination of such primary layer with the proposed secondary coordinated controllers.

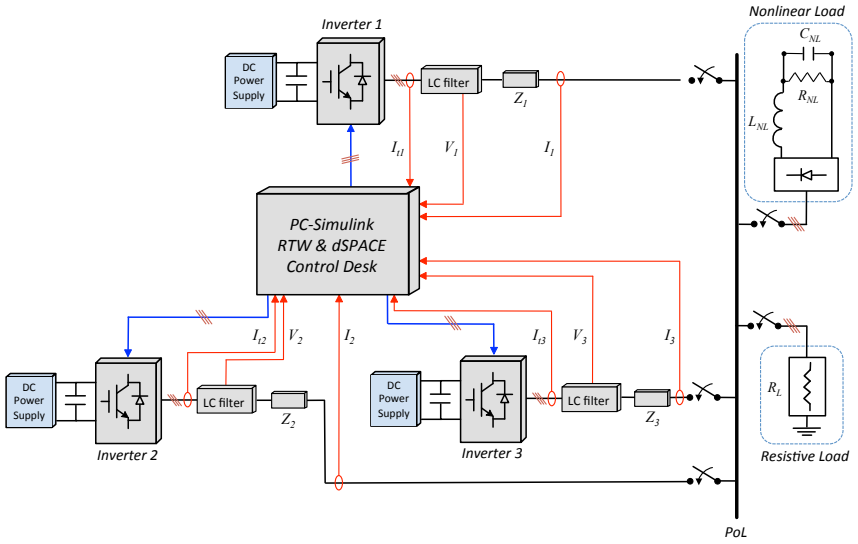

(a) Scheme of the experimental setup. Red lines indicate the electrical variables measured at each DGU level. Blue lines represent the control commands to the inverters.

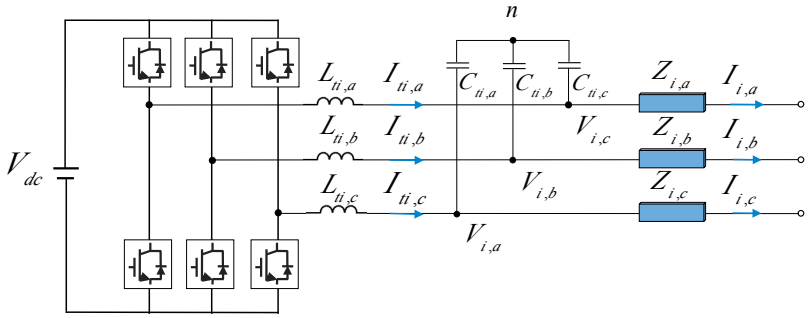

(b) Zoom of the i-th DGU in Figure 7.8a: three-phase electrical signals and parameters are shown.

Figure 7.8: Experimental validation: ImG setup and implemented control scheme.

7.5.2 Primary control layer validation

Voltage regulation at the PCCs with resistive load

In this first experiment, we test the capability of PnP primary controllers to handle connection and disconnection of inverters in a bus-connected ImG. At this stage, coordinated controllers described in Section 7.4 are not used.

At time $t = 0$ s, the first and second inverter are connected to the bus; since there is no load at the PoL, the Root Mean Square (RMS) voltages at PCCs 1 and 2 (red and green line, respectively, in Figure 7.9a) coincide with the reference.

At $t = 5$ s, we connect a resistive load ($R = 92\ \Omega$) at the PoL. Consequently, the active powers provided by inverters 1 and 2 increase in order to compensate the load (see Figure 7.9c). We also notice that the frequencies are promptly restored after the load connection (as shown in Figure 7.9b).

Since the voltage references at PCCs are fixed, PnP controllers alone cannot guarantee a good voltage regulation at the PoL. Moreover, as recalled in Section 7.3.1, the presence of a local virtual impedance induces a drop (proportional to the output current) in the corresponding reference voltage. This behavior is shown, for instance, in Figure 7.9a, where we notice a decrement in the voltages at PCCs 1 and 2 when the load is connected to the PoL (at $t = 5$ s).

At time $t = 15$ s, we plug-in inverter 3. This event induces spikes in the frequencies (see Figure 7.9b), whose maximal amplitude, however, is less than 0.2 Hz. Moreover, Figure 7.9c shows that all the inverters provide the same active power to compensate the load.

At times $t = 25$ s and $t = 35$ s, we change the load to $R = 460\ \Omega$ and $R = 154\ \Omega$, respectively. These events generate drops in the active power of more than 50%. Moreover, voltages and frequencies are instantaneously restored (see Figures 7.9a and 7.9b). Differently from droop-controllers, PnP controllers are not inertia-based and hence they are capable to provide faster transients.

Finally, at $t = 40$ s and $t = 45$ s we plug-out inverters 3 and 2, respectively, thus eventually feeding the resistive load with inverter 1 only. Also in this case, the impact of the unplugging events on the frequency profile is minor.

Voltage regulation at the PCCs with unbalanced load

In this experiment, we show performance of PnP controllers under unbalanced load conditions. For the sake of simplicity, in Figures 7.10b-7.10e we show the evolution of the main electrical quantities of inverter 1 only.

At $t = 0$ s, all the inverters are connected to the PoL and no load is present. Then, at $t = 5$ s we connect a balanced resistive load ($R = 115\ \Omega$) to the common bus. Consequently, inverter 1 provides the output current shown in Figure 7.10b.

At $t = 10$ s, we change phase b of the load to $R = 57\ \Omega$, thus causing

the unbalance in the output current 1 shown in Figure 7.10c. Moreover, the average of the imbalanced ratios [IEE09] for all the inverters is 0.5 % (see Figure 7.10a).

At $t = 15$ s, we change phase c of the load to $R = 230\ \Omega$. As a consequence, in Figure 7.10d we note an additional unbalance in the output current 1. Moreover, from Figure 7.10a, we see that the average of the imbalanced ratios increases to 0.75 %.

Finally, at $t = 20$ s and $t = 25$ s, we unplug inverters 2 and 3, respectively: since inverter 1 must provide all the power required by the load, the amplitude of its output current increases (Figure 7.10e). Figure 7.10a shows that also its imbalance ratio increases to 1 % and then to 1.65 %. However, we notice that, during the whole experiment, the imbalance ratio is quite small and always lower than the maximum value (3 %) recommended by IEEE in [IEE09].

Voltage regulation at the PCCs with nonlinear load

In this scenario, we use nonlinear loads in order to evaluate the capability of PnP controllers to reject higher-order harmonics.

At time $t = 0$ s, inverters 1 and 2 are connected to the diode rectifier shown in Figure 7.8a. Hence, the active power provided by inverter 3 is zero (see Figure 7.11c) and the Total Harmonic Distortion (THD) index[6] [IEE09] is higher for the voltages at PCCs 1 and 2 (as shown in Figure 7.11e).

At $t = 5$ s, we increase the power required at the PoL by connecting a resistive load ($R = 154\ \Omega$) in parallel with the nonlinear one.

The plugging in operation of inverter 3 is performed at $t = 15$ s. Notice that the frequencies are promptly restored to the nominal value (variations less than 0.2 Hz), total active power is equally shared between all inverters and THDs are reduced for all inverters.

In order to assess the robustness of local PnP regulators to unknown load dynamics, at times $t = 25$ s and $t = 35$ s, we switch the resistive load to $R = 460\ \Omega$ and $R = 154\ \Omega$, respectively. Figures 7.11a and 7.11b show fast transients of voltages and frequencies at the PCCs.

Finally, at $t = 40$ s and $t = 45$ s, we unplug inverter 3 and 2, respectively. Consequently, the THD of the voltage at PCC 1 increases. However, as shown in Figure 7.11e, the THD values are always below the maximum limit (5%) recommended in [IEE09]. Concluding, this experiment reveals

[6] For the sake of simplicity, in Figure 7.11e we show only the THD indices of phase a of the corresponding PCC voltages.

that, even in absence of inner resonant controllers, PnP regulators are capable to guarantee high levels of robustness to load variations and harmonic attenuation.

7.5.3 Primary and secondary layers validation

In this section, we validate the combination of the coordinated control layer presented in Section 7.4 and PnP primary regulators.

As a first test, we consider the same experimental scenario as in Section 7.5.2, complemented with the coordinated controllers presented in Section 7.4.1 for voltage tracking at the PoL. This operation is desirable because, as shown in Figure 7.11a, PnP regulators alone fail to keep the PoL voltage at the nominal value, even though the voltages at the PCCs are stabilized. As highlighted in Section 7.4, this issue is due to the fixed voltage set-points for the PnP controllers.

In this experiment, we activate coordinated controllers at time $t = 20$ s. Consequently, as shown in Figure 7.12a, the voltages at the PCCs increase in order to track the nominal PoL voltage. Moreover, the proposed coordinated controllers are capable to keep the PoL voltage at the desired level (by regulating the voltages at the PCCs) even when load changes (at times $t = 25$ s and $t = 35$ s) and disconnection of inverters (at $t = 40$ s and $t = 45$ s) are performed (see Figure 7.12). We also highlight that the presence of the coordinated controllers does not affect the frequency profiles (see Figure 7.12b). On the other hand, Figure 7.12d reveals that the total reactive power is still not shared equally between the inverters.

In order to ameliorate also aspect, we run a second experiment in which the previous control scheme is complemented with coordinated controllers for reactive power sharing (described in Section 7.4.2). In particular, we notice that, right after their activation (at time $t = 20$ s), the total reactive power is equally shared (see Figure 7.13b, to be compared with Figure 7.12d). This goal is achieved through the computation of terms ΔV_i^Q in (7.11), which are shown in Figure 7.13a.

7.6 Final comments

In this chapter, we showed how to adapt the PnP control scheme [RSFT15] for voltage and frequency regulation in AC ImGs to bus-connected topologies. We have also proposed a secondary control layer and performed an experimental validation of the overall control architecture. Using the parallel connection of three VSCs, we showed that stability, accurate tracking

of the voltage at PoL and reactive power sharing can be successfully ensured. Moreover, experiments with linear and nonlinear loads show that the harmonic distortion is kept within acceptable bounds. In our implementation, time-synchronization of DGU clocks and the secondary control layer assume all-to-all communication among DGUs. Future research will focus on distributing these computations as well, by exploiting only partial communication among DGUs and, as in [SSD+14], consensus-like protocols for estimating the average of global variables.

In the next chapter, we present two network reduction methods that allow to design decentralized PnP voltage and frequency controllers for AC ImGs with general topologies (hence also for bus-connected networks).

7.7 Appendix

7.7.1 Proof of Lemma 7.1

Proof. Let us consider a bus-connected ImG composed of N DGUs (see, e.g., Figure 7.2), and let (7.1a) describe the dynamics of DGU i. For $1 \leq j \leq N$, $j \neq i$, by applying KVL and Park's transformation, one gets

$$V_i^{dq} - V_j^{dq} = R_i I_i^{dq} + L_i \frac{\mathrm{d}}{\mathrm{d}t} I_i^{dq} + \mathrm{i}\omega_0 L_i I_i^{dq} - R_j I_j^{dq} - L_j \frac{\mathrm{d}}{\mathrm{d}t} I_j^{dq} - \mathrm{i}\omega_0 L_j I_j^{dq}. \quad (7.12)$$

By exploiting QSL approximations [RSFT15, VSZ95], in (7.12), we set $\frac{\mathrm{d}}{\mathrm{d}t} I_i^{dq} = 0$, $\forall i \in \mathcal{V}$. Hence, equation (7.12) becomes

$$V_i^{dq} - V_j^{dq} = R_i I_i^{dq} + \mathrm{i}\omega_0 L_i I_i^{dq} - R_j I_j^{dq} - \mathrm{i}\omega_0 L_j I_j^{dq}\,, \qquad 1 \leq j \leq N,\ j \neq i.$$

Next, recalling that $Z_i = R_i + \mathrm{i}\,\omega_0 L_i$, one gets

$$I_j^{dq} = \frac{V_j^{dq} - V_i^{dq}}{Z_j} + \frac{Z_i}{Z_j} I_i^{dq}\,, \qquad 1 \leq j \leq N,\ j \neq i. \quad (7.13)$$

Applying KCL at the PoL, we have

$$I_i^{dq} + \sum_{j \neq i} I_j^{dq} = I_L^{dq} \quad (7.14)$$

and, inserting (7.13) in (7.14), we obtain

$$I_i^{dq} = \frac{I_L^{dq}}{\left(1 + \sum_{j \neq i} \frac{Z_i}{Z_j}\right)} + \left(\sum_{j \neq i} \frac{1}{Z_j}\right) \frac{V_i^{dq}}{\left(1 + \sum_{j \neq i} \frac{Z_i}{Z_j}\right)} - \sum_{j \neq i} \frac{V_j^{dq}}{Z_j} \frac{1}{\left(1 + \sum_{j \neq i} \frac{Z_i}{Z_j}\right)}.$$

(7.15)

Since in (7.15) it holds

$$\frac{1}{\left(1+\sum_{j\neq i}\frac{Z_i}{Z_j}\right)}=\frac{1}{\left(Z_i\sum_{k=1}^{N}\frac{1}{Z_k}\right)},$$

by defining $\frac{1}{Z_{ij}}$ as in (7.2), one has

$$\left(\sum_{j\neq i}\frac{1}{Z_j}\right)\frac{1}{\left(Z_i\sum_{k=1}^{N}\frac{1}{Z_k}\right)}=\sum_{j\neq i}\frac{1}{Z_{ij}}. \tag{7.16}$$

At this point, by replacing (7.16) in (7.15), and then substituting the resulting expression into (7.1a), one gets that the dynamics of V_i^{dq} have the form (6.9a), where the admittances of the equivalent load-connected network are given by (7.2), while the effect of the eliminated node (i.e. the PoL) at the i-th PCC is accounted by (7.3). □

7.7.2 Derivation of the approximate model (7.10)

We start by using the following first-order approximation of each DGU equipped with the corresponding stabilizing PnP controller

$$V_i^d=\frac{1}{1+sT_i^d}V_i^{*d}\qquad V_i^q=\frac{1}{1+sT_i^q}V_i^{*q}.$$

Since the overall PnP architecture is stable, and due to the presence of output impedance for each DGU, we can also state that

$$V_{PoL,i}^d=\mu_i^d e^{-s\tau_i^d}V_i^d\qquad V_{PoL,i}^q=\mu_i^q e^{-s\tau_i^q}V_i^q$$

where μ_i^d, μ_i^q, τ_i^d and τ_i^q depend on the output impedance. Using (7.8), assuming $\tau_i=\tau_i^d\approx\tau_i^q$, $T_i=T_i^d\approx T_i^q$, and setting $\mu_i=\sqrt{(\mu_i^d)^2+(\mu_i^q)^2}$, we obtain

$$V_{PoL,i}=\frac{\mu_i e^{-s\tau_i}}{1+sT_i}V_i^*\qquad \phi_{PoL,i}=\phi_i^*. \tag{7.17}$$

Therefore, using (7.17) and (7.7), we can provide a linear model of the effect of V_i^* and ϕ_i^* on V_{PoL} and ϕ_{PoL}, respectively. Furthermore, since

$V_i^* = V_{PoL}^* + \Delta V_{PoL}$ and $\phi_i^* = 0 + \Delta\phi_{PoL}$, we also obtain a small-signal model of the effect of ΔV_{PoL} and $\Delta\phi_{PoL}$ on V_{PoL} and ϕ_{PoL}, respectively.

As regards the phase deviation, since $\phi_{PoL,i} = \phi_i^* = \Delta\phi_{PoL}$, we can easily derive a simplified model as

$$\phi_{PoL} = \frac{\Delta\phi_{PoL}}{N}$$

which can be used for computing the PI control action in (7.9b).

For deriving a simplified model of the amplitude deviation, the closed-loop dynamics of the DGU equipped with its corresponding voltage and frequency regulator must be considered. The second control layer should act mostly when the primary PnP layer is at steady-state. Hence, using (7.17), we can write a local approximate dynamics as

$$V_{PoL,i} = \frac{\mu_i e^{-s\tau_{PoL}}}{1 + sT_{PoL}} V_i^* = \frac{\mu_i e^{-s\tau_{PoL}}}{1 + sT_{PoL}} (V_{PoL}^* + \Delta V_{PoL})$$

where $\tau_{PoL} = \max(\tau_1, \ldots, \tau_N)$ and $T_{PoL} = \max(T_1, \ldots, T_N)$. Next, using (7.7), we can derive

$$V_{PoL} = \frac{\mu e^{-s\tau_{PoL}}}{1 + sT_{PoL}} V_{PoL}^* + \frac{\mu e^{-s\tau_{PoL}}}{1 + sT_{PoL}} \Delta V_{PoL} \tag{7.18}$$

where $\mu = \sum_{i=1}^{N} \frac{\mu_i}{N}$. Concluding, from (7.18), one has that the transfer function that describes the relation between ΔV_{PoL} and V_{PoL} is (7.10).

7.7.3 Electrical and control parameters of the experimental tests

Parameter	Symbol	Value	Units
Virtual resistance	$R_{i,v}$	3	Ω
Virtual inductance	$L_{i,v}$	0.03	H

Table 7.1: Virtual impedance parameters.

Parameter	Symbol	Value
Module proportional term	K_{PV}	10^{-3}
Module integral term	K_{IV}	0.6
Phase proportional term	$K_{P\phi}$	10^{-3}
Phase integral term	$K_{I\phi}$	4

Table 7.2: Voltage tracking at the PoL.

Parameter	Symbol	Value
Reactive power proportional term	K_{PQ}	10^{-4}
Reactive power integral term	K_{IQ}	10^{-2}

Table 7.3: Reactive power sharing.

Parameter	Symbol	Value	Units
PCC reference voltage	V_{ref}	230	V
ImG frequency	f_0	50	Hz
Switching frequency	f_{sw}	10	kHz
Filter resistance	R_{ti}	0.1	Ω
Filter inductance	L_{ti}	1.8	mH
Filter capacitance	C_{ti}	25	μF
Line resistance	R_i	0.1	Ω
Line inductance	L_i	1.8	mH
Phase resistive load	$R_{a,b,c}$	57-115-230-460	Ω
Nonlinear load	R_{NL}	460	Ω

Table 7.4: Electrical setup parameters.

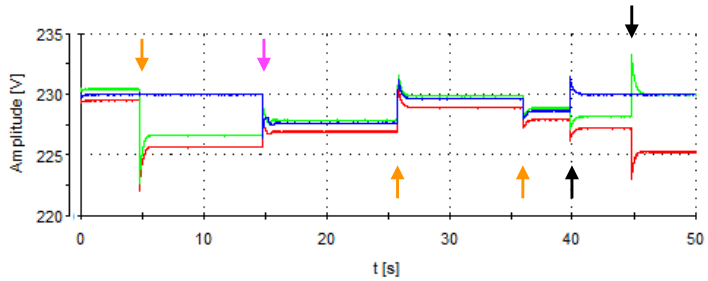

(a) RMS voltages of phase a at PCCs.

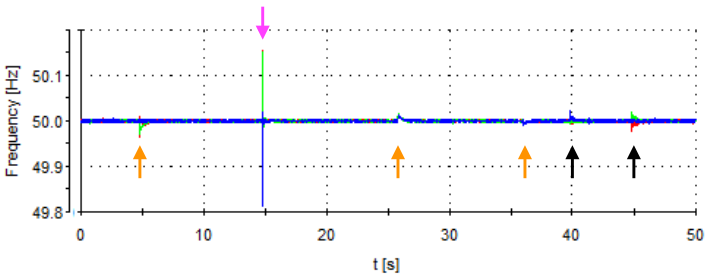

(b) Frequencies of phase a voltages at PCCs.

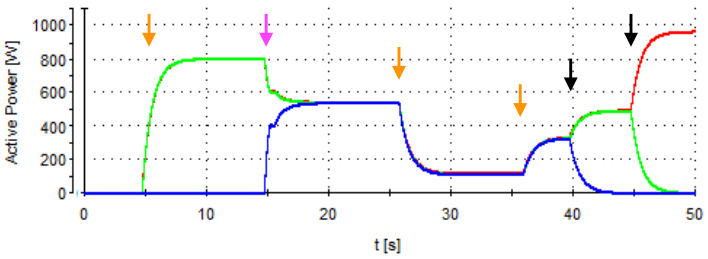

(c) Active power provided by the inverters to the load.

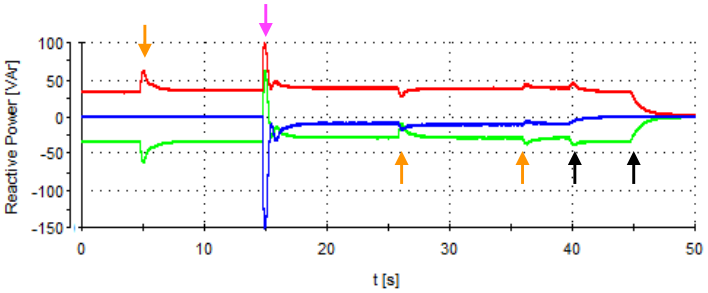

(d) Reactive power provided by the inverters to the load.

Figure 7.9: Voltage regulation at the PCCs with resistive load (Section 7.5.2). Red, green and blue lines are, respectively, for VSCs 1, 2 and 3. Load change, plug-in and unplugging events are indicated with orange, magenta and black arrows, respectively. The plots in Figures 7.9a and 7.9b refer to the voltages of phase a of the three-phase converters composing the ImG (see the scheme in Figure 7.8b).

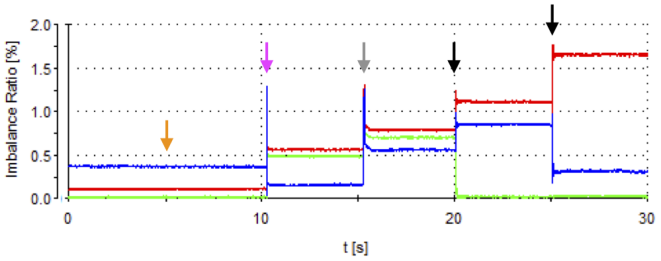

(a) Imbalance ratios. Red, green and blue lines are, respectively, for VSC 1, 2 and 3. Load connection, phase b load unbalancing, phase c load unbalancing and unplugging events are indicated with orange, magenta, grey and black arrows, respectively.

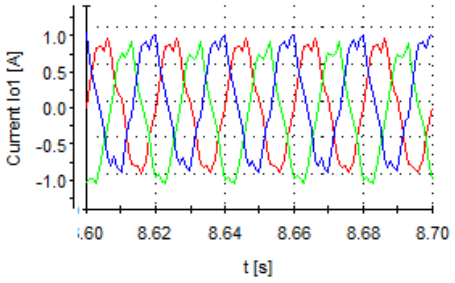

(b) Output current for inverter 1 around time $t = 8.65$ s (effect of balanced load connection at $t = 5$ s). Red, green and blue lines are for phase a, b and c, respectively.

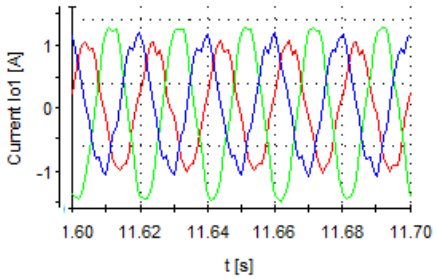

(c) Output current for inverter 1 around time $t = 11.65$ s (effect of load phase b unbalancing at $t = 10$ s). Red, green and blue lines are for phase a, b and c, respectively.

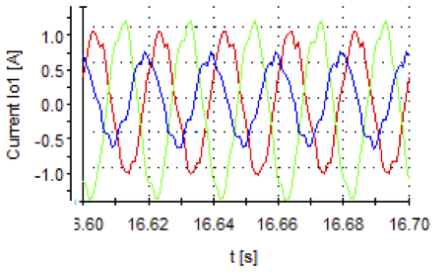

(d) Output current for inverter 1 around time $t = 16.65$ s (effect of load phase c unbalancing at $t = 15$ s). Red, green and blue lines are for phase a, b and c, respectively.

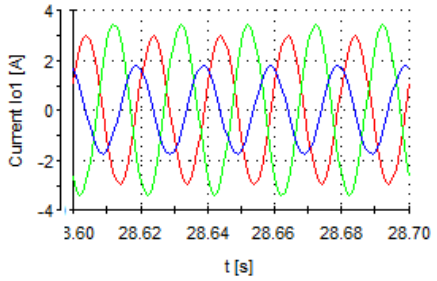

(e) Output current for inverter 1 around time $t = 28.65$ s (after the unplugging of VSCs 2 and 3). Red, green and blue lines are for phase a, b and c, respectively.

Figure 7.10: Voltage regulation at the PCCs with unbalanced load (Section 7.5.2).

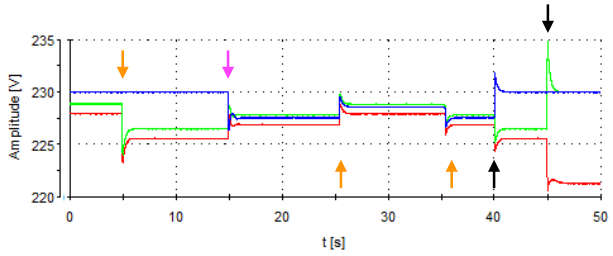

(a) RMS voltages of phase a at PCCs.

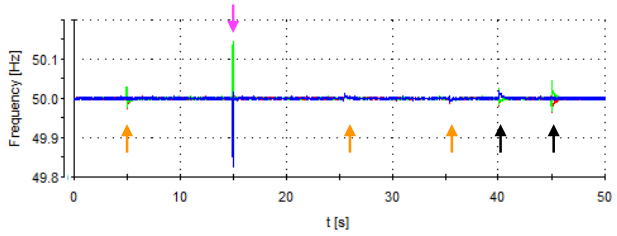

(b) Frequencies of phase a voltages at PCCs.

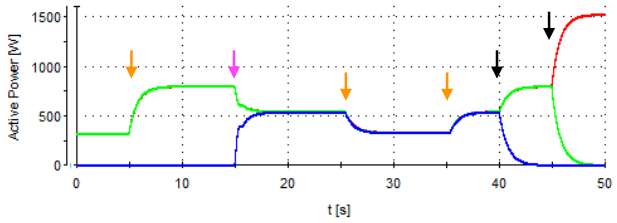

(c) Active power provided by the inverters to the load.

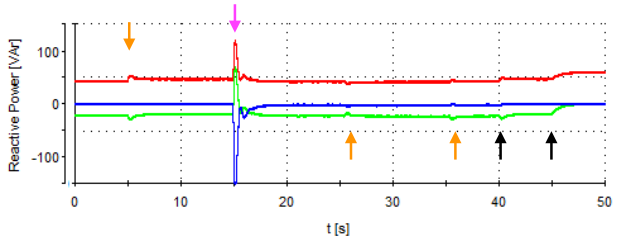

(d) Reactive power provided by the inverters to the load.

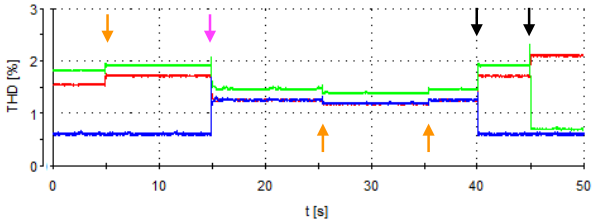

(e) Total harmonic distortion.

Figure 7.11: Voltage regulation at the PCCs with nonlinear load (Section 7.5.2). Red, green and blue lines are, respectively, for VSC 1, 2 and 3. Load change, plug-in and unplugging events are indicated with orange, magenta and black arrows, respectively. The plots in Figures 7.11a and 7.11b refer to the voltages of phase a of the three-phase converters composing the microgrid (see the scheme in Figure 7.8b).

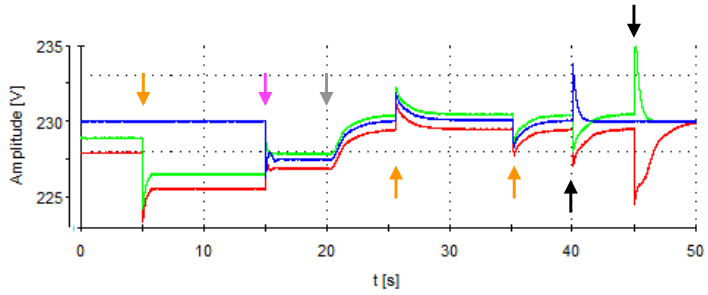

(a) RMS voltages of phase a at PCCs.

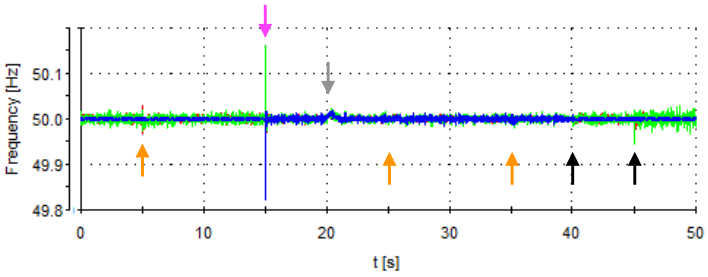

(b) Frequencies of phase a voltages at PCCs.

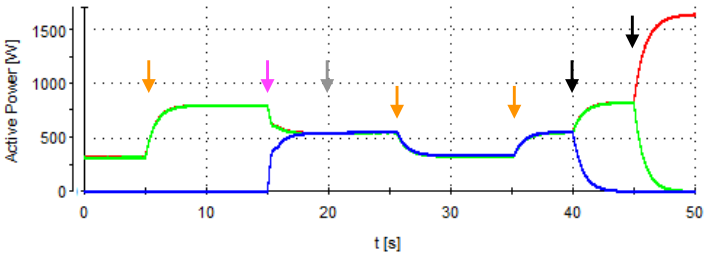

(c) Active power provided by the inverters to the load.

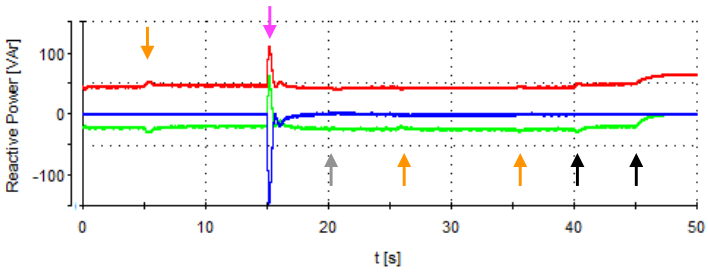

(d) Reactive power provided by the inverters to the load.

Figure 7.12: PnP regulators and coordinated controllers for voltage tracking at the PoL with nonlinear load. Red, green and blue lines are, respectively, for VSC 1, 2 and 3. Load change, plug-in and unplugging events are indicated with orange, magenta and black arrows, respectively. Moreover, the grey arrow denotes the activation of secondary controllers described in Section 7.4.1. The plots in Figures 7.12a and 7.12b refer to the voltages of phase a of the three-phase converters composing the microgrid (see the scheme in Figure 7.8b).

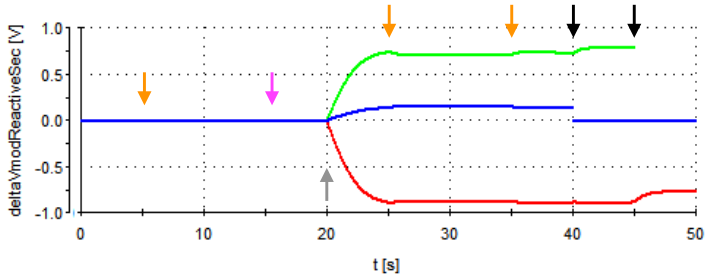

(a) Amplitude deviations ΔV_i^Q in (7.11) leading to the sharing of total reactive power.

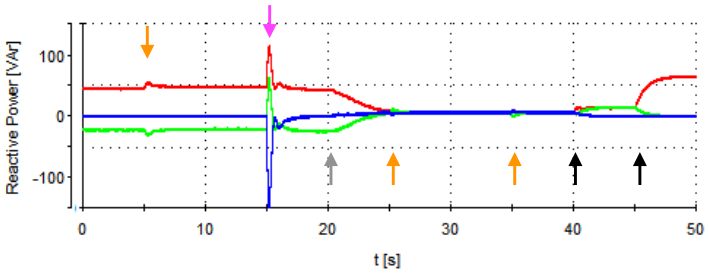

(b) Reactive power produced by each VSC.

Figure 7.13: PnP regulators and coordinated controllers for voltage tracking at the PoL and reactive power sharing with nonlinear load. Red, green and blue lines are respectively for VSC 1, 2 and 3. Load change, plug-in and unplugging events are indicated with orange, magenta and black arrows, respectively. Moreover, the grey arrow denotes the simultaneous activation of secondary controllers described in Sections 7.4.1 and 7.4.2.

Chapter 8

Plug-and-play control of AC islanded microgrids with general topologies

Contents

8.1 Introduction 184
8.2 Kron reduction methods for electrical networks 186
8.2.1 AC-KR 187
8.2.2 Instantaneous KR 191
8.3 Approximate KR methods 192
8.3.1 Approximate AC-KR 193
8.3.2 Hybrid KR 194
8.3.3 Asymptotic equivalence between original and reduced network models 196
8.3.4 Generalization to three-phase linear networks in *dq* coordinates 198
8.4 Numerical examples 199
8.5 Kron reduction of microgrids 203
8.5.1 Islanded microgrid associated graph 203
8.5.2 DGU and line electrical models 203
8.5.3 Plug-and-play design for microgrids with general topologies 204
8.6 Simulation of a 21-bus network 205
8.6.1 Islanded microgrid topology 206
8.6.2 Plug-and-play control design 207
8.6.3 Simulation results 209
8.7 Final comments 211
8.8 Appendix 212
8.8.1 Original and reduced parameters of Examples 8.3 and 8.4 212

8.8.2 Electrical parameters of the 21-bus network . . . 212

8.1 Introduction

In this chapter, we present two methods for simplifying AC linear electrical network. As will be detailed in the sequel, the proposed procedures rely on Kron Reduction (KR) and can be exploited for designing PnP decentralized voltage and frequency controllers for AC ImGs with arbitrary topologies. The presented algorithms aim to overcome one relevant limitation of the existing network reduction approaches based on KR.

KR is standard tool for simplifying linear electrical networks [Kro39] while preserving the behavior of electrical variables at target nodes. KR assumes network nodes are classified either as internal or boundary nodes, and provides an algebraic procedure for computing: (i) the topology of a new network connecting boundary nodes only, (ii) the value of admittances related to new edges and (iii) equivalent currents supplied at boundary nodes accounting for the effect of internal currents in the original network. Graph-theoretical properties of KR have been analyzed in [VdS10, DB13] for DC resistive networks. A general analysis of AC three-phase balanced circuits in Periodic Sinusoidal Steady State (PSSS), termed AC-KR, can be found in [CT12]. Recently, several studies focused on generalizations of KR methods preserving the electrical behavior of boundary variables not only in PSSS, but also during transients [VdS10, CT12, CT14, DJDH14]. In these *instantaneous* KR procedures, network line admittances are replaced by differential models, and sufficient conditions guaranteeing well-posedness of the network reduction process have been studied. Existing instantaneous KR methods, however, have a relevant limitation: they do not guarantee that reduced line models will have the same structure of the original ones, e.g. simple *RL* lines could result in reduced lines with more complex dynamics [DJDH14]. Therefore, even though this does not happen for simple cases such as DC resistive or homogeneous networks [CT12, DB13, VdS10], in general one faces the problem of devising *approximate* instantaneous KR methods for preserving selected features of line models.

In this chapter, we consider *RL* lines and propose two novel approximate KR methods termed, respectively, approximate AC Kron Reduction (aAC-KR) and hybrid Kron Reduction (hKR). We show that these techniques ensure asymptotic equivalence between original and reduced

models, if networks reach a PSSS. Unlike the instantaneous KR procedures in [VdS10, CT12, CT14, DJDH14], aAC-KR and hKR provide reduced circuits whose lines have first-order transfer functions, as the original lines. The features of our methods are then validated through numerical simulations.

In order to demonstrate the practical relevance of aAC-KR and hKR, in the second part of the chapter we show how to use them to design decentralized voltage and frequency controllers for AC ImGs. KR has already found applications to ImGs; for instance, in [LD14, SOA$^+$14] KR is advocated as the procedure for mapping ImGs with general topologies into their equivalent load-connected circuits[1]. This can be done by labeling other load nodes as internal and applying KR to eliminate them. Following this procedure, any control design method for load-connected ImG could be directly extended to ImGs with arbitrary topologies by performing control synthesis on the reduced network. In particular, we focus on the PnP decentralized scheme summarized in Chapter 6. We show that both aAC-KR and hKR can be used to extend the aforementioned design method (which assumes load-connected ImGs and RL lines) to arbitrary interconnections of DGUs and loads, while preserving the structure of transfer functions describing power lines. The design of PnP controllers based on the proposed approximate KR methods is tested on a 21-bus ImG derived from the IEEE test feeder in [fee11], enhanced with switches yielding changes of line topology and plug-in/out of DGUs. Simulations performed in PSCAD confirm the applicability of our methods to control of ImGs.

The chapter is structured as follows. Section 8.2 summarizes the existing KR methods, highlighting the corresponding features and limitations. In Section 8.3, we present the approximate KR methods (aAC-KR and hKR), and in Section 8.4 we assess their performances through numerical simulations. In Section 8.5 we show how to combine the control design methodology summarized in Chapter 6 with the proposed approximate KR techniques. Simulations illustrating the joint use of aAC-KR/hKR and PnP design are given in Section 8.6. Section 8.7 is devoted to conclusions.

When clear from the context, we omit time dependence of electrical quantities.

[1] We recall that, in load-connected ImGs, loads appear only at the output terminals of inverters.

8.2 Kron reduction methods for electrical networks

Let $\mathcal{G} = (\mathcal{V}, \mathcal{E}, W)$ be the weighted directed graph[2] associated with a given circuit. We notice that, in this chapter, weights can be real numbers, complex numbers or SISO transfer functions (in this case, we replace W with $W(s)$). Following the formalism introduced in [VdS10, CT12, CT14], each vertex corresponds to a node of the network and each edge is a branch of the circuit (see the example in Figure 8.1). For performing KR, the vertex set $\mathcal{V}$ is partitioned into a set of *boundary* nodes $\mathcal{V}_b$ and a set of *internal* nodes $\mathcal{V}_\ell$. More specifically, subset $\mathcal{V}_b$ identifies the nodes at which the behavior of electrical variables must be preserved, while $\mathcal{V}_\ell$ contains the nodes to be eliminated.

We denote the *nodal* currents injected at boundary nodes with I_b; the nodal currents injected at internal nodes are I_ℓ and they are positive if entering into nodes. *Nodal* voltages V are partitioned analogously. In this work, each edge $e_1, ..., e_{|\mathcal{E}|} \in \mathcal{E}$ corresponds to an electric RL line and the orientation of the edges is arbitrary. We adopt the following sign convention: reference directions of *line* currents coincide with edges orientations and *line* voltages V_e, $e = (i, j) \in \mathcal{E}$ are defined as $V_i - V_j$. Moreover, the weight of every edge is given by its admittance transfer function $W_e(s)$ accounting for the dynamics of line $e \in \mathcal{E}$.

Let us now consider an electrical network composed of $n > 0$ nodes, partitioned into $n_b > 0$ boundary nodes and $n_\ell = n - n_b > 0$ internal nodes. We collect the nodal currents in the following vector: $I = \left[I_b^T, I_\ell^T\right]^T$, where $I_b = \left[I_{b_1}, ..., I_{b_{n_b}}\right]^T$ and $I_\ell = \left[I_{\ell_1}, ..., I_{\ell_{n_\ell}}\right]^T$. Nodal voltages $V = \left[V_b^T, V_\ell^T\right]^T$ are partitioned analogously. In order to account for the network interconnections, by KCL and KVL one obtains [DJDH14]:

$$\begin{bmatrix} I_b(s) \\ I_\ell(s) \end{bmatrix} = \begin{bmatrix} \mathbb{L}_{bb}(s) & \mathbb{L}_{b\ell}(s) \\ \mathbb{L}_{\ell b}(s) & \mathbb{L}_{\ell\ell}(s) \end{bmatrix} \begin{bmatrix} V_b(s) \\ V_\ell(s) \end{bmatrix}, \tag{8.1}$$

that is $I(s) = \mathbb{L}(s)V(s)$. Matrix $\mathbb{L}(s)$ is the graph Laplacian[3] of the graph $\mathcal{G}$ with weights

$$W_{ij}(s) = \frac{1}{R_{ij} + sL_{ij}} \tag{8.2}$$

[2] See Appendix A.2 for basic definitions in algebraic graph theory.
[3] See Appendix A.2 for the definition of Laplacian matrix of a graph.

modeling the admittance transfer function associated with edges $(i,j) \in \mathcal{E}$. We recall that, with a Laplacian matrix is possible to associate a unique graph, up to the orientation of edges. By construction, one has $\mathbb{L}_{ij}(s) = -W_{ij}(s)$ if $(i,j) \in \mathcal{E}$ and $\mathbb{L}_{ii}(s) = -\sum_{j \in \mathcal{N}_i} \mathbb{L}_{ij}(s)$.

At this point, we have all the elements for introducing KR. In particular, in the sequel we will focus on summarizing two existing approaches, namely KR in phasors domain [CT12] (called hereafter AC-KR) and instantaneous KR [DJDH14].

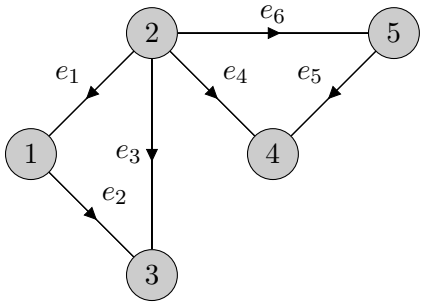

Figure 8.1: Graph representing an electrical network.

8.2.1 AC-KR

Let us consider the directed graph $\mathcal{G} = (\mathcal{V}, \mathcal{E}, W(s))$, where transfer functions $W_{ij}(s)$ in the form (8.2) represent the relation between $\mathscr{L}[V_i(t) - V_j(t)]$ and $\mathscr{L}[I_{ij}(t)]$, with $\mathscr{L}[\cdot]$ identifying the Laplace-transform operator. We assume the network is in PSSS with angular frequency ω_0, hence $V_i(t) = A_i \cos(\omega_0 t + \phi_i)$ and $I_i(t) = B_i \cos(\omega_0 t + \gamma_i)$, $\forall i \in \mathcal{V}$. Moreover, we can associate each cosinusoid $V_i(t)$ with the corresponding rotating phasor $\vec{V}_i = A_i \exp(\mathrm{i}(\omega_0 t + \phi_i))$ [DK84]. Current phasors $\vec{I}_i$ are defined analogously. Let us now define vectors $\vec{V} = [\vec{V}_1, \vec{V}_2, ..., \vec{V}_n]^T$, $\vec{I} = [\vec{I}_1, \vec{I}_2, ..., \vec{I}_n]^T$, and the impedance $Z_{ij} = R_{ij} + \mathrm{i}\omega_0 L_{ij}$ of line (i,j). The relation between nodal currents and nodal voltages is then given by:

$$\vec{I} = \mathbb{L}^{AC} \cdot \vec{V}, \tag{8.3}$$

where $\mathbb{L}^{AC}_{ij} = -1/Z_{ij}$, if $(i,j) \in \mathcal{E}$, and $\mathbb{L}^{AC}_{ii} = \sum_{j \in \mathcal{N}_i} 1/Z_{ij}$. In particular, by construction, $\mathbb{L}^{AC} = \mathbb{L}(\mathrm{i}\omega_0)$, with $\mathbb{L}$ defined in (8.1).

Definition 8.1 (AC-KR)**.** *Let $\vec{V}$, $\vec{I}$ and $\mathbb{L}^{AC}$ be partitioned into boundary and internal components as in* (8.1) *and assume $\mathbb{L}^{AC}_{\ell\ell}$ is invertible*[4]*. AC-*

[4]Conditions for the invertibility of $\mathbb{L}^{AC}_{\ell\ell}$ have been studied in [Sch15, Lemma 2.4.20].

KR is given by the graph $\mathcal{G}_{red}^{AC} = \left(\mathcal{V}_b, \mathcal{E}_{red}, W_{red}^{AC}\right)$ *associated with the reduced Laplacian*

$$\mathbb{L}_{red}^{AC} = \mathcal{K}\left(\mathbb{L}^{AC}\right) = \mathbb{L}_{bb}^{AC} - \mathbb{L}_{b\ell}^{AC}(\mathbb{L}_{\ell\ell}^{AC})^{-1}\mathbb{L}_{\ell b}^{AC}, \tag{8.4a}$$

and

$$\vec{I}_b = \mathbb{L}_{red}^{AC}\vec{V}_b - \mathcal{T}^{AC}\vec{I}_\ell \tag{8.4b}$$

$$\mathcal{T}^{AC} = -\mathbb{L}_{b\ell}^{AC}(\mathbb{L}_{\ell\ell}^{AC})^{-1}, \tag{8.4c}$$

where $\mathcal{K}(\cdot)$ *denotes the KR operator and* $\mathcal{T}^{AC}$ *is the accompanying matrix of* $\mathbb{L}^{AC}$*.*

It can be shown that the matrix $\mathbb{L}_{red}^{AC}$ in (8.4a)-(8.4b) is still the Laplacian of the Kron reduced graph $\mathcal{G}_{red}^{AC}$ [CT12] that is uniquely defined up to the orientation of edges (which can be arbitrarily chosen). Moreover, $W_{red,ij}^{AC} = -\left(\mathbb{L}_{red}^{AC}\right)_{ij}$ for $(i,j) \in \mathcal{E}_{red}$, while $\mathcal{T}^{AC}$ provides the vector of equivalent nodal currents

$$\tilde{\vec{I}}_b = \mathcal{T}^{AC}\vec{I}_\ell \tag{8.5}$$

to be injected at boundary nodes of $\mathcal{G}_{red}^{AC}$ in order to account for the effect of eliminated currents $\vec{I}_\ell$.

It can be shown that, as long as one provides the same voltages $\vec{V}_b$ in $\mathcal{G}$ and $\mathcal{G}_{red}^{AC}$, the same current absorption I_b is obtained in both cases, if currents (8.5) are injected into boundary nodes $\mathcal{G}_{red}^{AC}$ [DB13, CT12].

At this point, it is convenient to show, through a simple example, how to perform AC-KR, hence computing $\mathbb{L}^{AC}$, $\mathbb{L}_{red}^{AC}$ and $\mathcal{T}^{AC}$, defined in (8.3), (8.4a) and (8.4c), respectively.

Example 8.1. *We consider the linear, single-phase circuit* $\mathcal{G}$ *shown in Figure 8.2a, and we assume the network is PSSS with angular frequency* $\omega_0 = 2\pi f_0$*,* $f_0 = 50$ Hz. Consequently, all the voltages and currents can be represented through their associated rotating phasors, i.e. $\vec{V} = [\vec{V}_1, \vec{V}_2, \vec{V}_3, \vec{V}_4]^T$, $\vec{I} = [\vec{I}_1, \vec{I}_2, \vec{I}_3, \vec{I}_4]^T$. The vertex set of $\mathcal{G}$ is partitioned in boundary and internal nodes as follows: $\mathcal{V} = \{\mathcal{V}_b, \mathcal{V}_\ell\}$, where $\mathcal{V}_b = \{1,2,3\}$ and $\mathcal{V}_\ell = \{4\}$. As regards the edges $e_1, e_2, e_3 \in \mathcal{E}$, they correspond to RL power lines, and their parameters are reported in Table 8.1. Our aim is to derive, via AC-KR, the equivalent network $\mathcal{G}_{red}^{AC}$ connecting boundary nodes only (see

Figure 8.2b). Notice that this operation amounts to a Y−Δ transformation. We start by writing the incidence and weights matrices of $\mathcal{G}$. These are

$$B = \begin{bmatrix} -1 & 0 & 0 \\ 0 & -1 & 0 \\ 0 & 0 & -1 \\ 1 & 1 & 1 \end{bmatrix} \tag{8.6}$$

and

$$W^{AC} = \begin{bmatrix} W_{14}^{AC} & 0 & 0 \\ 0 & W_{24}^{AC} & 0 \\ 0 & 0 & W_{34}^{AC} \end{bmatrix},$$

where

$$W_{14}^{AC} = \frac{1}{Z_{14}} = 0.247 - 1.552\mathrm{i}$$
$$W_{24}^{AC} = \frac{1}{Z_{24}} = 0.041 - 0.451\mathrm{i}$$
$$W_{34}^{AC} = \frac{1}{Z_{34}} = 0.092 - 0.290\mathrm{i}.$$

Then, we compute the Laplacian matrix $\mathbb{L}^{AC} = B \cdot W^{AC} \cdot B^T$, and partition it as in (8.1), thus having:

$$\mathbb{L}^{AC} = \begin{bmatrix} \mathbb{L}_{bb}^{AC} & \mathbb{L}_{b\ell}^{AC} \\ \mathbb{L}_{\ell b}^{AC} & \mathbb{L}_{\ell\ell}^{AC} \end{bmatrix},$$

with

$$\mathbb{L}_{bb}^{AC} = \mathrm{diag}\left[0.247 - 1.552\mathrm{i}, 0.041 - 0.451\mathrm{i}, 0.092 - 0.289\mathrm{i}\right],$$

$$\mathbb{L}_{b\ell}^{AC} = \begin{bmatrix} -0.247 + 1.552\mathrm{i} \\ -0.041 + 0.451\mathrm{i} \\ -0.092 + 0.289\mathrm{i} \end{bmatrix}, \qquad \mathbb{L}_{\ell b}^{AC} = (\mathbb{L}_{b\ell}^{AC})^T,$$

and

$$\mathbb{L}_{\ell\ell}^{AC} = 0.380 - 2.292\mathrm{i}.$$

Next, using (8.4a), one obtains the reduced Laplacian

$$\mathbb{L}_{red}^{AC} = \begin{bmatrix} 0.087 - 0.501\mathrm{i} & -0.026 + 0.305\mathrm{i} & -0.061 + 0.196\mathrm{i} \\ -0.026 + 0.305\mathrm{i} & 0.039 - 0.363\mathrm{i} & -0.014 + 0.057\mathrm{i} \\ -0.061 + 0.196\mathrm{i} & -0.014 + 0.057\mathrm{i} & 0.075 - 0.253\mathrm{i} \end{bmatrix}, \tag{8.7}$$

while the accompanying matrix $\mathcal{T}^{AC}$, is given by (8.4c), as

$$\mathcal{T}^{AC} = \begin{bmatrix} 0.676 - 0.004\mathrm{i} \\ 0.194 - 0.014\mathrm{i} \\ 0.129 + 0.019\mathrm{i} \end{bmatrix}. \tag{8.8}$$

At this point, we have all the elements for computing the weights of the reduced edges $r_1, r_2, r_3 \in \mathcal{E}_{red}$ as $W^{AC}_{red,ij} = -\left(\mathbb{L}^{AC}_{red}\right)_{ij}$ (see Table 8.1 for the corresponding line parameters). Moreover, from (8.5) the equivalent vector of currents injected at boundary nodes of $\mathcal{G}^{AC}_{red}$ is

$$\tilde{\vec{I}}_b = \mathcal{T}^{AC}\vec{I}_4.$$

Edge	Resistance (Ω)	Inductance (mH)
e_1	0.1	2
e_2	0.2	7
e_3	1	10
r_1	0.2746	10.354
r_2	1.4482	14.8132
r_3	3.9315	52.3706

Table 8.1: Example 8.1 - Line parameters of the original and reduced network.

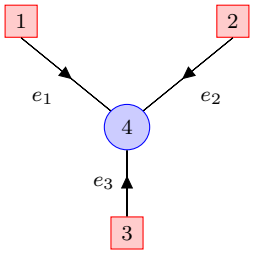

(a) Original network $\mathcal{G}$.

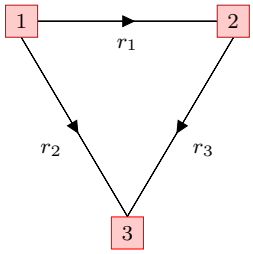

(b) Reduced network $\mathcal{G}^{AC}_{red}$.

Figure 8.2: Example 8.1 - Original and reduced networks. Boundary and interior nodes are represented by red squares and blue circles, respectively.

In the next section, we summarize a KR method which, differently from AC-KR, allows to reduce linear circuits while preserving the behavior of boundary variables also in non-stationary regime (e.g. during transients).

8.2.2 Instantaneous KR

Instantaneous KR is a general reduction method which can be applied to any system composed of passive R, L, C components while guaranteeing the equivalence between original and reduced boundary variables not necessarily in PSSS [DJDH14]. This method, however, presents some drawbacks (discussed later in this section) which further motivate the need for the approximated KR methods proposed in Section 8.3.

Definition 8.2 (Instantaneous KR)**.** *Assume $\mathbb{L}_{\ell\ell}(s)$ in (8.1) is invertible*[5] *for some $s \in \mathbb{C}$. Instantaneous KR is given by the graph $\mathcal{G}_{red} = (\mathcal{V}_b, \mathcal{E}_{red}, W_{red}(s))$ associated with $\mathbb{L}_{red}(s) = \mathcal{K}(\mathbb{L}(s))$ (up to the orientation of edges, which can be arbitrarily chosen) and [DJDH14]*

$$I_b(s) = \mathbb{L}_{red}(s)V_b(s) - \mathcal{T}(s)I_\ell(s) \tag{8.9a}$$

$$\mathcal{T}(s) = -\mathbb{L}_{b\ell}(s)\mathbb{L}_{\ell\ell}^{-1}(s). \tag{8.9b}$$

We highlight that (8.9b) corresponds to (8.4c) when $\mathbb{L}^{AC}$ is replaced by $\mathbb{L}(s)$. Moreover, (8.9a) provides a relation similar to (8.4b). In particular, the vector

$$\tilde{I}_b(s) = \mathcal{T}(s)I_\ell(s) \tag{8.10}$$

identifies the equivalent currents to be injected into the boundary nodes. We further notice that, by construction, for given internal currents $I_\ell(t)$ and voltages $V_b(t)$, $t \geq 0$ (assuming null initial conditions), currents $I_b(t)$ computed through (8.1) and (8.9a) are identical at all times (hence the name instantaneous KR).

Remark 8.1. *Instantaneous KR has some limitations. More specifically, the branch admittances of the reduced network might have different dynamics with respect to those in the original circuit and, what is worse, might not even represent a physical circuit built with passive R, L, C elements. Consequently, a key issue is to understand when weights $W_{red,ij}(s)$ can be written as in (8.2) replacing R_{ij} and L_{ij} with suitable parameters $\tilde{R}_{ij}$ and $\tilde{L}_{ij}$. It has been shown that this is guaranteed only under special assumptions, for instance if original lines are homogeneous [CT12], i.e. $\frac{R_{e_i}}{L_{e_i}} = \frac{R_{e_j}}{L_{e_j}}$, $\forall e_i, e_j \in \mathcal{E}$. In this case, one also has $\tilde{R}_{ij} > 0$ and $\tilde{L}_{ij} > 0$.*

[5] Conditions for the invertibility of $\mathbb{L}_{\ell\ell}(s)$ have been studied in [DJDH14].

8.3 Approximate KR methods

In this section, we propose two approximated KR approaches, termed *approximate AC-KR* (aAC-KR) and *hybrid KR* (hKR), respectively. Both the methods allow to (i) extend the application of AC-KR to electrical variables not necessarily in PSSS, and (ii) overcome the realization problems of instantaneous KR discussed in Remark 8.1 (at least, as long as the parameters of the reduced circuit are positive). In particular, the proposed approximate techniques provide reduced circuits whose lines have the same *RL* "nature" as the original ones.

From a practical point of view, aAC-KR and hKR share the idea of using the line parameters (resistances and inductances) obtained from AC-KR at frequency ω_0, while differ in the way equivalent internal currents referred to boundary nodes are computed.

In the sequel, we first define the approximated Kron reduced graph; it is exploited in both aAC-KR and hKR for preserving the *RL* nature of the reduced lines. Then, we separately characterize the proposed methods by describing how the equivalent boundary currents (accounting for the effects of eliminated internal currents) are computed. Finally, in Proposition 8.1, we prove that both aAC-KR and hKR ensure asymptotic equivalence between original and reduced models if the considered network reaches a PSSS.

Definition 8.3 (Approximate Kron reduced graph)**.** *The approximate Kron reduced graph $\mathcal{G}_{red}^{\mathcal{A}}$ of the original network $\mathcal{G}$ with respect to a specified angular frequency ω_0 is obtained by:*

1) *computing $\mathbb{L}_{red}^{AC} = \mathcal{K}\left(\mathbb{L}^{AC}\right)$ and the associated directed graph $\mathcal{G}_{red}^{AC} = \left(\mathcal{V}_b, \mathcal{E}_{red}, W_{red}^{AC}\right)$, at the given ω_0;*

2) *setting $\mathcal{G}_{red}^{\mathcal{A}} = \left(\mathcal{V}_b, \mathcal{E}_{red}, W_{red}^{\mathcal{A}}(s)\right)$ where, for $(i,j) \in \mathcal{E}_{red}$*

$$W_{red,ij}^{\mathcal{A}}(s) = \frac{1}{\tilde{R}_{ij} + s\tilde{L}_{ij}}, \tag{8.11a}$$

$$\tilde{Z}_{ij} = -\left(\mathbb{L}_{red,ij}^{AC}\right)^{-1}, \tilde{R}_{ij} = \mathrm{Re}\left(\tilde{Z}_{ij}\right), \tilde{L}_{ij} = \frac{1}{\omega_0}\mathrm{Im}\left(\tilde{Z}_{ij}\right). \tag{8.11b}$$

Notice that, in $\mathcal{G}_{red}^{\mathcal{A}}$ line impedances have still the dynamics (8.2) but resistances $\tilde{R}_{ij}$ and inductances $\tilde{L}_{ij}$ are those predicted by AC-KR at angular frequency ω_0. Note also that, by construction, the graphs associated

with $\mathbb{L}_{red}^{AC}$ and $\mathbb{L}_{red}(s)$ have the same set of undirected edges. Therefore, by choosing the same orientation, the set of directed edges of $\mathcal{G}_{red}$ and $\mathcal{G}_{red}^{AC}$ can be made identical (this is why they have been both denoted with $\mathcal{E}_{red}$).

Remark 8.2. *AC-KR does not guarantee positivity of the reduced resistances and inductances. Based on the results of [CT12], one expects that negative values can occur if the time constants of the original lines are spread in a wide range. In practical applications such as microgrids, however, electrical lines are usually similar and so are their time constants.*

8.3.1 Approximate AC-KR

The idea behind aAC-KR is to use the accompanying matrix $\mathcal{T}^{AC}$ in (8.4c), computed with respect to ω_0, to obtain an approximation of the equivalent internal currents referred to boundary nodes when the network is in non-stationary regime. Since, by construction, $\mathcal{T}^{AC}$ is a complex valued matrix (to be multiplied by phasors $\vec{I}_\ell$ so as to give other phasors, as shown in (8.10)), we must now find a way to represent non-sinusoidal internal currents $I_\ell(t)$ through complex functions.

In general, given a real-valued function $f(t)$, there is not a unique way to represent it though a complex function $\tilde{f}(t)$, such that $\mathrm{Re}(\tilde{f}(t)) = f(t)$ [Vak96]. However, from e.g. [Vak96], one has that, among all these possible complex functions, the analytic signal[6] $\bar{f}(t) = \mathscr{A}(f(t))$ is the only representation which guarantees harmonic correspondence (i.e. if $f(t)$ becomes a sinusoid, then $\bar{f}(t)$ coincides with the corresponding phasor $\vec{f}$) and simultaneously verifies the generalized Tellegen's theorem [PSD70]. For this reason, the first approximate KR method we propose exploits the notion of analytic signal of the real function $I_\ell(t)$, and it is defined as follows.

Definition 8.4 (aAC-KR)**.** *Let $\bar{J}_\ell(t) = \mathscr{A}(I_\ell(t))$ be a complex function denoting the analytic signal of the real function $I_\ell(t)$, and let $\mathrm{Re}\left(\mathcal{T}^{AC}\bar{J}_\ell(t)\right)$ indicate the approximated internal currents to be injected into the boundary nodes of the reduced network. aAC-KR is given by the network $\mathcal{G}_{red}^{\mathcal{A}}$ and the relation*

$$I_b(s) = \mathbb{L}_{red}^{\mathcal{A}}(s)V_b(s) - \tilde{J}_b(s), \tag{8.12a}$$

where $\mathbb{L}_{red}^{\mathcal{A}}(s)$ is the Laplacian of $\mathcal{G}_{red}^{\mathcal{A}}$ and

$$\tilde{J}_b(s) = \mathscr{L}\left[\mathrm{Re}\left(\mathcal{T}^{AC}\bar{J}_\ell(t)\right)\right]. \tag{8.12b}$$

[6] Analytic signal generalizes the phasor concept. Notably, the latter one is restricted to time-invariant amplitude, phase and frequency, while the analytic signal allows for time-varying parameters [Bra86]. See Appendix A.4 for a definition.

From (8.12b), we notice that the interior currents reduction is performed using the entries of $\mathcal{T}^{AC}$, which, by definition, refer to variables in PSSS. Therefore, we expect the aAC-KR to lose accuracy when applied to nonlinear circuits or networks at a frequency $\omega \neq \omega_0$ (where ω_0 is used to compute $\mathcal{G}^{\mathcal{A}}_{red}$ and $\mathcal{T}^{AC}$). To overcome this issue, in the sequel we present a more sophisticated approximate KR method.

8.3.2 Hybrid KR

We recall that aAC-KR and hKR differs exclusively in the way equivalent internal currents to be injected into the boundary nodes of the reduced network are computed. In hKR, the mapped internal currents are the same as in (8.10), as described in the following.

Definition 8.5 (hKR)**.** *hKR is given by the network $\mathcal{G}^{\mathcal{A}}_{red}$ and the relation*

$$I_b(s) = \mathbb{L}^{\mathcal{A}}_{red}(s)V_b(s) - \tilde{I}_b(s) \tag{8.13}$$

where $\mathbb{L}^{\mathcal{A}}_{red}(s)$ is the Laplacian of $\mathcal{G}^{\mathcal{A}}_{red}$ and $\tilde{I}_b(s)$ is defined in (8.10)*.*

In Section 8.4, we will show that, compared to aAC-KR, hKR provides more accurate approximations of the boundary electrical variables; this is due to the fact that, with hKR, internal currents are mapped into boundary ones with no approximations (currents $\tilde{I}_b$ in (8.13) are the same as in (8.10)). On the other hand, performing the interior currents reduction using the entries of $\mathcal{T}(s)$ is more complex than implementing (8.12). In fact, the transfer functions of $\mathcal{T}(s)$ may have a high degree, in the case of large networks, and this could be an implementation limit.

Example 8.2. *We want to apply (separately) aAC-KR and hKR to the circuit described in Example 8.1 (Figure 8.2a), assuming that electric variables are not necessarily in PSSS.*

The incidence matrix B has the form (8.6)*, while the weights matrix $W(s)$ is:*

$$W(s) = \begin{bmatrix} \frac{10}{1+0.02s} & 0 & 0 \\ 0 & \frac{5}{1+0.035s} & 0 \\ 0 & 0 & \frac{1}{1+0.01s} \end{bmatrix},$$

where resistances and inductances of the weights in $W(s)$ are the same of Example 8.1. It follows that, at PSSS with $\omega_0 = 2\pi 50$ rad/s, $W(\mathrm{i}\omega_0) = W^{AC}$.

The Laplacian $\mathbb{L}(s) = B \cdot W(s) \cdot B^T$, partitioned as in (8.1), is

$$\mathbb{L}(s) = \begin{bmatrix} \mathbb{L}_{bb}(s) & \mathbb{L}_{b\ell}(s) \\ \mathbb{L}_{\ell b}(s) & \mathbb{L}_{\ell\ell}(s) \end{bmatrix}$$

with

$$\mathbb{L}_{bb}(s) = \begin{bmatrix} \dfrac{10}{1+0.02s} & 0 & 0 \\ 0 & \dfrac{5}{1+0.035s} & 0 \\ 0 & 0 & \dfrac{1}{1+0.01s} \end{bmatrix},$$

$$\mathbb{L}_{b\ell}(s) = \begin{bmatrix} -\dfrac{10}{1+0.02s} \\ -\dfrac{5}{1+0.035s} \\ -\dfrac{1}{1+0.01s} \end{bmatrix}, \qquad \mathbb{L}_{\ell b}(s) = (\mathbb{L}_{b\ell}(s))^T,$$

and

$$\mathbb{L}_{\ell\ell}(s) = \frac{16(1+0.011s)(1+0.030s)}{(1+0.01s)(1+0.02s)(1+0.035s)}.$$

The accompanying matrix $\mathcal{T}(s)$ is obtained from (8.9b) *as*

$$\mathcal{T}(s) = \begin{bmatrix} \frac{0.625(1+0.01s)(1+0.035s)}{(1+0.030s)(1+0.011s)} \\ \frac{0.312(1+0.01s)(1+0.02s)}{(1+0.030s)(1+0.011s)} \\ \frac{0.063(1+0.02s)(1+0.035s)}{(1+0.011s)(1+0.030s)} \end{bmatrix}. \tag{8.14}$$

We can now characterize $\mathcal{G}^{\mathcal{A}}_{red}$ computed with respect to ω_0, and then compute $\mathbb{L}^{\mathcal{A}}_{red}(s)$. Sets $\mathcal{V}_b$ and $\mathcal{E}_{red}$ are the same as in Example 8.1, whereas, following Definition 8.3, the weights matrix $W^{\mathcal{A}}_{red}(s)$ is obtained applying (8.11) *to the Laplacian $\mathbb{L}^{AC}_{red}$ in* (8.7)*. Consequently, one has*

$$W^{\mathcal{A}}_{red}(s) = \mathrm{diag}\left[W^{\mathcal{A}}_{red,12}(s), W^{\mathcal{A}}_{red,13}(s), W^{\mathcal{A}}_{red,23}(s)\right] = \\ = \begin{bmatrix} \frac{3.642}{1+0.038s} & 0 & 0 \\ 0 & \frac{0.69}{1+0.010s} & 0 \\ 0 & 0 & \frac{0.254}{1+0.013s} \end{bmatrix},$$

where $W^{\mathcal{A}}_{red,12}(s), W^{\mathcal{A}}_{red,13}(s), W^{\mathcal{A}}_{red,23}(s)$ *are the admittance transfer functions of the reduced edges* r_1, r_2, r_3*, respectively (see Figure 8.2b). Next, let*

$$B_{red} = \begin{bmatrix} -1 & -1 & 0 \\ 1 & 0 & -1 \\ 0 & 1 & 1 \end{bmatrix}$$

be the incidence matrix of the reduced network in Figure 8.2b. The Laplacian $\mathbb{L}^{\mathcal{A}}_{red}(s)$ *of* $\mathcal{G}^{\mathcal{A}}_{red}$ *is given by*

$$\begin{aligned} \mathbb{L}^{\mathcal{A}}_{red}(s) &= B_{red} \cdot W^{\mathcal{A}}_{red}(s) \cdot B^T_{red} = \\ &= \begin{bmatrix} \mathbb{L}^{\mathcal{A}}_{red,11}(s) & \mathbb{L}^{\mathcal{A}}_{red,12}(s) & \mathbb{L}^{\mathcal{A}}_{red,13}(s) \\ \mathbb{L}^{\mathcal{A}}_{red,12}(s) & \mathbb{L}^{\mathcal{A}}_{red,22}(s) & \mathbb{L}^{\mathcal{A}}_{red,23}(s) \\ \mathbb{L}^{\mathcal{A}}_{red,13}(s) & \mathbb{L}^{\mathcal{A}}_{red,23}(s) & \mathbb{L}^{\mathcal{A}}_{red,33}(s) \end{bmatrix}, \end{aligned} \tag{8.15}$$

with

$$\begin{aligned} \mathbb{L}^{\mathcal{A}}_{red,11}(s) &= \frac{4.332(1+0.015s)}{(1+0.038s)(1+0.010s)} \\ \mathbb{L}^{\mathcal{A}}_{red,12}(s) &= -\frac{3.642}{(1+0.038s)} \\ \mathbb{L}^{\mathcal{A}}_{red,13}(s) &= -\frac{0.690}{(1+0.010s)} \\ \mathbb{L}^{\mathcal{A}}_{red,22}(s) &= \frac{3.896(1+0.015s)}{(1+0.038s)(1+0.013s)} \\ \mathbb{L}^{\mathcal{A}}_{red,23}(s) &= -\frac{0.254}{(1+0.013s)} \\ \mathbb{L}^{\mathcal{A}}_{red,33}(s) &= \frac{0.945(1+0.012s)}{(1+0.010s)(1+0.013s)} \end{aligned}$$

Finally, equivalent boundary currents are obtained substituting (8.15) *in* (8.12a) *and* (8.8) *in* (8.12b) *(aAC-KR case), or replacing* (8.15) *in* (8.13) *and* (8.14) *in* (8.10) *(hKR case).*

8.3.3 Asymptotic equivalence between original and reduced network models

The next proposition characterizes the asymptotic behaviors preserved by aAC-KR and hKR.

Proposition 8.1. *Consider the network represented by the graph $\mathcal{G}$, whose Laplacian is partitioned as in* (8.1)*, and assume parameters $\tilde{R}_{ij}$ and $\tilde{L}_{ij}$ obtained through* (8.11) *with respect to ω_0 are strictly positive. Then,*

(i) if I_ℓ and V_b converge to a PSSS with angular frequency ω_0, then the asymptotic behavior of I_b computed from (8.1) *is the same as when I_b is computed through aAC-KR (i.e. using* (8.12)*);*

(ii) if V_b converge to a PSSS with angular frequency ω_0, then the asymptotic behavior of I_b computed from (8.1) *is the same as when I_b is computed through hKR (i.e. using* (8.13)*).*

Proof of (i). Since I_ℓ and V_b are sinusoidal with angular frequency ω_0, the reduced system will reach a PSSS and the currents I_b will also be sinusoidal, by virtue of the Frequency Response Theorem [DK84]. In particular, it holds $\bar{J}_\ell(t) = \mathscr{A}(I_\ell(t)) = \vec{I}_\ell$, by definition of analytic signal. Therefore, if we write (8.12a) in time domain at frequency ω_0, we get that the relation between phasors $\vec{V}_b$, $\vec{I}_b$ and $\vec{I}_\ell$ is

$$\vec{I}_b = \underbrace{\mathbb{L}_{red}^{\mathcal{A}}(\mathrm{i}\omega_0)}_{\mathbb{L}_{red}^{AC}} \vec{V}_b - \mathcal{T}^{AC}\vec{I}_\ell, \tag{8.16}$$

that is (8.4b). Concluding, we have retrieved the AC-KR case, where the equivalence between original and reduced models is always guaranteed [CT12].

Proof of (ii). After applying hKR, the Laplace transforms of signals $I_b(t)$, $V_b(t)$ and $I_\ell(t)$ are related by

$$I_b(s) = \mathbb{L}_{red}^{\mathcal{A}}(s)V_b(s) - \mathcal{T}(s)I_\ell(s),$$

where $\mathcal{T}(s)$ is given by (8.9b), and $\mathbb{L}_{red}^{\mathcal{A}}$ is the Laplacian of approximate Kron reduced graph $\mathcal{G}_{red}^{\mathcal{A}}$ with weights $W_{red,ij}(s)$ (see Definition 8.3). We note that, by hypothesis, the poles of all entries of $\mathbb{L}_{red}^{\mathcal{A}}$ have strictly negative real parts. Let us denote $I_b(s)$ and $\hat{I}_b(s)$ as the boundary currents computed from (8.1) and (8.13), respectively, and let us introduce $I_\Delta(s) = I_b(s) - \hat{I}_b(s)$. Then, by (8.1) and (8.13), one has:

$$I_\Delta(s) = \left(\mathbb{L}_{red}(s) - \mathbb{L}_{red}^{\mathcal{A}}(s)\right) V_b(s).$$

Suppose the inputs V_b are sinusoids with angular frequency ω_0. By the Frequency Response Theorem [DK84], each element of $\mathbb{L}_{red}(s)V_b(s)$ and

$\mathbb{L}_{red}^{\mathcal{A}}(s)V_b(s)$ tends to a sinusoid, so that the relation between the phasors $\vec{I}_\Delta$ and $\vec{V}_b$ is given by $\vec{I}_\Delta = \left(\mathbb{L}_{red}(\mathrm{i}\omega_0) - \mathbb{L}_{red}^{\mathcal{A}}(\mathrm{i}\omega_0)\right)\vec{V}_b$. However, $\mathbb{L}_{red}(\mathrm{i}\omega_0) = \mathbb{L}_{red}^{\mathcal{A}}(\mathrm{i}\omega_0)$ by construction, hence $\vec{I}_\Delta = 0$, which means that $I_\Delta \to 0$ asymptotically.

The proofs of (i) and (ii) can be straightforwardly extended to the case where I_ℓ and V_b are not sinusoids, but asymptotically reach a PSSS with frequency ω_0. □

8.3.4 Generalization to three-phase linear networks in dq coordinates

All the considerations reported in Sections 8.2 and 8.3 so far (along with the related formulae) hold, without restrictions, for any linear network. In this paragraph, we focus on three-phase linear networks in dq coordinates. From this point on, we assume balanced RL lines, and three-phase electrical signals without zero-sequence components. It follows that, under these circumstances, we can split the circuit into three independent and identical single-phase circuits. Each one is associated with the equivalent "single-phase" directed graph $\mathcal{G}^{sp} = (\mathcal{V}^{sp}, \mathcal{E}^{sp}, W^{sp}(s))$ where transfer functions $W_{ij}^{sp}(s) = 1/(R_{ij} + sL_{ij})$ represent, independently of the phase $\star \in \{a, b, c\}$, the relation between $\mathscr{L}[V_i^\star(t) - V_j^\star(t)]$ and $\mathscr{L}[I_{ij}^\star(t)]$, $(i, j) \in \mathcal{E}^{sp}$.

Three-phase signals can be conveniently represented in the $dq0$ coordinates. In this case, under our assumptions, the graph $\mathcal{G}$ representing the considered three-phase network has the same topology of the corresponding single-phase circuit $\mathcal{G}^{sp}$. Moreover, it can be shown that, in the $dq0$ reference frame, the RL line associated with the edge $(i, j) \in \mathcal{E}^{sp}$ has the dynamics

$$\frac{\mathrm{d}}{\mathrm{d}t} I_{ij}^{dq} = -\left(\frac{R_{ij}}{L_{ij}} + \mathrm{i}\omega_0\right) I_{ij}^{dq} + \frac{1}{L_{ij}}\left(V_i^{dq} - V_j^{dq}\right)$$

and its corresponding transfer function has the form

$$I_{ij}^{dq}(s) = W_{ij}(s)\left(V_i^{dq}(s) - V_j^{dq}(s)\right),$$

with

$$W_{ij}(s) = \frac{1}{Z_{ij} + sL_{ij}}, \qquad Z_{ij} = R_{ij} + \mathrm{i}\omega_0 L_{ij}. \tag{8.17}$$

Also in this case, the current-balance equations $I^{dq}(s) = \mathbb{L}^{dq}(s)V^{dq}(s)$ can be partitioned as in (8.1), with $I^{dq} = \left[I_b^{dq^T}, I_\ell^{dq^T}\right]^T$ and $V^{dq} = \left[V_b^{dq^T}, V_\ell^{dq^T}\right]^T$.

In dq coordinates, instantaneous KR is characterized analogously to Section 8.2.2. Moreover, also aAC-KR and hKR can be redefined in dq coordinates; notably, by performing AC-KR on $\mathcal{G}^{sp}$, one obtains the topology of the approximate Kron reduced graph $\mathcal{G}^{\mathcal{A}}_{r\xi d}$ in dq reference frame, as well as the reduced lines parameters $\tilde{R}_{ij}$ and $\tilde{L}_{ij}$ characterizing its weights

$$W^{\mathcal{A}}_{red,ij}(s) = \frac{1}{\tilde{Z}_{ij} + s\tilde{L}_{ij}}, \tag{8.18a}$$

$$\tilde{Z}_{ij} = -\left(\mathbb{L}^{AC}_{red,ij}\right)^{-1} = \tilde{R}_{ij} + \mathrm{i}\omega_0\tilde{L}_{ij}, \qquad \tilde{L}_{ij} = \frac{1}{\omega_0}\mathrm{Im}\left(\tilde{Z}_{ij}\right). \tag{8.18b}$$

As regards the computation of the equivalent internal currents to be injected into the boundary nodes of the reduced network, (8.12b) and (8.10) become, respectively

$$\tilde{J}^{dq}_b(s) = \mathscr{L}\left[T(\theta)\cdot \mathrm{Re}\left(\mathcal{T}^{AC}\bar{J}^{abc}_\ell(t)\right)\right] \tag{8.19}$$

and

$$\tilde{I}^{dq}_b(s) = \mathcal{T}(s) I^{dq}_\ell(s), \tag{8.20}$$

depending on whether we are using aAC-KR or hKR.

8.4 Numerical examples

In this section, we assess the features of aAC-KR and hKR through numerical examples. In particular, we consider the three-phase network in Figure 8.3a, composed of three ideal voltage sources and balanced RL lines connecting the generators to a common load. In this simple case, both aAC-KR and hKR amount to a Y$-\Delta$ transformation. The reduced network is shown in Figure 8.3b. Since the corresponding three-phase balanced voltage generators are identical for the original and reduced networks, from Proposition 8.1 we expect I_b in the original and reduced models to be the same, if a PSSS is reached. All the power line parameters are collected in Appendix 8.8.

Example 8.3 (Linear unbalanced load)**.** *In this example, we assume that the resistive load is unbalanced. Figures 8.4a-8.4b compare the original output current of phase a of generator 1 with its corresponding signal in the reduced networks obtained through aAC-KR and hKR, respectively. The plots reveal that the proposed methods ensure asymptotic equivalence, even if*

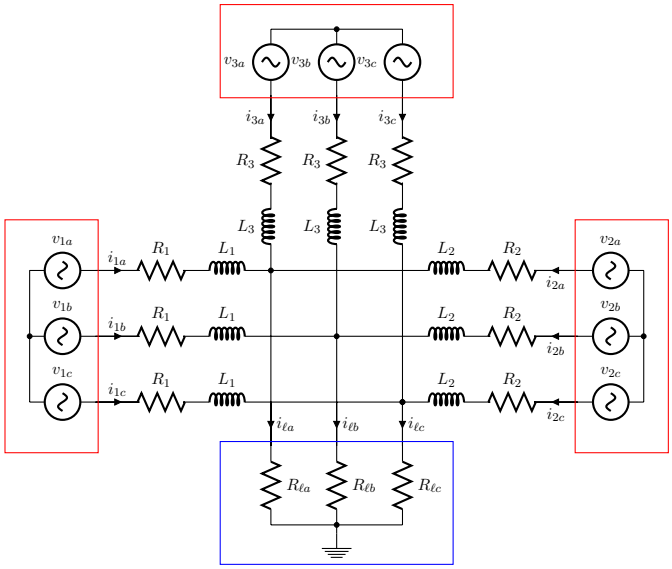

(a) Original network.

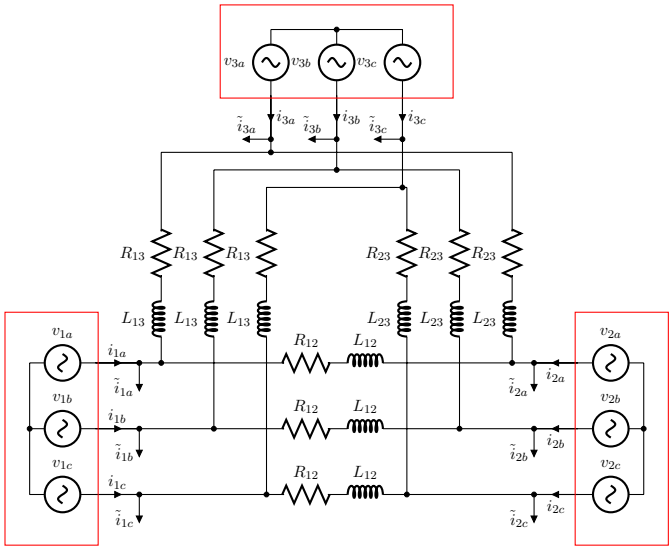

(b) Reduced model obtained via approximate KR methods.

Figure 8.3: Numerical examples: original and reduced networks. Red and blue boxes enclose boundary and interior nodes, respectively.

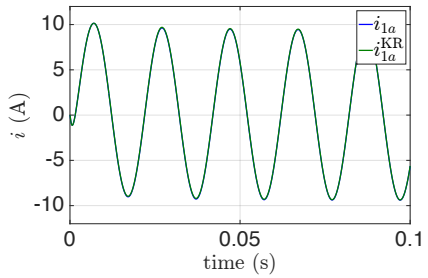

(a) Comparison between original and reduced current of phase a currents of generator 1 - aAC-KR.

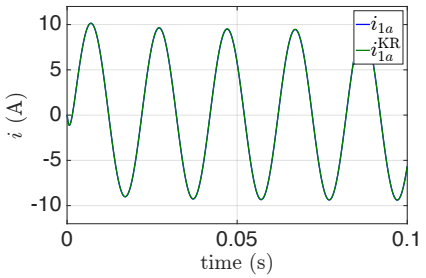

(b) Comparison between original and reduced current of phase a currents of generator 1 - hKR.

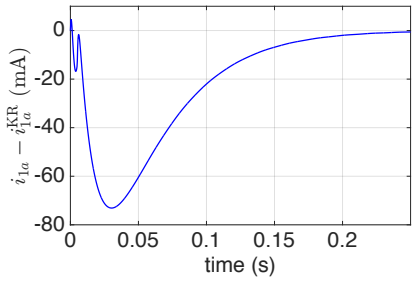

(c) Error between original and reduced current of phase a currents of generator 1 - aAC-KR.

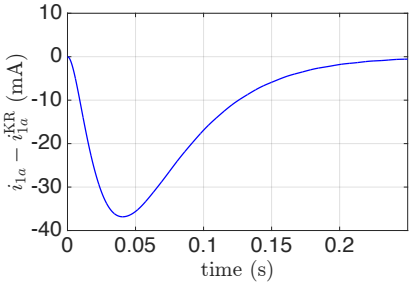

(d) Error between original and reduced current of phase a currents of generator 1 - hKR.

Figure 8.4: Example 8.3 - Evaluation of the output currents generated through aAC-KR and hKR, in presence of a linear load.

the load is unbalanced but a PSSS is achieved. In particular, from Figures 8.4c-8.4d, we notice that both the aAC-KR and hKR model errors go to zero after short transients. Analogous results are obtained for all the other phases and nodes.

Example 8.4 (Nonlinear load)**.** *For this second example, we replace the resistive load in Figure 8.3a by a six-pulse bridge rectifier. As in the previous example, we compare the currents at boundary nodes of the original circuit with those of the reduced models and, for the sake of simplicity, we concentrate on the output currents of generator 1, phase a (see Figures 8.5a-8.5b). In particular, from Figure 8.5c, one can see that the aAC-KR model error increase substantially with respect to Example 8.3, while the one of the hybrid Kron reduced network goes asymptotically to zero (see*

Figure 8.5d). Analogous results are obtained for all the other phases and generators.

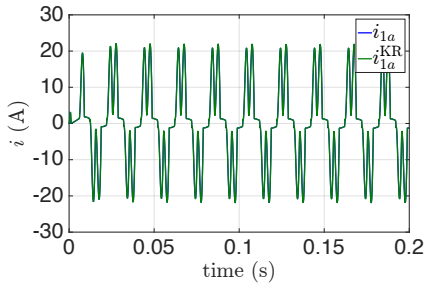

(a) Original (in blue) and reduced (in green) currents of phase a of generator 1 - aAC-KR.

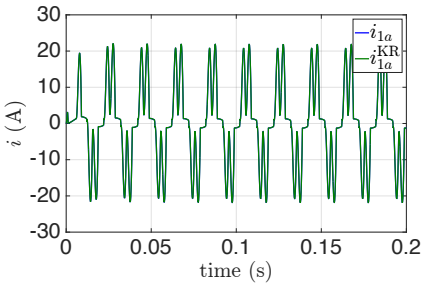

(b) Original (in blue) and reduced (in green) currents of phase a of generator 1 - hKR.

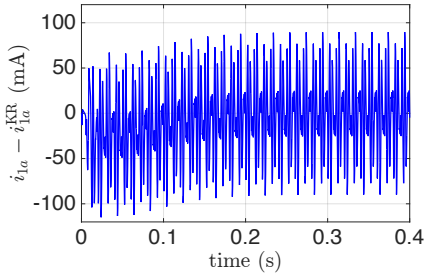

(c) Error between original and reduced current of phase a currents of generator 1 - aAC-KR.

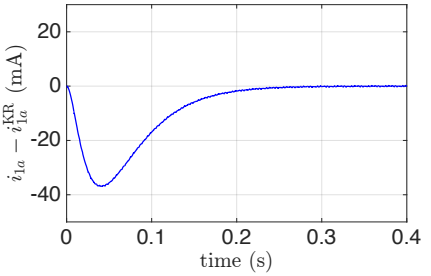

(d) Error between original and reduced current of phase a currents of generator 1 - hKR.

Figure 8.5: Example 8.4 - Evaluation of the features of aAC-KR and hKR in presence of a nonlinear load.

Remark 8.3. *The proposed approximate methods produce similar results in networks reaching PSSS regime at frequency ω_0, but hKR provides better performances (i.e. faster convergence and lower errors) than aAC-KR in case of networks with nonlinear loads. This is due to the fact that $\tilde{I}_b^{dq}$ in* (8.13) *represents the "true" internal currents mapped to boundary nodes (they are the same as in equation* (8.10)*). Indeed, hKR differs from KR* (8.9) *only in the dynamics of the branches, and not in the equivalent internal currents. On the other hand, as highlighted in Section 8.3.2, this better accuracy of hKR with respect to aAC-KR comes at the expenses of an higher implementation complexity.*

8.5 Kron reduction of microgrids

In this section, we show how to apply the approximate KR methods described in Section 8.3 to the control of AC ImGs. Our aim is to exploit aAC-KR and hKR to generalize the PnP algorithm summarized in Chapter 6 for designing decentralized controllers for AC ImGs guaranteeing voltage and frequency stability. In fact, we recall that the aforementioned design method assumes (i) load-connected ImG topologies, and (ii) RL power lines connecting DGUs. In this context, we can resort to one of our approximate KR method to map arbitrarily interconnected ImGs into their corresponding load-connected networks (by labeling as internal nodes those representing loads that are not directly attached to DGU). Then, since both aAC-KR and hKR preserve the RL structure of the reduced lines, we can use the procedure detailed in Sections 6.3.2-6.3.3 to design PnP regulators with respect to the equivalent simplified circuit.

In the sequel, we introduce the graph associated with an ImG, and briefly summarize the electrical models of DGUs and lines used for controller synthesis. Then, we describe how to combine the PnP design procedure discussed in Chapter 6 with the proposed approximate KR methods.

8.5.1 Islanded microgrid associated graph

As for any linear electrical network, we can associate with an ImG a weighted directed graph $\mathcal{G} = (\mathcal{V}, \mathcal{E}, W(s))$ (see the example in Figure 8.6) where the vertex set $\mathcal{V}$ is partitioned into boundary and internal nodes. In this case, the subset $\mathcal{V}_b$ identifies PCC nodes, i.e. the output terminals of each DGU (see, e.g., Figure 6.2), while $\mathcal{V}_\ell$ contains load nodes. Nodal currents injected by the DGUs and loads are denoted with I_b and I_ℓ, respectively, and they are positive if entering into the nodes. Nodal voltages are denoted analogously. As regards the edges, they correspond to RL power lines with arbitrary orientation and same sign convention as in Section 8.2.

8.5.2 DGU and line electrical models

The design of stabilizing voltage and frequency controllers is performed considering DGUs having the single-phase equivalent circuit shown in Figure 6.2, and described by the set of equations (6.9). We recall that three-phase electrical signals without zero sequence components and balanced network parameters are assumed. Note also that we do not assume balanced signals; hence, the case of unbalanced load currents is included in the considered framework.

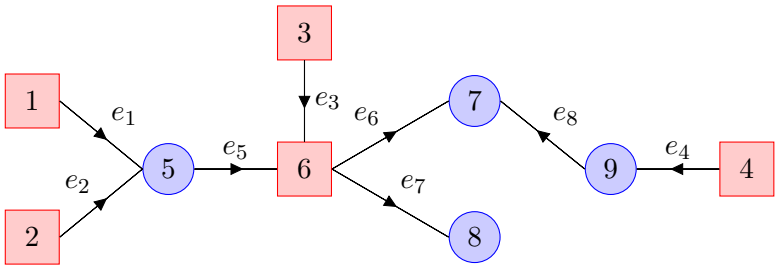

Figure 8.6: Example of a graph associated with an ImG. Red squares denote DGUs (i.e. boundary nodes), while blue circles represent loads (i.e. internal nodes).

Remark 8.4. *As already observed in Section 2.3, local loads I_{Li} connected to each PCC are treated as exogenous disturbances in control design. However, it must be highlighted that they are different from load currents I_ℓ defined in Section 8.5.1. The latter ones, in fact, identify loads that are not directly connected to PCCs (see, e.g., the blue circles in Figure 8.6).*

Consider an ImG composed of n nodes partitioned into n_b boundary nodes and n_ℓ internal nodes. If $n = n_b$, then $n_\ell = 0$, which means that we retrieve a load-connected ImG, with load currents appearing only at the PCCs. Otherwise, we can write nodal currents and voltages as $I^{dq} = \left[I_b^{dq^T}, I_\ell^{dq^T}\right]^T$ and $V^{dq} = \left[V_b^{dq^T}, V_\ell^{dq^T}\right]^T$, respectively. At this point, it is possible to express the current-balance equations as $I^{dq}(s) = \mathbb{L}(s)V^{dq}(s)$, where $\mathbb{L}(s)$ is the Laplacian of the graph $\mathcal{G}$ associated with the ImG, with weights $W_{ij}(s)$ in the form (8.17).

8.5.3 Plug-and-play design for microgrids with general topologies

Now we show how to extend the design algorithm in Chapter 6 to ImGs with arbitrary topologies.

Let us $\mathcal{G}$ be the directed graph associated with an ImG and let us assume we have selected one KR method among aAC-KR and hKR. When the plug-in of a DGU or a load node (say node i) is required, one should first update $\mathcal{G}$ accordingly, thus obtaining the graph $\mathcal{G}^{new}$. Then, the chosen approximate method is applied to $\mathcal{G}^{new}$ for obtaining the reduced ImG $\mathcal{G}_{red}^{\mathcal{A},new}$ with load-connected topology. If some resistances or inductances of reduced lines are negative, the plugging in of node i is denied, as one of the

assumption of the PnP algorithm in Chapter 6 is not fulfilled. Otherwise, one compares the reduced graphs $\mathcal{G}_{red}^{\mathcal{A}}$ (associated with $\mathcal{G}$) and $\mathcal{G}_{red}^{\mathcal{A},new}$ for finding the set $\mathcal{U} \subseteq \mathcal{V}_b$ of DGUs that have new neighbors or that are connected to lines whose impedance has changed. The LMI (6.28) is then solved for all DGUs $j \in \mathcal{U}$ (and also for $j = i$, if node i is a DGU), hence producing new controllers $\mathcal{C}_j$. If no LMI is infeasible, controllers in the original ImG are updated and connection of node i is allowed.

Unplugging of a node can be performed in a similar way.

Remark 8.5. *While line changes are not common in ImGs, they could happen in the equivalent reduced network because of the addition/removal of load nodes in the original ImG. These phenomena are considered in the next section.*

Remark 8.6. *According to the procedure described in Section 8.5.3, aAC-KR and hKR are performed in a centralized fashion every time there is a change in the network topology. This is in contrast with PnP design, whose main feature is to avoid any centralized computations. In the future, we will study how to perform the proposed approximate KR methods in a distributed fashion. Notably, one can develop this generalization according to the iterative KR procedure [DB13] proposed for both AC networks in PSSS and resistive networks. In a similar spirit, we will study how to avoid the centralized computation of the set $\mathcal{U}$ by exploiting existing distributed algorithms for path-finding over directed graphs.*

8.6 Simulation of a 21-bus network

In this section, we assess the capability of PnP control and approximate KR methods to deal with networks characterized by complex topologies. Since we are interested in evaluating only the stabilizing effect of PnP controllers, local pre-filters and compensators have not been implemented. Now, recalling that (i) each compensator takes as input the load current I_{Li} absorbed at the corresponding PCC (see Section 3.3. of [RSFT14] for details), and (ii) the proposed approximate KR methods differ only in the way equivalent internal currents referred to PCCs are computed, in this scenario it is equivalent to use aAC-KR or hKR, as they both provide the same reduced graph $\mathcal{G}_{red}^{\mathcal{A}}$.

We use a network derived from the top half of IEEE 37 topology [fee11] and identify generation nodes and loads as in [BZ13]. The simulation has been performed in PSCAD.

8.6.1 Islanded microgrid topology

The ImG in Figure 8.7 has 21 nodes, with six DGUs, electrical RL lines having time constants spread in a wide range, linear R and RL loads, as well as highly nonlinear and highly inductive loads.

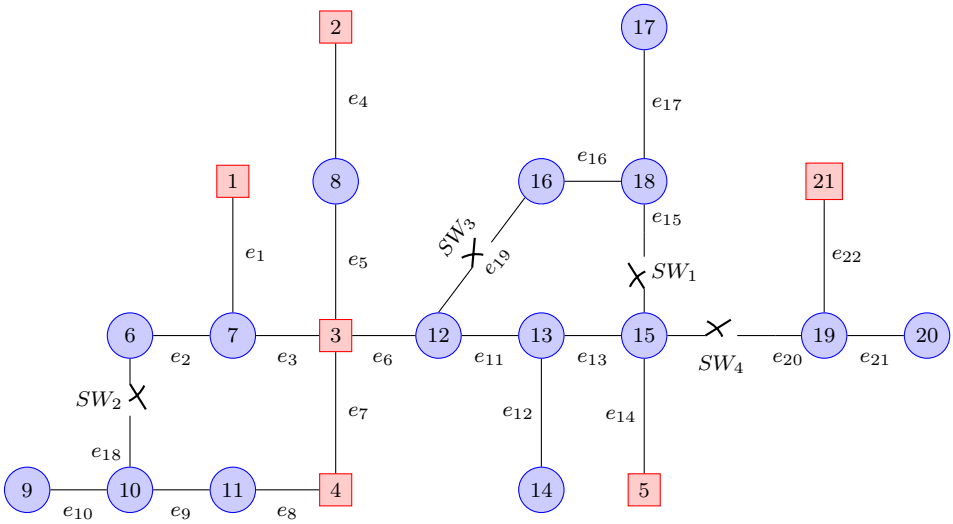

Figure 8.7: 21-bus network: red squares denote boundary nodes (i.e. DGUs), blue circles represent internal nodes (i.e. loads).

Compared to the IEEE 37 network, a switch SW_1 has been introduced, allowing the plugging in/unplugging of loads at nodes 16, 17 and 18. Moreover, two branches (e_{18} and e_{19}) were added and connected to the microgrid through switches SW_2 e SW_3, respectively. The edge e_{18} creates a mesh between DGUs 1, 3 and 4; this allows us to show that PnP controllers can also stabilize meshed networks. The edge e_{19} simply changes the impedance between DGUs 3 and 5 (as long as SW_1 is closed). Finally, one generation node (vertex 21) and two loads (at nodes 19 and 20) have been introduced, so as to simulate the plugging in of a new DGU. The new generation unit is connected to the ImG via switch SW_4.

At time $t = 0$ s, there is no energy stored in all the inductors and capacitors and all the switches are open. At $t = 5$ s, switch SW_1 closes, causing an increase in electrical loads, mainly supplied by DGUs 3 and 5. Next, SW_2 e SW_3 close at instants $t = 6.5$ s and $t = 8$ s, respectively, connecting new branches to the network. Finally, at time $t = 9.5$ s switch SW_4 closes, so that the sixth generation unit is connected to the ImG. All

the electrical parameters of the 21-bus network are collected in Appendix 8.8.2.

8.6.2 Plug-and-play control design

As described in Section 8.5.3, the first step in control design consists in applying the chosen approximate method (aAC-KR or hKR) to the original network, thus obtaining the equivalent load-connected model. In particular, the reduced line impedances are computed using (8.18b), with $\omega_0 = 2\pi 50$ rad/s.

The topology of the reduced network actually depends on the state of the switches in the original network. As long as SW_2, SW_3 and SW_4 are open, the network in Figure 8.7 has a radial topology. Therefore, the equivalent impedance between nodes 3 and 5 is equal to the sum of the impedances of edges e_6, e_{11}, e_{13} and e_{14}, irrespectively of the state of switch SW_1. On the contrary, when switches SW_2, SW_3 and SW_4 are closed, the topology of the Kron reduced network and its impedances change. Figure 8.8 collects the reduced networks that arise during the simulation. In particular, Figure 8.8a holds when all the four switches are open, or when only SW_1 is closed. The network in Figure 8.8b refers to the case when switches SW_2 and SW_3 become closed, while the diagram in Figure 8.8c holds when all the four switches are closed. We further highlight that the resistances and inductances of the Kron reduced circuits in Figure 8.8, collected in Appendix 8.8.2, are positive.

At time $t = 5$ s, SW_1 closes, but the Kron reduced network does not change, and no redesign of the controllers is needed. In fact, the connection of load nodes 16, 17 and 18 changes the term accounting for the effect of internal currents ($\tilde{J}_b(s)$ in aAC-KR or $\tilde{I}_b(s)$ in hKR), which is mapped into an additional contribution to the load at PCCs 3 and 5. This is, however, not critical since DGU loads are treated as disturbances by PnP controllers.

At instant $t = 6.5$ s, the equivalent impedances between nodes 1, 3 and 4 change; therefore, the controllers of DGUs 1, 3 and 4 must be redesigned (all the other controllers do not change).

At instant $t = 8$ s, the equivalent impedance between boundary nodes 3 and 5 changes: the corresponding DGUs must update their controllers.

At $t = 9.5$ s, DGU 6 is connected to the network: controllers of DGUs 3 e 5 must be redesigned again.

We highlight that the proposed controllers effectively stabilize voltage and frequency in the ImG. This is illustrated by Figures 8.9 -8.12 that show, for every configuration of the switches, the singular values of the closed

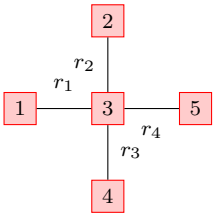

(a) Equivalent reduced network for $t < 6.5$ s.

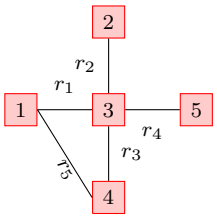

(b) Equivalent reduced network for $6.5 \text{ s} \leq t < 9.5$ s.

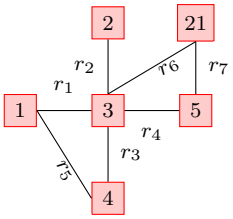

(c) Equivalent reduced network for $t \geq 9.5$ s.

Figure 8.8: Simulation of a 21-bus ImG: Kron reduced networks.

loop QSL ImG, as well as its eigenvalues, with and without couplings. In particular, Figures 8.9a, 8.10a, 8.11a and 8.12a show that all the eigenvalues are on the left half-plane.

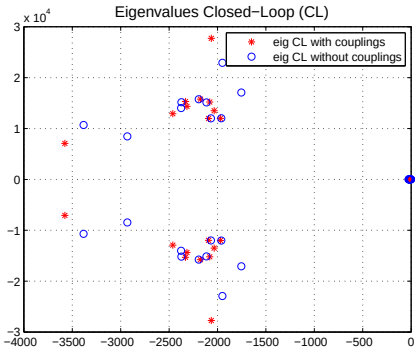

(a) Eigenvalues of the closed-loop QSL ImG with (red) and without (blue) couplings.

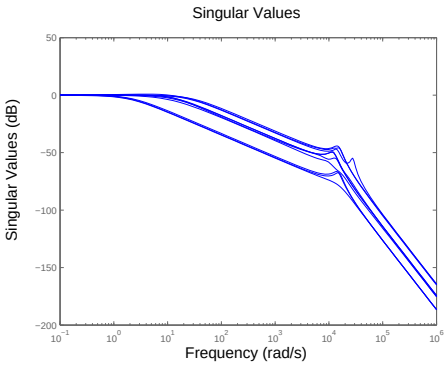

(b) Singular values of the closed-loop QSL ImG.

Figure 8.9: Eigenvalues and singular values of the QSL ImG when all the switches are open, or only SW_1 is closed.

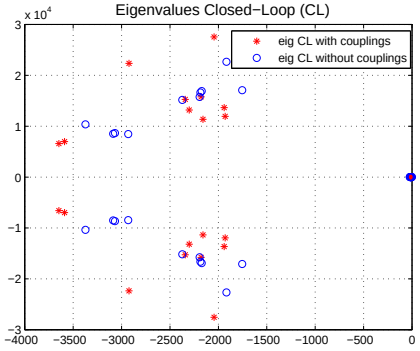

(a) Eigenvalues of the closed-loop QSL ImG with (red) and without (blue) couplings.

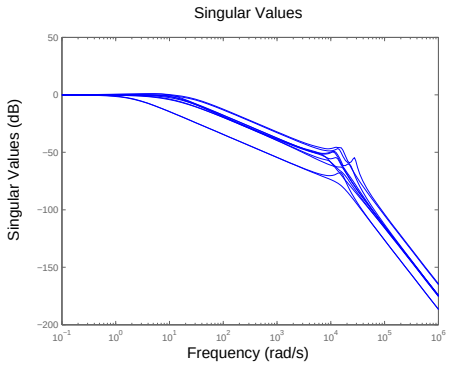

(b) Singular values of the closed-loop QSL ImG.

Figure 8.10: Eigenvalues and singular values with SW_1, SW_2 closed, and SW_3, SW_4 open.

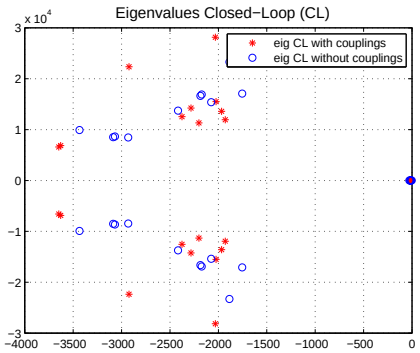

(a) Eigenvalues of the closed-loop QSL ImG with (red) and without (blue) couplings.

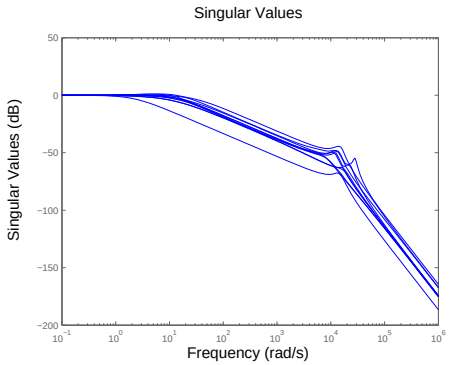

(b) Singular values of the closed-loop QSL ImG.

Figure 8.11: Eigenvalues and singular values when SW_1, SW_2, SW_3 are closed, and SW_4 open.

8.6.3 Simulation results

The reference signals for all the generation units are $V_d^{ref} = \sqrt{2} \cdot 230\ V$ and $V_q^{ref} = 0\ V$. Figure 8.13 shows the RMS voltage, frequency and THD of phase a at the PCCs of the boundary nodes (i.e nodes 1-5 and 21), respec-

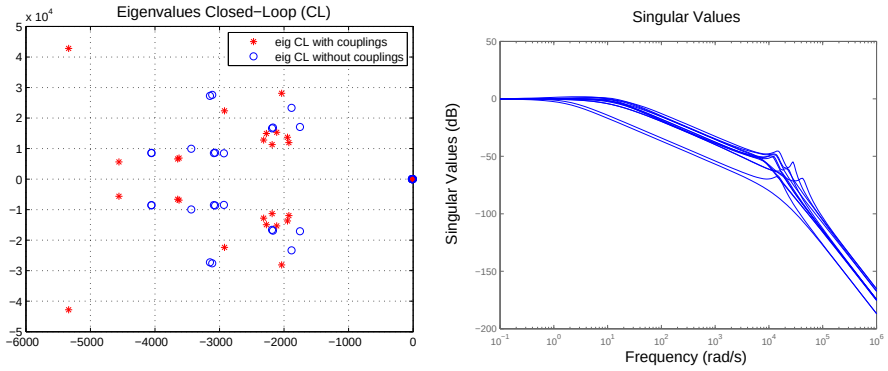

(a) Eigenvalues of the closed-loop QSL ImG with (red) and without (blue) couplings.

(b) Singular values of the closed-loop QSL ImG.

Figure 8.12: Eigenvalues and singular values of the QSL ImG when all the switches are closed.

tively. We highlight that, in spite of all the variations of the ImG topology, PnP decentralized control ensures good tracking of voltage references for all DGUs (see Figure 8.13a). We note that real-time switch between different controllers has been implemented using a bumpless control transfer scheme similar to the one used in classical PID regulators [ÅH06]. This guarantees control variables do not have sudden variations at switching times. In our case, bumpless controllers are effective in limiting voltage surges and dips to a few volts when updates of controllers take place (for $t \geq 4$ s, the maximal deviation from the reference RMS voltage is of less than 20 volts). Figure 8.13b shows that the impact of the topology commutations is minor also on the frequency profiles. In fact, PnP controllers promptly restore the frequencies to the nominal value, ensuring negligible variations (i.e. less than 0.5 Hz when the highly inductive load is connected and less than 0.1 Hz when other events occur). Finally, from Figure 8.13c, we notice that THD values are below the maximum limit (5%) recommended in [IEE09].

Overall, the fact that voltage and frequency stability is guaranteed even for such a complicated network, proves that the proposed approximate KR methods are well suited tools for extending the PnP scalable design to ImGs with arbitrary topologies.

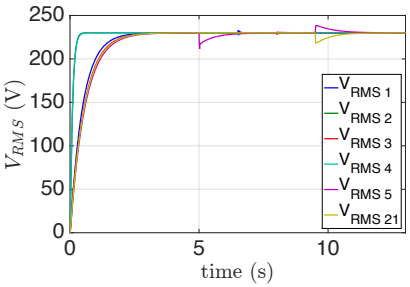

(a) RMS voltages at boundary nodes.

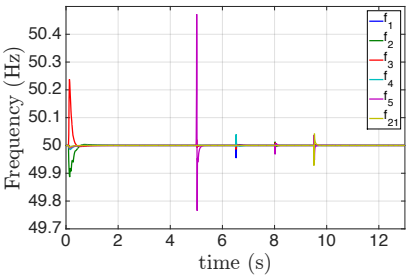

(b) Frequencies at boundary nodes.

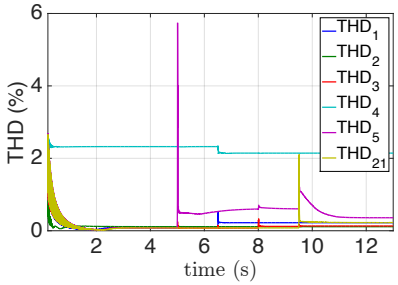

(c) THD at boundary nodes.

Figure 8.13: Performance of PnP control and approximate KR methods with a 21-bus network. Switches SW_1, SW_2, SW_3 and SW_4 are closed at times $t = 5$ s, $t = 6.5$ s, $t = 8$ s and $t = 9.5$ s, respectively.

8.7 Final comments

In this chapter, we introduced two approximate network reduction algorithms based on KR and capable to preserve exactly the asymptotic periodic behavior of voltages and currents at target nodes. We also used the proposed KR methods for extending the PnP control design summarized in Chapter 6 to AC ImGs with arbitrary topologies. Future research will address the problems described in Remark 8.6.

8.8 Appendix

8.8.1 Original and reduced parameters of Examples 8.3 and 8.4

Edge	From node	To node	Resistance (Ω)	Inductance (mH)
e_1	1	4	0.1	2
e_2	2	4	0.2	7
e_3	3	4	1	10

Table 8.2: Parameters of the original networks.

Edge	From node	To node	Resistance (Ω)	Inductance (mH)
e_{12}	1	2	0.2746	10.354
e_{13}	1	3	1.4482	14.8132
e_{23}	2	3	3.9315	52.3706

Table 8.3: Parameters of the reduced networks.

8.8.2 Electrical parameters of the 21-bus network

This appendix lists the electrical parameters of the 21-bus network shown in Figure 8.7. The resistances and inductances of the RL lines of network in Figure 8.7 are collected in Table 8.4. The loads connected to the buses are listed in Tables 8.5 and 8.6.

All the electrical parameters of the Kron reduced networks are positive (the nature of the original circuits is preserved). The reduced parameters, when all the four switches are open, are listed in Table 8.7. Table 8.8 shows the reduced R and L when SW_1 and SW_2 are closed, with SW_3 and SW_4 open. The reduced parameters, relative to the network with SW_1, SW_2 and SW_3 closed and SW_4 open, are collected in Table 8.9. Finally, Table 8.10 is referred to the case with all four switches closed.

Edge	From node	To node	Resistance (Ω)	Inductance (mH)
e_1	1	7	1	20
e_2	6	7	0.1	1.8
e_3	3	7	1	200
e_4	2	8	0.6	6
e_5	8	3	0.4	35
e_6	3	12	0.1	1.8
e_7	3	4	1	600
e_8	4	11	0.1	2
e_9	10	11	0.1	2.5
e_{10}	9	10	0.2	4.5
e_{11}	12	13	1.1	300
e_{12}	13	15	1	40
e_{13}	13	14	0.1	2
e_{14}	14	5	0.3	8
e_{15}	14	18	0.1	1
e_{16}	16	18	0.3	30
e_{17}	17	18	0.1	2
e_{18}	6	10	1.1	20
e_{19}	12	16	2.1	300
e_{20}	14	19	0.5	10
e_{21}	19	20	0.3	7
e_{22}	19	21	0.1	1.8

Table 8.4: Parameters of the original 21-bus network.

Node	Resistance (Ω)	Inductance (H)
6	80	0.2
7	80	0
8	50	0
10	100	0
11	100	0
12	50	0.05
13	100	0
14	50	0
15	60	0
17	3	1
18	45	0.02
19	50	0
20	50	0

Table 8.5: Linear loads parameters.

Node	Resistance (Ω)	Filter Inductance (μH)	Filter Capacitance (μF)
9	80	84	235
16	80	84	235

Table 8.6: Nonlinear loads connected to the buses.

Edge	From node	To node	Resistance (Ω)	Inductance (mH)
r_1	1	3	2	220
r_2	2	3	1	41
r_3	3	4	1	600
r_4	3	5	1.6	311.8

Table 8.7: Equivalent parameters when SW_2, SW_3 and SW_4 are open.

Edge	From node	To node	Resistance (Ω)	Inductance (mH)
r_1	1	3	2.2813	371.9
r_5	1	4	2.6589	48.9
r_2	2	3	1	41
r_3	3	4	1.58	269.7
r_4	3	5	1.6	311.8

Table 8.8: Equivalent parameters when SW_1 SW_2 are closed, while SW_3 and SW_4 are open.

Edge	From node	To node	Resistance (Ω)	Inductance (mH)
r_1	1	3	2.2813	371.9
r_5	1	4	2.6586	48.9
r_2	2	3	1	41
r_3	3	4	1.58	269.7
r_4	3	5	1.2971	167.7

Table 8.9: Equivalent parameters when SW_1, SW_2 and SW_3 are closed, and SW_4 is open.

Edge	From node	To node	Resistance (Ω)	Inductance (mH)
r_1	1	3	2.2813	371.9
r_5	1	4	2.6586	48.9
r_2	2	3	1	41
r_3	3	4	1.58	269.7
r_4	3	5	0.5602	275.4
r_6	3	21	6.1756	408.1
r_7	5	21	0.9486	20.4

Table 8.10: Equivalent parameters when all the four switches are open.

Chapter 9

Line-independent plug-and-play control of AC islanded microgrids

Contents

9.1 Introduction 217
9.2 AC microgrid model 219
9.3 Design of plug-and-play stabilizing controllers . 220
9.3.1 Structure of local controllers 220
9.3.2 Conditions for stability of the closed-loop microgrid 221
9.3.3 Computation of local controllers through numerical optimization 224
9.3.4 Plug-and-play operations 225
9.4 Simulation results 226
9.5 Final comments 228
9.6 Appendix 229
9.6.1 Proof of Proposition 9.2 229
9.6.2 Proof of Theorem 9.1 231
9.6.3 Feasibility of the plug-in test (9.15) 235

9.1 Introduction

In this chapter, we propose an extension of the decentralized control synthesis procedure for AC ImGs discussed in Chapter 6. Notably, we develop a PnP control scheme that, differently from the approach in Chapter 6, does not require the knowledge of power lines (hence the name *line-independent* design), whose parameters are often uncertain. We do not assume either to know bounds on electrical coupling parameters, as done in [SSK17]. These simplifications are desirable for the following reasons.

1. The addition/removal of a DGU does not require to update any existing controller in the ImG. Indeed, plugging in/out operations do add/remove lines connected to neighboring DGUs, but DGU controllers are line-independent.

2. DGUs with identical electrical parameters will always be equipped with the same regulator, which can be computed off-line only once. Therefore, for ImGs using a limited set of VSC models, no control synthesis is required at the plug-in/-out time of a DGU.

3. While the PnP design in Chapter 6 is dependent on a global tuning parameter, which must be sufficiently small for ensuring collective ImG stability, here this constraint is removed. Indeed, we propose a different proof of voltage and frequency stability (see Assumption 6.1-(iii)). Notably, we first exploit the fact that DGU interactions can be represented by the admittance matrix of the electric graph (which has a Laplacian structure) for guaranteeing the decrease of a separable Lyapunov function along state trajectories. Then, we complement this result with the application of the LaSalle invariance principle.

Through numerical analysis, we show another important feature of the presented control design procedure: the computation of local stabilizing regulators is always feasible when typical electrical parameters for LV and MV AC ImGs are considered.

The approach presented in this chapter shares several similarities with the one discussed in Chapter 4, where DC mGs are considered and a line-independent variant of the PnP design algorithm in Chapter 3 has been proposed. There is however a fundamental difference: in the AC case, one must handle three-phase balanced signals or, in an equivalent way, their dq representation. Besides making the proofs more involved, this impacts on the optimization problems that have to be solved for the design of local controllers. Indeed, differently from those in Chapter 4 (see (4.16)), LMI constraints are not sufficient for guaranteeing stability, and they must be complemented with nonlinear constraints.

This chapter is structured as follows. Exploiting results from Chapter 6, in Sections 9.2 and 9.3.1, we summarize the considered ImG model and the structure of PnP local controllers, respectively. In the remainder of Section 9.3, we describe the line-independent procedure for designing PnP regulators, and present the stability analysis of the closed-loop ImG. Simulation results using a 10-DGUs ImG with linear and nonlinear loads are shown in Section 9.4. Finally, Section 9.5 is devoted to conclusions.

Notation. Let $A \in \mathbb{R}^{n\times m}$ be a matrix inducing the linear map $A : \mathbb{R}^m \to \mathbb{R}^n$: with $A\big|_B$ we denote the restriction of the map A to the domain B.

9.2 AC microgrid model

We consider the DGU model whose single-phase equivalent scheme is shown in the left dashed frame of Figure 6.2. Notice that, by assuming loads connected to the PCC of each DGU only, we do not loose generality. Indeed fact, as shown in [DB13] and in Chapter 8, general interconnections of loads and DGUs can always be mapped into load-connected topologies by means of KR. We also highlight that sets $\mathcal{V}$ and $\mathcal{N}_i$ ($i \subset \mathcal{V}$) are defined as in Chapter 6. Let us indicate with $\mathcal{G}_{el}$ the undirected electric graph[1] induced by the neighboring relation over the node set $\mathcal{V}$.

Being ω_0 the reference network frequency, the DGU model under QSL approximations and in dq reference frame (rotating with speed ω_0) is described by the set of equations (6.9). At this point, we derive the state-space model of the ImG with dynamics (6.9). Notably, we can write

$$\Sigma_{[i]}^{DGU} : \begin{cases} \dot{x}_{[i]}(t) = A_{ii}x_{[i]}(t) + B_i u_{[i]}(t) + M_i d_{[i]}(t) + \xi_{[i]}(t) \\ y_{[i]}(t) = C_i x_{[i]}(t) \\ z_{[i]}(t) = H_i y_{[i]}(t) \end{cases} \tag{9.1}$$

recalling that $x_{[i]} = [V_i^d, V_i^q, I_{ti}^d, I_{ti}^q]^T$ is the state, $u_{[i]} = [V_{ti}^d, V_{ti}^q]^T$ the control input, $d_{[i]} = [I_{Li}^d, I_{Li}^q]^T$ the exogenous input and $z_{[i]} = [V_i^d, V_i^q]^T$ the controlled variable of the system. Moreover, we highlight that the output $y_{[i]} = x_{[i]}$ is measurable, while the term $\xi_{[i]} = \sum_{j\in\mathcal{N}_i} A_{ij}(x_{[j]} - x_{[i]})$ accounts for the couplings with each DGU $j \in \mathcal{N}_i$.

Remark 9.1. *We highlight that model* (9.1) *is identical to the one in Chapter 6 (see* (6.5)*), except that the coupling terms have been embedded in the contribution* $\xi_{[i]}$.

As regards the matrices in (9.1), they have the following form:

$$A_{ii} = \begin{bmatrix} 0 & \omega_0 & \frac{1}{C_{ti}} & 0 \\ -\omega_0 & 0 & 0 & \frac{1}{C_{ti}} \\ -\frac{1}{L_{ti}} & 0 & -\frac{R_{ti}}{L_{ti}} & \omega_0 \\ 0 & -\frac{1}{L_{ti}} & -\omega_0 & -\frac{R_{ti}}{L_{ti}} \end{bmatrix}, \quad A_{ij} = \frac{1}{C_{ti}} \begin{bmatrix} \frac{R_{ij}}{Z_{ij}^2} & \frac{X_{ij}}{Z_{ij}^2} & \mathbf{0}_{1\times 2} \\ -\frac{X_{ij}}{Z_{ij}^2} & \frac{R_{ij}}{Z_{ij}^2} & \mathbf{0}_{1\times 2} \\ \mathbf{0}_{2\times 1} & \mathbf{0}_{2\times 1} & \mathbf{0}_2 \end{bmatrix},$$

[1] See Appendix A.2 for basic definitions in graph theory.

(9.2)

$$B_i = \begin{bmatrix} \mathbf{0}_{2\times1} & \mathbf{0}_{2\times1} \\ \frac{1}{L_{ti}} & 0 \\ 0 & \frac{1}{L_{ti}} \end{bmatrix}, \qquad M_i = \begin{bmatrix} -\frac{1}{C_{ti}} & 0 \\ 0 & -\frac{1}{C_{ti}} \\ \mathbf{0}_{2\times1} & \mathbf{0}_{2\times1} \end{bmatrix}, \tag{9.3}$$

$$C_i = I_4, \qquad H_i = \begin{bmatrix} 1 & 0 & \mathbf{0}_{1\times2} \\ 0 & 1 & \mathbf{0}_{1\times2} \end{bmatrix}, \tag{9.4}$$

where $X_{ij} = \omega_0 L_{ij}$ and $Z_{ij} = |R_{ij} + \mathrm{i}X_{ij}|$. Moreover, the overall QSL-ImG model is given by (6.16).

9.3 Design of plug-and-play stabilizing controllers

9.3.1 Structure of local controllers

As in Section 6.3.1, in order to track constant references $\mathbf{z_{ref}}(t) = \bar{\mathbf{z}}_{\mathbf{ref}}$, we augment the ImG model with integrators, thus obtaining the following augmented model for the i-th DGU

$$\hat{\Sigma}_{[i]}^{DGU} : \begin{cases} \dot{\hat{x}}_{[i]}(t) = \hat{A}_{ii}\hat{x}_{[i]}(t) + \hat{B}_i u_{[i]}(t) + \hat{M}_i \hat{d}_{[i]}(t) + \hat{\xi}_{[i]}(t) \\ \hat{y}_{[i]}(t) = \hat{C}_i \hat{x}_{[i]}(t) \\ z_{[i]}(t) = \hat{H}_i \hat{y}_{[i]}(t) \end{cases} \tag{9.5}$$

where $\hat{x}_{[i]} = [x^T{}_{[i]}, v_{[i]}^T]^T \in \mathbb{R}^6$ is the state, $\hat{y}_{[i]} = \hat{x}_{[i]}$ the measurable output, $\hat{d}_{[i]} = [d_{[i]}^T, z_{ref}{}_{[i]}^T]^T \in \mathbb{R}^4$ the exogenous signals and

$$\hat{\xi}_{[i]} = \sum_{j\in\mathcal{N}_i} \hat{A}_{ij}(\hat{x}_{[j]} - \hat{x}_{[i]}).$$

Matrices in (9.5) have the form

$$\hat{A}_{ii} = \begin{bmatrix} A_{ii} & \mathbf{0}_{4\times2} \\ -H_i C_i & \mathbf{0}_2 \end{bmatrix}, \qquad \hat{A}_{ij} = \begin{bmatrix} A_{ij} & \mathbf{0}_{4\times2} \\ \mathbf{0}_{2\times4} & \mathbf{0}_2 \end{bmatrix}, \qquad \hat{B}_i = \begin{bmatrix} B_i \\ \mathbf{0}_2 \end{bmatrix},$$
$$\hat{C}_i = \begin{bmatrix} C_i & \mathbf{0}_{4\times2} \\ \mathbf{0}_{2\times4} & I_2 \end{bmatrix}, \qquad \hat{M}_i = \begin{bmatrix} M_i & \mathbf{0}_{4\times2} \\ \mathbf{0}_2 & I_2 \end{bmatrix}, \qquad \hat{H}_i = \begin{bmatrix} H_i & \mathbf{0}_{2\times4} \end{bmatrix}.$$

We highlight that, since all the electrical parameters are positive, the pair $(\hat{A}_{ii}, \hat{B}_i)$ is controllable (see Proposition 2 in [RSFT15]). Therefore, system (9.5) can be stabilized.

The overall augmented system, obtained from (9.5), has the form (6.16).

At this point, we equip each DGU $\hat{\Sigma}_{[i]}^{DGU}$ with the decentralized state-feedback controller described in Section 6.3.2 and shown in Figure 6.2, i.e.

$$\mathcal{C}_{[i]}: \qquad u_{[i]}(t) = K_i \hat{y}_{[i]}(t) = K_i \hat{x}_{[i]}(t).$$

9.3.2 Conditions for stability of the closed-loop microgrid

If coupling terms $\hat{\xi}_i(t)$ are not present, the asymptotic stability of the overall ImG can be ensured by simply stabilizing each closed-loop subsystem

$$\dot{\hat{x}}_{[i]}(t) = \underbrace{(\hat{A}_{ii} + \hat{B}_i K_i)}_{F_i} \hat{x}_{[i]}(t) + \hat{M}_i \hat{d}_{[i]}, \tag{9.6}$$

where, by construction, matrix F_i has the following structure

$$F_i = \left[\begin{array}{c|cc} \mathcal{F}_{11,i} & \mathcal{F}_{12,i} & \mathbf{0}_2 \\ \hline \mathcal{F}_{21,i} & \mathcal{F}_{22,i} & \mathcal{F}_{23,i} \\ -I_2 & \mathbf{0}_2 & \mathbf{0}_2 \end{array}\right] = \left[\begin{array}{c|c} F_{11,i} & F_{12,i} \\ \hline F_{21,i} & F_{22,i} \end{array}\right], \tag{9.7}$$

with

$$\mathcal{F}_{11,i} = \omega_0 \begin{bmatrix} 0 & 1 \\ -1 & 0 \end{bmatrix} \text{ and } \mathcal{F}_{12,i} = \frac{1}{C_{ti}} I_2. \tag{9.8}$$

According to Lyapunov theory, system (9.6) is asymptotically stable if there exists a Lyapunov function $\mathscr{V}_i(\hat{x}_{[i]}) = \hat{x}_{[i]}^T P_i \hat{x}_{[i]}$, with $P_i = P_i^T > 0$, such that

$$Q_i = F_i^T P_i + P_i F_i \tag{9.9}$$

is negative definite.

In a real ImG, however, electric interactions between subsystems exist. For this reason, in the following we present the conditions which allows us to guarantee collective ImG stability by designing totally decentralized controllers, even in presence of couplings between DGUs.

Assumption 9.1. *Each matrix gain K_i, $i \in \mathcal{V}$ is designed using P_i in* (9.9) *with the following structure*

$$P_i = \left[\begin{array}{c|c} \eta_i I_2 & \mathbf{0}_{2\times 4} \\ \hline \mathbf{0}_{4\times 2} & P_{22,i} \end{array}\right], \tag{9.10}$$

where the entries of $P_{22,i} \in \mathbb{R}^{4\times 4}$ *are arbitrary and* $\eta_i > 0$ *is a local parameter.*

Remark 9.2. *Assumption 9.1 amounts to use local separable Lyapunov functions in the form*

$$\mathscr{V}_i(\hat{x}_{[i]}) = \eta_i \hat{x}_{[i],1}^T \hat{x}_{[i],1} + \tilde{x}_{[i]}^T \, P_{22,i} \tilde{x}_{[i]},$$

where $\hat{x}_{[i]} = [\hat{x}_{[i],1}^T, \tilde{x}_{[i]}^T]^T$, $\tilde{x}_{[i]} \in \mathbb{R}^4$.

The second condition regards the values of parameters η_i.

Assumption 9.2. *Let* $\bar{\sigma} > 0$ *be a constant parameter, common to all the DGUs. Parameters* η_i *in* (9.10) *are given by*

$$\eta_i = \bar{\sigma} C_{ti}, \qquad \forall i \in \mathcal{V}.$$

The stability analysis continues by showing that, if Assumption 9.1 holds, Lyapunov theory certifies at most marginal stability of (9.6). To this purpose, we provide the following result.

Proposition 9.1. *Under Assumption 9.1, matrix* Q_i *in* (9.9) *cannot be negative definite. Moreover,*

$$Q_i \leq 0 \tag{9.11}$$

implies that Q_i *has the following structure:*

$$Q_i = \left[\begin{array}{c|cc} \mathbf{0}_2 & \mathbf{0}_2 & \mathbf{0}_2 \\ \hline \mathbf{0}_2 & \mathcal{Q}_{22,i} & \mathcal{Q}_{23,i} \\ \mathbf{0}_2 & \mathcal{Q}_{23,i} & \mathcal{Q}_{33,i} \end{array}\right] = \left[\begin{array}{c|c} \mathbf{0}_2 & \mathbf{0}_{2\times 4} \\ \hline \mathbf{0}_{4\times 2} & Q_{22,i} \end{array}\right]. \tag{9.12}$$

Proof. By substituting (9.7) and (9.10) in (9.9), one gets that the first two diagonal elements of Q_i are zero. This shows that Q_i cannot be negative definite. Moreover, from basic linear algebra, if a negative semidefinite matrix has a zero element on its diagonal, the corresponding row and column have zero entries (see the proof of Proposition 4.10). Then (9.11) implies (9.12). □

Next, we consider the overall closed-loop ImG model, given by

$$\begin{cases} \dot{\hat{\mathbf{x}}}(t) = (\hat{\mathbf{A}} + \hat{\mathbf{B}}\mathbf{K})\hat{\mathbf{x}}(t) + \hat{\mathbf{M}}\hat{\mathbf{d}}(t) \\ \hat{\mathbf{y}}(t) = \hat{\mathbf{C}}\hat{\mathbf{x}}(t) \\ \mathbf{z}(t) = \hat{\mathbf{H}}\hat{\mathbf{y}}(t) \end{cases} \tag{9.13}$$

where $\mathbf{K} = \text{diag}[K_1, \dots, K_N]$. Being $\mathbf{P} = \text{diag}[P_1, \dots, P_N]$, the collective Lyapunov function is

$$\mathscr{V}(\hat{\mathbf{x}}) = \sum_{i=1}^{N} \mathscr{V}_i(\hat{x}_{[i]}) = \hat{\mathbf{x}}^T \mathbf{P} \hat{\mathbf{x}}.$$

Consequently, one has that $\dot{\mathscr{V}}(\hat{\mathbf{x}}) = \hat{\mathbf{x}}^T \mathbf{Q} \hat{\mathbf{x}}$, where

$$\mathbf{Q} = (\hat{\mathbf{A}} + \hat{\mathbf{B}}\mathbf{K})^T \mathbf{P} + \mathbf{P}(\hat{\mathbf{A}} + \hat{\mathbf{B}}\mathbf{K}).$$

From Proposition 9.1, we know that, if Assumption 9.1 holds, then (i) matrix $\mathbf{Q}$ cannot be negative definite, and (ii), at most, one can have

$$\mathbf{Q} \leq 0. \tag{9.14}$$

At this point, we notice that, even if (9.11) is verified for all $i \in \mathcal{V}$, the inequality (9.14) might be violated because of the nonzero coupling terms $\hat{A}_{ij}$ in matrix $\hat{\mathbf{A}}$ (an example is provided in Appendix B of [RSFT14]). However, through the next proposition, we show that (9.14) is always satisfied if also Assumption 9.2 is fulfilled.

Proposition 9.2. *Under Assumptions 9.1 and 9.2, if matrix gains K_i are computed to satisfy* (9.11) *for all $i \in \mathcal{V}$, then* (9.14) *holds.*

Proof. The proof of Proposition 9.2 is reported in Appendix 9.6.1. □

Remark 9.3. *The proof of Proposition 9.2 reveals that, under Assumptions 9.1 and 9.2, interactions between local Lyapunov functions $\mathscr{V}_i(\hat{x}_{[i]})$ due to terms $\hat{A}_{ij}$, $i \neq j$, take the form of a weighted Laplacian matrix associated with the graph $\mathcal{G}_{el}$. Furthermore, differently from the idea in Chapter 6 of nullifying interactions by choosing $\eta_i > 0$ in* (9.10) *sufficiently small, here* (9.14) *holds true even if parameters η_i are large.*

In order to show the asymptotic stability of the ImG, we need to complement Proposition 9.2 with the application of the LaSalle invariance theorem. This will be done in the next theorem.

Theorem 9.1. *If Assumptions 9.1 and 9.2 are fulfilled, the graph $\mathcal{G}_{el}$ is connected,* (9.11) *holds, $Q_{22,i}\big|_{Im(F_{22,i}^T)}$ is invertible and* $\det(\mathcal{F}_{22,i}\mathcal{F}_{21,i} - \mathcal{F}_{23,i}) \neq 0$, $\forall i \in \mathcal{V}$, the origin of (9.13) is asymptotically stable.

Proof. The proof of Theorem 9.1 is reported in the Appendix 9.6.2. □

9.3.3 Computation of local controllers through numerical optimization

The problem of computing matrices K_i and P_i so as to fulfill the assumptions of Theorem 9.1, can be split into two subproblems.

SP1 Let parameters η_i be computed as in Assumption 9.2, where the ImG parameter $\bar{\sigma}$ is assumed to be fixed. Compute matrices K_i and P_i so that Assumption 9.1 and inequality (9.11) hold.

SP2 Check if $Q_{22,i}\big|_{\mathrm{Im}(F_{22,i}^T)}$ and $(\mathcal{F}_{22,i}\mathcal{F}_{21,i} - \mathcal{F}_{23,i})$ are invertible maps.

SP1 can be recast into an LMI problem. To this purpose, we enforce, when possible, a margin of robustness by designing controllers K_i such that inequality

$$(\hat{A}_{ii} + \hat{B}_i K_i)^T P_i + P_i(\hat{A}_{ii} + \hat{B}_i K_i) + \Gamma_i^{-1} \leq 0,$$

with $\Gamma_i = \mathrm{diag}[\gamma_{1i}, \gamma_{2i}, \gamma_{3i}, \gamma_{4i}, \gamma_{5i}, \gamma_{6i}]$, is verified for $\gamma_{ki} \geq 0$, $k = 1, \ldots, 6$ and matrix P_i structured as in (9.10). Then, we solve the following LMI problem

$$\mathcal{O}_i : \min_{Y_i, G_i, \{\gamma_{ki}\}_{k=1}^6, \beta_i, \zeta_i} \quad \sum_{k=1}^{6} \alpha_{ki}\gamma_{ki} + \alpha_{7i}\beta_i + \alpha_{8i}\zeta_i$$

$$Y_i = \begin{bmatrix} \eta_i^{-1} & 0 & 0 & 0 & 0 & 0 \\ 0 & \eta_i^{-1} & 0 & 0 & 0 & 0 \\ 0 & 0 & \bullet & \bullet & \bullet & \bullet \\ 0 & 0 & \bullet & \bullet & \bullet & \bullet \\ 0 & 0 & \bullet & \bullet & \bullet & \bullet \\ 0 & 0 & \bullet & \bullet & \bullet & \bullet \end{bmatrix} > 0 \tag{9.15a}$$

$$\begin{bmatrix} Y_i\hat{A}_{ii}^T + G_i^T\hat{B}_i^T + \hat{A}_{ii}Y_i + \hat{B}_i G_i & Y_i \\ Y_i & -\Gamma_i \end{bmatrix} \leq 0 \tag{9.15b}$$

$$\begin{bmatrix} -\beta_i I & G_i^T \\ G_i & -I \end{bmatrix} < 0, \tag{9.15c}$$

$$\begin{bmatrix} Y_i & I \\ I & \zeta_i I \end{bmatrix} > 0 \tag{9.15d}$$

$$\gamma_{ki} \geq 0, i = 1, \ldots, 6, \quad \beta_i > 0, \quad \zeta_i > 0, \tag{9.15e}$$

where α_{ji}, $j = 1, \ldots, 8$ represent positive weights and $\bullet$ are arbitrary entries. Similarly to what has been shown in Chapter 6, feasible solutions

of (9.15) provide $P_i = Y_i^{-1}$, with the structure (9.10) and $K_i = Y_i^{-1}G_i$. Furthermore, the cost penalizes aggressive control actions because it minimizes β_i and ζ_i that, in view of (9.15c), provide the bound $||K_i||_2 \leq \sqrt{\beta_i}\zeta_i$ [RSFT15].

SP2 provides constraints that can be either verified a posteriori or added to (9.15). While the latter solution is preferable, constraints are nonlinear in the optimization variables of problem $\mathcal{O}_i$, and therefore spoil the LMI nature of (9.15). Future research will focus on finding convex formulations (or convex approximations) of conditions in SP2.

We highlight that the computation of controller $\mathcal{C}_{[i]}$ is completely decentralized (i.e. independent from the synthesis of controllers $\mathcal{C}_{[j]}$, $j \neq i$), as constraints in (9.15) depend upon local fixed matrices ($\hat{A}_{ii}$, $\hat{B}_i$) and local design parameters α_{ki}, $k = 1, \ldots, 8$.. Finally, if problems SP1 and SP2 are feasible for all DGUs, then the overall closed-loop QSL-ImG is asymptotically stable.

Remark 9.4. *Controllers $\mathcal{C}_{[i]}$ yield a closed-loop DGU model that is linear. Hence, it can be easily complemented with pre-filters (for tuning the local bandwidth) and load-current compensators. These enhancements (not used in the simulation in Section 9.4) are described in [RSFT15].*

Remark 9.5. *Similarly to what we has been done in Chapter 4 for the line-independent PnP design in DC mGs, we assess the conservativeness of the LMIs* (9.15) *by solving it for $\bar{\sigma} = 10^4$, and for different combinations of DGU parameters (R_t, L_t, C_t). Numerical results, detailed in Appendix 9.6.3, reveal that the computation of local stabilizing regulators is always feasible when typical electrical parameters for LV and MV AC ImGs are considered.*

9.3.4 Plug-and-play operations

In this section, we describe the operations to be performed whenever the plug-in/-out of a DGU is required, in order to preserve the overall ImG stability.

Plug-in operation. Suppose that we want to connect a new DGU (say $\hat{\Sigma}^{DGU}_{[N+1]}$) to the ImG and let $\mathcal{N}_{[N+1]}$ be the set of DGUs that will be directly connected to $\hat{\Sigma}^{DGU}_{[N+1]}$ through power lines. Then, we first solve subproblems SP1 and SP2 in Section 9.3.3 for the new unit. If at least one subproblem is infeasible, the plug-in is denied. Otherwise, $\hat{\Sigma}^{DGU}_{[N+1]}$ can be connected and,

differently from the protocol described in Section 6.3.3, DGUs in $\mathcal{N}_{[N+1]}$ do not have to retune their local controllers in order to fulfill stability conditions. Indeed, the computation of each local controller is performed solving (9.15), which, under Assumption 9.2, depends exclusively upon local quantities (namely, matrices $\hat{A}_{ii}$ and $\hat{B}_i$) not affected by changes in the ImG topology.

Unplugging operation. When a DGU is disconnected, this has no impact on the controllers of the remaining units, if they are designed using the line-independent method described in Section 9.3.3. Therefore, in view of Theorem 9.1, stability of the ImG is preserved.

Remark 9.6. *In Theorem 9.1, the connectivity of $\mathcal{G}_{el}$ is assumed in order to prove that the origin of* (9.13) *is asymptotic stable. On the other hand, we should notice that unplugging operations might make $\mathcal{G}_{el}$ disconnected. These events, however, do not affect the main results since the same analysis presented in Section 9.3 can be conducted with respect to each connected subgraph $\mathcal{G}_{el}^s$ (which, in turn, can be seen as an independent ImG) arising from the unplugging operations. In the next section, we show, through simulations, the capability of PnP line-independent regulators to preserve voltage and frequency stability in spite of the creation of sub-islands caused by multiple power line trips.*

9.4 Simulation results

In this section, we study the performance of the proposed PnP controllers. We consider the ImG in Figure 9.1, composed of 10 DGUs. All DGUs feed *RL* loads, except DGU 2 which is connected to a three-phase six-pulse diode rectifier. We notice a loop in the network that complicates the voltage regulation. Furthermore, DGUs are non-identical and all the electrical parameters are similar to those of the 11-DGUs example in [RSFT14].

The simulation (conducted in PSCAD) starts with DGUs 1-9 connected together and equipped with PnP controllers $\mathcal{C}_{[i]}$, $i = 1, \ldots, 9$.

As a first test, we validate the capability of PnP regulators to deal with real-time plugging in of DGUs. Therefore, at time $t = 7.5$ s, we simulate the connection of DGU 10, with DGUs 2 and 8 (see Figure 9.1a). Before this event, as described in Section 9.3.4, we solve subproblems SP1 and SP2 for computing $\mathcal{C}_{[10]}$ and, since both of them result to be feasible, the connection of DGU 10 is allowed. The *dq* component of the voltages at PCCs 2, 8, 10 are shown in Figures 9.2a, 9.2d and 9.2e, respectively. Notably, we

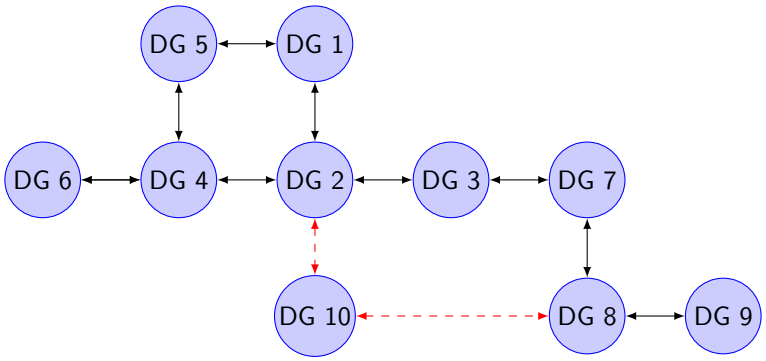

(a) ImG topologies until $t = 12$ s. For $0 \leq t < 7.5$ s, DGUs 1-9 are interconnected (in black); at $t = 7.5$ s, DGU 10 joins the network (in red).

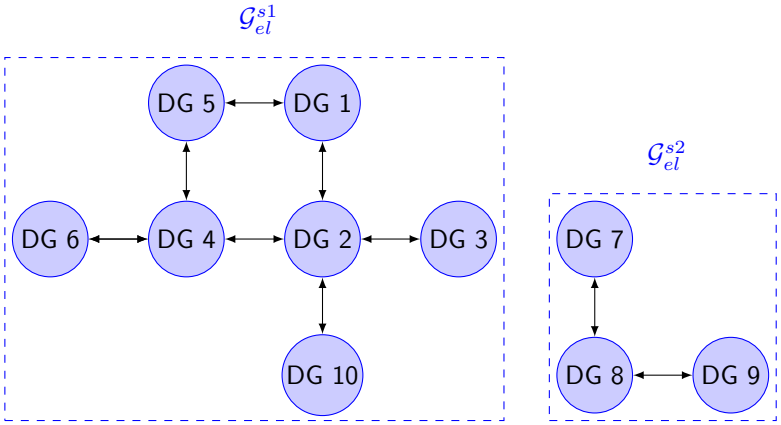

(b) Independent ImGs after the trip of lines 3-7 and 8-10 occurred at time $t = 12$ s.

Figure 9.1: Simulation of a 10-DGUs ImGs: considered network topologies.

notice very small deviations of the DGUs voltages from their respective reference signals ($V_{2,ref}^{d} = 0.6$ p.u., $V_{2,ref}^{q} = 0.5$ p.u., $V_{8,ref}^{d} = 0.7$ p.u., $V_{8,ref}^{q} = 0.6$ p.u., and $V_{10,ref}^{q} = 0.8$ p.u., $V_{10,ref}^{q} = 0.6$ p.u.). Furthermore, these deviations are compensated after a short transient.

In order to assess the robustness of the PnP-controlled ImG to load dynamics, at time $t = 10$ s we simulate an abrupt switch of the RL load at PCC 10 (i.e. from $R = 60\ \Omega$, $L = 0.02$ mH to $R = 120\ \Omega$, $L = 0.02$ mH).

From Figures 9.2a, 9.2d and 9.2e, we notice that the d and q components of the voltages at PCCs 2, 8 and 10, do not significantly deviate from their references, thus revealing that step changes in the loads can be rapidly absorbed. Figure 9.2f shows that the real-time plug-in of DGU 10 and the load change at its PCC produce minor effects also on the frequency profiles of the PCC voltages. Notably, PnP regulators are capable to promptly restore the frequencies to the reference value (50 Hz) guaranteeing, overall, variations smaller than 0.6 Hz. In a similar way, we do not notice significant deviations from the reference RMS voltages (see Figure 9.2g).

Next, we test the capabilities of PnP regulators to preserve voltage and frequency stability even when a sudden disconnection of a portion of the network occurs. To this purpose, at time $t = 12$ s, we simulate the simultaneous trip of lines 3-7 and 8-10, leading to the formation of two independent ImGs (see the corresponding subgraphs $\mathcal{G}_{el}^{s1}$ and $\mathcal{G}_{el}^{s2}$ Figure 9.1b). In the light of Remark 9.6, the stability of the two networks is preserved (as shown in Figures 9.2b-9.2g), without the need to redesign any local controller. This feature can be useful in those scenarios where the disconnection of DGUs might need to be performed abruptly, due, for instance, to faults in the power lines.

Finally, we notice that the THD of the voltage at PCC 2 (whose local load is nonlinear) always remains below 5%, which is the maximum limit recommended by IEEE standards [IEE09] (see Figure 9.2h).

9.5 Final comments

In this chapter, we presented a decentralized control approach to voltage and frequency stabilization in AC ImGs. Differently from the PnP methodology described in Chapter 6, the presented procedure guarantees overall ImG stability while computing local regulators in a line-independent fashion. This feature considerably simplifies the PnP protocol described in Section 6.3.3, since neighboring DGUs do not have anymore to update their local controllers when subsystems are added or removed. Moreover, compared to the method in Chapter 6, it may seem that the successful computation of regulators ensuring collective stability via the line-independent procedure is more involved (as LMI constraints 9.15 are now complemented with nonlinear constraints). However, in Appendix 9.6.3 we show that subproblems SP1-SP2 are always feasible for LV and MV AC ImGs.

Future research will focus on studying how to couple PnP local regulators with a higher control layer for power flow regulation among DGUs.

9.6 Appendix

9.6.1 Proof of Proposition 9.2

Proof. We start by decomposing the matrix $\hat{\mathbf{A}}$ as follows

$$\hat{\mathbf{A}} = \hat{\mathbf{A}}_{\mathbf{D}} + \hat{\mathbf{A}}_{\mathbf{\Xi}} + \hat{\mathbf{A}}_{\mathbf{C}}, \tag{9.16}$$

where (i) $\hat{\mathbf{A}}_{\mathbf{D}} = \text{diag}[\hat{A}_{ii}, \dots, \hat{A}_{NN}]$ collects the local dynamics only, (ii) $\hat{\mathbf{A}}_{\mathbf{\Xi}} = \text{diag}[\hat{A}_{\xi 1}, \dots, \hat{A}_{\xi N}]$ with

$$\hat{A}_{\xi i} = \frac{1}{C_{ti}} \left[\begin{array}{cc|c} \sum\limits_{j\in\mathcal{N}_i} -\widetilde{R}_{ij} & \sum\limits_{j\in\mathcal{N}_i} -\widetilde{X}_{ij} & \mathbf{0}_{1\times 4} \\ \sum\limits_{j\in\mathcal{N}_i} \widetilde{X}_{ij} & \sum\limits_{j\in\mathcal{N}_i} -\widetilde{R}_{ij} & \mathbf{0}_{1\times 4} \\ \hline \mathbf{0}_{4\times 1} & \mathbf{0}_{4\times 1} & \mathbf{0}_4 \end{array}\right], \tag{9.17}$$

$\widetilde{R}_{ij} = \frac{R_{ij}}{Z_{ij}^2}$ and $\widetilde{X}_{ij} = \frac{X_{ij}}{Z_{ij}^2}$, takes into account the dependence of each local state on the neighboring DGUs, and (iii) $\hat{\mathbf{A}}_{\mathbf{C}}$ includes the effect of couplings. Notably, this latter matrix is composed of zero blocks on the diagonal and blocks $\hat{A}_{ij}$, $i \neq j$ outside the diagonal. Our goal is to demonstrate (9.14), which, using (9.16), becomes

$$\underbrace{(\hat{\mathbf{A}}_{\mathbf{D}} + \hat{\mathbf{B}}\mathbf{K})^{\mathbf{T}}\mathbf{P} + \mathbf{P}(\hat{\mathbf{A}}_{\mathbf{D}} + \hat{\mathbf{B}}\mathbf{K})}_{(a)} + \underbrace{\hat{\mathbf{A}}_{\mathbf{\Xi}}^{\mathbf{T}}\mathbf{P} + \mathbf{P}\hat{\mathbf{A}}_{\mathbf{\Xi}}}_{(b)} + \underbrace{\hat{\mathbf{A}}_{\mathbf{C}}^{T}\mathbf{P} + \mathbf{P}\hat{\mathbf{A}}_{\mathbf{C}}}_{(c)} \leq 0. \tag{9.18}$$

Since (9.11) holds, we have that $(a) = \text{diag}[Q_1, \dots, Q_N] \leq 0$. At this point, we need to study the contribution of matrix $(b) + (c)$ in (9.18). By construction (recalling (9.10) and (9.17)), matrix (b) is block diagonal, collecting, on its diagonal, blocks $\hat{A}_{\xi i}^T P_i + P_i \hat{A}_{\xi i}$ in the form

$$\hat{A}_{\xi i}^T P_i + P_i \hat{A}_{\xi i} = \left[\begin{array}{cc|c} -\frac{\eta_i}{C_{ti}} \sum\limits_{j\in\mathcal{N}_i} \left(\widetilde{R}_{ij} + \widetilde{R}_{ij}\right) & \frac{\eta_i}{C_{ti}} \sum\limits_{j\in\mathcal{N}_i} \left(\widetilde{X}_{ij} - \widetilde{X}_{ij}\right) & \mathbf{0}_{1\times 4} \\ \frac{\eta_i}{C_{ti}} \sum\limits_{j\in\mathcal{N}_i} \left(\widetilde{X}_{ij} - \widetilde{X}_{ij}\right) & -\frac{\eta_i}{C_{ti}} \sum\limits_{j\in\mathcal{N}_i} \left(\widetilde{R}_{ij} + \widetilde{R}_{ij}\right) & \mathbf{0}_{1\times 4} \\ \hline \mathbf{0}_{4\times 1} & \mathbf{0}_{4\times 1} & \mathbf{0}_4 \end{array}\right] =$$

$$= \left[\begin{array}{cc|c} -\sum\limits_{j\in\mathcal{N}_i} 2\tilde{\eta}_{ij} & 0 & \mathbf{0}_{1\times 4} \\ 0 & -\sum\limits_{j\in\mathcal{N}_i} 2\tilde{\eta}_{ij} & \mathbf{0}_{1\times 4} \\ \hline \mathbf{0}_{4\times 1} & \mathbf{0}_{4\times 1} & \mathbf{0}_4 \end{array}\right],$$

(9.19)

with $\tilde{\eta}_{ij} = \frac{\eta_i}{C_{ti}}\widetilde{R}_{ij} = \bar{\sigma}\widetilde{R}_{ij}$. Regarding matrix (c), we have that each the block in position (i,j) is equal to

$$\begin{cases} P_i\hat{A}_{ij} + \hat{A}_{ji}^T P_j & \text{if } j \in \mathcal{N}_i \\ \mathbf{0}_6 & \text{otherwise} \end{cases} \tag{9.20}$$

In particular, recalling Assumption 9.2, by direct calculation, it results

$$P_i\hat{A}_{ij} + \hat{A}_{ji}^T P_j = \left[\begin{array}{cc|c} \frac{\eta_i}{C_{ti}}\widetilde{R}_{ij} + \frac{\eta_j}{C_{tj}}\widetilde{R}_{ji} & 0 & \mathbf{0}_{1\times 4} \\ 0 & \frac{\eta_i}{C_{ti}}\widetilde{R}_{ij} + \frac{\eta_j}{C_{tj}}\widetilde{R}_{ji} & \mathbf{0}_{1\times 4} \\ \hline \mathbf{0}_{4\times 1} & \mathbf{0}_{4\times 1} & \mathbf{0}_4 \end{array}\right] =$$

$$= \left[\begin{array}{cc|c} \tilde{\eta}_{ij} + \tilde{\eta}_{ji} & 0 & \mathbf{0}_{1\times 4} \\ 0 & \tilde{\eta}_{ij} + \tilde{\eta}_{ji} & \mathbf{0}_{1\times 4} \\ \hline \mathbf{0}_{4\times 1} & \mathbf{0}_{4\times 1} & \mathbf{0}_4 \end{array}\right] = \left[\begin{array}{c|c} 2\tilde{\eta}_{ij} I_2 & \mathbf{0}_{2\times 4} \\ \hline \mathbf{0}_{4\times 2} & \mathbf{0}_4 \end{array}\right]. \tag{9.21}$$

By looking at (9.19) and (9.21), we observe that only the elements in position $(1,1)$ and $(2,2)$ of each 6×6 block of $(b)+(c)$ can be different from zero. Therefore, the positive/negative definiteness of the $6N \times 6N$ matrix $(b)+(c)$ can be equivalently studied by considering the $2N \times 2N$ matrix

$$\mathcal{L} = \begin{bmatrix} \Phi_{11} & \Phi_{12} & \dots & \Phi_{1N} \\ \Phi_{21} & \ddots & \ddots & \vdots \\ \vdots & \ddots & \Phi_{N-1\ N-1} & \Phi_{N-1\ N} \\ \Phi_{N1} & \dots & \Phi_{N\ N-1} & \Phi_{NN} \end{bmatrix}, \tag{9.22}$$

obtained by deleting the last four rows and columns in each block of $(b)+(c)$. In particular, we can write (9.22) as $\mathcal{L} = \mathcal{M} + \mathcal{G}$, where

$$\mathcal{M} = \text{diag}[\Phi_{11}, \dots, \Phi_{NN}], \quad \Phi_{ii} = \begin{bmatrix} \sum\limits_{j\in\mathcal{N}_i} -2\tilde{\eta}_{ij} & 0 \\ 0 & \sum\limits_{j\in\mathcal{N}_i} -2\tilde{\eta}_{ij} \end{bmatrix},$$

and

$$\mathcal{G} = \begin{bmatrix} \mathbf{0}_2 & \Phi_{12} & \dots & \Phi_{1N} \\ \Phi_{21} & \mathbf{0}_2 & \ddots & \vdots \\ \vdots & \ddots & \ddots & \Phi_{N-1\ N} \\ \Phi_{N1} & \dots & \Phi_{N\ N-1} & \mathbf{0}_2 \end{bmatrix}.$$

We highlight that, from (9.20) and (9.21), blocks Φ_{ij}, $i \neq j$, are equal to

$$\Phi_{ij} = \begin{cases} \begin{bmatrix} 2\tilde{\eta}_{ij} & 0 \\ 0 & 2\tilde{\eta}_{ij} \end{bmatrix} & \text{if } j \in \mathcal{N}_i \\ \mathbf{0}_2 & \text{otherwise} \end{cases}$$

Next, we notice that $\mathcal{L}$ is symmetric, with non negative off-diagonal elements and zero row and column sum. In other words, $\mathcal{L}$ is a Laplacian matrix [GR01], and, as such, it is negative semidefinite. This allows us to show that (9.18) (and, equivalently, (9.14)) holds. □

9.6.2 Proof of Theorem 9.1

Before showing the proof of Theorem 9.1, in the next two propositions we provide some preliminary results which are instrumental in characterizing the states $\hat{\mathbf{x}}$ yielding $\dot{\mathscr{V}}(\hat{\mathbf{x}}) = 0$.

Proposition 9.3. *Let $f_i(v_i) = v_i^T Q_{22,i} v_i$, with $v_i \in \mathbb{R}^4$, and let Assumptions 9.1 and 9.2 hold. If* (9.11) *is guaranteed and $Q_{22,i}|_{Im(F_{22,i}^T)}$ is invertible, then*

$$f_i(\bar{v}_i) = 0 \Longleftrightarrow \bar{v}_i \in Ker(F_{22,i}).$$

Proof. For the sake of simplicity, in the sequel we omit the subscript i.

Step 1. We start by proving that

$$\bar{v} \in \mathrm{Ker}(F_{22}) \Longrightarrow f(\bar{v}) = 0. \tag{9.23}$$

To do so, we first replace (9.7) and (9.10) in (9.9), thus obtaining

$$Q_{22} = F_{22}^T P_{22} + P_{22} F_{22}.$$

Then, we write

$$\begin{aligned} f(\bar{v}) &= \bar{v}^T Q_{22} \bar{v} = \\ &= \bar{v}^T F_{22}^T P_{22} \bar{v} + \bar{v}^T P_{22} F_{22} \bar{v} = 2\bar{v}^T P_{22} \underbrace{F_{22}\bar{v}}_{=\mathbf{0}_{4\times 1}} = 0. \end{aligned}$$

Step 2. Next, we show that

$$f(\bar{v}) = 0 \Longrightarrow \bar{v} \in \mathrm{Ker}(F_{22}). \tag{9.24}$$

To this aim, we reformulate the condition $f(\bar{v}) = 0$ in (9.24). In particular, from basic linear algebra, we have the following orthogonal decomposition induced by F_{22}

$$\mathbb{R}^4 = \mathrm{Im}(F_{22}^T) \oplus \mathrm{Ker}(F_{22}),$$

which allows us to write any vector $v \in \mathbb{R}^4$ as

$$v = \hat{v} + \tilde{v}, \quad \hat{v} \in \mathrm{Im}(F_{22}^T), \tilde{v} \in \mathrm{Ker}(F_{22}). \tag{9.25}$$

Now, since we are assuming that Q is negative semidefinite and structured as in (9.12), vectors $\bar{v}$ satisfying $f(\bar{v}) = 0$ also maximize $f(\cdot)$. Hence,

$$f(\bar{v}) = 0 \Longleftrightarrow \frac{\mathrm{d}f}{\mathrm{d}v}(\bar{v}) = Q_{22}\bar{v} = \mathbf{0}_{4\times 1}, \tag{9.26}$$

which, decomposing $\bar{v}$ as in (9.25), translates into

$$f(\bar{v}) = 0 \Longleftrightarrow Q_{22}\hat{v} + \underbrace{Q_{22}\tilde{v}}_{=\mathbf{0}_{4\times 1}} = \mathbf{0}_{4\times 1}. \tag{9.27}$$

Notice that $Q_{22}\tilde{v} = \mathbf{0}_{4\times 1}$ in (9.27) comes from the fact that $\tilde{v} \in \mathrm{Ker}(F_{22})$. In particular, from (9.23), we know that $f(\tilde{v}) = 0$, and hence condition (9.26) must hold for $\bar{v} = \tilde{v}$. At this point, using (9.27), we can rewrite (9.24) as follows

$$Q_{22}\hat{v} = \mathbf{0}_{4\times 1} \Longrightarrow \bar{v} \in \mathrm{Ker}(F_{22}),$$

which, since $\bar{v} \in \mathrm{Ker}(F_{22}) \Longleftrightarrow \hat{v} = \mathbf{0}_{4\times 1}$, finally becomes

$$Q_{22}\hat{v} = \mathbf{0}_{4\times 1} \Longrightarrow \hat{v} = \mathbf{0}_{4\times 1}. \tag{9.28}$$

Since $Q_{22,i}\big|_{\mathrm{Im}(F_{22,i}^T)}$ is invertible, (9.28) is verified. The proof ends by observing that (9.28) is equivalent to (9.24). □

Proposition 9.4. *Let $g_i(w_i) = w_i^T Q_i w_i$, with $w_i \in \mathbb{R}^6$, and let the same assumptions of Proposition 9.3 hold. Then, only vectors $\bar{w}_i$ in the form*

$$\bar{w}_i = \begin{bmatrix} \alpha_i^T & \beta_i^T & \gamma_i^T \end{bmatrix}^T$$

with $\alpha_i, \beta_i, \gamma_i \in \mathbb{R}^2$ and $\mathcal{F}_{22,i}\beta_i + \mathcal{F}_{23,i}\gamma_i = \mathbf{0}_{2\times 1}$, fulfill

$$g_i(\bar{w}_i) = 0. \tag{9.29}$$

Proof. As for the proof of Proposition 9.3, we omit the subscript i. Using (9.12), we write

$$g(w) = \left[\begin{array}{c|c} w_1^T & w_2^T \end{array}\right] \left[\begin{array}{c|c} \mathbf{0}_2 & \mathbf{0}_{2\times 4} \\ \hline \mathbf{0}_{4\times 2} & Q_{22} \end{array}\right] \left[\begin{array}{c} w_1 \\ \hline w_2 \end{array}\right], \tag{9.30}$$

where $w_2 \in \mathbb{R}^4$. Since Q is negative semidefinite, vectors $\bar{w}$ satisfying (9.29) also maximize $g(\cdot)$. Hence, it must hold $\frac{\mathrm{d}g}{\mathrm{d}w}(\bar{w}) = Q\bar{w} = \mathbf{0}_{6\times 1}$, i.e.

$$\left[\begin{array}{c|c} \mathbf{0}_2 & \mathbf{0}_{2\times 4} \\ \hline \mathbf{0}_{4\times 2} & Q_{22} \end{array}\right] \left[\begin{array}{c} \bar{w}_1 \\ \hline \bar{w}_2 \end{array}\right] = \mathbf{0}_{6\times 1}. \tag{9.31}$$

Obviously, a set of solutions to (9.29) and (9.31) is composed of vectors

$$\bar{w} = \left[\begin{array}{cc} \alpha^T & \mathbf{0}_{1\times 4} \end{array}\right]^T, \quad \alpha \in \mathbb{R}^2. \tag{9.32}$$

Moreover, from (9.30), we have that (9.29) is also verified if there exist vectors

$$\tilde{w} = \left[\begin{array}{c|c} w_1^T & \underline{w}_2^T \end{array}\right]^T, \quad \underline{w}_2 \in \mathbb{R}^4, \underline{w}_2 \neq \mathbf{0}_{4\times 1}, \tag{9.33}$$

such that

$$\underline{w}_2^T Q_{22} \underline{w}_2 = 0, \tag{9.34}$$

$\forall w_1 \in \mathbb{R}^2$. At this point, we exploit the result of Proposition 9.3. We know, in fact, that vectors $\underline{w}_2$ satisfying (9.34) belong to $\mathrm{Ker}(F_{22})$, which can be characterized as follows

$$\begin{aligned} &\left\{ x \in \mathbb{R}^4 : \left[\begin{array}{cc} \mathcal{F}_{22} & \mathcal{F}_{23} \\ \mathbf{0}_2 & \mathbf{0}_2 \end{array}\right] x = \mathbf{0}_{4\times 1} \right\} = \\ &\{ x \in \mathbb{R}^4 : x = \left[\begin{array}{cc} \beta^T & \gamma^T \end{array}\right]^T, \beta, \gamma \in \mathbb{R}^2, \mathcal{F}_{22}\beta + \mathcal{F}_{23}\gamma = \mathbf{0}_{2\times 1} \}. \end{aligned} \tag{9.35}$$

The proof concludes by merging (9.32) and (9.33) (with $\underline{w}_2$ as in (9.35)). □

Proof of Theorem 9.1. From Proposition 9.2, we have that (9.14) holds. Therefore, we aim to use the LaSalle invariance Theorem [Kha01] to show that the origin of the ImG is attractive. Let us compute the set $R = \{\mathbf{x} \in \mathbb{R}^{6N} : \mathbf{x}^T \mathbf{Q} \mathbf{x} = 0\}$, which, using (9.18), can be written as

$$\begin{aligned} R &= \{\mathbf{x} : \mathbf{x}^T \left((a) + (b) + (c)\right) \mathbf{x} = 0\} \\ &= \{\mathbf{x} : \mathbf{x}^T (a) \mathbf{x} + \mathbf{x}^T (b) \mathbf{x} + \mathbf{x}^T (c) \mathbf{x} = 0\} \\ &= \underbrace{\{\mathbf{x} : \mathbf{x}^T (a) \mathbf{x} = 0\}}_{X_1} \cap \underbrace{\{\mathbf{x} : \mathbf{x}^T \left[(b) + (c)\right] \mathbf{x} = 0\}}_{X_2}, \end{aligned} \tag{9.36}$$

and first focus on characterizing the vectors of set X_1. Recalling that $(a) = \text{diag}[Q_1, \dots, Q_N]$, we can exploit Proposition 9.4, thus having

$$X_1 = \{\mathbf{x} : \mathbf{x} = \left[\begin{array}{c|c|c|c} \alpha_1^T & \beta_1^T & \gamma_1^T & \cdots \end{array} \right. \left. \begin{array}{c|c|c} \alpha_N^T & \beta_N^T & \gamma_N^T \end{array} \right]^T, \\ \alpha_i, \beta_i, \gamma_i \in \mathbb{R}^2, \mathcal{F}_{22,i}\beta_i + \mathcal{F}_{23,i}\gamma_i = \mathbf{0}_{2\times 1}\}.$$

Next, we focus on the elements of X_2. We have seen that the term $(b)+(c)$ is an "expansion" of the Laplacian matrix in (9.22), obtained by augmenting each 2×2 block Φ_{ij} of $\mathcal{L}$ with zero rows and columns, so as to retrieve blocks of dimension 6×6. It follows that, by construction, X_2 contains vectors in the form

$$\tilde{\mathbf{x}} = \left[\begin{array}{c|c|c|c} \mathbf{0}_{1\times 2} & \tilde{x}_{12}^T & \tilde{x}_{13}^T & \cdots \end{array} \right. \left. \begin{array}{c|c|c} \mathbf{0}_{1\times 2} & \tilde{x}_{N2}^T & \tilde{x}_{N3}^T \end{array} \right]^T, \quad \tilde{x}_{i2}, \tilde{x}_{i3} \in \mathbb{R}^2, \forall i \in \mathcal{V}. \tag{9.37}$$

Moreover, since the kernel of the Laplacian matrix of a connected graph contains only vectors with identical entries [GR01], we also have that

$$\{\bar{\mathbf{x}} = \left[\begin{array}{c|c|c|c} \bar{x}^T & \mathbf{0}_{1\times 2} & \mathbf{0}_{1\times 2} & \cdots \end{array} \right. \left. \begin{array}{c|c|c} \bar{x}^T & \mathbf{0}_{1\times 2} & \mathbf{0}_{1\times 2} \end{array} \right]^T, \ \bar{x} \in \mathbb{R}^2\} \subset X_2. \tag{9.38}$$

At this point, by merging (9.37) and (9.38), we obtain

$$X_2 = \left\{\mathbf{x} : \mathbf{x} = \left[\begin{array}{c|c|c|c} \bar{x}^T & \tilde{x}_{12}^T & \tilde{x}_{13}^T & \cdots \end{array} \right. \left. \begin{array}{c|c|c} \bar{x}^T & \tilde{x}_{N2}^T & \tilde{x}_{N3}^T \end{array} \right]^T, \bar{x}, \tilde{x}_{i2}, \tilde{x}_{i3} \in \mathbb{R}^2\right\},$$

and then, from (9.36), it follows

$$R = \left\{\mathbf{x} : \mathbf{x} = \left[\begin{array}{c|c|c|c} \bar{\alpha}^T & \beta_1^T & \gamma_1^T & \cdots \end{array} \right. \left. \begin{array}{c|c|c} \bar{\alpha}^T & \beta_N^T & \gamma_N^T \end{array} \right]^T, \bar{\alpha}, \beta_i, \gamma_i \in \mathbb{R}^2, \mathcal{F}_{22,i}\beta_i + \mathcal{F}_{23,i}\gamma_i = \mathbf{0}_{2\times 1}\right\}. \tag{9.39}$$

For concluding the proof, we must show that the largest invariant set $M \subseteq R$ is the origin. To this purpose, we consider (9.6), include coupling terms $\hat{\xi}_{[i]}$ and neglect inputs. Then, we choose the initial state $\hat{\mathbf{x}}(0) = \left[\hat{x}_1^T(0) | \dots | \hat{x}_N^T(0)\right]^T \in R$, where, according to (9.39), $\hat{x}_i(0) = \left[\begin{array}{c|c|c} \bar{\alpha}^T & \beta_i^T & \gamma_i^T \end{array} \right]^T$, $i = 1, \dots, N$. Our aim is to find conditions on the elements of $\hat{\mathbf{x}}(0)$ that must hold in order to guarantee $\dot{\hat{\mathbf{x}}} \in R$. Recalling (9.6) and (9.7), we compute $\dot{\hat{x}}_i(0)$ as

$$F_i\hat{x}_i(0) + \sum_{j\in\mathcal{N}_i} \underbrace{\hat{A}_{ij}\left(\hat{x}_j(0) - \hat{x}_i(0)\right)}_{=0} = \left[\begin{array}{ccc} \mathcal{F}_{11,i} & \mathcal{F}_{12,i} & \mathbf{0}_2 \\ \mathcal{F}_{21,i} & \mathcal{F}_{22,i} & \mathcal{F}_{23,i} \\ -I_2 & \mathbf{0}_2 & \mathbf{0}_2 \end{array} \right] \left[\begin{array}{c} \bar{\alpha} \\ \beta_i \\ \gamma_i \end{array} \right] = \\ = \left[\begin{array}{c} \mathcal{F}_{11,i}\bar{\alpha} + \mathcal{F}_{12,i}\beta_i \\ \mathcal{F}_{21,i}\bar{\alpha} + \delta_i \\ -\bar{\alpha} \end{array} \right],$$

(9.40)

where $\delta_i = \mathcal{F}_{22,i}\beta_i + \mathcal{F}_{23,i}\gamma_i = \mathbf{0}_{2\times 1}$ since $\hat{x}_i(0) \in R$. In order to have $\dot{\hat{x}}_i(0) \in R$, it must hold, $\forall i, j \in \mathcal{V}$

$$\mathcal{F}_{11,i}\bar{\alpha} + \mathcal{F}_{12,i}\beta_i = \mathcal{F}_{11,j}\bar{\alpha} + \mathcal{F}_{12,j}\beta_j$$

which, from (9.8), implies

$$\frac{1}{C_{ti}}\beta_i = \frac{1}{C_{tj}}\beta_j.$$

This means that there is $\bar{\beta} \in \mathbb{R}^2$, such that $C_{ti}\bar{\beta} = \beta_i$, $\forall i \in \mathcal{V}$. Moreover, $\dot{\hat{x}}_i(0) \in R$ implies the following relation between the two last sub-vectors in (9.40)

$$\mathcal{F}_{22,1}(\mathcal{F}_{21,i}\bar{\alpha}) + \mathcal{F}_{23,i}(-\bar{\alpha}) = \mathbf{0}_{2\times 1}.$$

Using the assumption that $(\mathcal{F}_{22,1}\mathcal{F}_{21,i} - \mathcal{F}_{23,i})$ is invertible, one has $\bar{\alpha} = \mathbf{0}_{2\times 1}$. Therefore, in order to have $\dot{\hat{x}}_i(0) \in R$, it must hold $\hat{x}_i(0) = \left[\ \mathbf{0}_{1\times 2}\ \bar{\beta}^T\ \gamma_i^T\ \right]^T$, with $\mathcal{F}_{22,i}C_{ti}\bar{\beta} + \mathcal{F}_{23,i}\gamma_i = \mathbf{0}_{2\times 1}$. Let

$$S = \left\{\mathbf{x} : \mathbf{x} = \left[\ \mathbf{0}_{1\times 2}\ C_{t1}\bar{\beta}^T\ \gamma_1^T \mid \cdots \mid \mathbf{0}_{1\times 2}\ C_{tN}\bar{\beta}^T\ \gamma_1^T\ \right]^T, \mathcal{F}_{22,i}C_{ti}\bar{\beta} + \mathcal{F}_{23,i}\gamma_i = \mathbf{0}_{2\times 1}\right\}. \tag{9.41}$$

Since $M \subseteq S$, we pick $\tilde{\mathbf{x}}(0) \in S$ and impose $\dot{\tilde{\mathbf{x}}}(0) \in S$. This gives

$$\dot{\tilde{x}}_i(0) = F_i \begin{bmatrix} \mathbf{0}_{2\times 1} \\ C_{ti}\bar{\beta} \\ \gamma_i \end{bmatrix} = \begin{bmatrix} \bar{\beta} \\ \mathbf{0}_{2\times 1} \\ \mathbf{0}_{2\times 1} \end{bmatrix}, \qquad \forall i \in \mathcal{V}.$$

It follows that $\dot{\tilde{\mathbf{x}}}(0) \in S$ only if $\bar{\beta} = \mathbf{0}_{2\times 1}$. Since $M \subseteq S$, from (9.41), one has $M = \{0\}$. □

9.6.3 Feasibility of the plug-in test (9.15)

In order to better assess the applicability of the presented control design procedure, we perform the following analysis. For $\bar{\sigma} = 10^4$, we evaluate subproblems SP1-SP2 (see Section 9.3.3) assuming different DGU converter parameters (R_t, L_t, C_t), and then check for which combinations of parameters both subproblems are feasible. Figure 9.3 shows the points associated with triples (R_t, L_t, C_t) returning successfully passed tests (blue

circles); failed tests (indicated with red stars) refer to parameters for which at least one subproblem is infeasible. Although wide ranges for converter parameters have been considered, numerical results reveal that subproblems SP1-SP2 are always feasible when typical parameters for LV and MV AC ImGs, taken from [FSG$^+$ar, LCS$^+$ar, GLG17, GHMK12, HKM12] are used (see the green box in Figure 9.3). This means that plugging in and out operations are never denied for converters commonly found in real ImGs. Furthermore, we recall that local controllers of DGUs with same converter parameters (i.e. units associated with identical values (R_t, L_t, C_t) in the green box in Figure 9.3) can share the same matrix gain K_i. In particular, by virtue of the line-independent feature of our design method, this common quantity can be computed off-line and only once, with no need to be updated when power lines are connected/disconnected to/from DGUs.

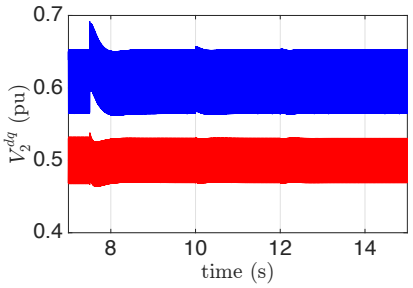

(a) d (blue) and q (red) components of the voltage at PCC_2.

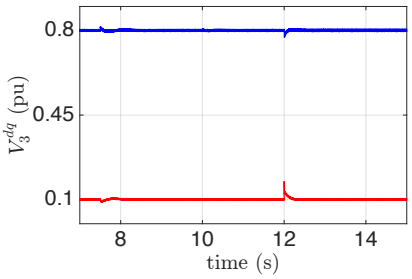

(b) d (blue) and q (red) components of the voltage at PCC_3.

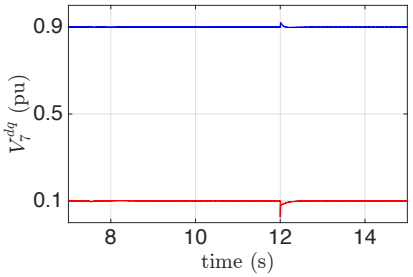

(c) d (blue) and q (red) components of the voltage at PCC_7.

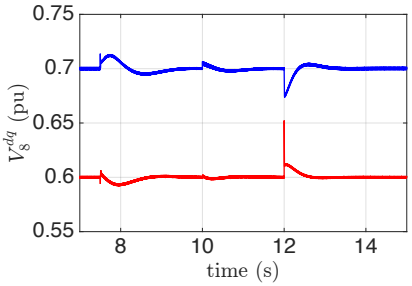

(d) d (blue) and q (red) components of the voltage at PCC_8.

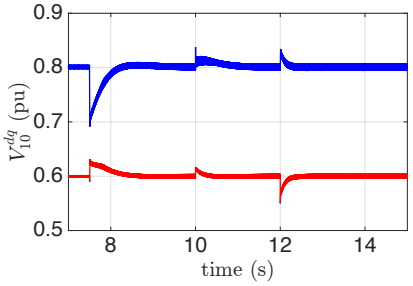

(e) d (blue) and q (red) components of the voltage at PCC_{10}.

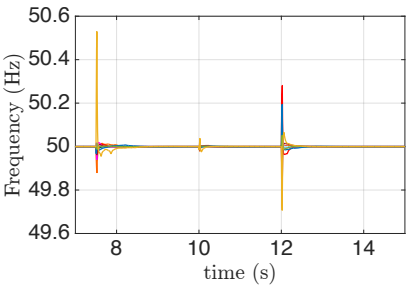

(f) Frequency of phase a at the PCCs.

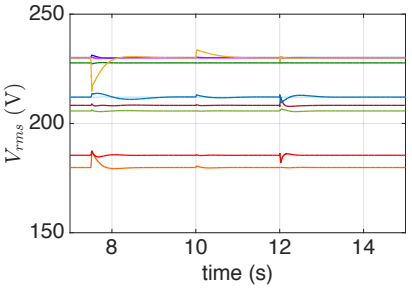

(g) RMS voltages of phase a at the PCCs.

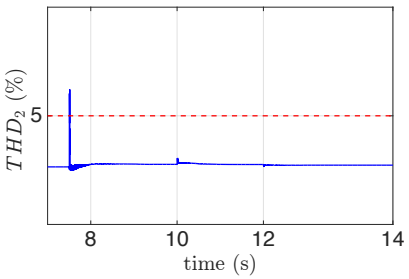

(h) THD of phase a of the voltage at PCC_2.

Figure 9.2: Performance of PnP voltage and frequency control. Connection of DGU 10, load change at PCC 10, and disconnection of DGUs 3 and 7, are performed at times $t = 7.5$ s, $t = 10$ s and $t = 12$ s, respectively.

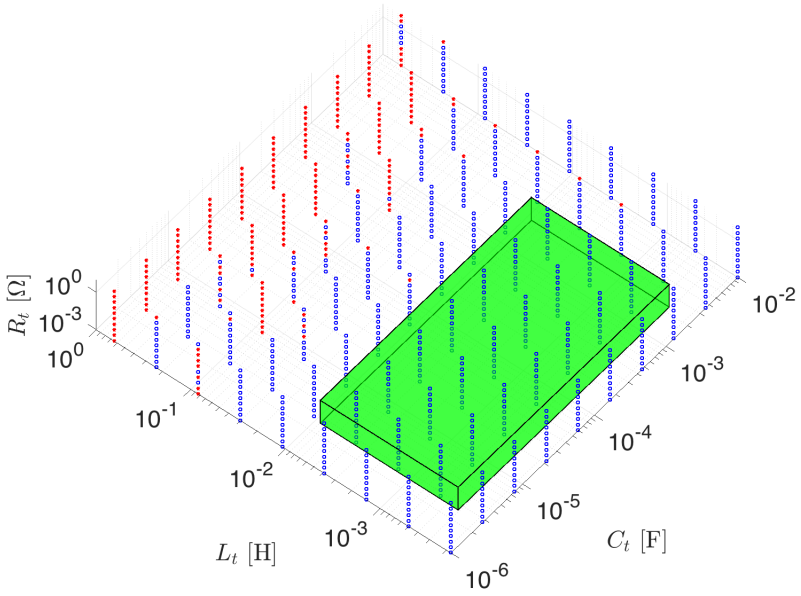

Figure 9.3: Results of subproblems SP1 and SP2 for different combinations of R_t, L_t and C_t. Blue circles indicate successfully passed tests while red stars correspond to failed ones. The green box encloses typical DGU parameters for LV and MV AC ImGs.

Chapter 10

Conclusions and future research

In this thesis, we proposed scalable control design methods for AC and DC islanded microgrids, allowing safe and reliable PnP operations of DGUs and loads.
Microgrids have recently attracted the attention of many researchers. Indeed, they are seen as one of the potential solutions for facilitating the paradigmatic change in power system operation required by the increasing penetration of RESs into electrical networks. In this context, modular control architectures (that can be easily updated when the mG topology changes) are desirable. This work proposed solutions for guaranteeing a high level of flexibility of mGs structures while addressing the main challenges arising in control of such electrical systems. Moreover, our contributions aimed at overcoming the limitations of the existing approaches from the literature. More precisely, in Part I we presented decentralized and distributed schemes for primary and secondary control of DC ImGs. At the primary layer, we proposed a PnP procedure for designing local voltage regulators capable to ensure (i) offset-free tracking of reference signals, and (ii) collective stability of the mG in spite of variations in the network topology and in the load conditions. On top the primary regulation scheme, we built a consensus-based secondary layer guaranteeing stable current sharing and voltage balancing. Moreover, we described how to design secondary regulators in a PnP manner when DGUs are added/removed to/from the network.
In Part II, we focused on AC ImGs, introducing, at the primary layer, an extension of the PnP methodology described in [RSFT15] for designing stabilizing voltage and frequency regulators capable to ensure offset-free tracking of reference signals. In order to handle totally general interconnections of DGUs and loads, we proposed two novel approximate network reduction methods. Notably, we exploited KR for deriving an equivalent load-connected model of the original ImG, thus designing PnP stabilizing regulators independently of the network topology. At the secondary layer, we proposed a distributed scheme ensuring accurate reactive power sharing.

We validated the theoretical results via extensive simulations. Moreover, some of the proposed methodologies have been also tested on real ImG platforms, showing satisfactory performance.
The methods presented in this thesis lend themselves to follow-up investigations. Specific problems deserving further study have been mentioned in the concluding remarks of Chapters 5, 7, 8 and 9. Hereafter, we describe broader research directions for the future.

- The distributed consensus scheme presented in Chapter 5 exploits a communication network for transmitting information between neighboring DGUs. So far, we have considered ideal communication links, however, in real-world applications, several non-idealities (such as transmission delays, data quantization and packet drops) must be taken into account. For this reason, future works will focus on studying the impact of such phenomena on the performance of closed-loop mGs. Analysis of networked control systems has received considerable attention from the control community in the recent past [HNX07, ZBP01]. The goal will be to reappraise methods and tools developed within this area in the context of microgrids.

- Another fundamental challenge that must be addressed when higher-level networked schemes are included in the mG control architecture is security against cyberattacks. While cyberattacks have been traditionally studied in the context of communication networks, approaches based on the analysis of the dynamics of CPSs started to appear recently [PDB13, TSJ10, Pas12]. In particular, the detection of cyberattacks requires advanced countermeasures that go beyond classic fault detection strategies for control systems. Hence, future research will study these topics in the context of mGs.

- PnP controllers can also play a crucial role in grid-connected mGs managed by an aggregator. In this framework, the main goal will be to design, in a PnP fashion, an Energy Management System (EMS) in order to let the mG behave as a *virtual* power plant. At the same time, it will be desirable to preserve the internal flexibility of the mG structure, meaning that (i) DGUs should feed local loads, and (ii) the control architecture should let DGUs and loads enter/leave the network with minimal human intervention. This will facilitate the participation of individual DGU owners to the aggregator-managed local power plant. In a broader vision, one can imagine to form mGs coalitions giving rise to virtual power plants. The scale of these larger

electrical systems could be tuned by allowing mGs to enter/leave the coalition in a modular and safe way.

- More complex models of loads (such as constant power loads or ZIP loads) will be considered. Future research will also study methods for designing PnP controllers for mGs feeding *smart loads* (like, e.g. smart buildings, smart appliances in houses, home charging stations for electric vehicles and remotely controllable smart batteries). These latter loads are controllable, hence they can be exploited for optimizing the mG operation. In addition, one can study how to apply PnP control to design an EMS with a networked structure so that, when a smart load is plugged in or out, just a limited number of local regulators are updated in an automatic fashion.

Part III

Appendices

Appendix A

Mathematical notation and definitions

Contents

A.1 Basic notation 245
A.2 Algebraic graph theory 246
A.3 AC three-phase signals 246
A.4 Signals representation 246

A.1 Basic notation

$\mathbb{R}$	Set of real numbers.
$\text{diag}[B_1, \ldots, B_n]$	Block-diagonal matrix composed of blocks B_i, $i = 1 : n$.
$\text{rank}(A)$	Rank of matrix A.
$\text{Im}(A)$	Image of matrix A.
$\text{Ker}(A)$	Kernel of matrix A.
$\|\|A\|\|_p$	Norm p of matrix A.
A^T	Transpose of matrix A.
I_α	α by α identity matrix.
$A > 0$ (resp. $A \geq 0$)	Positive definite (resp. positive-semidefinite) real symmetric matrix.
$A < 0$ (resp. $A \leq 0$)	Negative definite (resp. negative-semidefinite) real symmetric matrix.
$\mathbf{1}_\alpha$	Column vector with all α elements equal to 1.
$\mathbf{0}_\alpha$	$\alpha \times \alpha$ matrix with all elements equal to 0.
$\mathbf{0}_{\alpha\times\beta}$	$\alpha \times \beta$ matrix with all elements equal to 0.
$\times$	Product of two subspaces, $\mathbb{X} \times \mathbb{Y}$.

$\oplus$	Minkowski sum of two subspaces (orthogonal direct sum), $\mathbb{X} \oplus \mathbb{Y}$.
$\otimes$	Kronecker product of two matrices.
$\bigcup$	Set union.
$\bigcap$	Set intersection.
$\lvert S \rvert$	Cardinality of finite set S.

A.2 Algebraic graph theory

According to the definitions in [Bol98], a weighted graph $\mathcal{G} = (\mathcal{V}, \mathcal{E}, W)$ of order $n = |\mathcal{V}|$ is given by a finite set of nodes $\mathcal{V} = \{1, \ldots, n\}$, a set of edges $\mathcal{E} \subseteq \mathcal{V} \times \mathcal{V}$ and a diagonal matrix W of dimension $|\mathcal{E}| \times |\mathcal{E}|$, collecting on its diagonal weights W_e, $e \in \mathcal{E}$. An edge $e \in \mathcal{E}$ is a self-loop if $e = (i, i)$, for some $i \in \mathcal{V}$. A graph is *undirected* if $(x, y) \in \mathcal{E} \implies (y, x) \in \mathcal{E}$. In this case, the pairs (x, y) and (y, x) are considered as identical and unordered. Otherwise, the graph is said to be directed (or *digraph*). A digraph $\mathcal{G}$ is *weakly connected* if its undirected version is connected [Bulns]. The set of neighbors of node $i \in \mathcal{V}$ is $\mathcal{N}_i = \{j : (i, j) \in \mathcal{E} \text{ or } (j, i) \in \mathcal{E}\}$. The *incidence* matrix of $\mathcal{G}$ [Bol98] is denoted with $B \in \mathbb{R}^{|\mathcal{V}| \times |\mathcal{E}|}$. The *Laplacian* of $\mathcal{G}$ is the matrix $\mathbb{L} = B \cdot W \cdot B^T$ [Bol98]. With a Laplacian matrix is possible to associate a unique graph, up to the orientation of edges.

A.3 AC three-phase signals

We use $f^{abc}(t) = [f_a(t), f_b(t), f_c(t)]^T \in \mathbb{R}^3$ for denoting three-phase signals in the *abc* frame. With $f^{abc}(t)$, we associate its representation in the $dq0$ reference frame (i.e. $f^{dq0}(t)$). It is obtained from $f^{abc}(t)$ through the Park transformation [Par29], denoted with $T(\theta(t))$, $\theta(t) = \omega_0 t$, ω_0 being the nominal network angular frequency. To three-phase signals without zero-sequence component (i.e. $f^0(t) = 0$) we can associate their complex dq-representation $f^{dq}(t) = f^d(t) + \mathrm{i}\, f^q(t)$ without loss of generality.

A.4 Signals representation

For a real valued function $f(t)$, we indicate with $\mathcal{H}[f(t)]$ and $\mathscr{A}[f(t)]$ the corresponding Hilbert transform and analytic signal, respectively. They are defined as follows.

Definition A.1 (Hilbert transform)**.** *The Hilbert transform $\mathcal{H}$ of a real*

function $f(t)$ is defined as [Bra86]:

$$\mathcal{H}(f(t))(t) = p.v. \int_{-\infty}^{\infty} f(\tau)h(t-\tau)\,d\tau = \frac{1}{\pi}\ p.v. \int_{-\infty}^{\infty} \frac{f(\tau)}{t-\tau}\,d\tau$$

where $h(t) = 1/(\pi t)$ and p.v. denotes the Cauchy principal value (since the integral is improper).

Definition A.2 (Analytic signal)**.** *The analytic signal $\bar{f}(t) = \mathscr{A}[f(t)]$ is a complex-valued function, whose real part is equal to $f(t)$, and its imaginary part is $\mathcal{H}[f(t)]$. In formulae [Bra86]:*

$$\bar{f}(t) = \mathscr{A}[f(t)] = f(t) + \mathrm{i}\mathcal{H}[f(t)]\,.$$

Bibliography

[AAS01] T. Ackermann, G. Andersson, and L. Söder, "Distributed generation: a definition," *Electric power systems research*, vol. 57, no. 3, pp. 195–204, 2001.

[Abe86] E. H. Abed, "Decomposition and stability for multiparameter singular perturbation problems," *Automatic Control, IEEE Transactions on*, vol. 31, no. 10, pp. 925–934, 1986.

[AC05] R. Agaev and P. Chebotarev, "On the spectra of nonsymmetric Laplacian matrices," *Linear Algebra and its Applications*, vol. 399, pp. 157–168, 2005.

[ADSJ14] M. Andreasson, D. V. Dimarogonas, H. Sandberg, and K. H. Johansson, "Control of MTDC transmission systems under local information," in *53rd IEEE Conference on Decision and Control*, Dec 2014, pp. 1335–1340.

[ÅH06] K. J. Åström and T. Hägglund, *Advanced PID control*. ISA-The Instrumentation, Systems, and Automation Society; Research Triangle Park, NC 27709, 2006.

[AH13] J. Allmeling and W. Hammer, "PLECS-User Manual," 2013.

[AWA07] H. Akagi, E. H. Watanabe, and M. Aredes, *Instantaneous power theory and applications to power conditioning*. John Wiley & Sons, 2007.

[Bai66] F. N. Bailey, "The application of Lyapunov's second method to interconnected systems," *SIAM Journal on Control and Optimization*, vol. 3, no. 3, pp. 443–462, 1966.

[BCCZ15] S. Bolognani, R. Carli, G. Cavraro, and S. Zampieri, "Distributed reactive power feedback control for voltage regulation and loss minimization," *IEEE Transactions on Automatic Control*, vol. 60, no. 4, pp. 966–981, April 2015.

[BDL14] H. Behjati, A. Davoudi, and F. Lewis, "Modular DC–DC converters on graphs: cooperative control," *IEEE Transactions on Power Electronics*, vol. 29, no. 12, pp. 6725–6741, 2014.

[BDLG13] A. Bidram, A. Davoudi, F. L. Lewis, and J. M. Guerrero, "Distributed cooperative secondary control of microgrids using feedback linearization," *IEEE Transactions on Power Systems*, vol. 28, no. 3, pp. 3462–3470, 2013.

[BEGFB94] S. P. Boyd, L. El Ghaoui, E. Feron, and V. Balakrishnan, *Linear matrix inequalities in system and control theory*, ser. Studies in Applied Mathematics. SIAM, 1994, vol. 15.

[BFT08] P. A. Bliman and G. Ferrari-Trecate, "Average consensus problems in networks of agents with delayed communications," *Automatica*, vol. 44, no. 8, pp. 1985–1995, 2008.

[BK13] M. Babazadeh and H. Karimi, "A robust two-degree-of-freedom control strategy for an islanded microgrid," *IEEE Transactions on Power Delivery*, vol. 28, no. 3, pp. 1339–1347, 2013.

[BL88] L. Bakule and J. Lunze, "Decentralized design of feedback control for large-scale systems," *Kybernetika*, vol. 24, no. 8, pp. 3–96, 1988.

[BM05] A. Bensoussan and J. L. Menaldi, "Difference equations on weighted graphs," *Journal of Convex Analysis*, vol. 12, no. 1, pp. 13–44, 2005.

[Bol98] B. Bollobás, *Modern graph theory*, ser. Graduate Texts in Mathematics. Springer Science & Business Media, 1998, vol. 184.

[Bra86] R. N. Bracewell, *The Fourier transform and its applications*. McGraw-Hill New York, 1986, vol. 31999.

[Bulns] F. Bullo, *Lectures on Network Systems*. Version 0.85, 2016, http://motion.me.ucsb.edu/book-lns.

[BVL15] S. Bodenburg, D. Vey, and J. Lunze, "Plug-and-play reconfiguration of decentralised controllers of interconnected systems," *IFAC-PapersOnLine*, vol. 48, no. 21, pp. 353–359, 2015.

[BWAT09] S. Bando, H. Watanabe, H. Asano, and S. Tsujita, "Impact of various characteristics of electricity and heat demand on the

optimal configuration of a microgrid," *Electrical Engineering in Japan*, vol. 169, no. 2, pp. 6–13, 2009.

[BZ13] S. Bolognani and S. Zampieri, "A distributed control strategy for reactive power compensation in smart microgrids," *IEEE Transactions on Automatic Control*, vol. 58, no. 11, pp. 2818–2833, 2013.

[CD96] M. Chandorkar and D. Divan, "Decentralized operation of distributed UPS systems," in *Power Electronics, Drives and Energy Systems for Industrial Growth, 1996., Proceedings of the 1996 International Conference on*, vol. 1. IEEE, 1996, pp. 565–571.

[CD12] F. M. Callier and C. A. Desoer, *Linear system theory*. Springer Science & Business Media, 2012.

[CDGH15] S. T. Cady, A. D. Domínguez-García, and C. N. Hadjicostis, "A distributed generation control architecture for islanded AC microgrids," *IEEE Transactions on Control Systems Technology*, vol. 23, no. 5, pp. 1717–1735, Sept 2015.

[CGS+16] Y. Chen, J. M. Guerrero, Z. Shuai, Z. Chen, L. Zhou, and A. Luo, "Fast reactive power sharing, circulating current and resonance suppression for parallel inverters using resistive-capacitive output impedance," *IEEE Transactions on Power Electronics*, vol. 31, no. 8, pp. 5524–5537, Aug 2016.

[CRZ15] G. Cezar, R. Rajagopal, and B. Zhang, "Stability of interconnected DC converters," in *Decision and Control (CDC), 2015 IEEE 54th Annual Conference on*. IEEE, 2015, pp. 9–14.

[CT12] S. Y. Caliskan and P. Tabuada, "Kron reduction of power networks with lossy and dynamic transmission lines," in *Proceedings of the 51st IEEE Annual Conference on Decision and Control (CDC), 2012*. IEEE, 2012, pp. 5554–5559.

[CT14] ——, "Towards Kron reduction of generalized electrical networks," *Automatica*, vol. 50, no. 10, pp. 2586–2590, 2014.

[DB13] F. Dörfler and F. Bullo, "Kron reduction of graphs with applications to electrical networks," *IEEE Transactions on Circuits and Systems I: Regular Papers*, vol. 60, no. 1, pp. 150–163, 2013.

[DC90] E. J. Davison and T. N. Chang, "Decentralized stabilization and pole assignment for general proper systems," *IEEE Transactions on Automatic Control*, vol. 35, no. 6, pp. 652–664, Jun 1990.

[dGC12] M. da Graça Carvalho, "EU energy and climate change strategy," *Energy*, vol. 40, no. 1, pp. 19–22, 2012.

[DGVS14] T. Dragicevic, J. M. Guerrero, J. C. Vasquez, and D. Skrlec, "Supervisory control of an adaptive-droop regulated DC microgrid with battery management capability," *IEEE Transactions on Power Electronics*, vol. 29, no. 2, pp. 695–706, Feb 2014.

[DJDH14] S. V. Dhople, B. B. Johnson, F. Dörfler, and A. O. Hamadeh, "Synchronization of nonlinear circuits in dynamic electrical networks with general topologies," *IEEE Transactions on Circuits and Systems I: Regular Papers*, vol. 61, no. 9, pp. 2677–2690, 2014.

[DK84] C. A. Desoer and E. S. Kuh, *Basic circuit theory.* Tata McGraw-Hill Education, 1984.

[DLVG16] T. Dragicevic, X. Lu, J. Vasquez, and J. Guerrero, "DC microgrids–part I: A review of control strategies and stabilization techniques," *IEEE Transactions on Power Electronics*, vol. 31, no. 7, pp. 4876–4891, 2016.

[DWSM17] T. Dragicevic, D. Wu, Q. Shafiee, and L. Meng, "Distributed and decentralized control architectures for converter-interfaced microgrids," *Chinese Journal of Electrical Engineering*, vol. 3, no. 2, pp. 41–52, September 2017.

[EDI12] A. H. Etemadi, E. J. Davison, and R. Iravani, "A decentralized robust control strategy for multi-DER microgrids - part i: Fundamental concepts," *IEEE Trans. Power Del.*, vol. 27, no. 4, pp. 1843–1853, 2012.

[EMM15] A. T. Elsayed, A. A. Mohamed, and O. A. Mohammed, "DC microgrids and distribution systems: An overview," *Electric Power Systems Research*, vol. 119, pp. 407–417, 2015.

[Eur98] European Council, *The EU climate and energy package*, 1998, brussel, July 2009.

[Far10] H. Farhangi, "The path of the smart grid," *Power and Energy Magazine, IEEE*, vol. 8, no. 1, pp. 18–28, 2010.

[FC15] M. Farina and R. Carli, "Plug and play partition-based state estimation based on kalman filter," in *2015 54th IEEE Conference on Decision and Control (CDC)*, Dec 2015, pp. 3155–3160.

[fee11] Distribution Test Feeders. IEEE PES distribution system analysis subcommittee, 2011, available: http://www.ewh.ieee.org/soc/pes/dsacom/testfeeders/index.html.

[FHE17] Y. Fan, G. Hu, and M. Egerstedt, "Distributed reactive power sharing control for microgrids with event-triggered communication," *IEEE Transactions on Control Systems Technology*, vol. 25, no. 1, pp. 118–128, Jan 2017.

[FSG$^+$ar] W. Feng, K. Sun, Y. Guan, J. Guerrero, and X. Xiao, "Active power quality improvement strategy for grid-connected microgrid based on hierarchical control," *IEEE Transactions on Smart Grid*, 2017, to appear.

[FTBG06] G. Ferrari-Trecate, A. Buffa, and M. Gati, "Analysis of coordination in multi-agent systems through partial difference equations," *IEEE Transactions on Automatic Control*, vol. 51, no. 6, pp. 1058–1063, June 2006.

[FTRFTed] A. Floriduz, M. Tucci, S. Riverso, and G. Ferrari-Trecate, "Approximate kron reduction methods for electrical networks with applications to plug-and-play control of AC islanded microgrids," *IEEE Transactions on Control Systems Technology*, 2017, submitted.

[GCLL13] J. M. Guerrero, M. Chandorkar, T. Lee, and P. C. Loh, "Advanced control architectures for intelligent microgrids—part I: Decentralized and hierarchical control," *IEEE Transactions on Industrial Electronics*, vol. 60, no. 4, pp. 1254–1262, 2013.

[GHMK12] A. Ghazanfari, M. Hamzeh, H. Mokhtari, and H. Karimi, "Active power management of multihybrid fuel cell/supercapacitor power conversion system in a medium voltage microgrid," *IEEE Transactions on Smart Grid*, vol. 3, no. 4, pp. 1903–1910, Dec 2012.

[GLG17] M. S. Golsorkhi, D. D. C. Lu, and J. M. Guerrero, "A GPS-based decentralized control method for islanded microgrids," *IEEE Transactions on Power Electronics*, vol. 32, no. 2, pp. 1615–1625, Feb 2017.

[GMdV+07] J. M. Guerrero, J. Matas, L. G. de Vicuna, M. Castilla, and J. Miret, "Decentralized control for parallel operation of distributed generation inverters using resistive output impedance," *IEEE Transactions on industrial electronics*, vol. 54, no. 2, pp. 994–1004, 2007.

[GR01] C. Godsil and G. Royle, "Algebraic graph theory, volume 207 of graduate texts in mathematics," 2001.

[GVL12] G. H. Golub and C. F. Van Loan, *Matrix computations*. JHU Press, 2012, vol. 3.

[GVM+11] J. M. Guerrero, J. C. Vasquez, J. Matas, L. G. de Vicuna, and M. Castilla, "Hierarchical control of droop-controlled AC and DC microgrids–a general approach toward standardization," *IEEE Transactions on Industrial Electronics*, vol. 58, no. 1, pp. 158–172, Jan 2011.

[GZ89] R. Gusella and S. Zatt, "The accuracy of the clock synchronization achieved by tempo in berkeley unix 4.3 bsd," *IEEE Trans. Softw. Eng.*, vol. 15, no. 7, pp. 847–853, 1989.

[HGK+16] M. Hamzeh, M. Ghafouri, H. Karimi, K. Sheshyekani, and J. M. Guerrero, "Power oscillations damping in DC microgrids," *IEEE Transactions on Energy Conversion*, vol. 31, no. 3, pp. 970–980, 2016.

[HH91] Y. Hong and R. A. Horn, "The Jordan cononical form of a product of a hermitian and a positive semidefinite matrix," *Linear Algebra and Its Applications*, vol. 147, pp. 373–386, 1991.

[HHY+16] H. Han, X. Hou, J. Yang, J. Wu, M. Su, and J. M. Guerrero, "Review of power sharing control strategies for islanding operation of AC microgrids," *IEEE Transactions on Smart Grid*, vol. 7, no. 1, pp. 200–215, 2016.

[HJ12] R. A. Horn and C. R. Johnson, *Matrix analysis*. Cambridge university press, 2012.

[HKM12] M. Hamzeh, H. Karimi, and H. Mokhtari, "A new control strategy for a multi-bus MV microgrid under unbalanced conditions," *IEEE Transactions on Power Systems*, vol. 27, no. 4, pp. 2225–2232, Nov 2012.

[HL10] J. He and Y. Lee, "Analysis and design of interfacing inverter output virtual impedance in a low voltage microgrid," in *IEEE Energy Conversion Congress and Exposition (ECCE)*, Atlanta, GA, USA, September 12-16, 2010, p. 2857–2864.

[HNX07] J. P. Hespanha, P. Naghshtabrizi, and Y. Xu, "A survey of recent results in networked control systems," *Proceedings of the IEEE*, vol. 95, no. 1, pp. 138–162, 2007.

[HST79] M. F. Hassan, M. G. Singh, and A. Titli, "Near optimal decentralised control with a pre-specified degree of stability," *Automatica*, vol. 15, no. 4, pp. 483–488, 1979.

[IA09] A. Ipakchi and F. Albuyeh, "Grid of the future," *IEEE Power and Energy Magazine*, vol. 7, no. 2, pp. 52–62, March 2009.

[IEE09] "IEEE recommended practice for monitoring electric power quality," *IEEE Std 1159-2009 (Revision of IEEE Std 1159-1995)*, pp. c1–81, June 2009.

[IEE11] IEEE, "IEEE Guide for Design, Operation, and Integration of Distributed Resource Island Systems with Electric Power Systems," IEEE Standards Coordinating Committee 21, Std 1547.4, Tech. Rep. July, 2011.

[IEE17] "IEEE draft standard profile for use of IEEE 1588 precision time protocol in power system applications," *IEEE PC37.238/D21.3, January 2017*, pp. 1–40, Jan 2017.

[JLM03] A. Jadbabaie, J. Lin, and A. S. Morse, "Coordination of groups of mobile autonomous agents using nearest neighbor rules," *IEEE Transactions on Automatic Control*, vol. 48, no. 6, pp. 988–1001, 2003.

[JMLJ13] J. J. Justo, F. Mwasilu, J. Lee, and J.-W. Jung, "AC-microgrids versus DC-microgrids with distributed energy resources: A review," *Renewable and Sustainable Energy Reviews*, vol. 24, pp. 387–405, 2013.

[Kha01] H. K. Khalil, *Nonlinear systems (3rd edition).* Prentice Hall, 2001.

[KI06] F. Katiraei and M. R. Iravani, "Power management strategies for a microgrid with multiple distributed generation units," *IEEE transactions on power systems*, vol. 21, no. 4, pp. 1821–1831, 2006.

[KIL05] F. Katiraei, M. R. Iravani, and P. W. Lehn, "Micro-grid autonomous operation during and subsequent to islanding process," *IEEE Transactions on power delivery*, vol. 20, no. 1, pp. 248–257, 2005.

[KKO99] P. Kokotovic, H. K. Khalil, and J. O'reilly, *Singular perturbation methods in control: analysis and design.* Siam, 1999, vol. 25.

[KM15] S. K. Khaitan and J. D. McCalley, "Design techniques and applications of cyberphysical systems: A survey," *IEEE Systems Journal*, vol. 9, no. 2, pp. 350–365, June 2015.

[KNVD85] J. Kautsky, N. K. Nichols, and P. Van Dooren, "Robust pole assignment in linear state feedback," *International Journal of Control*, vol. 41, no. 5, pp. 1129–1155, 1985.

[Kro39] G. Kron, *Tensor analysis of networks.* J. Wiley & Sons, 1939.

[Lan87] S. Lang, "Linear algebra. Undergraduate texts in mathematics," Springer-Verlag, 1987.

[Las02] R. H. Lasseter, "Microgrids," in *Power Engineering Society Winter Meeting, 2002. IEEE*, vol. 1. IEEE, 2002, pp. 305–308.

[LCS+ar] C. Li, S. K. Chaudhary, M. Savaghebi, J. C. Vasquez, and J. M. Guerrero, "Power flow analysis for low-voltage AC and DC microgrids considering droop control and virtual impedance," *IEEE Transactions on Smart Grid*, 2017, to appear.

[LD14] L. Luo and S. V. Dhople, "Spatiotemporal model reduction of inverter-based islanded microgrids," *IEEE Transactions on Energy Conversion*, vol. 29, no. 4, pp. 823–832, 2014.

[LKF15] S. Lucia, M. Kögel, and R. Findeisen, "Contract-based predictive control of distributed systems with plug and play capabilities," *IFAC-PapersOnLine*, vol. 48, no. 23, pp. 205–211, 2015.

[LM06] H. Lund and E. Münster, "Integrated energy systems and local energy markets," *Energy Policy*, vol. 34, no. 10, pp. 1152 – 1160, 2006. [Online]. Available: http://www.sciencedirect.com/science/article/pii/S0301421504003118

[LP04] R. H. Lasseter and P. Paigi, "Microgrid: A conceptual solution," in *Power Electronics Specialists Conference, 2004. PESC 04. 2004 IEEE 35th Annual*, vol. 6. IEEE, 2004, pp. 4285–4290.

[Lu13] L.-Y. Lu, "Consensus-based pf and qv droop control for multiple parallel-connected inverters in lossy networks," in *Industrial Electronics (ISIE), 2013 IEEE International Symposium on*. IEEE, 2013, pp. 1–6.

[Lun92] J. Lunze, *Feedback control of large scale systems*. Upper Saddle River, NJ, USA: Prentice Hall, Systems and Control Engineering, 1992.

[MASSG12] A. Micallef, M. Apap, C. Spiteri-Staines, and J. M. Guerrero, "Secondary control for reactive power sharing in droop-controlled islanded microgrids," in *Industrial Electronics (ISIE), 2012 IEEE International Symposium on*. IEEE, 2012, pp. 1627–1633.

[MBB97] J. Machowski, J. Bialek, and J. R. Bumby, *Power system dynamics and stability*. John Wiley & Sons, 1997.

[MDGV14] L. Meng, T. Dragicevic, J. M. Guerrero, and J. C. Vasquez, "Dynamic consensus algorithm based distributed global efficiency optimization of a droop controlled DC microgrid," in *Energy Conference (ENERGYCON), 2014 IEEE International*, 2014, pp. 1276–1283.

[MDRP+16] L. Meng, T. Dragicevic, J. Roldán-Pérez, J. C. Vasquez, and J. M. Guerrero, "Modeling and sensitivity study of consensus

algorithm-based distributed hierarchical control for DC microgrids," *IEEE Transactions on Smart Grid*, vol. 7, no. 3, pp. 1504–1515, 2016.

[Mic] Microgrid Research Laboratory, Aalborg University, http://www.et.aau.dk/department/laboratory-facilities/intelligent-microgrid-lab/.

[MKKG10] R. Moradi, H. Karimi, and M. Karimi-Ghartemani, "Robust decentralized control for islanded operation of two radially connected DG systems," in *Proceedings of IEEE International Symposium on Industrial Electronics (ISIE 2010)*, Bari, Italy, 4-7 July, 2010, pp. 2272–2277.

[MNLD15] S. Moayedi, V. Nasirian, F. L. Lewis, and A. Davoudi, "Team-oriented load sharing in parallel DC–DC converters," *IEEE Transactions on Industry Applications*, vol. 51, no. 1, pp. 479–490, 2015.

[MQLD14] A. Maknouninejad, Z. Qu, F. L. Lewis, and A. Davoudi, "Optimal, nonlinear, and distributed designs of droop controls for DC microgrids," *IEEE Transactions on Smart Grid*, vol. 5, no. 5, pp. 2508–2516, 2014.

[MS11] L. Miclea and T. Sanislav, "About dependability in cyber-physical systems," in *Design & Test Symposium (EWDTS), 2011 9th East-West*. IEEE, 2011, pp. 17–21.

[MSFT+17] L. Meng, Q. Shafiee, G. Ferrari-Trecate, H. Karimi, D. Fulwani, X. Lu, and J. M. Guerrero, "Review on control of DC microgrids and multiple microgrid clusters," *IEEE Journal of Emerging and Selected Topics in Power Electronics*, vol. 5, no. 3, pp. 928–948, Sept 2017.

[Mul10] C. Muller, "User's guide on the use of pscad," *Manitoba: Manitoba HVDC research centre*, 2010.

[MVVG15] V. Mariani, F. Vasca, J. Vasquez, and J. Guerrero, "Model order reductions for stability analysis of islanded microgrids with droop control," *Industrial Electronics, IEEE Transactions on*, vol. 62, no. 7, pp. 4344–4354, July 2015.

[MZT+16] L. Meng, X. Zhao, F. Tang, M. Savaghebi, T. Dragicevic, J. C. Vasquez, and J. M. Guerrero, "Distributed voltage unbalance compensation in islanded microgrids by using a dynamic consensus algorithm," *IEEE Transactions on Power Electronics*, vol. 31, no. 1, pp. 827–838, 2016.

[OSM04] R. Olfati-Saber and R. M. Murray, "Consensus problems in networks of agents with switching topology and time-delays," *IEEE Transactions on Automatic Control*, vol. 49, no. 9, pp. 1520–1533, 2004.

[Par29] R. H. Park, "Two-reaction theory of synchronous machines generalized method of analysis-part I," *Transactions of the American Institute of Electrical Engineers*, vol. 48, no. 3, pp. 716–727, 1929.

[Pas12] F. Pasqualetti, *Secure control systems: a control-theoretic approach to cyber-physical security.* University of California, Santa Barbara, 2012.

[PDB13] F. Pasqualetti, F. Dörfler, and F. Bullo, "Attack detection and identification in cyber-physical systems," *IEEE Transactions on Automatic Control*, vol. 58, no. 11, pp. 2715–2729, 2013.

[Pea65] M. C. Pease, *Methods of matrix algebra.* Academic Press New York, 1965.

[PL06] P. Piagi and R. H. Lasseter, "Autonomous control of microgrids," in *Power Engineering Society General Meeting, 2006. IEEE.* IEEE, 2006, pp. 8–pp.

[PMar] C. D. Persis and N. Monshizadeh, "Bregman storage functions for microgrid control," *IEEE Transactions on Automatic Control*, to appear.

[PSD70] P. Penfield, R. Spence, and S. Duinker, "A generalized form of Tellegen's theorem," *IEEE Transactions on Circuit Theory*, vol. 17, no. 3, pp. 302–305, Aug 1970.

[PTP08] A. Phadkeand, J. Thorp, and M. Pai, *Synchronized Phasor Measurements and Their Applications.* New York, NY, USA: Springer, 2008.

[RBFTP16] S. Riverso, F. Boem, G. Ferrari-Trecate, and T. Parisini, "Plug-and-play fault detection and control-reconfiguration for a class of nonlinear large-scale constrained systems," *IEEE Transactions on Automatic Control*, vol. 61, no. 12, pp. 3963–3978, 2016.

[RE09] A. M. Rahimi and A. Emadi, "Active damping in DC/DC power electronic converters: A novel method to overcome the problems of constant power loads," *IEEE Transactions on Industrial Electronics*, vol. 56, no. 5, pp. 1428–1439, 2009.

[RFFT13] S. Riverso, M. Farina, and G. Ferrari-Trecate, "Design of plug-and-play model predictive control: an approach based on linear programming," in *Proceedings of the 52nd IEEE Conference on Decision and Control*, Florence, Italy, December 10-13, 2013, pp. 6530–6535.

[RFFT15] ——, "Plug-and-play state estimation and application to distributed output-feedback model predictive control," *European Journal of Control*, vol. 25, pp. 17–26, 2015.

[RFSFT13] S. Riverso, M. Farina, R. Scattolini, and G. Ferrari-Trecate, "Plug-and-play distributed state estimation for linear systems," in *Proceedings of the 52nd IEEE Conference on Decision and Control*, Florence, Italy, December 10-13, 2013, pp. 4889–4894.

[RFT15] S. Riverso and G. Ferrari-Trecate, "Plug-and-play distributed model predictive control with coupling attenuation," *Optimal Control Applications and Methods*, vol. 36, no. 3, pp. 292–305, 2015.

[RMC+07] M. R. Raupach, G. Marland, P. Ciais, C. Le Quéré, J. G. Canadell, G. Klepper, and C. B. Field, "Global and regional drivers of accelerating CO2 emissions," *Proceedings of the National Academy of Sciences*, vol. 104, no. 24, pp. 10 288–10 293, 2007.

[RSFT14] S. Riverso, F. Sarzo, and G. Ferrari-Trecate, "Plug-and-play voltage and frequency control of islanded microgrids with meshed topology," Dipartimento di Ingegneria Industriale e dell'Informazione, Università degli Studi di Pavia, Pavia, Italy, Tech. Rep., 2014. [Online]. Available: arXiv:1405.2421

[RSFT15] ——, "Plug-and-play voltage and frequency control of islanded microgrids with meshed topology," *IEEE Transactions on Smart Grid*, vol. 6, no. 3, pp. 1176–1184, 2015.

[RTV+17] S. Riverso, M. Tucci, J. C. Vasquez, J. M. Guerrero, and G. Ferrari-Trecate, "Plug-and-play and coordinated control for bus-connected AC islanded microgrids," Dipartimento di Ingegneria Industriale e dell'Informazione, Università degli Studi di Pavia, Tech. Rep., 2017. [Online]. Available: arXiv:1703.10222

[RTV+ar] ——, "Stabilizing plug-and-play regulators and secondary coordinated control for AC islanded microgrids with bus-connected topology," *Applied Energy*, 2017, to appear.

[Sch15] J. Schiffer, "Stability and power sharing in microgrids," Ph.D. thesis, TU Berlin, Germany, 2015, available: https://opus4.kobv.de/opus4-tuberlin/files/6940/schiffer_johannes.pdf.

[SDA+14] Q. Shafiee, T. Dragicevic, F. Andrade, J. C. Vasquez, and J. M. Guerrero, "Distributed consensus-based control of multiple DC-microgrids clusters," in *Industrial Electronics Society, IECON 2014-40th Annual Conference of the IEEE*. IEEE, 2014, pp. 2056–2062.

[SDVG14a] Q. Shafiee, T. Dragicevic, J. C. Vasquez, and J. M. Guerrero, "Modeling, stability analysis and active stabilization of multiple DC-microgrid clusters," in *2014 IEEE International Energy Conference (ENERGYCON)*, May 2014, pp. 1284–1290.

[SDVG14b] Q. Shafiee, T. Dragičević, J. C. Vasquez, and J. M. Guerrero, "Hierarchical control for multiple DC-microgrids clusters," *IEEE Transactions on Energy Conversion*, vol. 29, no. 4, pp. 922–933, 2014.

[SGV14] Q. Shafiee, J. M. Guerrero, and J. C. Vasquez, "Distributed secondary control for islanded microgrids—a novel approach," *IEEE Transactions on power electronics*, vol. 29, no. 2, pp. 1018–1031, 2014.

[SHK+17] J. Schiffer, C. A. Hans, T. Kral, R. Ortega, and J. Raisch, "Modeling, analysis, and experimental validation of clock drift

effects in low-inertia power systems," *IEEE Transactions on Industrial Electronics*, vol. 64, no. 7, pp. 5942–5951, July 2017.

[SOA+14] J. Schiffer, R. Ortega, A. Astolfi, J. Raisch, and T. Sezi, "Conditions for stability of droop-controlled inverter-based microgrids," *Automatica*, vol. 50, no. 10, pp. 2457–2469, 2014.

[SP96] S. Skogestad and I. Postlethwaite, *Multivariable feedback control: analysis and design*. New York, NY, USA: John Wiley & Sons, 1996.

[SPDB13] J. W. Simpson-Porco, F. Dörfler, and F. Bullo, "Synchronization and power sharing for droop-controlled inverters in islanded microgrids," *Automatica*, vol. 49, no. 9, pp. 2603–2611, 2013.

[SSD+14] Q. Shafiee, C. Stefanovic, T. Dragicevic, P. Popovski, J. Vasquez, and J. Guerrero, "Robust networked control scheme for distributed secondary control of islanded microgrids," *IEEE Trans. Ind. Electron.*, vol. 61, no. 10, pp. 5363–5374, 2014.

[SSK17] M. S. Sadabadi, Q. Shafiee, and A. Karimi, "Plug-and-play voltage stabilization in inverter-interfaced microgrids via a robust control strategy," *IEEE Transactions on Control Systems Technology*, vol. 25, no. 3, pp. 781–791, May 2017.

[SSRS16] J. Schiffer, T. Seel, J. Raisch, and T. Sezi, "Voltage stability and reactive power sharing in inverter-based microgrids with consensus-based distributed voltage control," *IEEE Transactions on Control Systems Technology*, vol. 24, no. 1, pp. 96–109, 2016.

[TFRFT15] M. Tucci, A. Floriduz, S. Riverso, and G. Ferrari-Trecate, "Kron reduction methods for plug-and-play control of AC islanded microgrids with arbitrary topology," Dipartimento di Ingegneria Industriale e dell'Informazione, Università degli Studi di Pavia, Tech. Rep., 2015. [Online]. Available: arXiv:1510.07873

[TFRFT16] ——, "Plug-and-play control of AC islanded microgrids with general topology," in *Proceedings of the 15th European Control Conference*, 2016, pp. 1493–1500.

[TFT17a] M. Tucci and G. Ferrari-Trecate, "A scalable line-independent design algorithm for voltage and frequency control in ac islanded microgrids," Dipartimento di Ingegneria Industriale e dell'Informazione, Università degli Studi di Pavia, Tech. Rep., 2017. [Online]. Available: arXiv:1703.02336

[TFT17b] ——, "Voltage and frequency control in AC islanded microgrids: a scalable, line-independent design algorithm," in *Proceedings of the 20th IFAC World Congress*, 2017, pp. 13 922–13 927.

[TFTed] ——, "A scalable, line-independent control design algorithm for voltage and frequency stabilization in AC islanded microgrids," *Automatica*, 2017, submitted.

[TJUM97] A. Tuladhar, K. Jin, T. Unger, and K. Mauch, "Parallel operation of single phase inverter modules with no control interconnections," in *Proceedings of Applied Power Electronics Conference and Exposition, 1997. APEC'97*, vol. 1. IEEE, 1997, pp. 94–100.

[TLR11] R. Teodorescu, M. Liserre, and P. Rodriguez, *Grid converters for photovoltaic and wind power systems*. Chichester, West Sussex, UK: John Wiley & Sons, 2011.

[TMGFT16] M. Tucci, L. Meng, J. M. Guerrero, and G. Ferrari-Trecate, "A consensus-based secondary control layer for stable current sharing and voltage balancing in DC microgrids," Dipartimento di Ingegneria Industriale e dell'Informazione, Università degli Studi di Pavia, Tech. Rep., 2016. [Online]. Available: arXiv:1603.03624

[TMGFT17] ——, "Plug-and-play control and consensus algorithms for current sharing in DC microgrids," in *Proceedings of the 20th IFAC World Congress*, 2017, pp. 12 440–12 445.

[TMGFTed] ——, "Stable current sharing and voltage balancing in DC microgrids: a consensus-based secondary control layer," *Automatica*, 2017, submitted.

[TRFT16] M. Tucci, S. Riverso, and G. Ferrari-Trecate, "Voltage stabilization in DC microgrids through coupling-independent plug-

and-play controllers," in *Proceedings of the 55th IEEE Conference on Decision and Control*, 2016, pp. 4944–4949.

[TRFT17] ——, "Voltage stabilization in DC microgrids: an approach based on line-independent plug-and-play controllers," Dipartimento di Ingegneria Industriale e dell'Informazione, Università degli Studi di Pavia, Tech. Rep., 2017. [Online]. Available: arXiv:1609.02456

[TRFTar] ——, "Line-independent plug-and-play controllers for voltage stabilization in DC microgrids," *IEEE Transactions on Control Systems Technology*, 2017, to appear.

[TRV+15a] M. Tucci, S. Riverso, J. C. Vasquez, J. M. Guerrero, and G. Ferrari-Trecate, "A decentralized scalable approach to voltage control of DC islanded microgrids," Dipartimento di Ingegneria Industriale e dell'Informazione, Università degli Studi di Pavia, Tech. Rep., 2015. [Online]. Available: arXiv:1503.06292

[TRV+15b] ——, "Voltage control of DC islanded microgrids: a decentralized scalable approach," in *Proceedings of the 54th IEEE Conference on Decision and Control*, 2015, pp. 3149–3154.

[TRV+16] ——, "A decentralized scalable approach to voltage control of DC islanded microgrids," *IEEE Transactions on Control Systems Technology*, vol. 24, no. 6, pp. 1965–1979, 2016.

[TSJ10] A. Teixeira, H. Sandberg, and K. H. Johansson, "Networked control systems under cyber attacks with applications to power networks," in *American Control Conference (ACC), 2010*. IEEE, 2010, pp. 3690–3696.

[Uni98] United Nations, "Kyoto protocol to the united nations framework convention on climate change," 1998, available: http://unfccc.int/resource/docs/convkp/kpeng.pdf.

[Vak96] D. Vakman, "On the analytic signal, the Teager-Kaiser energy algorithm, and other methods for defining amplitude and frequency," *IEEE Transactions on Signal Processing*, vol. 44, no. 4, pp. 791–797, Apr 1996.

[VDBH+05] K. Vanthournout, K. De Brabandere, E. Haesen, J. Van den Keybus, G. Deconinck, and R. Belmans, "Agora: Distributed tertiary control of distributed resources," in *Proc. 15th Power Systems Computation Conf*, 2005, pp. 1–7.

[VDH08] K. Visscher and S. W. H. De Haan, "Virtual synchronous machines (VSG's) for frequency stabilisation in future grids with a significant share of decentralized generation," in *SmartGrids for Distribution, 2008. IET-CIRED. CIRED Seminar*. IET, 2008, pp. 1–4.

[VdS10] A. Van der Schaft, "Characterization and partial synthesis of the behavior of resistive circuits at their terminals," *Systems & Control Letters*, vol. 59, no. 7, pp. 423–428, 2010.

[VGS+13] J. C. Vasquez, J. M. Guerrero, M. Savaghebi, J. Eloy-Garcia, and R. Teodorescu, "Modeling, analysis, and design of stationary-reference-frame droop-controlled parallel three-phase voltage source inverters," *IEEE Trans. Ind. Electron.*, vol. 60, no. 4, pp. 1271–1280, 2013.

[Vig09] J. Vig, "Quartz crystal resonators and oscillators for frequency control and timing applications: A tutorial," U.S. Army Communications-Electronics Command, Fort Monmouth, NJ, USA, Tech. Rep. Tech. Rep. SLCET-TR-88-1 (Rev. 8.4.2), 2009.

[VSZ95] V. Venkatasubramanian, H. Schattler, and J. Zaborszky, "Fast Time-Varying Phasor Analysis in the Balanced Three-Phase Large Electric Power System," *IEEE Transactions on Automatic Control*, vol. 40, no. 11, pp. 1975–1982, 1995.

[VWB11] P. P. Varaiya, F. F. Wu, and J. W. Bialek, "Smart operation of smart grid: Risk-limiting dispatch," *Proceedings of the IEEE*, vol. 99, no. 1, pp. 40–57, 2011.

[YI10] A. Yazdani and R. Iravani, *Voltage-Sourced Converters in Power Systems: Modeling, Control, and Applications*. Hoboken, New Jersey, USA: John Wiley & Sons, 2010.

[YJY16] H. Yang, B. Jiang, and H. Yang, "Fault tolerant cooperative control for multiple unmanned aerial vehicle systems with

plugging operations," *Proceedings of the Institution of Mechanical Engineers, Part I: Journal of Systems and Control Engineering*, vol. 230, no. 8, pp. 820–829, 2016.

[ZBP01] W. Zhang, M. S. Branicky, and S. M. Phillips, "Stability of networked control systems," *IEEE Control Systems*, vol. 21, no. 1, pp. 84–99, 2001.

[ZD15] J. Zhao and F. Dörfler, "Distributed control and optimization in DC microgrids," *Automatica*, vol. 61, pp. 18–26, 2015.

[ZPR+13] M. N. Zeilinger, Y. Pu, S. Riverso, G. Ferrari-Trecate, and C. N. Jones, "Plug and play distributed model predictive control based on distributed invariance and optimization," in *Decision and Control (CDC), 2013 IEEE 52nd Annual Conference on*. IEEE, 2013, pp. 5770–5776.

[ZS10] A. Zecevic and D. D. Siljak, *Control of complex systems: Structural constraints and uncertainty*. Springer Science & Business Media, 2010.

[ZW09] Q.-C. Zhong and G. Weiss, "Static synchronous generators for distributed generation and renewable energy," in *Power Systems Conference and Exposition, 2009. PSCE'09. IEEE/PES*. IEEE, 2009, pp. 1–6.